IMPERIAL COLLEGE LONDON

DEPARTMENT OF MECHANICAL ENGINEERING

SHOCK–INDUCED ENERGY TRANSFERS IN MHD

Francis Obiora Nwobu

A thesis submitted for the degree of Doctor of Philosophy

May 2019

Abstract

In magnetohydrodynamic (MHD) flow control, an applied magnetic field can manipulate the flow properties of an ionised gas in order to improve vehicle performance in high–speed flight applications. Shock–wave turbulence interactions (SWTIs) are a fundamental feature of high–speed flows. They play a key role in predictions of transition, drag and heat transfer in flow control configurations. In hydrodynamics, linear theory is a good predictor of turbulent kinetic energy amplification in SWTIs, however, at present similar linear analysis is missing from MHD.

In the present study, linear theory is developed and combined with direct numerical simulations (DNS) to investigate the production of vorticity (an indicator of turbulent kinetic energy) by small–amplitude entropy disturbances incident on an isolated fast shock in two– and three–dimensions. Entropy disturbances in the form of planar waves and Gaussian-distributed spots are considered. The angle of an imposed mean magnetic field is varied in order to study downstream vorticity production for thermodynamic and magnetic pressure–dominated regimes respectively. Linear theory indicates total vorticity production is suppressed for magnetic pressure–dominated flows, however, vorticity transport in the fastest refracted mode is amplified. DNS results of two–dimensional planar waves (of amplitude 1% the base flow) incident on a fast shock at angles above and below a critical value compare well with linear theory predictions. DNS results near the critical angle noticeably diverge from the linear theory. However, the linear reconstruction of the two–dimensional entropy spot–fast shock interaction shows very good agreement with DNS for 1% and 10% disturbances - a 10% upstream turbulence intensity is common in SWTIs studies. DNS of the three–dimensional entropy spot–fast shock interaction shows in–plane vorticity production similar to the two–dimensional case with the three–dimensional distribution appearing to constitute an extrusion of in–plane structures.

Acknowledgements

I am sincerely grateful to my supervisor, Dr. Emile Touber, for his help and support throughout my PhD. Our many interesting discussions greatly aided me in forming a deeper understanding of my topic and how it may relate to other areas of research. I would also like to thank my associate supervisor, Dr. Salvador Navarro-Martinez, for his advice and development of the numerical solver, CompReal, which has been put to significant use throughout my PhD. Dr. Nicolas Alferez is another who has my sincere gratitude. The help you have provided me in developing various codes throughout my PhD has been essential and your questions during our discussions always thoughtful. I am also grateful to Dr. Teddy Szemberg O'Connor for being a helpful presence throughout much of my PhD.

I would like to thank my family, as I would not have been able to persevere through all of the difficult periods in my PhD without their love, support and understanding.

Finally, I extend my gratitude to the EPSRC as my research would not have been possible without the financial support of an EPSRC studentship.

Declaration of Authorship

I, Francis Obiora Nwobu, declare that this thesis and all work presented in it is my own and based on the results of original research completed during my PhD studentship at Imperial College London. Any work contained that belongs to other authors is properly referenced.

Copyright Declaration

The copyright of this thesis rests with the author. Unless otherwise indicated, its contents are licensed under a Creative Commons Attribution-Non Commercial 4.0 International Licence (CC BY-NC). Under this licence, you may copy and redistribute the material in any medium or format. You may also create and distribute modified versions of the work. This is on the condition that: you credit the author and do not use it, or any derivative works, for a commercial purpose.

When reusing or sharing this work, ensure you make the licence terms clear to others by naming the licence and linking to the licence text. Where a work has been adapted, you should indicate that the work has been changed and describe those changes. Please seek permission from the copyright holder for uses of this work that are not included in this licence or permitted under UK Copyright Law.

Contents

1 Introduction **24**

1.1 MHD flow control 24

1.2 Linear interaction analysis 25

1.3 Thesis objectives 29

2 Governing Equations **31**

2.1 Plasmas 31

2.1.1 Ionisation 31

2.1.2 Quasi-neutrality 33

2.1.3 Plasma kinetic theory 33

2.2 Ideal MHD equations 44

2.2.1 Formulation 44

2.2.2 Hyperbolicity of the ideal MHD equations 46

3 Numerical Methods **51**

3.1 Finite difference methods for conservation laws 51

3.1.1 Dispersion-Relation-Preserving schemes 53

3.1.2 Selective filters 56

3.1.3 Shock capture: localised artificial diffusivity 57

3.1.4 Characteristic boundary conditions 60

3.2 The $\nabla \cdot \boldsymbol{B} = 0$ constraint 64

3.3 Validation of MHD solver 66

3.3.1 Slow shock-wave 67

3.3.2 Dai and Woodward shock problem 69

3.3.3 Magnetic Sod shock problem 71

3.3.4 Advection of B_x . . . 73
3.3.5 Circularly-polarised Alfvén wave . . . 76
3.3.6 Orszag-Tang vortex . . . 77
3.3.7 Rotor problem . . . 80
3.3.8 Blast wave problem . . . 81

4 Shock Refraction Problem **83**

4.1 Base flow: MHD shocks . . . 83
4.1.1 Rankine–Hugoniot jump conditions . . . 84
4.1.2 Hugoniot curves . . . 86
4.1.3 Solutions to MHD shocks in terms of density ratio . . . 91
4.2 Linear interaction analysis . . . 94
4.2.1 Eigen-decomposition of ideal MHD Equations . . . 94
4.2.2 Linearised Rankine–Hugoniot jump conditions . . . 99
4.2.3 Fast shock linear interaction problem . . . 102
4.2.4 Refraction coefficients: comparison with Westphal & McKenzie . . . 109
4.2.5 Modal response of magneto–acoustic vorticity transport . . . 110
4.3 Plane wave interaction with a fast shock . . . 124
4.3.1 Numerical method . . . 124
4.3.2 Perturbed field contours . . . 129
4.3.3 Error analysis in physical space . . . 133
4.4 Gaussian-distributed entropy spot interaction with a fast shock . . . 149
4.4.1 Numerical method . . . 149
4.4.2 LIA reconstruction . . . 152
4.4.3 Two–dimensional post–shock field topology . . . 153
4.4.4 DNS vs. LIA reconstruction . . . 160
4.4.5 Mean magnetic field angle influence and the “magnetosonic” condition . . . 163
4.4.6 Three-dimensional interaction: in–plane vorticity generation . . . 167

5 Conclusions **169**

A Magneto–acoustic eigenmodes **183**

A.1 Parallel alignment between wavevector and mean magnetic field . . . 183
A.2 Perpendicular alignment between wavevector and mean magnetic field . . . 186

B Shock refraction problem **188**

B.1 Scattering matrix: Three–dimensional perturbed shock system 188

B.2 Scattering matrix: Decoupled perturbed shock system 193

List of Figures

1.1 Boeing X-51A Waverider, an experimental research scramjet, under the wing of a Air Force Flight Test Center B-52 (U.S. Air Force photo/Chad Bellay). 26

1.2 Projection of weak turbulent fluctuations onto eigenmode basis of an Euler flow. 28

3.1 Slow switch–off shock profiles of B_y at a non–dimensional time, $t = 0.2$, for different values of the user defined artificial resistivity constant; $C_\eta = 0.0$ (black circles), $C_\eta = 0.1$ (blue crosses), $C_\eta = 1.0$ (red triangles), $C_\eta = 10.0$ (green asterisk), $C_\eta = 100.0$ (pink crosses). 68

3.2 (Left) Maximum relative spurious noise (%) in semi-logarithmic scale on the left-axis (circles) for B_y and non–dimensional numerical shock thickness on right axis (triangles) at a non–dimensional time, $t = 0.2$, for different values of , artificial resistivity constant, C_η. (Right) Slow switch–off shock B_y profiles at non–dimensional time, $t = 0.2$, for $C_\eta = 10.0$. CompReal data (black) and data from [Kawai, 2013] (red crosses) both shown. 69

3.3 Dai-Woodward shock problem profiles of thermodynamic and flow properties, at a non–dimensional time, $t = 0.2$, for different grid sizes; $N = 4000$ (solid black line), $N = 800$ (blue circles), $N = 400$ (red crosses). Reference data (grey line) extracted from [Ryu and Jones, 1995]. 70

3.4 Dai-Woodward shock problem profiles of magnetic field components at a non–dimensional time, $t = 0.2$, for different grid sizes; $N = 4000$ (solid black line), $N = 800$ (blue circles), $N = 400$ (red crosses). Reference data (grey line) extracted from [Ryu and Jones, 1995]. . . 71

3.5 1.5d Magnetic Sod shock problem flow property profiles at a non–dimensional time, $t = 0.1$, for different grid sizes; $N = 4000$ (solid black line), $N = 800$ (blue circles), $N = 400$ (red crosses). Reference data (grey line) extracted from [Ryu and Jones, 1995]. 72

3.6 $x - t$ contours of 1.5d magnetic Sod shock problem with non-reflecting boundary conditions. 8 equally-spaced contours of density, pressure, x-velocity and y-magnetic field plotted for $N = 800$ 74

3.7 2d advection of B_x. (Left) Time integral of L_2-error in $\nabla \cdot \boldsymbol{B}$ within the time interval, $0 \leq t \leq 1$. Results shown for different c_r values on $N \times N$ grid of resolution $N = 64$ (solid line) and $N = 256$ (dashed line). (Right) Time evolution of maximum $\nabla \cdot \boldsymbol{B}$ error on $N \times N$ grid of resolution $N = 64$ - no divergence–cleaning (dashed line) and mixed–correction GLM cleaning for $c_r = 0.19$ (solid line) shown. 75

3.8 2d advection of B_x. $\nabla \cdot \boldsymbol{B}$ contours shown in the range, $-0.3 \leq \nabla \cdot \boldsymbol{B} \leq 0.3$ at $t =$ 0.0, 0.1, 0.25, 0.5 (left to right) for $N = 256$. 75

3.9 (Left) Grid size ($N \times N$) dependency of L_2 (crosses) and L_∞ (circles) errors in the perpendicular component of the magnetic field in the orthogonal wavevector basis, $B_\perp$, after 5 passages through the computational domain of a circularly–polarised Alfvén wave propagating at 30° with respect to the x-axis. Slope, error $\propto N^{-4}$, also shown (solid red line). (Right) $B_\perp$ of c–p Alfvén wave at $y = 1/(2 \sin 30°)$, for non–dimensional time, $t = 5.0$, equivalent to 5 wave passages through the domain. Profiles shown for exact solution (black line) and different grid sizes: $N = 32$ (blue crosses), $N = 48$ (green circles) and $N = 64$ (pink triangles). 77

3.10 2.5d numerical simulation of Orszag-Tang vortex. 20 equally-spaced contours of density, ρ, magnetic pressure, $p_b = ||\boldsymbol{B}||^2/2$, and artificial resistivity, η_{art}, plotted for (from left-to-right) $N = 200$ result at $t = 0.5$, 1.0, 2.0, 3.14 and $N = 1600$ result at $t = 3.14$. Domain is restricted to $x \in [0, \pi]$, $y \in [0, 2\pi]$ 78

3.11 Density and normalised artificial resistivity profiles for 2.5d numerical simulation of Orszag-Tang vortex. Results plotted for $t = 3.14$ at $y = 0.5\pi$ on different grid sizes; $N = 200$ (blue circles), $N = 400$ (red triangles), $N = 800$ (green crosses), $N = 1600$ (black line). 79

3.12 2.5d numerical simulation of rotor problem. 20 equally-spaced contours plotted for pressure, $0.03 \leq p \leq 1.98$, Mach number, $0.0 \leq M = ||\boldsymbol{u}||/c \leq 4.0$, and magnetic pressure, $0.0018 \leq p_b = ||\boldsymbol{B}||^2/2 \leq 2.6$, at $t = 0.15$ on $N = 400, 1600$ grids ($N \times N$ grid points) 81

3.13 2.5d numerical simulation of blast wave problem. 20 equally-spaced contours of density, ρ, magnetic pressure, $p_b = ||\boldsymbol{B}||^2/2$, and artificial resistivity, η_{art}, plotted for $N = 400$ ($N \times N$ grid points) at $t = 0.02$ 82

4.1 Intersections between "Hugoniot" curves in MHD (thick solid line) and gas dynamics (red dashed line) and MHD "Rankine" line (thin solid line) shown for Mach number, $M_1 = 2.0$, and magnetic field incidence angle, $\varphi_1 = 26.56505°$ at a range of normal magnetic field strengths, $r_{n,1} = b_{n,1}/c_{o,1} = B_n/\sqrt{\gamma p_1}$. In (b), solid lines become lighter with decreasing $r_{n,1}$. Only intersections between thin and thick solid lines of identical lightness (i.e. identical upstream state) indicate a shock solution. 88

4.2 Myong MHD Hugoniot curves in $\boldsymbol{U} = (U, V)$ phase space, where $U = \gamma p/B_n^2$ and $V = B_\perp/B_n$, for a fixed upstream U_1 and $V_1 \in [0.5, 2.0]$ (equivalent to range of magnetic field incidence angles, $\varphi_1 \in [26.56505°, 63.43494°]$). Solid lines become lighter with decreasing V_1. Shocks where $p_2/p_1 > 1$ indicated by black, and red otherwise. Fast and slow shocks located above horizontal line, $V_2 = 0$, intermediate shocks located below. Curved dashed line corresponds to unity ratio between post–shock Alfvén and sound speeds, $U_2 = 1 + V_2^2$. 90

4.3 Fast shock solutions at fixed upstream magnetic field incidence angle, φ_1, for upstream normal Alfvén to sound speed ratio in the range, $r_{n,1} \in [10^{-6}, 8/\sqrt{\gamma}]$, where $r_{n,1} = b_{n,1}/c_{o,1} = B_n/\sqrt{\gamma p_1}$ and $\gamma = 5/3$. Lines become lighter with decreasing $r_{n,1}$. Red dots corresponds to shocks where the ratio between downstream Alfvén and sound speeds is unity. 93

4.4 Re–scaled magnitude of magneto–acoustic mode vorticity fluctuation, $\hat{\omega} = ||\hat{\boldsymbol{k}} \times \boldsymbol{u}'||/||\boldsymbol{u}'||$, where $\hat{\boldsymbol{k}}$ is the unit wavevector, $\hat{\boldsymbol{k}} = \boldsymbol{k}/||\boldsymbol{k}||$. $\hat{\omega}$ for fast magneto–acoustic (left) and slow magneto–acoustic (right) modes shown to vary with $\hat{k}_\perp$ (perpendicular unit wavevector component in a coordinate system orthogonal to the mean magnetic field), and ratio between Alfvén and sound speeds, $r = b/c_o$. Magnetosonic condition (Alfvén speed equal to sound speed, $b = c_o$) indicated on plots, $r = 1.0$ (red dashed line). 98

4.5 Unitary entropy mode prescribed with ($\boldsymbol{k}_1$, θ_1) refracted at fast MHD shock in decoupled system generating backward slow mode (orange), ($\boldsymbol{k}_{s-}$, θ_{s-}); entropy mode (brown), ($\boldsymbol{k}_E$, θ_E); forward slow mode (purple), ($\boldsymbol{k}_{s+}$, θ_{s+}); forward fast mode (blue), ($\boldsymbol{k}_{f+}$, θ_{f+}). Normal wave speeds, U_μ, defined as, $U_{s-} = \bar{u}_2 - V_{sn,2}$, $U_E = \bar{u}_2$, $U_{s+} = \bar{u}_2 + V_{sn,2}$, $U_{s-} = \bar{u}_2 + V_{fn,2}$. . . . 105

4.6 Validating incidence angle, θ_1, dependency of real component of pressure amplification factor, Υ_p, for backward (thin line) and forward (thick line) fast magneto–acoustic waves incident on a parallel fast MHD shock at upstream Mach number, $M_1 = 8$ (grey) and, $M_1 = 11$ (black). LIA data from present study using the formulation in [Westphal and McKenzie, 1969] (a) and corrected (b). LIA data extracted from [Westphal and McKenzie, 1969] is also shown (red dashed line). [$r_1 = 5/8$, $\gamma = 5/3$]. 110

4.7 Influence of magnetic field orientation on vorticity distribution of refracted forward fast mode generated by an entropy mode-fast shock interaction. Real component of non–dimensional complex vorticity amplitude computed in the $M_1 - \theta_1$ plane for multiple upstream magnetic field angles, φ_1. Forward fast refraction angle (white line) shown, with 40.0° separation between thick lines, and critical incidence angle (green line) are projected on plot. Note that minimum allowable upstream (sound) Mach number, M_1, for an admissible fast shock increases with mean magnetic field angle, φ_1. $\beta_{n,1} = 2$ and $\gamma = 5/3$ for all plots. 113

4.8 Imaginary component of forward fast mode non–dimensional complex vorticity amplitude computed in the $M_1 - \theta_1$ plane for multiple upstream magnetic field angles, φ_1, at $\beta_{n,1} = 2$ and $\gamma = 5/3$. See figure 4.7 for additional details. 114

4.9 Influence of magnetic field orientation on vorticity distribution of refracted forward slow mode generated by an entropy mode-fast shock interaction. Real component of non–dimensional complex vorticity amplitude computed in the $M_1 - \theta_1$ plane for multiple upstream magnetic field angles, φ_1. Forward slow refraction angle (white line) shown, with 40.0° separation between thick lines, and critical incidence angle (green line) are projected on plot. Note that minimum allowable upstream (sound) Mach number, M_1, for an admissible fast shock increases with mean magnetic field angle, φ_1. $\beta_{n,1} = 2$ and $\gamma = 5/3$ for all plots. 116

4.10 Imaginary component of forward slow mode non–dimensional complex vorticity amplitude computed in the $M_1 - \theta_1$ plane for multiple upstream magnetic field angles, φ_1, at $\beta_{n,1} = 2$ and $\gamma = 5/3$. See figure 4.9 for additional details. 117

4.11 Influence of magnetic field orientation on vorticity distribution of refracted backward slow mode generated by an entropy mode-fast shock interaction. Real component of non–dimensional complex vorticity amplitude computed in the $M_1 - \theta_1$ plane for multiple upstream magnetic field angles, φ_1. Backward slow refraction angle (white line) shown, with 40.0° separation between thick lines, and critical incidence angle (green line) are projected on plot. Note that minimum allowable upstream (sound) Mach number, M_1, for an admissible fast shock increases with mean magnetic field angle, φ_1. $\beta_{n,1} = 2$ and $\gamma = 5/3$ for all plots. 118

4.12 Imaginary component of backward slow mode non–dimensional complex vorticity amplitude computed in the $M_1 - \theta_1$ plane for multiple upstream magnetic field angles, φ_1, at $\beta_{n,1} = 2$ and $\gamma = 5/3$. See figure 4.11 for additional details. 119

4.13 Mach number dependency of integrated non–dimensional complex vorticity amplitude (in θ_1-space) for downstream magneto–acoustic modes generated in refraction of a normal entropy mode across a fast MHD shock. Forward fast (solid), forward slow (dashed) and backward slow (dotted) modes shown [$\beta_{n,1} = 2$, $\gamma = 5/3$]. 120

4.14 Mach number dependency of integrated non–dimensional complex vorticity amplitude (in θ_1-space for range within critical angle for all modes) for downstream magneto–acoustic modes generated in refraction of a normal entropy mode across a fast MHD shock. Forward fast (solid), forward slow (dashed) and backward slow (dotted) modes shown [$\beta_{n,1} = 2$, $\gamma = 5/3$]. 121

4.15 Mach number dependency of integrated non–dimensional complex vorticity amplitude (in θ_1-space for range within critical angle for all modes) summed across all downstream magneto–acoustic modes. Results shown for different $\beta_{n,1}$ regimes for $\varphi_1 \in [0.0°, 56.30993°]$ - line becomes lighter with decreasing φ_1. [$\gamma = 5/3$]. 122

4.16 Mach number dependency of integrated non–dimensional complex vorticity amplitude (in θ_1-space for range within critical angle for all modes) summed across all downstream magneto–acoustic modes. Results shown for different β_1 regimes for $\varphi_1 \in [0.0°, 56.30993°]$ - line becomes lighter with decreasing φ_1. [$\gamma = 5/3$]. 123

4.17 Five–block grid stretching configuration in x-direction. Uniform (non-uniform) regions represented by pink (gray) shading. Centre–line of shock, x_{sh}, located in region 2 at $x_{sh} = (x_a + x_b)/2$. Sampling region for errors between DNS and LIA results located within region 4, in $x_c \leq x \leq x_d$. Length of sampling region, L_u, selected such that $L_u > \lambda_x$, where λ_x is the normal component of the incident disturbance wavelength. x_0 and x_e indicate the limits of the computational domain, $x_0 \leq x \leq x_e$. 124

4.18 Seeding of flow within shock between prescribed upstream Mach number, M_1, and M_{min}, for which $\bar{\rho}_2 = \bar{\rho}_1 = 1.0$. 125

4.19 DNS density profiles for parallel fast shock captured using constant artificial bulk viscosity. Theoretical post–shock value given by dashed line. Close–up of profile shown on the right–hand–side. 127

4.20 DNS density profiles for oblique fast shock captured using constant artificial bulk viscosity. Theoretical post–shock value given by dashed line. Close–up of profile shown on the right–hand–side. 128

4.21 DNS y-magnetic field profiles for oblique fast shock captured using constant artificial bulk viscosity. Theoretical post–shock value given by dashed line. Close–up of profile shown on the right–hand–side. 128

4.22 Relative error between theoretical and DNS values for parallel (a) and oblique (b) fast MHD shocks captured using constant artificial bulk and conductivity computed from the weak shock approximation [Salas, 2009]. Upstream magnetic field angle given by φ_1. Error computed by subtracting initial solution from DNS flowfield at steady state for ρ (black circles), p (black crosses), u (blue square), v (blue triangle) and B_y field (pink triangles). Errors normalised by upstream theoretical value (normal component of velocity and magnetic field used for velocity and magnetic field errors respectively). DNS density profiles for steady–state initial flow (red) and steady–state (black) shown. Theoretical post–shock density (dashed line) shown as reference for shock location (centre-line of shock is at $x = 9.95$). 129

4.23 Density (white/black), ρ', and vorticity (green/red), $\omega' = [\boldsymbol{\nabla} \times \boldsymbol{u}']_z$, contours of normal entropy mode refraction (incident below critical angle at $\theta_1 = 50.00°$) across parallel and oblique fast MHD shocks respectively. Upstream mean magnetic field angle, φ_1, shown. Steady–state shock located at $x = 0$ (blue line). Snapshot taken at early time for which separation between refracted modes still visible in selected domain. Intense vorticity transport corresponds with backward slow mode. Entropy mode indicated by strong post–shock density fluctuations. Weak vorticity and density transport visible for forward slow mode. 130

4.24 Density (white/black), ρ', and vorticity (green/red), $\omega' = [\boldsymbol{\nabla} \times \boldsymbol{u}']_z$, contours in $x - t$ space (along centre–line, $y = \lambda_y = 10.0/\tan\theta_1$) of normal entropy mode refraction (incident below critical angle at $\theta_1 = 50.00°$) across parallel and oblique fast MHD shocks respectively. Upstream mean magnetic field angle, φ_1, shown. Steady–state shock located at $x = 0$ (blue line). Modes visibly separate in time as a result of differing normal speeds. Intense vorticity transport corresponds with backward slow mode (which propagates faster in oblique MHD shock case). Entropy mode indicated by strong post–shock density fluctuations. Weak vorticity and density transport visible for forward slow mode. 131

4.25 Density (white/black), ρ', and current density (green/red), $j' = [\boldsymbol{\nabla} \times \boldsymbol{B}']_z$, contours of normal entropy mode refraction (incident below critical angle at $\theta_1 = 50.00°$) across parallel and oblique fast MHD shocks respectively. Upstream mean magnetic field angle, φ_1, shown. Steady–state shock located at $x = 0$ (blue line). Snapshot taken at early time for which separation between refracted modes still visible in selected domain. Current density fluctuations highest in backward slow mode (like–signed with vorticity fluctuations - see figure 4.23). Entropy mode indicated by strong post–shock density fluctuations. Weak current density and density transport visible for forward slow mode. 131

4.26 Density (white/black), ρ', and dilatation rate (green/red), $d' = \nabla \cdot \boldsymbol{u}'$, contours of normal entropy mode refraction (incident below critical angle, $\theta_1 = 50.00°$) across parallel and oblique fast MHD shocks respectively. Upstream mean magnetic field angle, φ_1, shown. Steady–state shock located at $x = 0$ (blue line). Snapshot taken at early time for which separation between refracted modes still visible in selected domain. Dilatation rate contours visible for $x < 0$ indicate displacement of shock from steady–state position. Weak dilatation rate production in both slow modes. 132

4.27 Comparison between DNS (top plane in both plots) and LIA projection (bottom plane in both plots) density (black/white) and vorticity contours (green/red) for entropy mode refracted incident at $\theta_1 = 50.00°$ on parallel and obliquefast MHD shocks respectively. Upstream mean magnetic field angle, φ_1, shown. Shock located at $x = 0$ (blue line). Displacement of shock from steady–state position visible in DNS result. Snapshot taken after propagation of backward slow mode through selected domain, $t = 28$. 134

4.28 Fluctuating post–shock density, ρ' at $t = 28$ shown for refraction of two–dimensional entropy plane waves (amplitude, $\epsilon = 0.01$, and incidence angle, θ_1) across a parallel ($\varphi_1 = 0.0°$) fast MHD shock (located at $x = 0$). DNS data (black solid line), LIA projection (dashed red line) and error between DNS and LIA (thin grey line). Slice through domain taken along y position at which maximum error between DNS and LIA projection computed. Plots shown for incidence angles above, close to and below critical angle, $\theta^{c\pm} \approx \pm 58.63°$. Propagative regime in the range, $\theta^{c-} < \theta_1 < \theta^{c+}$. 136

4.29 Fluctuating post–shock vorticity, ω' at $t = 28$ shown for refraction of two–dimensional entropy plane waves (amplitude, $\epsilon = 0.01$, and incidence angle, θ_1) across a parallel ($\varphi_1 = 0.0°$) fast MHD shock. See figure 4.28 for additional information. 137

4.30 Fluctuating post–shock density, ρ', and vorticity, ω', at $t = 28$ shown for refraction of two–dimensional entropy plane waves (amplitude, $\epsilon = 0.001$, and incidence angle, θ_1) across a parallel ($\varphi_1 = 0.0°$) fast MHD shock. See figure 4.28 for additional information. 138

4.31 Transient behaviour of post–shock fluctuating density flowfield at an incident normal wavelength distance away from the shock, $x = \lambda_x = 10.0$ (shock located at $x = 0.0$), along the centre–line, $y = \lambda_y = 10.0/\tan\theta_1$, for refraction of two–dimensional entropy plane waves (amplitude, $\epsilon = 0.01$, and incidence angle, θ_1) across a parallel ($\varphi_1 = 0.0°$) fast MHD shock. Maximum and minimum values of density fluctuation (ρ'_{max} and ρ'_{min} respectively, indicated by solid red lines) extracted from shaded region which spans peak–to–peak in the range, $28 < t < 28 + 23T_w = 117$, where T_w is the time period of the refracted waves. 139

4.32 Fluctuating post–shock density (left) and vorticity (right) at $t = 110$ shown for refraction of a two–dimensional entropy plane wave (amplitude, $\epsilon = 0.01$, and incidence angle, $\theta_1 = 58.64°$) across a parallel ($\varphi_1 = 0.0°$) fast MHD shock. See figure 4.28 for additional information. . . 140
4.33 Fluctuating post–shock density (left) and vorticity (right) at $t = 110$ shown for refraction of a two–dimensional entropy plane wave (amplitude, $\epsilon = 0.001$, and incidence angle, $\theta_1 = 58.64°$) across a parallel ($\varphi_1 = 0.0°$) fast MHD shock. See figure 4.28 for additional information. . . 141
4.34 Convergence of relative error between DNS data and LIA projection for post–shock density (left) and vorticity (right). Relative error computed at time, $t = 110$, for entropy mode of normal wavelength, λ_x, and amplitude, $\epsilon = 0.001$, incident at $\theta_1 = 58.64°$, on a parallel shock of thickness, Δ. Relative root–mean–squared error (circles) and maximum error (crosses) shown. 142
4.35 Fluctuating post–shock density (left) and vorticity (right) at $t = 28$ shown for refraction of a two–dimensional entropy plane wave (amplitude, $\epsilon = 0.01$, and incidence angle, $\theta_1 = -30.00°$) across an oblique ($\varphi_1 = 26.56505°$) fast MHD shock. DNS data (black solid line), LIA projection (dashed red line) and error between DNS and LIA (thin grey line). Slice through domain taken along y position at which maximum error between DNS and LIA projection computed. Critical angles for $\theta_1 > 0$ and $\theta_1 < 0$ are $\theta_1^{c+} \approx 53.51°$ and $\theta_1^{c-} \approx -75.00°$ respectively. Propagative regime in the range, $\theta_1^{c-} < \theta_1 < \theta_1^{c+}$. 144
4.36 Fluctuating post–shock density (left) and vorticity (right) at $t = 110$ shown for refraction of a two–dimensional entropy plane wave (amplitude, $\epsilon = 0.001$, and incidence angle, $\theta_1 = 53.50°$) across an oblique ($\varphi_1 = 26.56505°$) fast MHD shock. See figure 4.35 for additional information. 145
4.37 Fluctuating post–shock density (left) and vorticity (right) at $t = 28$ shown for refraction of a two–dimensional entropy plane wave (amplitude, $\epsilon = 0.001$, and incidence angle, $\theta_1 = 75.00°$) across an oblique ($\varphi_1 = 26.56505°$) fast MHD shock. See figure 4.35 for additional information. 145
4.38 Relative density field error between DNS data and projection of LIA onto physical space for the interaction of two–dimensional entropy plane waves (incidence angle, θ_1, and amplitude, $\epsilon = 0.01$) with a parallel ($\varphi_1 = 0.0°$) MHD shock. Relative root–mean–squared error (circles), and maximum error (crosses). Vertical dashed line indicates the critical incidence angle. . . 146
4.39 Relative vorticity field error between DNS data and projection of LIA onto physical space for the interaction of two–dimensional entropy plane waves (incidence angle, θ_1, and amplitude, $\epsilon = 0.01$) with a parallel ($\varphi_1 = 0.0°$) MHD shock. Relative root–mean–squared error (circles), and maximum error (crosses). Vertical dashed line indicates the critical incidence angle. . . 147
4.40 Relative density field error between DNS data and projection of LIA onto physical space for the interaction of two–dimensional entropy plane waves (incidence angle, θ_1, and amplitude, $\epsilon = 0.01$) with an oblique ($\varphi_1 = 26.56505°$) MHD shock. Relative root–mean–squared error (circles), and maximum error (crosses). Vertical dashed line indicates critical incidence angles. 147

4.41 Relative vorticity field error between DNS data and projection of LIA onto physical space for the interaction of two–dimensional entropy plane waves (incidence angle, θ_1, and amplitude, $\epsilon = 0.01$) with a oblique ($\varphi_1 = 26.56505°$) MHD shock. Relative root–mean–squared error (circles), and maximum error (crosses). Vertical dashed line indicates critical incidence angles. 148
4.42 Five–block grid stretching configuration in transverse directions (z direction stretching is equivalent). Uniform (non-uniform) regions represented by pink (grey) shading. Entropy spot–shock interaction studied in uniform region 3. Uniform regions 1 and 5 are the length of ghost cells at domain boundaries to enable periodicity to be enforced. 150
4.43 Time–lapse of density/vorticity contours for entropy spot–fast shock interaction for two different upstream mean magnetic field angles, φ_1. Shock location indicated by solid black line. Cases A1 (a) and A3 (b) shown. Colour bars are given in figure 4.44. 155
4.44 Topology of entropy spot–parallel fast shock interaction (case A1). Entropy, forward fast (fast +), forward slow (slow +) and backward slow (slow −) modes indicated on plots. Density/vorticity (left) and pressure (right) shown at $t = 4.40$. 156
4.45 Topology of entropy spot–oblique fast shock interaction (case A3). Entropy, forward fast (fast +), forward slow (slow +) and backward slow (slow −) modes indicated on image. Density/vorticity (left) and pressure (right) shown at $t = 4.40$. 156
4.46 Normalised group/phase velocity (with respect to speed of sound), $\hat{\boldsymbol{V}} = \boldsymbol{V}/c_{o,2}$, diagrams for acoustic and fast magneto–acoustic modes in a moving flow (i.e. non–zero drift velocity). Acoustic mode phase/group velocity (thin grey solid line), fast magneto–acoustic phase velocity (red dashed line), fast magneto–acoustic group velocity (black solid line). Plots shown for magnetic field and drift velocity parallel to the normal direction (top) and oblique to the normal direction (bottom). 157
4.47 Forward slow mode evolution in entropy spot–parallel fast shock interaction (case A1). Arrows in direction of increasing time. Colour bars are given in figure 4.44. 158
4.48 Normalised group/phase velocity (with respect to speed of sound), $\hat{\boldsymbol{V}} = \boldsymbol{V}/c_{o,2}$, diagrams for backward (grey) and forward (black) slow magneto–acoustic modes in a moving flow (i.e. non–zero drift velocity). Phase velocity (dashed line) and group velocity (solid line) shown. Plot given for magnetic field and drift velocity parallel to the normal direction. Close–up of forward slow mode group velocity shown on the right. 159
4.49 DNS results vs. LIA reconstruction of entropy spot interacting with a parallel (left, case A1) and oblique (right, case A3) fast shock. Density and vorticity contours shown in left/right half–planes for LIA/DNS (top) and DNS/LIA (bottom). Asymmetry of oblique interaction well–captured by LIA reconstruction. 160

4.50 Comparison of DNS and LIA for 1% amplitude entropy spot–parallel fast shock interaction (Case A1). Top: LIA (left) and DNS (right) half planes of density/vorticity contours, blue line indicates linear theory propagation of fast mode, $(x, y) = (V^g_{x,f+}(\theta_2)t, V^g_{y,f+}(\theta_2)t)$, where the fast mode group velocity, $\boldsymbol{V}^g_{f+}$, has been computed for the range of t values, $t = 0.9T_0, T_0, 1.1T_0$, in which T_0 is the time elapsed after the centre-line of incident entropy spot has passed through the shock, and $\theta_2 \in [\theta^{c-}_{f+}, \theta^{c+}_{f+}]$, in which θ^{c+}_{f+} (θ^{c-}_{f+}) correspond to the fast mode refraction angle at the critical incidence angle, θ^{c+} (θ^{c-}). Bottom: Dependency of maximum positive (negative) fluctuations shown in grey (blue) for the density (left), ρ', and vorticity (right), ω', fields within the region bounded by linear theory fast mode contours at $t \in [0.9T_0, 1.1T_0]$. Values given for DNS (solid line) and LIA (shaded region) data. 161

4.51 Comparison of DNS and LIA for 1% amplitude entropy spot–oblique fast shock interaction (Case A3). See figure 4.50 for description. 162

4.52 Comparison of DNS and LIA for 10% amplitude entropy spot–parallel fast shock interaction (Case A2). See figure 4.50 for description. 164

4.53 Comparison of DNS and LIA for 10% amplitude entropy spot–oblique fast shock interaction (Case A4). See figure 4.50 for description. 165

4.54 Time–lapse of density/vorticity contours for entropy spot–fast shock interaction with varying upstream mean magnetic field angle, φ_1. Downstream plasma beta, $\beta_2 = 2\bar{p}_2/||\bar{\boldsymbol{B}}||^2$, given. Shock location indicated by solid black line. Cases A5 (a) and A6 (b) shown. 166

4.55 Density and in–plane vorticity contours shown for entropy spot–parallel fast shock interaction in two–dimensions (left, case A1) and three–dimensions (right, case B1). 167

4.56 Density and in–plane vorticity contours shown for entropy spot–oblique fast shock interaction in two–dimensions (left, case A2) and three–dimensions (right, case B2). 167

4.57 Three–dimensional iso-contours of z-component vorticity in parallel MHD shock interaction. Top view (left) and iso–metric view (right) shown for case B1. 168

4.58 Three–dimensional iso-contours of z-component vorticity in oblique MHD shock interaction. Top view (left) and iso–metric view (right) shown for case B2. 168

List of Tables

4.1 Five–block grid stretching configuration for the plane wave-fast MHD shock interaction. L is the reference length of the computational domain. Number of points ($Nbpts$), upper/lower bounds in x (x_{up}/x_{lo}) and grid spacing ($\Delta x_{up}/\Delta x_{lo}$) given for each region of stretched grid. Regions X_2 and X_4 are uniform. X_1, X_3, X_5 are non–uniform and utilise a x^{th} grid. 125

4.2 Maximum relative error between DNS and LIA projection in post–shock fluctuating density, L^{ρ}_{∞}, and vorticity, L^{ω}_{∞}, (see (4.4.2) for definition of L^{ϕ}_{∞}) for the refraction of two–dimensional entropy plane waves of amplitude, ϵ, incident at θ_1, across a parallel ($\varphi_1 = 0.0°$) fast MHD shock. Sample time, T_s, given in time units. 142

4.3 Maximum relative error between DNS and LIA projection in post–shock fluctuating density, L^{ρ}_{∞}, and vorticity, L^{ω}_{∞}, (see (4.4.2) for definition of L^{ϕ}_{∞}) for the refraction of two–dimensional entropy plane waves of amplitude, ϵ, incident at θ_1, across an oblique ($\varphi_1 = 26.56505°$) fast MHD shock. Sample time, T_s, given in time units. 144

4.4 Five–block stretched grid configuration in the x-direction for the two–dimensional entropy spot–fast MHD shock interaction. Total number of grid points in x- direction is 2016. L is the reference length of the computational domain, $L = 100$. Number of points ($Nbpts$), upper/lower bounds in x (x_{up}/x_{lo}) and grid spacing ($\Delta x_{up}/\Delta x_{lo}$) given for each region of stretched grid. Regions X_2 and X_4 are uniform. X_1, X_3, X_5 are non–uniform and utilise a polynomial grid. 151

4.5 Five–block stretched grid configuration in the x-direction for the three–dimensional entropy spot–fast MHD shock interaction. Total number of grid points in x- direction is 1680. L is the reference length of the computational domain, $L = 100$. Number of points ($Nbpts$), upper/lower bounds in x (x_{up}/x_{lo}) and grid spacing ($\Delta x_{up}/\Delta x_{lo}$) given for each region of stretched grid. Regions X_2 and X_4 are uniform. X_1, X_3, X_5 are non–uniform and utilise a polynomial grid. 151

4.6 Two–dimensional entropy spot–fast shock interaction DNS test cases. Upstream mean magnetic field angle (φ_1), amplitude of perturbation (ϵ), minimum M_1 used to seed shock (M_{min}), grid points in transverse direction (N_y and N_z), time–step (Δt) and maximum inviscid CFL number (CFL_{max}) shown. 152

4.7 Three–dimensional entropy spot–fast shock interaction DNS test cases. Upstream mean magnetic field angle (φ_1), amplitude of perturbation (ϵ), minimum M_1 used to seed shock (M_{min}), grid points in transverse directions (N_y and N_z), time–step (Δt) and maximum inviscid CFL number (CFL_{max}) shown. 153

List of Symbols

Operators	
$\boldsymbol{\nabla}$	gradient operator
$\boldsymbol{\nabla}\cdot$, $\nabla\cdot$	divergence operator
$\boldsymbol{\nabla}\times$	curl operator
Roman	
$\boldsymbol{b}$	Alfvén velocity, $\boldsymbol{b} = [b_x,\, b_y,\, b_z]^\intercal$
b	Alfvén speed, $b = \|\|\boldsymbol{b}\|\|$
$\boldsymbol{B}$	magnetic field vector, $\boldsymbol{B} = [B_x,\, B_y,\, B_z]^\intercal$
c	speed of light
c_o	speed of sound, $c_o^2 \equiv (\partial p/\partial \rho)_s$
$\mathbf{D}$	strain-rate tensor, $\mathbf{D} \equiv (\boldsymbol{\nabla u} + \boldsymbol{\nabla u}^t)/2$
$\mathbf{D}^\bullet$	deviatoric part of the strain-rate tensor, $\mathbf{D}^\bullet \equiv \mathbf{D} - (1/3)Tr(\mathbf{D})\mathbf{I} = \mathbf{D} - (\nabla\cdot\boldsymbol{u})\mathbf{I}/3$
$\boldsymbol{E}$	electric field vector, $\boldsymbol{E} = [E_x,\, E_y,\, E_z]^\intercal$
e_i	specific internal energy
e_k	specific kinetic energy
e_t	specific total energy
e	elementary charge
$\mathbf{I}$	identity matrix
$\boldsymbol{J}$	current density vector
$\boldsymbol{k}$	wavevector, $\boldsymbol{k} = [k_x,\, k_y,\, k_z]^\intercal$
k	wavevnumber
k_B	Boltzman constant
M	Mach number

M_A	Alfvén Mach number
m_α	mass of a particle
n_α	number density of a particle
p	thermodynamic pressure
q_α	charge of a particle
r	ratio of Alfvén and sound speeds, $r = b/c_o$
$\boldsymbol{r}$	ratio of Alfvén velocity and sound speed, $\boldsymbol{r} = \boldsymbol{b}/c_o = [r_x,\, r_y,\, r_z]^\intercal$
T	temperature
t	time
$\boldsymbol{u}$	fluid velocity vector, $\boldsymbol{u} = [u,\, v,\, w]^\intercal$
$\mathbf{v}$	particle velocity vector, $\mathbf{v} = [\mathrm{v}_x,\, \mathrm{v}_y,\, \mathrm{v}_z]^\intercal$
$\boldsymbol{x}$	position vector, $\boldsymbol{x} = [x,\, y,\, z]^\intercal$

Greek	
β	plasma beta
χ	refraction coefficient
$\Delta x, \Delta y, \Delta z$	grid spacing
Δt	time increment
δ_s	amplitude of shock displacement
δ	ratio of tangential and normal speeds, $\delta = v/u$
ε_o	vacuum permittivity
ε	ratio of tangential and normal magnetic field, $\varepsilon = B_y/B_x$
η	resistivity
η_c	density ratio
γ	ratio of specific heats
γ	Lorentz factor
κ	thermal conductivity
λ	magnetic diffusivity
λ	wavelength
ρ	density
ρ_c	charge density
μ_o	dynamic (shear) viscosity

μ'	second (dilatational) viscosity ($= -(2/3)\mu$ under Stokes' hypothesis)
μ_m	vacuum permeability
μ_b	bulk viscosity, $\mu_b \equiv (2/3)\mu_o + \mu'$ ($= 0$ under Stokes' hypothesis)
ν	kinematic viscosity, $\nu \equiv \mu_o/\rho$
$\boldsymbol{\omega}$	frequency
ω	vorticity
σ	electrical conductivity
$\boldsymbol{\Sigma}$	viscous stress tensor, $\boldsymbol{\Sigma} = 2\mu\mathbf{D}^{\bullet} + \mu_b(\nabla \cdot \boldsymbol{u})\mathbf{I}$ for Newtonian fluids
$\theta^{c+,-}$	critical incidence angles
ϑ	specific volume
φ	magnetic field angle

Abbreiviations	
CFD	Computational fluid dynamics
CFL	Courant-Friedrichs-Lewy number
DRP	Dispersion–relation–preserving
FDS	Finite difference scheme
DNS	Direct numerical simulation
LAD	Local artificial diffusivity
LIA	Linear interaction analysis
GLM	Generalised Lagrangian multiplier

Chapter 1

Introduction

1.1 MHD flow control

The re-emerging field of magnetohydrodynamics (MHD) involves the study of fluids such as plasma that display electrically conductive properties in addition to classic fluid dynamic behaviour. In recent years, interest in computational MHD has grown as computer advancements have enabled the simulation of complex phenomena exhibited by compressible, ionised gases in aerospace, power generation and astrophysical applications.

Within the field of aerospace, the possibility of using plasma-based methods to enact flow control over a wide range of speeds has led to many new developments in the area of compressible MHD. Mechanisms such as energy deposition via ionisation of airflows or exploitation of the interaction between an ionised flow and a magnetic field to generate Lorentz forces/Joule dissipation can be utilised to manipulate flowfields and improve aerodynamic performance. A key advantage of these techniques over conventional flow control methods is that they provide "active control" over the flow. Active control describes the regulated addition of energy to the flowfield - i.e. plasma actuation devices are able to rapidly add energy to the flow in high amounts and be switched off when necessary, unlike "passive" control methods such as vortex generators and suction/blowing devices, which permanently modify the aircraft geometry and can reduce aerodynamic performance when operating outside of design point [Lin, 2002]. Despite its relatively recent increase in popularity, plasma's potential role within aerodynamics was already recognised in the 1950s by Kantrowitz who commented on disassociation processes in high speed flows [Kantrowitz, 1955]. Experiments involving plasma-based flow control methods emerged as early as the 1960s - research on blunt body flows showed the bow shock stand-off distance increased significantly if the incoming ionised flow was subjected to a magnetic field [Bulen et al., 1967]. With respect to atmospheric–entry vehicles, the reduced heat flux [Poggie and

Gaitonde, 2002] and increased drag [Bityurin et al., 2005] produced by this effect could allow implementation of lighter aerostructures and optimised trajectory control [Bityurin et al., 2005]. Interest in plasma-based flow control decreased during the 1970s and 1980s, however, a re-emergence in the 1990s came about after the development of the hypersonic vehicle concept, "AJAX", which proposed using an MHD device to extract energy from the inlet flow of a scramjet to generate electrical power and provide more favourable conditions within the combustor [Gurijanov and Harsha, 1996].

The range of plasma-based flow control methods has become quite extensive since "AJAX", however, in general, they can be thought to fall into two categories. The first concerns volume plasma-inviscid gas flow interactions [Bletzinger et al., 2005] and involves the use of plasma to manipulate the bulk flow in high–speed applications. Examples include applying a magnetic field to an ionised flow upstream of a scramjet inlet and using a Lorentz body force to enable shock positioning; electron beam ionisation to create heated regions ("virtual cowls") that deflect flow streamlines into the inlet thereby increasing mass capture in off-design conditions [Macheret et al., 2001], [Macheret et al., 2002], [Shneider et al., 2004], [Shneider and Macheret, 2006]. Application of a magnetic field to an incoming ionised blunt body flow for drag reduction, heat–load mitigation and/or trajectory control [Poggie and Gaitonde, 2002], [Takizawa et al., 2006], [Fujino et al., 2008], [Kawamura et al., 2009]. Several studies have also been conducted on plasma jet injection upstream of a blunt body flow in which plasma filaments interacting with the bow shock reduce centre–line drag through Joule heating or vorticity production [Soloviev et al., 2001], [Leonov et al., 2001], [Kolesnichenko et al., 2004]. The other class of flow control relates to surface plasma–viscid gas flow interactions, where the effect is local and on lower–momentum parts of the flow. Considerable interest has been shown in the application of these techniques to flow separation control. Flow separation can be a source of issues such as fatigue loading [Quiroz et al., 2012] and reduced mass flow at scramjet inlets [Yao et al., 2012]. Plasma actuation devices ionising near–surface regions have been shown to add heat and/or momentum to regions within a turbulent boundary layer and suppress or reduce the separation bubble behind the shock [Minton et al., 2005], [Gaitonde, 2008], [Atkinson et al., 2012], [Gaitonde, 2013], [Greene et al., 2015]. The mechanisms behind these shock-wave turbulent boundary layer interactions in ionised flows are generally quite complex with a myriad of factors such as chemistry (via recombination), flow geometry and boundary layer effects all playing a role.

1.2 Linear interaction analysis

The interaction of turbulence with a shock is a fundamental feature of high speed flows - in particular, phenomena such as flow separation. Studies have shown upstream turbulent fluctuations are linked to low–



Fig. 1.1: Boeing X-51A Waverider, an experimental research scramjet, under the wing of a Air Force Flight Test Center B-52 (U.S. Air Force photo/Chad Bellay).

frequency unsteadiness in separated flows [Poggie and Smits, 2005], [Ganapathisubramani et al., 2007]. The complexity of these interactions makes both numerical and experimental studies difficult [Andreopoulos et al., 2000]. Efforts to gain a fundamental understanding of the interaction have lay in the study of isotropic turbulence passing through an isolated shock [Lee et al., 1997]. In the field of hydrodynamic shockwave–turbulence interactions (SWTIs), significant work has been completed to the aim of understanding, predicting and modelling turbulent kinetic energy redistribution at an isolated shock [Ribner, 1955], [Ribner, 1969], [Lee et al., 1997], [Larsson and Lele, 2009], [Lele and Larsson, 2009], [Larsson et al., 2013]. Most notably the technique of linear interaction analysis (LIA), first developed in the 1950s by Ribner [Ribner, 1954], has proved accurate in predicting the near–shock flow in SWTIs [Larsson and Lele, 2009]. In LIA, the upstream turbulence is assumed weak with respect to the mean flow, and thus decomposable into a series of Fourier modes comprised of plane waves projected onto the eigenmode basis of an Euler flow (i.e. the vortical, acoustic and entropy eigenmodes). As the waves are assumed linear, one eigenmode can only generate another upon interaction with the shock boundary. In this interaction, the shock redistributes energy from the incident wave to all other eigenmodes. To compute the refraction properties of a given incident wave the linearised Rankine–Hugoniot jump conditions are solved at the discontinuity, obtaining the unknown amplitudes of the refracted waves and shock distortion. The superposition of wave interactions is integrated in spectral space to reconstruct the refracted field. Linear analysis by Ribner predicted SWTIs involving purely vortical

turbulence - i.e. a superposition of incident vortical plane waves - would produce an amplification of the fluctuating velocity and transverse vorticity variance in the form of a refracted shear wave and generation of both an entropy mode and acoustic mode that rapidly decays for incident wave angles above a critical value [Ribner, 1954]. Ribner extended LIA to the interaction of initially isotropic turbulence with a weak shock and found that TKE to be amplified [Ribner, 1955]. Later numerical studies of SWTIs indicated LIA predictions of post–shock TKE evolution are accurate only in the near–shock region as the anisotropy and intensity of turbulence are increasingly influenced by nonlinear effects as the flow penetrates the downstream region [Larsson and Lele, 2009], [Lele and Larsson, 2009]. With respect to separated flows, LIA methods have also been applied to study fluctuating pressure fields behind an oscillating separation shock [Lowson, 1966]. However, in application of LIA to shockwave boundary layer interactions (SBLI), Plotkin noted shock motion is modelled only for a sinusoidal forcing function and that the net shock motion amplitude is determined solely by the incoming turbulence intensity [Plotkin, 1975]. Plotkin concluded that it is insufficient to use only LIA for modelling separated shock systems as it is unable to predict the spectrum of shock motion and does not incorporate the influence of randomness in convection of incoming turbulence or mean flow properties [Plotkin, 1975].

LIA indicates that entropy modes in the incoming turbulence will contribute to TKE redistribution across a shock. Through a combination of direct numerical simulations and inviscid linear analysis, Mahesh investigated the influence of entropy fluctuations on the TKE amplification process, finding that correlations between upstream temperature and velocity fluctuations can have an enhancing/suppressing effect [Mahesh et al., 1997]. With respect to MHD flow control applications, shock-entropy interactions may be of particular importance when considering regions of flow passing through the shock can be thermally-excited upstream with a Gaussian-distribution by plasma actuation methods such as electron beam ionisation [Macheret et al., 2000], [Shneider et al., 2004]. In work by Fabre, the interaction of a two–dimensional Gaussian-distributed entropy spot with a gasdynamic shock was investigated using a combination of numerical simulations and linear theory [Fabre et al., 2001]. Using the spectral form of the Gaussian, Fabre computed the amplitudes of refracted modes in wavespace and derived exact integrals of their inverse Fourier transform in order to reconstruct the real-space flowfield. The resulting post–shock vorticity distribution constituted of a pair of primary counter-rotating vortices, a secondary pair of weaker amplitude vortices and a pair of waves attached to the shock at the critical vortical refraction angle [Fabre et al., 2001]. DNS and LIA results were compared for a range of linear (density fluctuation amplitude $< 10\%$ of mean flow) and truly nonlinear (density fluctuation amplitude $\sim$ mean flow) incident entropy mode amplitudes. At the crossing of the shock, the difference in LIA and DNS values for the maximum vorticity generated by a nonlinear entropy mode (amplitude equal to mean flow) was found to be only 6%. Only when the post–shock vortices rolled-up (transitioning to tur-

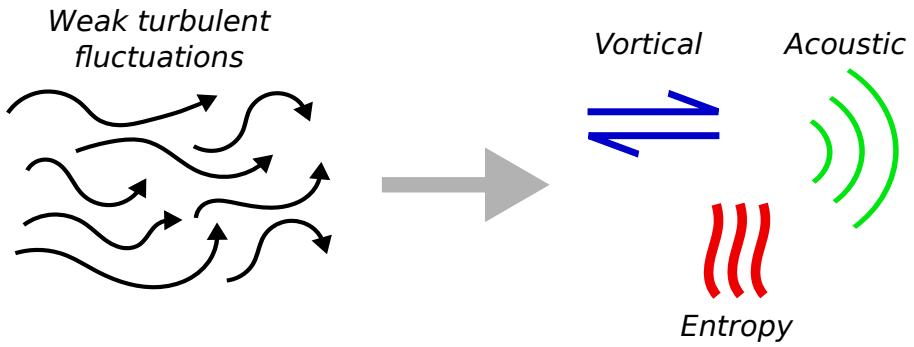


Fig. 1.2: Projection of weak turbulent fluctuations onto eigenmode basis of an Euler flow.

bulence) in the numerical simulation did the result significantly diverge from the linear theory. Following on from work by Fabre, several other authors have investigated the shock refraction of Gaussian–distributed disturbances for gas mixtures, differing equations of state and heat–releasing shocks [Griffond, 2005], [Griffond and Soulard, 2012], [Touber and Alferez, 2019], [Farag et al., 2019].

Performing a wave decomposition analogous to that of gasdynamic LIA on an ideal MHD flow reveals weak turbulent MHD fluctuations are composed of four wave types, fast and slow magneto–acoustic, entropy and Alfvén. However, a key difference in MHD is that Alfvén and magneto–acoustic waves can all support fluctuating fluid motion transverse to the wavevector direction and thus transport vorticity in the post–shock flow at speeds faster/slower than the local flow. In gas dynamics, vorticity transport occurs via a single wave type, the vortical mode, convected downstream with the flow. With respect to MHD SWTIs, vorticity fluctuations transported by the refracted Alfvén and magneto–acoustic modes all contribute to TKE amplification in the downstream plasma flow. In the context of MHD flow control, plasmas encountered are typically weakly–ionised and thus exhibit a small and finite conductivity (during re–entry air conductivity generally reaches values of the order $\sim 10^2 mho/m$ [Resler Jr., 1958]). Consequently, linear damping experienced by MHD waves [Braginskii, 1965] will lead to a rapid attenuation of the amplitude of fluctuations in the magnetic field (and coupled flow properties) transported by each respective wave as they penetrate the downstream region [Gaitonde and Poggie, 2000]. This damping effect therefore presents a potential restriction of MHD LIA to the near–shock region in SWTIs in addition to the influence of nonlinear effects noted in gasdynamic flows.

Early work in the field of MHD LIA consisted of plane wave-shock interaction analyses by McKenzie and Westphal in the late 1960s and early 1970s in the context of solar wind interacting with Earth's bow shock [Westphal and McKenzie, 1969], [McKenzie and Westphal, 1969], [McKenzie, 1970], [McKenzie and Westphal, 1970]. Quantitative results were restricted mainly to the respective excitations of Alfvén modes

[McKenzie and Westphal, 1969] and entropy/magneto–acoustic modes [Westphal and McKenzie, 1969] for a decoupled three–dimensional system in which the wavevector lies in the plane containing the shock normal and mean magnetic field. For the out–of–plane Alfvén wave-shock interaction, the amplification of magnetic and kinetic energy in the post–shock flow was found to be independent of the wave vector direction and a function only of the base flow properties. The amplification factors approach their maximum in line with the asymptotic limit of the MHD shock compression ratio (identical to that of a gasdynamic shock). The incidence angle-dependence of in–plane entropy/magneto–acoustic wave amplification factors were also computed for the special case of a parallel fast MHD shock (upstream flow is super-fast and the mean magnetic field is aligned with shock normal) [Westphal and McKenzie, 1969]. The amplification of a given incident wave is a function of both the base flow and the refracted wavevectors, obtained via graphical solutions to Snell's laws. However, Westphal & McKenzie limited analysis of amplification factors to angles of incidence below a critical value at which the normal component of the refracted fast magneto–acoustic modes's group velocity was equal to zero. Earlier work by Kontorovich showed this condition coincided with the refracted fast magneto–acoustic mode wavevector becoming complex–valued and thus the wave exhibiting a non–propagating decaying component [Kontorovich, 1959]. Kontorovich termed this refracted fast mode a "surface wave". Later studies on fast MHD shock LIA by authors such as Zhang and Russel (ZR) [Zhuang and Russell, 1982] and Whang et al. [Whang et al., 1987] also omitted calculations of plane wave interactions past certain "limiting angles". ZR solved for the refracted wave vectors using solutions of the quartic describing the magneto–acoustic dispersion relationship but restricted calculations of amplification factors to incidence angles for which at least three normal wavevector component solutions were positive - i.e. the refracted wavevectors are directed away from the shock. Solutions that did not obey this condition were described as non–physical. A similar analysis was conducted by Whang et al. who also investigated the dependence of this particular "critical angle" on the plasma beta of the base flow. The concluding statements of Whang et al. on the nature of solutions past the critical angle went further than ZW, stating that the fast shock is unstable to perturbations with such incidence angles and thus non–evolutionary [Whang et al., 1987]. This is in direct opposition to earlier studies by Akheizer et al. [Akhiezer et al., 1959] in which shocks were observed as always evolutionary if stable to normally incident fluctuations. Subsequent work by Kontorovich [Kontorovich, 1959] and Anderson [Anderson, 2003] confirmed the stability of fast shocks to disturbances of arbitrary incidence angle.

In the context of extending MHD linear theory to turbulence or any type of "broadband" fluctuations interacting with a shock, the full range of incidence angles will be excited by the impinging disturbance. At present, studies involving the refraction of "broadband" fluctuations across an MHD shock have been primarily numerical in nature [Giacalone and Jokipii, 2007], [Ji et al., 2016]. As such, to the author's

best knowledge, there exists a gap in the literature with respect to computing the refraction properties of plane waves incident past the critical angle (individually or as a superposition to construct a "broadband" disturbance) on a shock for which a mean magnetic field of arbitrary orientation is imposed.

1.3 Thesis objectives

In MHD flow control applications, there exists a considerable amount of complexity behind the behaviour of turbulent plasma, its interaction with shocks and how that influences the efficacy of the flow control mechanism. For the performance and reliability of plasma's usage in high speed applications to be improved, an understanding of the fundamental phenomena involved in shock wave–turbulence interactions in ionised gases will be necessary. If this interaction is to be manipulated by the presence of a magnetic field, the influence of magnetic field strength and direction on the amplification or attenuation of downstream turbulent kinetic energy, will potentially be of interest. The aims of this research will be to investigate the mechanisms for shock-induced production of vorticity (an indicator of turbulent kinetic energy) in a plasma permeated by a mean magnetic field. A single-fluid ideal MHD model will be used to simulate the ionised flow in both two- and three–dimensions. A study will be carried out of the vorticity produced in the interaction of small constant–pressure density perturbations (entropy modes) with an MHD isolated shock. Important questions to be considered include:

- Can this interaction be accurately predicted by linear theory?
- What is the influence of the imposed magnetic field orientation on the distribution and intensity of vorticity produced in the post shock flow?

Direct numerical simulations (DNS) of a compressible MHD flowfield will be carried out using an in-house Fortran-based solver, CompReal, with non-dissipative, low dispersion error and shock-capturing capabilities. Shock-capturing schemes utilising localised artificial dissipation will be employed. Research studies will include the development of a linear theory to predict the passage of weak entropy fluctuations through an MHD shock to validate/test the code in the linear limit and explore potential configurations for fully nonlinear interactions. The analysis of the results obtained from this research will aim to provide a more in-depth understanding of mechanisms involved in shock-induced TKE transfer in MHD, and thus serve as a basis for more accurate turbulence models, aiding development of MHD flow control configurations through better predictions of flow properties such as transition, heat transfer and drag.

Chapter 2 outlines the governing equations of single–fluid ideal MHD. Assumptions made in their derivation with respect to characteristic length and time scales are considered in addition to their formulation mod-

elled by numerical simulations in this study. In chapter 3 the numerical methods employed throughout the present work are described and validated against various test cases. Chapter 4 provides a description of the refraction of a disturbance through a shock. Both the uniform base flow and perturbations are investigated for different magnetic field regimes. The influence of magnetic field strength and direction on post–shock vorticity production is also studied through a combination of linear theory and direct numerical simulations. In chapter 5 conclusions are drawn.

Chapter 2

Governing Equations

In this chapter, a system of partial differential equations describing plasma dynamics modelled as a fluid, also known as the magneto-hydrodynamic equations, are derived from the non-relativistic form of Maxwell's equations and the reduced form of Boltzmann equations for plasma in which the ions and electrons are approximated as a single fluid. The first section details the properties of plasma, with respect to its interaction within an electromagnetic field, ionisation and quasi–neutrality. Subsequently, both single particle and fluid motion of a plasma is modelled using the equation of motion and reduced Boltzmann's equations respectively. The validity of the assumptions required for deriving the single-fluid magneto-hydrodynamic equations, with respect to relevant time and length scales, are investigated. The second section details the formulation of the ideal MHD equations implemented in CompReal and modelled in numerical simulations within this study. The hyperbolicity and waves present in an ideal magneto-hydrodynamic flow are also discussed.

2.1 Plasmas

2.1.1 Ionisation

Plasma is an ionised gas containing a sufficient number of separately free ions and electrons to exhibit collective behaviour and thus have its dynamics (and properties) significantly influenced by electromagnetic forces [Thompson, 2013]. A relatively small proportion of charged particles are required for the dynamics of a plasma to be controlled by electromagnetic forces. An ionisation fraction of only 0.01 (ratio of ion number density to total particle number density) is sufficient for a plasma to display the maximum possible conductivity [Boyd and Sanderson, 2003]. Plasmas with an ionisation fraction of unity are termed fully–ionised. If the ionisation fraction is less than unity, the plasma is said to be partially–ionised.

Fully–ionised plasmas can be either simple or multi-species. The designation "simple" refers to plasmas composed only of electrons and one type of ion. As its name suggests, this is the most simple type of plasma to model and as such, appears most frequently in numerical MHD studies. Despite its popular usage, simple plasmas are relatively rare in nature as normally various ion impurities are also present [Connor, 1973]. A plasma with ion impurities (i.e. two or more ion species present in the medium) is multi-species. Depending on the proportion of each unique ion specie in a multi-species plasma, the behaviour of transport properties such as viscosity and conductivity can differ quite significantly from that of a simple plasma [Connor, 1973]. Examples of multi-species plasmas include solar wind [Gloeckler et al., 1992] and inertial confinement fusion products [Bellei et al., 2013].

Partially–ionised plasmas are composed of a mixture of electrons, ions and neutral atoms. The plasma properties therefore are affected by neutral-neutral and neutral-charged particle collisions in addition to Coulomb force–based interactions between charged particles [Mitchner and Kruger, 1973]. This plasma type is most representative of naturally occurring plasmas on Earth. In particular plasmas observed during hypersonic flight, in which usually only a small fraction of the total air flow has been ionised [Bityurin et al., 2005].

A common ionisation route (in nature) known as thermal agitation relates to the process in which a neutral gas is heated to a sufficiently high temperature such that electrons dissociate from their parent atoms. If a plasma is weakly ionised and at local thermal equilibrium (LTE) - i.e. constituent particles in localised regions have the same temperature (and their kinetic energies follow a Maxwell–Boltzmann distribution) - the degree of ionisation can be estimated using the Saha equation (given in approximate steady state form [Woods, 2008]):

$$\frac{n_i}{n_o} = \frac{1}{p_e}\left(\frac{2\pi m_e}{h^2}\right)^{3/2}(k_B T)^{5/2}\exp\left[-\frac{E_i}{k_B T}\right], \tag{2.1.1}$$

where p_e is the electron pressure, $p_e = n_e k_B T$, n_o, n_i and n_e are the number densities of the neutral particles, ions and electrons respectively, m_e is the mass of an electron, E_i is the ionisation energy per particle, h is Plank's constant and k_B is Boltzmann's constant.

The Saha equation can be used to estimate the properties of weakly–ionised hypersonic flows [Huber et al., 1971], [Borghi et al., 2006], [Bityurin and Bocharov, 2010] and has also been applied in numerical models of reentry flight to aid predictions of ionisation profiles behind the bow shock [Potter, 2001]. For a given vehicle geometry, flight velocity, trajectory and altitude, the properties of the ionised region, or "plasma sheath", can be modelled [Potter, 2001].

With respect to MHD, several assumptions are usually made of the plasma in order to simplify the model. Plasma sources are assumed to contain non-diffusive electrons and are observed on characteristic time scales

greater than that required to reach LTE. Additionally, in the context of the present study, the primary aim is to analyse the influence of electromagnetic effects on compressible flow phenomena already seen in neutral fluids. As such, flow behaviour that arises due to complex interactions between particles in partially–ionised or multi-species plasmas is seen as outside the scope of the investigation. We shall therefore consider only simple plasmas.

2.1.2 Quasi-neutrality

2.1.2.1 Debye length

In plasmas, above a certain length scale, the collective behaviour of the constituent species will maintain a quasi–neutrality over the entire medium - i.e. regions are shielded against the electric potential of charge carriers. The Debye length denotes the finite range of influence of localised charge imbalances (i.e. individual charge carriers) within the plasma. Assuming the plasma is at LTE, non-reacting and the particles are free-streaming (i.e. the potential energy of particles due to the electrostatic field is much smaller than their thermal energy), the Debye length, λ_D, is defined as [Inan and Gołkowski, 2011]:

$$\lambda_D = \sqrt{\frac{\varepsilon_o k_b T_e}{n_e e^2}}, \tag{2.1.2}$$

where, ε_o is the permittivity of free space, k_B is the Boltzmann constant, T_e is the electron temperature, n_e is the electron number density and e is the elementary charge.

To ensure quasi–neutrality is observed throughout all plasma flows modelled, it is assumed the characteristic length scale, l_c, is much greater than the Debye length, $l_c \gg \lambda_D$. Additionally, for the earlier assumption of LTE plasma to be valid, the number of particles within the *Debye sphere*, must also be large, $n_e {\lambda_D}^3 \gg 1$.

2.1.2.2 Plasma frequency

Plasma frequency describes the collective oscillation of a body of electrons against an ion background. As such, quasi–neutrality is observed if the plasma is studied at characteristic time scales, τ_c, much larger than the time period of oscillating localised regions of charge induced by electron displacement, $1/\omega_{pe}$, for which we define the frequency of oscillation, ω_{pe}, as [Inan and Gołkowski, 2011]:

$$\omega_{pe} = \sqrt{\frac{n_e e^2}{\varepsilon_o m_e}}. \tag{2.1.3}$$

2.1.3 Plasma kinetic theory

2.1.3.1 Maxwell's equations

The interaction between electric and magnetic fields generated and altered by charge carriers within the plasma can be modelled by a set of four partial differential equations also known as the Maxwell equations. The equations are Lorentz invariant - i.e. they remain consistent when transformed between two coordinate frames moving at constant relativistic velocities relative to each other.

Gauss' law:

$$\nabla \cdot \boldsymbol{E} = \frac{\rho_c}{\varepsilon_o}. \tag{2.1.4}$$

Gauss' law for magnetism:

$$\nabla \cdot \boldsymbol{B} = 0. \tag{2.1.5}$$

Maxwell-Faraday equation:

$$\boldsymbol{\nabla} \times \boldsymbol{E} = -\frac{\partial \boldsymbol{B}}{\partial t}. \tag{2.1.6}$$

Ampere's circuital law:

$$\boldsymbol{\nabla} \times \boldsymbol{B} = \mu_m \boldsymbol{J} + \varepsilon_o \mu_m \frac{\partial \boldsymbol{E}}{\partial t}, \tag{2.1.7}$$

2.1.3.2 Non-relativistic approximation

Plasma is ubiquitous within the universe - most observable matter exists in a plasma state [Martín and Puerta, 1999]. In numerous astrophysical phenomena such as stellar winds, supernovae explosions and astrophysical jets, the plasma speed, v, can reach a significant fraction of the speed of light - i.e. it is relativistic. However, in the present study, our main interest resides in plasmas present during the operation of aircraft/spacecraft travelling at hypersonic/re-entry speeds. This plasma is therefore non-relativistic ($v < 0.01c$). As such, in the following equations derived to model plasma dynamics, the limit $\mathrm{v} \ll c$ is applied throughout.

The dynamics of plasmas are governed by the behaviour of individually or collectively moving charges and their interaction with an electromagnetic field. Formally, Maxwell's equations are invariant in any inertial frame. However, in the reference frame of a moving charge, electromagnetic fields are subject to the following transformation (also known as the Joules-Bernoulli equation):

$$\boldsymbol{E}' = \gamma(\boldsymbol{E} + \mathbf{v} \times \boldsymbol{B}) - (\gamma - 1)(\boldsymbol{E} \cdot \hat{\mathbf{v}})\hat{\mathbf{v}}, \tag{2.1.8}$$

$$\boldsymbol{B}' = \gamma\left(\boldsymbol{B} - \frac{\mathbf{v}\times\boldsymbol{E}}{c^2}\right) - (\gamma-1)(\boldsymbol{B}\cdot\hat{\mathbf{v}})\hat{\mathbf{v}}, \tag{2.1.9}$$

where $\square'$ and $\square$ denotes electromagnetic field properties in the rest frame and moving charge's reference frame respectively, $\mathbf{v}$, the velocity of the moving charge, for which we define the unit vector, $\hat{\mathbf{v}} = \mathbf{v}/||\mathbf{v}||$, and γ is the Lorentz factor, $\gamma = 1/\sqrt{1-v^2/c^2}$.

In the non–relativistic limit, $\gamma = 1$, (2.1.8) and (2.1.9) reduce to the form:

$$\boldsymbol{E}' = \boldsymbol{E} + \mathbf{v}\times\boldsymbol{B}, \tag{2.1.10}$$

$$\boldsymbol{B}' = \boldsymbol{B} - \frac{\mathbf{v}\times\boldsymbol{E}}{c^2}. \tag{2.1.11}$$

By order of magnitude analysis, it is possible to show $\boldsymbol{B}' = \boldsymbol{B}$. First, the magnitudes of magnetic and electric fields in the moving reference frame are approximated as $||\boldsymbol{B}|| \sim B_o$ and $||\boldsymbol{E}|| \sim E_o$ respectively. Additionally, the characteristic angular frequency, ω_o, and inverse of the wavenumber, $1/k_o$, of electromagnetic waves within the plasma medium are used to characterise the respective time and length scales. We apply B_o and ω_o to Maxwell–Faraday's law (2.1.6):

$$\boldsymbol{\nabla}\times\boldsymbol{E}\frac{1}{\omega_o B_o} = -\frac{\partial\boldsymbol{B}}{\partial t}\frac{1}{\omega_o B_o}, \tag{2.1.12}$$

where we note $||(\partial\boldsymbol{B}/\partial t)|| \sim (\omega_o B_o)$ and $||\boldsymbol{\nabla}\times\boldsymbol{E}|| \sim (k_o E_o)$. As such, it can be concluded from (2.1.12) that $E_o \sim B_o\omega_o/k_o$. Consequently, the magnitude of the last term in (2.1.11) is approximated as, $||\mathbf{v}\times\boldsymbol{E}||/c^2 \sim \mathrm{v}_o E_o/c^2 \sim \mathrm{v}_o B_o\omega_o/(c^2 k_o)$, in which v_o is the characteristic plasma velocity, $||\mathbf{v}|| \sim \mathrm{v}_o$.

It is assumed that the frequency and the wavenumber of electromagnetic fields vary on the same time and length scales as the plasma, $\omega_o\tau_o \sim 1$, and $k_o L_o \sim 1$, where τ_o and L_o are the respective time and length scales. If the characteristic plasma velocity is defined as $\mathrm{v}_o = L_o/\tau_o$, and known to be non–relativistic, $\mathrm{v}_o \ll c$, then $(\mathrm{v}_o/c)^2 B_o$, is negligible compared to B_o. As a result, the following relation is derived from (2.1.11):

$$\boldsymbol{B}' \simeq \boldsymbol{B}. \tag{2.1.13}$$

A non-relativistic or "low frequency" approximation of Ampere's circuital law can also be derived using order of magnitude analysis. The relation, $E_o \sim \omega_o B_o/k_o$, is applied to terms in (2.1.7):

$$\boldsymbol{\nabla}\times\boldsymbol{B}\frac{1}{B_o k_o} = \mu_m\boldsymbol{J}\frac{1}{B_o k_o} + \varepsilon_o\mu_m\frac{\partial\boldsymbol{E}}{\partial t}\frac{1}{B_o k_o}, \tag{2.1.14}$$

in which $||(\boldsymbol{\nabla}\times\boldsymbol{B})|| \sim (B_o k_o)$, $\mu_m||\boldsymbol{J}||/(B_o k_o) \sim \mu_m J_o/(B_o k_o)$ and $\varepsilon_o\mu_m||(\partial\boldsymbol{E}/\partial t)||/(B_o k_o) \sim \mathrm{v}_o^2/c^2$, where J_o is the order of magnitude of the current density, $||\boldsymbol{J}|| \sim J_o$.

Therefore the displacement current (second term on right-hand side of (2.1.14)), is negligible compared to the curl of the magnetic field, $\mathrm{v}_o^2/c^2 \ll 1$. If $J_o \sim B_o k_o/\mu_m$, the low–frequency Ampere's circuital law is obtained:

$$\boldsymbol{\nabla} \times \boldsymbol{B} = \mu_m \boldsymbol{J}. \tag{2.1.15}$$

Additionally, if the magnetic field vector is assumed sufficiently smooth, taking the divergence of (2.1.15) leads to zero on the LHS of (2.1.15), which indicates that the current density vector is solenoidal and therefore that there exists no point sources of current within a non-relativistic plasma:

$$\nabla \cdot (\boldsymbol{\nabla} \times \boldsymbol{B}) = \mu_m (\nabla \cdot \boldsymbol{J}) = 0. \tag{2.1.16}$$

2.1.3.3 Single particle motion

The motion of a single charged particle travelling at non-relativistic speeds within an electric and magnetic field can be modelled by the following equation of motion [Boyd and Sanderson, 2003]:

$$m_\alpha \frac{\mathrm{d}\mathbf{v}}{\mathrm{d}t} = q_\alpha (\boldsymbol{E} + \mathrm{v} \times \boldsymbol{B}), \tag{2.1.17}$$

where subscript "α" represents either an electron, "e", or a single ion type, " i", for which we define the respective charge densities as $n_e q_e = -n_e e$ and $n_i q_i = n_i Z e$ (Z is the charge state of the ion).

If it is assumed that the magnetic field is constant and unidirectional, $\boldsymbol{B} = B_z \mathbf{e}_z$, it is trivial to show from (2.1.17) that the velocity parallel to the magnetic field, $\mathbf{v}_\parallel = \mathrm{v}_z \mathbf{e}_z$, is constant:

$$\frac{\mathrm{d}\mathbf{v}_\parallel}{\mathrm{d}t} = \mathbf{0}. \tag{2.1.18}$$

In the plane perpendicular to the magnetic field, the time rate of change of the orthogonal velocity components reduces to the following ordinary differential equations (ODEs):

$$\frac{\mathrm{d}\mathrm{v}_x}{\mathrm{d}t} = \frac{q_\alpha \mathrm{v}_y B_z}{m}, \tag{2.1.19}$$

$$\frac{\mathrm{d}\mathrm{v}_y}{\mathrm{d}t} = -\frac{q_\alpha \mathrm{v}_x B_z}{m}. \tag{2.1.20}$$

The solution to the system of equations in (2.1.19) and (2.1.20) indicates the particle experiences a periodic circular motion in the plane perpendicular to the magnetic field about a specific point called the guiding centre [Inan and Gołkowski, 2011]:

$$x(t) = x_o + R_\alpha \cos(\Omega_\alpha t), \tag{2.1.21}$$

$$y(t) = y_o - R_\alpha \cos(\Omega_\alpha t), \tag{2.1.22}$$

$$z(t) = z_o + \mathrm{v}_\parallel t, \tag{2.1.23}$$

in which the position of the charged particle at $t = 0$ is the initial point along the guided centre, $\boldsymbol{x}(t = 0) = [x_o, y_o, z_o]^\intercal$ and Ω_α and R_α are the respective frequency and radius of the circular motion, $\Omega_\alpha = |q_\alpha|B_z/m_\alpha$, and, $R_\alpha = \mathrm{v}_\perp/\Omega_\alpha$, in which $\mathrm{v}_\perp$ is the magnitude of the perpendicular velocity, $\mathrm{v}_\perp = \sqrt{\mathrm{v}_x^2 + \mathrm{v}_y^2}$. From (2.1.19) and (2.1.20) it is trivial to show that $\mathrm{v}_\perp$ is constant.

Ω_α and R_α are known as the Larmor frequency and radius respectively and represent the time and length scales of gyromotion. As a result of the disparity between ion and electron mass, we find that, $\Omega_e \gg \Omega_i$, and, $R_i \gg R_e$. Consequently, for a magnetised plasma, the longest time and length scales of gyromotion are characterised by the Larmor frequency and radius of an ion.

2.1.3.4 Single-fluid MHD approximation

The MHD equations provide a fluid model description of plasma behaviour. Consequently, individual particle and microscopic-level effects - such as plasma-wall interactions and resonant particle behaviour - remain unresolved within the system along with the range of micro-instabilities that may arise due to their presence. A necessary assumption of the MHD model is that the plasma is collision-dominated. Its validity is predicated on a set of restrictions on the characteristic length/time scales that describe the plasma flow (to be discussed later on in this section). Despite these assumptions, MHD can be readily applied to a wide range of plasma applications such as fusion and astrophysics, serving as an effective tool for describing macroscopic equilibrium and stability properties of conductive flows.

The single-fluid MHD model approximates the properties of the constituent ions, electrons and neutral particles in a plasma to that of a single fluid element. To arrive at this approximation, it is necessary to first consider plasma behaviour from a single particle-type analysis. Despite single-particle models providing the closest description of plasma dynamics, the parameters modelled (e.g. particle position) and number of particles necessary to seek comparisons with observations make analyses of measurable quantities of interest (e.g. density, pressure, bulk velocity) impractical. As such, a statistical treatment of plasma provides the most fundamental method via which to reasonably evaluate plasma behaviour for a large number of particles. In this analysis, the velocity distribution function, $f_\alpha(\boldsymbol{x}, \mathbf{v}, t)$, is a key parameter that describes the probability density of particle specie, α, travelling at a given speed, $\mathbf{v}$, at position, $\boldsymbol{x}$, and time, t, in a medium:

$$n_\alpha(\boldsymbol{x}, t) = \int_{\mathrm{v}_z=-\infty}^{+\infty} \int_{\mathrm{v}_y=-\infty}^{+\infty} \int_{\mathrm{v}_x=-\infty}^{+\infty} f_\alpha \, \mathrm{d}\mathrm{v}_x \mathrm{d}\mathrm{v}_y \mathrm{d}\mathrm{v}_z, \tag{2.1.24}$$

where n_α is the specie number density.

We note that f_α is a finite, positive definite function that approaches zero as the particle velocity tends to infinity. f_α provides a microscopic description of plasma as it tells us the statistical information of all constituent particles at any given time instant in six–dimensional position and velocity phase space. It is possible to use f_α to compute macroscopic plasma quantities (e.g. density, bulk velocity and current) from a given particle property, $g(\boldsymbol{x}, \mathbf{v}, t)$, by taking the average of their product in velocity phase space:

$$g_{av}(\boldsymbol{x}, t) = \frac{1}{n_\alpha(\boldsymbol{x}, t)} \int_{\mathrm{v}_z=-\infty}^{+\infty} \int_{\mathrm{v}_y=-\infty}^{+\infty} \int_{\mathrm{v}_x=-\infty}^{+\infty} g(\boldsymbol{x}, \mathbf{v}, t) f_\alpha \, \mathrm{dv}_x \mathrm{dv}_y \mathrm{dv}_z. \tag{2.1.25}$$

Consequently, to study the evolution of a macroscopic quantity, it is necessary to consider that of the velocity distribution. The evolution of f_α is given by the Boltzmann equation [Inan and Gołkowski, 2011]:

$$\frac{\partial}{\partial t} f_\alpha(\boldsymbol{x}, \mathbf{v}, t) + \mathbf{v} \cdot \boldsymbol{\nabla} f_\alpha(\boldsymbol{x}, \mathbf{v}, t) + \frac{\boldsymbol{F}_\alpha}{m_\alpha} \cdot \nabla_{\mathbf{v}} f_\alpha(\boldsymbol{x}, \mathbf{v}, t) = \left(\frac{\partial f}{\partial t} \right)_{coll}, \tag{2.1.26}$$

in which $\boldsymbol{F}_\alpha$ is the external force acting on the plasma particle and is given by the Lorentz force, $\boldsymbol{F}_\alpha = q_\alpha[\boldsymbol{E} + \mathbf{v} \times \boldsymbol{B}]$ and the term on the right-hand-side relates to the net gain/loss of particles at a given velocity due to collisions.

(2.1.26) is general to a plasma with any given velocity distribution function, however, as noted in section 2.1.1, in the present study we only consider plasmas at local thermal equilibrium, thus f_α is given by the Maxwell–Boltzmann distribution:

$$f = N_0 \left(\frac{m}{2\pi k_B T} \right)^{3/2} \exp^{-m\mathrm{v}^2/(2k_B T)}, \tag{2.1.27}$$

where N_0 is the total number of particles in the system. We note that the Maxwell–Boltzmann distribution is both homogeneous (independent of $\boldsymbol{x}$) and isotropic (independent of direction of $\mathbf{v}$).

As we are interested in the fluid description of a plasma, it is not necessary to solve (2.1.26) explicitly for f_α, instead we consider forms of (2.1.26) in which only changes in macroscopic quantities are studied. To obtain these transformations, we multiply (2.1.26) by respective orders of $\mathbf{v}$ and integrate in velocity phase space. This is also known as taking moments of the Boltzmann equations. The zeroth-order moment is evaluated by taking the velocity integral of (2.1.26) multiplied by v^0. From this computation we obtain the continuity equation (which relates to conservation of mass and charge):

$$\frac{\partial n_\alpha}{\partial t} + \nabla \cdot (n_\alpha \boldsymbol{u}_\alpha) = 0. \tag{2.1.28}$$

where we define the mean or "fluid" velocity of a given particle specie, $\boldsymbol{u}_\alpha$, as:

$$\boldsymbol{u}_\alpha(\boldsymbol{x}, t) = \frac{1}{n_\alpha(\boldsymbol{x}, t)} \int_{\mathrm{v}_z=-\infty}^{+\infty} \int_{\mathrm{v}_y=-\infty}^{+\infty} \int_{\mathrm{v}_x=-\infty}^{+\infty} \mathbf{v} f_\alpha \, \mathrm{dv}_x \mathrm{dv}_y \mathrm{dv}_z, \tag{2.1.29}$$

and have assumed that the total particle number of each respective specie remains constant irrespective of collisions (i.e. recombination, ionisation, charge exchange and dissociation events are all neglected).

To obtain the momentum equation we take the first–order moment ((2.1.26) multiplied by $\mathbf{v}^1$) and multiply each specie equation by their respective particle mass, m_α:

$$\frac{\partial}{\partial t}(m_\alpha n_\alpha \boldsymbol{u}_\alpha) + \boldsymbol{\nabla}\cdot\{m_\alpha n_\alpha \boldsymbol{u}_\alpha \boldsymbol{u}_\alpha + \boldsymbol{\Psi}_\alpha\} - q_\alpha n_\alpha(\boldsymbol{E} + \boldsymbol{u}_\alpha \times \boldsymbol{B}) = \mathbf{R}_\alpha, \tag{2.1.30}$$

in which $\boldsymbol{\Psi}_\alpha$ is the total pressure tensor:

$$\boldsymbol{\Psi}_\alpha = \boldsymbol{\Pi}_\alpha + p_\alpha \mathbf{I} = m_\alpha n_\alpha \langle \mathbf{w}_\alpha \mathbf{w}_\alpha \rangle, \tag{2.1.31}$$

where $\mathbf{w}_\alpha$ is the random thermal movement:

$$\mathbf{w}_\alpha = \mathbf{v} - \boldsymbol{u}_\alpha(\boldsymbol{x}, t),$$

$\boldsymbol{\Pi}_\alpha$ is the anisotropic pressure and p_α is the scalar pressure:

$$p_\alpha = \frac{1}{3} m_\alpha n_\alpha \langle \mathrm{w}_\alpha^2 \rangle.$$

$\boldsymbol{R}_\alpha$ is the mean rate of momentum transfer between unlike particles due to collisions:

$$\boldsymbol{R}_\alpha = \int_{\mathrm{v}_z=-\infty}^{+\infty}\int_{\mathrm{v}_y=-\infty}^{+\infty}\int_{\mathrm{v}_x=-\infty}^{+\infty} m_\alpha \mathbf{v}\left(\frac{\partial f}{\partial t}\right)_{coll} \mathrm{dv}_x \mathrm{dv}_y \mathrm{dv}_z. \tag{2.1.32}$$

The energy equation is obtained by taking the second order moment ((2.1.26) multiplied by v^2) and multiplying by the respective particle mass:

$$\begin{aligned}\frac{\partial}{\partial t}\left(m_\alpha n_\alpha \left[e_{i,\alpha} + \frac{\boldsymbol{u}_\alpha \cdot \boldsymbol{u}_\alpha}{2}\right]\right) + \nabla \cdot \left\{m_\alpha n_\alpha \boldsymbol{u}_\alpha \left[e_{i,\alpha} + \frac{\boldsymbol{u}_\alpha \cdot \boldsymbol{u}_\alpha}{2}\right] + \boldsymbol{\Psi}_\alpha \boldsymbol{u}_\alpha + \boldsymbol{q}_\alpha\right\} = \\ = q_\alpha n_\alpha \boldsymbol{u}_\alpha \cdot \boldsymbol{E} + Q_\alpha + \boldsymbol{u}_\alpha \cdot \boldsymbol{R}_\alpha,\end{aligned} \tag{2.1.33}$$

$e_{i,\alpha}$ is the specific internal energy of the specie:

$$m_\alpha n_\alpha e_{i,\alpha} = \frac{s}{2} n_\alpha k_B T_\alpha = \frac{s}{2} p_\alpha, \tag{2.1.34}$$

where s is the number of degrees of freedom of each particle and takes the value of 3 for plasmas, representing the three translational degrees of freedom. It is defined in relation to the ratio of specific heats as:

$$\gamma = \frac{(s+2)}{s}.$$

Q_α is the heat generated and transferred due to unlike particle collisional dissipation:

$$Q_\alpha = \int_{\mathrm{v}_z=-\infty}^{+\infty}\int_{\mathrm{v}_y=-\infty}^{+\infty}\int_{\mathrm{v}_x=-\infty}^{+\infty} \frac{m_\alpha}{2}\mathrm{w}_\alpha^2\left(\frac{\partial f}{\partial t}\right)_{coll}\mathrm{dv}_x\mathrm{dv}_y\mathrm{dv}_z. \tag{2.1.35}$$

$\mathbf{q}_\alpha$ is the heat flux due to random motion:

$$\mathbf{q}_\alpha = \frac{1}{2}m_\alpha n_\alpha\langle \mathrm{w}_\alpha^2\mathbf{w}_\alpha\rangle. \tag{2.1.36}$$

In MHD, the plasma is modelled as a continuum. The continuum model requires statistical equilibrium to be reached on macroscopic scales, as such, it is assumed the plasma is collision-dominated. For this assumption to be valid we first we assume that the characteristic length, L_o, and time, τ_o, are much longer than the characteristic collision length, L_c, and time, τ_c; $L_o \gg L_c$ and $\tau_o \gg \tau_c$. We also assume the characteristic length and time is longer than that of gyromotion exhibited by charged particles in the presence of a magnetic field; $L_o \gg L_g$ and $\tau_o \gg \tau_g$, in which $L_g \sim R_i$ and $\tau_g \sim 1/\Omega_i$. Finally, it is also assumed that characteristic time scales are much longer than those of the electron plasma frequency, $\tau_o \gg \tau_{pe}$, where $\tau_{pe} \sim 1/\omega_{pe}$.

The governing equations of single–fluid MHD incorporate the low–frequency Maxwell's equations, derived in the previous section, along with the conservation equations for mass, charge, momentum, current density and energy for a single plasma fluid. Throughout these conservation equations it is assumed that ionisation, recombination and charge exchange within the plasma are all negligible on the time scales being observed in the plasma. We form the equations by completing a linear addition of the conservation equations for electrons and a single ion species. However, in reality, there exists nonlinear coupling between ion and electron motions which is not resolved by this linear operation.

To attain a single fluid approximation, we first give definitions to the bulk macroscopic plasma properties:

$$\rho \equiv n_e m_e + n_i m_i, \tag{2.1.37}$$

$$\rho_c \equiv n_e q_e + n_i q_i, \tag{2.1.38}$$

$$\boldsymbol{J} \equiv n_e q_e \boldsymbol{u}_e + n_i q_i \boldsymbol{u}_i, \tag{2.1.39}$$

$$\boldsymbol{u} \equiv \frac{n_e m_e \boldsymbol{u}_e + n_i m_i \boldsymbol{u}_i}{n_e m_e + n_i m_i}, \tag{2.1.40}$$

$$p \equiv p_e + p_i, \tag{2.1.41}$$

$$T \equiv T_e + T_i, \tag{2.1.42}$$

We can simplify the bulk definitions by first noting that in all plasmas, the ion mass will be at least three orders higher than that of the electron ($m_e/m_{proton} \simeq 1/1836 \ll 1$). As such, we take the electron mass in the zero limit ($m_e \to 0$) and infer that the momentum of the plasma is effectively carried by the ion only. This enables the following approximations to be applied to the bulk density and velocity:

$$\rho \simeq n_i m_i,$$

$$\boldsymbol{u} \simeq \boldsymbol{u}_i.$$

The high frequency of collisions means that particles are sufficiently restricted in their motion such that their motion can be represented by a local centre of mass. This also gives meaning to the material derivative $\left(\frac{\mathrm{d}}{\mathrm{d}t} = \frac{\partial}{\partial t} + u \cdot \nabla\right)$ - as it implies that there exists a fluid element that we are able to follow along a well defined path.

We assume the plasma to be quasi–neutral on length scales of interest, as such, the charge density of the single fluid plasma, ρ_c, can be taken as zero. This leads to the following relationship between the respective ion and electron charges and number densities (2.1.38):

$$n_e q_e = -n_i q_i.$$

If we assume that the ion is positive and singly charged, then we find that the number density of the ion and electrons must be equal:

$$n = n_e = n_i$$

As a result, the current density is given by:

$$\boldsymbol{J} = n q_e (\boldsymbol{u}_i - \boldsymbol{u}_e). \tag{2.1.43}$$

From (2.1.43) we make the assumption:

$$\boldsymbol{u}_e \simeq \boldsymbol{u} - \frac{\boldsymbol{J}}{n q_e}.$$

The conservation of mass and charge for a single fluid can be derived through the linear addition of the mass conservation and mass conservation multiplied by q_α/m_α for an ion and electron respectively:

$$\frac{\partial \rho}{\partial t} + \nabla \cdot (\rho \boldsymbol{u}) = 0, \tag{2.1.44}$$

$$\frac{\partial \rho_c}{\partial t} + \nabla \cdot \boldsymbol{J} = 0. \tag{2.1.45}$$

If we then apply the simplified single fluid plasma definitions, we find that the mass conservation equation remains in the same form. However, as a result of the quasi–neutrality condition ($\rho_c = 0$), the charge conservation equation reduces to the following:

$$\nabla \cdot \boldsymbol{J} = 0. \tag{2.1.46}$$

To derive the momentum and energy equations, we first assume that $\boldsymbol{R}_{ei} = \boldsymbol{R}_i = -\boldsymbol{R}_e$ - i.e. the total momentum must be conserved in collisional interactions with two species. From classical transport theory [Boyd and Sanderson, 2003], it is possible to obtain expressions for $\boldsymbol{R}_{ei}$ in addition to $\boldsymbol{\Pi}_\alpha$, Q_α and $\boldsymbol{q}_\alpha$. Classical transport theory applies to plasmas in which the momentum transfer is governed by binary collisions of particles in a slowly varying magnetic and electric field, in which the external magnetic field is assumed to be stationary, homogeneous and unidirectional. Under the assumption of infinitesimal electron mass limit, it is found that thermal and electrical conductivities are electron–dependent while the viscosity is ion–dependent [Boyd and Sanderson, 2003]. We therefore reduce the momentum equation to the following form:

$$\frac{\partial}{\partial t}(\rho \boldsymbol{u}) = \boldsymbol{\nabla} \cdot \left\{ \boldsymbol{B}\boldsymbol{B} - \rho \boldsymbol{u}\boldsymbol{u} - p\boldsymbol{I} - \frac{\boldsymbol{B} \cdot \boldsymbol{B}}{2\mu_m} + \boldsymbol{\Sigma} \right\}, \tag{2.1.47}$$

where $\boldsymbol{\Sigma}$ is the viscous stress tensor.

The generalised Ohm's law is an additional equation that can be derived from the initial set of two-fluid momentum equations. It can be found by summing together the result of multiplying the momentum equations for ions and electrons by their respective specific charges q_i/m_i and q_e/m_e [Inan and Gołkowski, 2011]:

$$\boldsymbol{E} = -\boldsymbol{u} \times \boldsymbol{B} + \frac{m_e}{q_e n} \frac{\partial \boldsymbol{J}}{\partial t} + \frac{1}{q_e n} \boldsymbol{\nabla} \cdot \boldsymbol{\Psi}_e - \frac{1}{q_e n} \boldsymbol{J} \times \boldsymbol{B} + \eta \boldsymbol{J}, \tag{2.1.48}$$

where from left–to–right on the right–hand–side, each respective term denotes contributions to the electric field (in a stationary reference frame) generated in a conductive fluid due to the motional electric field, electron inertia, ambipolar diffusion, Hall effect and collisional resistance [Inan and Gołkowski, 2011]. In the case of weakly–ionised hypersonic flows, all of these terms can be significant [Grasso and Capano, 1995], [Bityurin et al., 2003]. However, the present study aims to provide a comparison between analogous compressible energy transfer mechanisms in plasmas and gas dynamics. As such, the influence of phenomena that arises primarily from non-single fluid type behaviour of ions and electrons was not considered. Consequently, by assuming the characteristic length scale is significantly greater than the respective ion and electron inertial length scales it is possible to reduce Ohm's law to its simplified form, where only the motional electric field and collisional current resistance are considered:

$$\boldsymbol{E} + \boldsymbol{u} \times \boldsymbol{B} = \eta \boldsymbol{J}, \tag{2.1.49}$$

where $\boldsymbol{E}$ is the electric field, $\boldsymbol{u}$ is the fluid velocity and η is the resistivity.

An additional equation describing the time evolution of the magnetic field can be derived using Maxwell's

equations and the reduced Ohm's law (2.1.49):

$$\frac{\partial \boldsymbol{B}}{\partial t} = -\boldsymbol{\nabla} \cdot \{\boldsymbol{uB} - \boldsymbol{Bu}\} + \lambda \boldsymbol{\nabla} \times (\boldsymbol{\nabla} \times \boldsymbol{B}), \tag{2.1.50}$$

where λ is the magnetic diffusivity of the plasma defined as:

$$\lambda = \frac{1}{\sigma \mu_m}.$$

Applying classical transport theory to (2.1.33), we obtain the MHD conservation of energy equation:

$$\frac{\partial}{\partial t}(\rho e_t^*) = -\nabla \cdot \left\{ \left[\rho e_t^* + p + \frac{\boldsymbol{B} \cdot \boldsymbol{B}}{\mu_m} \right] \boldsymbol{u} - \boldsymbol{\Sigma u} - \frac{1}{\mu_m} (\boldsymbol{B} \cdot \boldsymbol{u}) \boldsymbol{B} - \kappa \boldsymbol{\nabla} T - \frac{\lambda \boldsymbol{B} \times (\boldsymbol{\nabla} \times \boldsymbol{B})}{\mu_m} \right\}, \tag{2.1.51}$$

where e_t^* is defined as,

$$\rho e_t^* = \rho \left[e_i + \frac{\boldsymbol{u} \cdot \boldsymbol{u}}{2} \right] + \frac{\boldsymbol{B} \cdot \boldsymbol{B}}{2\mu_m}.$$

The MHD conservation equations for mass, momentum, energy and magnetic flux now form a determinate set of eight equations from which the density, pressure, velocity and magnetic field within the plasma can be found.

2.2 Ideal MHD equations

2.2.1 Formulation

The single-fluid, viscous and resistive compressible MHD equations are given in non–dimensional divergence form (bulk viscosity is assumed equal to zero):

$$\frac{\partial}{\partial t}\begin{pmatrix}\rho\\ \rho\boldsymbol{u}\\ \rho e_t\\ \boldsymbol{B}\end{pmatrix}+\boldsymbol{\nabla}\cdot\begin{pmatrix}\rho\boldsymbol{u}\\ \rho\boldsymbol{u}\boldsymbol{u}+P\mathbf{I}-\dfrac{1}{M_A^2}(\boldsymbol{B}\boldsymbol{B})\\ (\rho e_t+P)\boldsymbol{u}-\dfrac{1}{M_A^2}(\boldsymbol{B}\cdot\boldsymbol{u})\boldsymbol{B}\\ \boldsymbol{u}\boldsymbol{B}-\boldsymbol{B}\boldsymbol{u}\end{pmatrix}=$$

$$\frac{1}{Re}\begin{pmatrix}0\\ \boldsymbol{\nabla}\cdot\mathbf{D}^{\bullet}\\ \nabla\cdot(\mathbf{D}^{\bullet}\boldsymbol{u}+\kappa\boldsymbol{\nabla}T)\\ 0\end{pmatrix}+\frac{1}{R_m}\begin{pmatrix}0\\ 0\\ \dfrac{1}{M_A^2}\nabla\cdot(\boldsymbol{B}\times[\boldsymbol{\nabla}\times\boldsymbol{B}])\\ -\boldsymbol{\nabla}\times(\boldsymbol{\nabla}\times\boldsymbol{B})\end{pmatrix}, \tag{2.2.1}$$

where $\mathbf{D}^{\bullet}$ is the deviatoric part of the strain-rate tensor, $\mathbf{D}^{\bullet}=\mathbf{D}-(\nabla\cdot\boldsymbol{u})\mathbf{I}/3$, $(\mathbf{D}\equiv(\boldsymbol{\nabla}\boldsymbol{u}+\boldsymbol{\nabla}\boldsymbol{u}^{\intercal})/2)$, P is the combined non–dimensional thermodynamic and magnetic pressure, $P=p+\boldsymbol{B}\cdot\boldsymbol{B}/(2M_A^2)$, and e_t is the non–dimensional specific total energy, $e_t=e+P/\rho+\boldsymbol{u}\cdot\boldsymbol{u}/2$, in which e is the non–dimensional specific internal energy.

We define $\rho\equiv\rho^*/\rho_r^*$, $\boldsymbol{u}\equiv\boldsymbol{u}^*/u_r^*$, $T\equiv T^*/T_r^*$, $p\equiv p^*/(\rho_r^*u_r^*u_r^*)$ and $\boldsymbol{B}\equiv\boldsymbol{B}^*/B_r^*$ as the respective dimensionless density, velocity, temperature, thermodynamic pressure and magnetic fields where $(\cdot)^*$ denotes a quantity in dimensional form and $(\cdot)_r$ denotes a reference quantity.

The flow is modelled in a three–dimensional Cartesian coordinate system with $\rho=\rho(\boldsymbol{x},t)$, $\boldsymbol{u}=u(\boldsymbol{x},t)\mathbf{e}_x+v(\boldsymbol{x},t)\mathbf{e}_y+w(\boldsymbol{x},t)\mathbf{e}_z$, $T=T(\boldsymbol{x},t)$, $p=p(\boldsymbol{x},t)$, $\boldsymbol{B}=B_x(\boldsymbol{x},t)\mathbf{e}_x+B_y(\boldsymbol{x},t)\mathbf{e}_y+B_z(\boldsymbol{x},t)\mathbf{e}_z$, where $\boldsymbol{x}$ denotes the dimensionless position vector, $\boldsymbol{x}=[x,\,y,\,z]^{\intercal}$, in the x, y and z directions given by the unit vectors, $\mathbf{e}_x=[1,\,0,\,0]^{\intercal}$, $\mathbf{e}_y=[0,\,1,\,0]^{\intercal}$ and $\mathbf{e}_z=[0,\,0,\,1]^{\intercal}$, for which $\boldsymbol{x}\equiv\boldsymbol{x}^*/L_r^*$ and t is the dimensionless time variable, $t\equiv t^*u_r^*/L_r^*$.

The reference speed of sound and Alfvén speed are defined as $c_r^*\equiv\sqrt{\gamma RT_r^*}$ and $b_r^*\equiv B_r^*/\sqrt{\mu_m\rho_r^*}$ respectively. Additionally, from the reference quantities we derive the following non–dimensional parameters; Mach number, $M_a\equiv u_r^*/c_r^*$; Alfvén Mach number, $M_A\equiv u_r^*/b_r^*$; Reynolds number, $Re\equiv\rho_r^*u_r^*L_r^*/\mu_o$, mag-

netic Reynolds number, $R_m \equiv u_r^* L_r^* \sigma \mu_m$; Prandtl number, $Pr \equiv \mu_o C_p/\kappa$ and non–dimensional conductivity, $\kappa = 1/(\gamma Pr M_a^2)$.

We take the MHD equations in the non-dissipative or "ideal" limit - i.e. viscous momentum transfer and conduction of heat are assumed negligible and there exists infinite electrical conductivity. With respect to the derivation of electrical conductivity, an infinite value implies the absence of collisions within the plasma. However, this presents a contradiction in our description of plasma as sufficiently collisional that it reaches local thermal equilibrium on relevant time scales. As such, we define ideal MHD simply as the limit in which the dissipative terms for momentum and current are insignificant in comparison to their respective convective terms. This is expressed in terms of the Reynolds and magnetic Reynolds numbers; $Re \gg 1$ and $R_m \gg 1$. Taking the Reynolds and magnetic Reynolds numbers in the large limit, the RHS of (2.2.1) vanishes, therefore forming the ideal MHD equations (note that M_A has been absorbed into $\boldsymbol{B}$):

$$\frac{\partial}{\partial t}\begin{pmatrix} \rho \\ \rho \boldsymbol{u} \\ \rho e_t \\ \boldsymbol{B} \end{pmatrix} + \boldsymbol{\nabla} \cdot \begin{pmatrix} \rho \boldsymbol{u} \\ \rho \boldsymbol{u}\boldsymbol{u} + P\mathbf{I} - \boldsymbol{B}\boldsymbol{B} \\ (\rho e_t + P)\boldsymbol{u} - (\boldsymbol{B}\cdot\boldsymbol{u})\boldsymbol{B} \\ \boldsymbol{u}\boldsymbol{B} - \boldsymbol{B}\boldsymbol{u} \end{pmatrix} = \mathbf{0}, \tag{2.2.2}$$

which is solved on the computational domain in Cartesian coordinates as:

$$\frac{\partial \boldsymbol{Q}}{\partial t} + \frac{\partial \boldsymbol{F}}{\partial x} + \frac{\partial \boldsymbol{G}}{\partial y} + \frac{\partial \boldsymbol{H}}{\partial z} = \mathbf{0}, \tag{2.2.3}$$

in which the solution vector, $\boldsymbol{Q}$, and flux vectors, $\boldsymbol{F}$, $\boldsymbol{G}$ and $\boldsymbol{H}$, are defined as:

$$\boldsymbol{Q} = \begin{pmatrix} \rho \\ \rho u \\ \rho v \\ \rho w \\ \rho e_t \\ B_x \\ B_y \\ B_z \end{pmatrix}, \boldsymbol{F} = \begin{pmatrix} \rho u \\ \rho u^2 + P - B_x^2 \\ \rho uv - (B_x B_y) \\ \rho uw - (B_x B_z) \\ (\rho e_t + P)u - B_x(\boldsymbol{u}\cdot\boldsymbol{B}) \\ 0 \\ uB_y - vB_x \\ uB_z - wB_x \end{pmatrix}, \boldsymbol{G} = \begin{pmatrix} \rho v \\ \rho uv - (B_x B_y) \\ \rho v^2 + P - B_y^2 \\ \rho vw - (B_y B_z) \\ (\rho e_t + P)v - B_y(\boldsymbol{u}\cdot\boldsymbol{B}) \\ vB_x - uB_y \\ 0 \\ vB_z - wB_y \end{pmatrix}, \boldsymbol{H} = \begin{pmatrix} \rho w \\ \rho uw - (B_x B_z) \\ \rho vw - (B_y B_z) \\ \rho w^2 + P - B_z^2 \\ (\rho e_t + P)w - B_z(\boldsymbol{u}\cdot\boldsymbol{B}) \\ wB_x - uB_z \\ wB_y - vB_z \\ 0 \end{pmatrix}.$$

2.2.2 Hyperbolicity of the ideal MHD equations

When solving physical problems it is possible to define their behaviour through a set of conservation laws. For certain problems, these laws can be written as a system of quasi–linear partial differential equations (PDEs), containing first-order derivatives of the dependent variables and coefficients that can also be functions of the dependent variables. By inspecting these coefficients we can prescribe the property of hyperbolicity, which, in its most general sense, describes flows where information propagates through the problem domain as waves in time and space. In general, this "propagation" can occur within any two (or more) variable parametric space. However, for the present study it is more pertinent to consider hyperbolicity in the context of spatio-temporal waves propagating through a flow, as such, we define a problem for which the governing conservation laws are expressed in the form:

$$\frac{\partial \boldsymbol{q}}{\partial t} + \sum_{k=1}^{3} \frac{\partial \boldsymbol{f}_k(\boldsymbol{q})}{\partial x_k} = \mathbf{0}, \tag{2.2.4}$$

where the conserved variables are represented by $\boldsymbol{q}$, a state vector in $\mathbb{R}^n$ taken to be a function of both time ($t \in \mathbb{R}_{\geq 0}$) and three–dimensional Euclidean space ($\boldsymbol{x} \in \mathbb{R}^3$), and $\boldsymbol{f}_k$, a function of $\boldsymbol{q}$. In the context of an ideal MHD flow, $\boldsymbol{q}$, $\boldsymbol{f}_1$, $\boldsymbol{f}_2$ and $\boldsymbol{f}_3$ are equivalent to $\boldsymbol{Q}$, $\boldsymbol{F}$, $\boldsymbol{G}$ and $\boldsymbol{H}$ respectively, defined in (2.2.3).

For certain PDEs, we can use the idea of information propagating as a wave through the problem domain to select a specific path in space along which the PDE reduces to an ordinary differential equation (ODE) and a solution can be found. This technique is called the method of characteristics, and corresponds to the idea that in a given time increment, a wave will have a finite domain of influence within the flow - i.e. the region of space it propagates through in that time period. It is therefore possible to consider local regions along this "characteristic" path, or curve, in time and space, on which an ODE can be integrated (analytically or numerically) and a solution obtained. A system of PDEs that can be solved via this method is termed hyperbolic. To prove this property, we must be able to decompose the original PDEs into characteristic form. With respect to (2.2.4), we first transform it to primitive form, in which the conservation laws are now written as a quasi–linear system of PDEs:

$$\frac{\partial \boldsymbol{\mu}}{\partial t} + \sum_{k=1}^{3} \mathbf{A}_k \frac{\partial \boldsymbol{\mu}}{\partial x_k} = \mathbf{0}, \tag{2.2.5}$$

where $\boldsymbol{\mu}$ is a vector of primitive variables in $\mathbb{R}^n$ and matrices $\mathbf{A}_k$ are functions of $\boldsymbol{\mu}$ in $\mathbb{R}^{n\times n}$.

The primitive system is related to (2.2.4) (also known as the divergence form) through the following definitions:

$$\frac{\partial \boldsymbol{\mu}}{\partial t} = \mathbf{P}\frac{\partial \boldsymbol{\mu}}{\partial t}, \qquad \frac{\partial \boldsymbol{f}_k}{\partial x_k} = \mathbf{Q}_k \frac{\partial \boldsymbol{\mu}}{\partial x_k}, \tag{2.2.6}$$

where the flux Jacobian matrix of $\boldsymbol{f}_k$, is given as $\mathbf{Q}_k = \partial \boldsymbol{f}_k / \partial \boldsymbol{\mu}$, and is related to $\mathbf{A}_k$ and $\mathbf{P}$ through the expression:

$$\mathbf{A}_k = \mathbf{P}^{-1}\mathbf{Q}_k, \tag{2.2.7}$$

in which $\mathbf{P}$ and $\mathbf{Q}_k$ are matrices in $\mathbb{R}^{n\times n}$.

In (2.2.5), the rate of change of $\boldsymbol{\mu}$ with respect to time is coupled with its rates of change in the spatial directions. Through the method of characteristics we aim to manipulate (2.2.5) and show that specific increments in both time and space can combine to give a certain increment in $\boldsymbol{\mu}$. First we take the product of (2.2.5) with the vector, $\boldsymbol{l}$:

$$\boldsymbol{l} \cdot \left(\frac{\partial \boldsymbol{\mu}}{\partial t} + \sum_{k=1}^{3} \mathbf{A}_k \frac{\partial \boldsymbol{\mu}}{\partial x_k} \right) = 0, \tag{2.2.8}$$

where $\boldsymbol{l}$ is function of t, $\boldsymbol{x}$ and $\boldsymbol{\mu}$ in $\mathbb{R}^n$, and ascertain whether (2.2.8) can be written in the form:

$$\boldsymbol{m} \cdot \left(\alpha \frac{\partial \boldsymbol{\mu}}{\partial t} + \sum_{k=1}^{3} \beta_k \frac{\partial \boldsymbol{\mu}}{\partial x_k} \right) = 0, \tag{2.2.9}$$

in which α, β_k and $\boldsymbol{m}$ exist in $\mathbb{R}$, $\mathbb{R}$ and $\mathbb{R}^n$ respectively.

For (2.2.8) to be shown equivalent to (2.2.9), there must exist a relation between the directional derivatives of $\boldsymbol{\mu}$ in a single direction $(\boldsymbol{\beta}, \alpha)$ in $(\boldsymbol{x}, t)$. We seek to define this direction or "path" in a single parameter space, η, which we relate to the time and spatial variables through the functions, $t = \tilde{t}(\eta)$, and, $x_k = \tilde{x}_k(\eta)$, respectively. Consequently, the total derivative of $\boldsymbol{\mu}$ with respect to η can be expressed as:

$$\frac{\mathrm{d}\boldsymbol{\mu}}{\mathrm{d}\eta} = \frac{\mathrm{d}\tilde{t}}{\mathrm{d}\eta}\frac{\partial \boldsymbol{\mu}}{\partial t} + \sum_{k=1}^{3} \frac{\mathrm{d}\tilde{x}_k}{\mathrm{d}\eta}\frac{\partial \boldsymbol{\mu}}{\partial x_k}. \tag{2.2.10}$$

From inspection of (2.2.8) and (2.2.9), we see it is possible to set $\eta \equiv t$ ($\alpha = 1$) and thus, without loss of generality:

$$\frac{\mathrm{d}\tilde{x}_k}{\mathrm{d}\eta} = \frac{\mathrm{d}\tilde{x}_k}{\mathrm{d}t} = \beta_k, \tag{2.2.11}$$

indicating that the relation between the directional derivatives is actually given by a characteristic velocity.

We can now write (2.2.9) as:

$$\boldsymbol{m} \cdot \frac{\mathrm{d}\boldsymbol{\mu}}{\mathrm{d}t} = 0, \tag{2.2.12}$$

which is equivalent to (2.2.8) if the following conditions are satisfied (note: $\alpha = 1$ has been applied):

$$\boldsymbol{l} = \boldsymbol{m}, \quad \text{and} \quad \boldsymbol{l} \cdot \mathbf{A}_k = \boldsymbol{m}\beta_k. \tag{2.2.13}$$

We eliminate $\boldsymbol{m}$ from (2.2.13) to derive the following relations:

$$\boldsymbol{l} \cdot (\mathbf{A}_k - \beta_k \mathbf{I}) = 0. \tag{2.2.14}$$

In (2.2.14), for each $\mathbf{A}_k$ there exist n equations of the characteristic velocity, β_k, and the multiplier, $\boldsymbol{l}$. For the solution to $\boldsymbol{l}$ to be non-trivial, it is necessary that the matrix, $(\mathbf{A}_k - \beta_k \mathbf{I})$, is non-invertible - i.e. its determinant equal to zero:

$$|\mathbf{A}_k - \beta_k \mathbf{I}| = 0. \tag{2.2.15}$$

The above condition sets the characteristic velocities and therefore defines the path in $\boldsymbol{x}$-t space along which a given characteristic form of the initial system of PDEs holds. From each characteristic equation we obtain an expression for how the n derivatives of $\boldsymbol{\mu}$ change along along the characteristic curve. As such, for a unique solution to the system to exist, n independent characteristic equations are required. The system is hyperbolic if this condition is met.

From (2.2.15) we observe that the possible n roots of β_k represent the eigenvalues of $\mathbf{A}_k$, and thus, $\boldsymbol{l}$, the corresponding left eigenvectors. As such, the system of PDEs given in (2.2.5) is hyperbolic if there exist n real and distinct eigenvectors - i.e. $\mathbf{A}_k$ is diagonalisable and has n real eigenvalues. If the eigenvalues are also distinct, the system is termed strictly hyperbolic [Dafermos, 2006].

To investigate the hyperbolicity of an ideal MHD system, we restrict eigen–analysis to matrix $\mathbf{A}_1$, however, it is trivial to extend analysis to matrices $\mathbf{A}_2$ and $\mathbf{A}_3$. We utilise a three–dimensional Cartesian coordinate system and define the vector of primitive variables for an ideal MHD flow as, $\boldsymbol{\mu} \equiv [\rho,\, \boldsymbol{u}^{\intercal},\, p,\, \boldsymbol{B}^{\intercal}]^{\intercal}$. Using the set of relations given in (2.2.6) and (2.2.7), an expression for $\mathbf{A}_1$ can be obtained:

$$\mathbf{A}_1 = \begin{bmatrix} u & \rho & 0 & 0 & 0 & 0 & 0 & 0 \\ 0 & u & 0 & 0 & \frac{1}{\rho} & 0 & \frac{B_y}{\rho} & \frac{B_z}{\rho} \\ 0 & 0 & u & 0 & 0 & 0 & -\frac{B_x}{\rho} & 0 \\ 0 & 0 & 0 & u & 0 & 0 & 0 & -\frac{B_x}{\rho} \\ 0 & \rho c_o^2 & 0 & 0 & u & 0 & 0 & 0 \\ 0 & 0 & 0 & 0 & 0 & u & 0 & 0 \\ 0 & B_y & -B_x & 0 & 0 & 0 & u & 0 \\ 0 & B_z & 0 & -B_x & 0 & 0 & 0 & u \end{bmatrix}, \tag{2.2.16}$$

where c_o is the speed of sound, $c_o^2 = (\partial p / \partial \rho)_s$.

Setting the determinant, $|\mathbf{A}_1 - \lambda \mathbf{I}|$, to zero results in an 8^{th} degree polynomial of λ:

$$|\mathbf{A}_1 - \lambda\mathbf{I}| = (\lambda - u)^2[(\lambda - u)^2 - b_x^2][(\lambda - u)^4 - (c_o^2 + b^2)(\lambda - u)^2 + c_o^2 b_x^2] = 0, \tag{2.2.17}$$

in which the Alfvén speed, b, is defined as the magnitude of the Alfvén velocity, $b = ||\boldsymbol{b}||$, where $\boldsymbol{b}$:

$$\boldsymbol{b} = \frac{\boldsymbol{B}}{\sqrt{\rho}}. \tag{2.2.18}$$

We find that (2.2.17) has eight real solutions - each corresponding to a real and distinct eigenvector. As such, the ideal MHD system is indeed hyperbolic (the same property can be shown for matrices $\mathbf{A}_2$ and $\mathbf{A}_3$). However, these (eigenvalue) solutions can have varying levels of multiplicity depending on the primitive state vector, $\boldsymbol{\mu}$, therefore the system is not strictly hyperbolic.

Each eigenvalue is associated with a characteristic wave speed of ideal MHD (whose respective wave fronts are normal to the x_1 direction). There exists the backward/forward fast magneto–acoustic (λ_1 & λ_7), backward/forward slow magneto–acoustic (λ_3 & λ_5) and backward/forward Alfvén (λ_2 & λ_6) modes propagating at speeds slower/faster than the local flow speed. The two remaining modes are convected with the flow. The first is the entropy mode (λ_4), which is physical and also exists in gas dynamics, carrying only density perturbations. The second is the $\nabla \cdot \boldsymbol{B}$ mode, which is non–physical and denotes transport of $\nabla \cdot \boldsymbol{B}$ perturbations. The governing equations (2.2.2) in their current form only stipulate that $\partial(\nabla \cdot \boldsymbol{B})/\partial t = 0$ (by taking the divergence of the induction equations). As such, if the initial condition is $\nabla \cdot \boldsymbol{B} = 0$, this will be true for all times. We eliminate the $\nabla \cdot \boldsymbol{B}$ eigenmode by setting the aforementioned condition. The remaining seven eigenvalues are well ordered, $\lambda_1 \leq \ldots \leq \lambda_7$:

$$\begin{aligned} &\lambda_1 = u - c_{f,x}, \quad \lambda_2 = u - b_x, \quad \lambda_3 = u - c_{s,x}, \quad \lambda_4 = u, \\ &\lambda_5 = u + c_{s,x}, \quad \lambda_6 = u + b_x, \quad \lambda_7 = u + c_{f,x}, \end{aligned} \tag{2.2.19}$$

where c_f and c_s are the fast and slow magneto–acoustic wave speeds:

$$c_{f,s,x}^2 = \frac{1}{2}\left\{(c_o^2 + b^2) \pm \sqrt{(c_o^2 + b^2)^2 - 4c_o^2 b_x^2}\right\}. \tag{2.2.20}$$

From the definitions given for the magneto–acoustic and Alfvén wave speeds, it is clear that the multiplicity of eigenvalues is dependent on both the thermodynamic properties (via sound speed) and magnetic field. Where the magnetic field component normal to wave front direction is zero, $B_x = 0$, the slow magneto–acoustic and Alfvén modes become degenerate with the entropy mode, $\lambda_2 = \lambda_3 = \lambda_4 = \lambda_5 = \lambda_6$. In contrast, if the magnetic field components parallel to the wave front are equal to zero, $B_y = B_z = 0$, three separate types of degeneracy are possible. If the Alfvén speed is greater than the sound speed ($b > c_o$) then the fast magneto–acoustic wave speed degenerates to the Alfvén speed; $\lambda_1 = \lambda_2$ and $\lambda_6 = \lambda_7$. Whereas, if the

Alfvén speed is lower than the sound speed ($b < c_o$) the slow magneto–acoustic wave speed degenerates to the Alfvén speed; $\lambda_2 = \lambda_3$ and $\lambda_5 = \lambda_6$. The third possibility, in which the Alfvén wave speed is equal to the sound speed ($b = c_o$), is known as the triple umbilic condition [Roe and Balsara, 1996], and results in the Alfvén and fast and slow magneto–acoustic wave speeds all degenerating to the same value, $\lambda_1 = \lambda_2 = \lambda_3$ and $\lambda_5 = \lambda_6 = \lambda_7$.

Chapter 3

Numerical Methods

3.1 Finite difference methods for conservation laws

In section 2.1.3.4, a set of nonlinear PDEs were derived to describe the momentum balance and conservation of mass, energy and magnetic flux of a magnetohydrodynamic flow. These conservation laws can be written in divergence form:

$$\frac{\partial \boldsymbol{q}}{\partial t} + \boldsymbol{\nabla} \cdot \mathbf{F}(\boldsymbol{q}) = \mathbf{0}, \tag{3.1.1}$$

where the conserved variables are represented by $\boldsymbol{q}$, a state vector in $\mathbb{R}^n$ taken to be a function of both time ($t \in \mathbb{R}_{\geq 0}$) and three–dimensional Euclidean space ($\boldsymbol{x} \in \mathbb{R}^3$), and $\mathbf{F}$ is a real–valued, rank 2 tensor which depends on $\boldsymbol{q}$.

From the integral form of (3.1.1), we know that the integrated quantity of the state vector variable over an arbitrary domain, $\int_V \boldsymbol{q}\,\mathrm{d}V$, must be conserved, $\frac{\mathrm{d}}{\mathrm{d}t}\int_V \boldsymbol{q}\,\mathrm{d}V = \mathbf{0}$. However, it is necessary to know the value of $\boldsymbol{q}$ at each point in $\boldsymbol{x} - t$ space in order to determine $\boldsymbol{F}(\boldsymbol{q})$ and thus evolve the flow in time.

For many nonlinear systems of PDEs, such as the MHD equations, it is not possible to derive an analytical solution to the state vector. As such, numerical methods are employed to compute an approximate solution to the governing conservation equations within an acceptable margin of error. Numerical approximations in which we compute a discrete representation of these PDEs are known as finite difference methods. However, it is common when modelling certain types of flows, such a turbulence, for modifications to be made to the governing set of PDEs in order to reduce the range of spatial and temporal scales required to accurately capture the flow dynamics (e.g. LES, RANS). Flows solved numerically without such models - i.e. the exact form of governing PDEs are used - are termed direct numerical simulations (DNS). DNS can be thought of as

"numerical experiments", in which theoretically, the accuracy of the flow solution compared to a real-world example is dependent only on the resolution of the spatio-temporal computational grid and the appropriate application of boundary conditions (if the underlying assumptions behind the governing conservation laws are valid). The computational grid represents a discrete sampling of the continuous flowfield. If we define the flow in a Cartesian coordinate system on a uniform cube grid, $0 \leq x \leq L$, $0 \leq y \leq L$, $0 \leq z \leq L$, we can define the displacement at the point (x_i, y_j, z_k) as:

$$(x_i,\, y_j,\, z_k) = (i\Delta, j\Delta, k\Delta), \quad (i,\, j,\, k) \in \{0, \ldots, N-1\}^3, \tag{3.1.2}$$

where Δ is the grid spacing, $\Delta = L/(N-1)$, for a grid with N points in each spatial direction. Similarly, the time elapsed at the nth timestep after flow initialisation is defined as, $t_n = n\Delta t$, where Δt is the time increment. Consequently, it is possible to describe a discrete sample of the continuous state vector solution at a given point (x_i, y_j, z_k, t_n) within the spatio-temporal computational domain as, $\boldsymbol{U}^n_{i,j,k}$.

To obtain a solution to (3.1.1), an initial condition and/or boundary conditions regarding the state vector must be supplied. This is known as a Cauchy problem. For a given initial state, $\boldsymbol{q}(\boldsymbol{x}, 0)$, a numerical method can be applied to estimate the solution at time, $t_{n+1} = t_n + \Delta t$, provided the solution is known for; $0 \leq t \leq t_n$. This can be achieved via a piece–wise time integration of the discrete form of (3.1.1) (given below), in which the fluxes are computed using a numerical approximation of the spatial derivatives:

$$\frac{\mathrm{d}\boldsymbol{U}_{i,j,k}}{\mathrm{d}t} = \mathcal{L}[\boldsymbol{U}^n], \tag{3.1.3}$$

where the term on the right-hand-side represents the numerical approximation of the flux term for which $\mathcal{L}$ is an operator on $\boldsymbol{U}^n$.

Accuracy, complexity and stability are all considered when selecting a numerical scheme to solve a system of PDEs. With respect to marching forward in time, numerical schemes can be either explicit, in which the solution for $\boldsymbol{U}^{n+1}$ at any point in space is determined from data at the previous time step, $\boldsymbol{U}^n$, or implicit, for which the solution to $\boldsymbol{U}^{n+1}$ is dependent on data at the same time step. Implicit methods are unconditionally stable and allow a greater time increment between steps, however, the complexity of such schemes is increased as any solution of (3.1.1) must be obtained as a coupled system involving $\boldsymbol{U}^{n+1}$ at every point. There exist several measures of stability, notably linear and nonlinear stability - i.e. whether the solution obtained via a given numerical method grows unbounded for linear and nonlinear problems [LeVeque and Leveque, 1992]. If a consistent and conservative numerical method is total variation diminishing (TVD) it is also nonlinearly stable and guarantees the convergence of a solution [LeVeque and Leveque, 1992]:

$$TV(\boldsymbol{U}^{n+1}) \leq TV(\boldsymbol{U}^n), \tag{3.1.4}$$

in which TV denotes the total variation of a discretised solution, which describes the sum of absolute difference in value for a given quantity between adjacent points in the domain - i.e. the L_1 norm (definition below given for a one–dimensional problem):

$$TV(\boldsymbol{U}^n) = \sum_i |\boldsymbol{U}^n_{i+1} - \boldsymbol{U}^n_i|. \tag{3.1.5}$$

In the present study, a TVD 3^{rd}-order explicit Runge-Kutta scheme is used to march the solution forward in time [Shu and Osher, 1988]. In explicit Runge-Kutta methods, the flux term in (3.1.5), $\mathcal{L}[\boldsymbol{U}^n]$ is evaluated at intermediate steps between t_n and t_{n+1}, with the number of intermediate steps affecting the order of accuracy. The general formula for an $(r+1)$-th order accurate scheme (for $r \leq 3$) is given as [Shu and Osher, 1988]:

$$\boldsymbol{U}^{(i)} = \sum_{k=0}^{i-1} \left[\alpha_{ik}\boldsymbol{U}^{(k)} + \beta_{ik}\Delta t\mathcal{L}[\boldsymbol{U}^{(k)}]\right], \quad i = 1, \ldots, r, \tag{3.1.6}$$

in which $\boldsymbol{U}^{(0)} = \boldsymbol{U}^n$, $\boldsymbol{U}^r = \boldsymbol{U}^{n+1}$, and α_{ik} and β_{ik} are coefficients to be found.

To decrease the error of a numerical approximation, the time (and spatial) increment in the computational domain can be reduced. The CFL condition defines the maximum level of refinement for which the numerical solution will still converge. The theory, developed by Courant, Friedrichs and Lewy in 1928 [de Moura and Kubrusly, 2012], dictates that a necessary stability condition is that the domain of dependence of any numerical method must contain the domain of dependence of the PDE it is approximating. If we were to restrict (3.1.1) to one spatial direction, x, the domain of dependence for the solution $q(x,t)$ at any given point $(\tilde{x},\tilde{t})$ is defined as the region of space for which changes to the initial data will affect the solution $q(\tilde{x},\tilde{t})$. For a hyperbolic system of PDEs, the domain of dependence represents an interval bounded by the characteristics of the system. If these characteristics lay outside the computational domain of dependence, then changing the initial data at an exterior point would influence the physical solution but not the numerical - preventing convergence. For centered three-point finite difference methods, the CFL condition is given by the following expression:

$$CFL = \frac{\lambda_{max}\Delta t}{\Delta x} \leq 1, \tag{3.1.7}$$

where CFL is the Courant number and λ_{max} is the largest eigenvalue of the system of PDEs, representing the maximum physical speed of wave (or information) propagation in the domain. With respect to ideal MHD, from (2.2.19), we find that λ_{max} is the forward fast magneto–acoustic wave speed, $\lambda_{max} = u + c_f$.

3.1.1 Dispersion-Relation-Preserving schemes

In direct numerical simulations of turbulence it is necessary to employ a numerical scheme able to capture the broad range of scales that contribute to the overall flow dynamics. A similar constraint is present in computational aeroacoustics in which accurate long-time integration of waves of varying length scale propagating in space is required to effectively model aeroacoustic noise. It is for this purpose that Tam & Webb developed a class of high-order finite difference schemes (FDS), dispersion-relation preserving (DRP) schemes, optimised in spectral space to minimise both dissipation and dispersion errors [Tam and Webb, 1993]. The wave dispersion is the functional relationship between its angular frequency, ω, and wavenumber, k, and therefore describes how the wave propagates in time and space. Coefficients within the finite difference stencil are computed in such a way to obtain accurate numerical representations of wave properties on all relevant spatial scales. As a result, DRP schemes are ideal for modelling compressible turbulent flows in which there exists a significant wave content (e.g. acoustic waves in hydrodynamic turbulence) in addition to a broad range of scales.

To compute the stencil coefficients for the first derivative of function, f, at the lth node of a uniform spatial grid, the following approximation is made:

$$\left(\frac{\partial f}{\partial x}\right)_l \simeq \frac{1}{\Delta x}\sum_{j=-N}^{M} a_j f_{l+j}, \tag{3.1.8}$$

where M and N denote the number of points in the finite difference stencil in the respective positive and negative directions with respect to the grid point l, and a_j are the coefficients weighting each neighbouring value of f's contribution to the approximation of $(\partial f/\partial x)_l$.

In standard schemes the coefficients would be determined by carrying out a Taylor series expansion of the RHS of (3.1.8) and pairing coefficients to the relevant powers of Δx truncated at the desired order of accuracy. To optimise the FDS with respect to wave propagation, we derive values for the coefficients such that the Fourier transform of the RHS of (3.1.8) closely approximates that on the left of (3.1.8). We note that (3.1.8) is the finite difference form of the below equation in which x is a continuous variable:

$$\frac{\partial f}{\partial x} \simeq \frac{1}{\Delta x}\sum_{j=-N}^{M} a_j f(x + j\Delta x), \tag{3.1.9}$$

where (3.1.8) is recovered via the substitution $x = l\Delta x$.

Taking the Fourier transform of (3.1.9):

$$\mathrm{i}k\tilde{f} = \left(\frac{1}{\Delta x}\sum_{j=-N}^{M} a_j e^{\mathrm{i}kj\Delta x}\right)\tilde{f}, \tag{3.1.10}$$

where $\tilde{f}$ is the Fourier transform of f:

$$\tilde{f}(k) = \mathcal{F}T[f(x)] = \int_{-\infty}^{\infty} f(x)e^{-\mathrm{i}kx}\mathrm{d}x. \tag{3.1.11}$$

Comparing the LHS and RHS of (3.1.10) we can define the effective wave number, $\bar{k}$, of the finite difference approximation of $\partial f/\partial x$:

$$\bar{k} = -\frac{\mathrm{i}}{\Delta x}\sum_{j=-N}^{M} a_j e^{\mathrm{i}kj\Delta x}. \tag{3.1.12}$$

To ensure the RHS of (3.1.10) is a good approximation of the LHS of (3.1.10) we wish to minimise the difference between $\bar{k}\Delta x$ and $k\Delta x$ over the range of wavenumbers of interest. In a discrete system we require a minimum of 5 points to describe a sinusoidal wave. This applies to waves for which $k\Delta x \leq \pi/2$ - i.e. waves with a wavelength, λ, greater than or equal to 4 grid spacings. Any waves for which $\lambda < 4$ are under-resolved and cannot be accurately propagated in space and time. As such, we select coefficients a_j, such that we minimise the integrated error, E, over the range $|k\Delta x| \leq \pi/2$:

$$E = \int_{-\pi/2}^{\pi/2} |k\Delta x - \bar{k}\Delta x|^2 \mathrm{d}(k\Delta x), \tag{3.1.13}$$

$$E = \int_{-\pi/2}^{\pi/2} \left| \mathrm{i}\kappa - \sum_{j=-N}^{M} a_j e^{\mathrm{i}j\kappa} \right|^2 \mathrm{d}\kappa, \tag{3.1.14}$$

in which $\kappa = \mathrm{i}k\Delta x$, and we define the conditions for which E can potentially be at a minimum:

$$\frac{\partial E}{\partial a_j} = 0. \tag{3.1.15}$$

If the finite difference stencil is symmetric, $N = M$, then $\bar{k}$ is real and the RHS of (3.1.12) is a truncated Fourier series of sine waves - i.e. the FDS approximates the first derivative by a Fourier sine series in wavenumber space. However, an asymmetric finite difference stencil results in a complex $\bar{k}$ which may lead to spatial instability if the scheme is applied over a large stencil width as the wave solution will be growing.

To derive a stencil with a specific order of error, we combine the expression to be satisfied for wavenumber–space optimised coefficients, (3.1.15), and the standard truncated Taylor series finite difference approximation [Wang et al., 2015]. There exists flexibility with a DRP scheme in regards to the size of a stencil when minimising E. For the truncated Taylor series, a first–order spatial derivative approximated by a symmetric stencil of size N, will have N equations to solve to obtain N stencil coefficients, a_j, where $a_{-j} = a_j$ and $a_0 = 0$, that provide an order of accuracy of $2N$. Therefore, to obtain an order of accuracy of $2N$ for a given DRP stencil of size, P, where $P > N$, we solve a linear system of algebraic equations including the N truncated Taylor series relations and $P - N$ equations using (3.1.15). The present study employs

the use of a symmetric finite difference stencil, $N = M = 6$, with a $4th$-order accuracy, also employed by the following authors [Szemberg O'Connor, 2018], [Touber and Alferez, 2019]. The vector of coefficients $\boldsymbol{a} = [a_1, a_2, a_3, a_4, a_5, a_6]$ are given below:

$$\boldsymbol{a} = \begin{bmatrix} 0.89106089234616859 \\ -0.31289581661993865 \\ 0.11265173140838566 \\ -3.3312568156311950 \times 10^{-2} \\ 6.8802952724707159 \times 10^{-3} \\ -7.2927617809234811 \times 10^{-4} \end{bmatrix}. \tag{3.1.16}$$

3.1.2 Selective filters

In the previous section we noted that structures below a certain size ($\lambda < 4$ grid spacings) cannot be accurately captured by the finite difference scheme. If not removed, these spurious "grid-to-grid" oscillations can grow in amplitude, causing numerical instability and potentially lead to simulation blow–up. As such, it is common to damp any under-resolved structures within the flow, either through artificial dissipation terms added to the governing equations [Jameson et al., 1981], or via the application of filters, specifically designed to dissipate high–wavenumber content while leaving physical, larger–scale structures undamped [Bogey and Bailly, 2004].

A filter of stencil length N, applied to function q, at the lth node of a spatial grid is represented by:

$$q^f(x_l) = q(x_l) - \sigma D^q(x_l), \tag{3.1.17}$$

where q^f is the filtered quantity and $D^q(x_l)$ is the damping function, defined as:

$$D^q(x_l) = \sum_{j=-N}^{N} d_j q(x_l + j\Delta x), \tag{3.1.18}$$

where the coefficients d_j are symmetric, $d_j = d_{-j}$, to prevent dispersion errors and σ is the weighting constant, $\sigma \in [0, 1]$.

In the present study, a method described in [Bogey and Bailly, 2004] is used to obtain the coefficients d_j . It is analogous to the method employed for deriving DRP scheme stencil coefficients, first proposed by [Tam and Webb, 1993], and outlined in the previous section. First, we consider a spatial Fourier transform of (3.1.18):

$$\tilde{D}_q \tilde{q} = \left(\sum_{j=-N}^{N} d_j e^{\mathrm{i}kj\Delta x} \right) \tilde{q} \tag{3.1.19}$$

where $\tilde{D}_q$ and $\tilde{q}$ are the respective Fourier transforms of D_q and q (see (3.1.11) for Fourier transform definition).

The dissipation at a specific wavenumber is given by the weighting function, $\tilde{D}_q$. From symmetry (3.1.19) can be simplified to the following form, (real-valued cosines sum whereas imaginary sinusoids cancel out) :

$$\tilde{D}_q(k) = d_0 + \sum_{j=1}^{N} 2d_j \cos(jk\Delta x). \tag{3.1.20}$$

From (3.1.20), we can obtain the integral of dissipation over the range of wavenumbers for which structures scale larger than 4 grid points per wavelength, $0 \leq k\Delta x \leq \pi/2$:

$$\epsilon_{diss} = \int_0^{\pi/2} \tilde{D}_q(k)\mathrm{d}(k\Delta x), \tag{3.1.21}$$

which can be minimised by optimising the filter coefficients, d_j, through the expression:

$$\frac{\partial \epsilon_{diss}}{\partial d_j} = 0. \tag{3.1.22}$$

Values of d_j are found such that dissipation at small, under–resolved scales is maximised, whereas large scales experience minimal dissipation. Similar to coefficients for the DRP finite difference scheme, coefficients are obtained by combining the minimised function, (3.1.22), with the Taylor series constraints. The present study employs the use of a symmetric selective filter stencil, $N = 6$, with a $8th$-order accuracy - as used by authors [Szemberg O'Connor, 2018], [Touber and Alferez, 2019]. The vector of coefficients $\boldsymbol{d} = [d_0, d_1, d_2, d_3, d_4, d_5, d_6]$ are given below:

$$\boldsymbol{d} = \begin{bmatrix} 0.2025290156983785 \\ -0.1794082631518038 \\ 0.1238033248972423 \\ -0.0648197120657933 \\ 0.0242842514706709 \\ -0.0057720247824029 \\ 0.0006479157828976 \end{bmatrix}. \tag{3.1.23}$$

3.1.3 Shock capture: localised artificial diffusivity

In the present study, a spectral-like FDS of high order and minimal dissipation is used to compute numerical simulations of non-dissipative flows. As such, localised artificial diffusivity (LAD) methods are applied at discontinuities to minimise spurious oscillations that may be arise at shocks as a result of the Gibbs phenomenon [Tadmor, 1990]. Two types of LAD strategies are employed. In the first method artificial

bulk viscosity (μ_b^a), conductivity (κ^a), resistivity (η^a) and mass diffusivity (χ_a) are added to the flow in regions where strong discontinuities are detected. This is based on a technique initially devised by Cook and Cabot [Cook and Cabot, 2004] in which an artificial diffusivity term is able to detect shocks and add sufficient amounts of dissipation to "smear" it over a several grid points. Discontinuity detection for the artificial bulk viscosity and conductivity is based on calculations of the gradient in the local dilatation/strain rate magnitude and internal energy respectively [Kawai and Lele, 2008]. Variations of this methodology have been used in numerical simulations of compressible turbulence to study shock behaviour. The author [Kawai and Lele, 2008] extended this method to MHD flows by utilising the local current density magnitude to compute the required amount of artificial resistivity at strong MHD discontinuities [Kawai, 2013]. The highly localised application of dissipation to discontinuities in compressible turbulent flow simulations aids numerical stability without dissipating wave content at small scales. The general form of the LAD terms, D_a, is given as:

$$D_a = C_D h_D \overline{\left| \sum_{l=1}^{3} \frac{\partial^r \mathcal{F}_D}{\partial \xi_l^r} (\Delta \xi_l)^r \Delta_l^3 \right|}, \tag{3.1.24}$$

where we define,

$$\Delta_l = \left| \Delta \boldsymbol{x}_l \cdot \frac{\boldsymbol{\nabla} f_D}{||\boldsymbol{\nabla} f_D||} \right|,$$

and C_D as a dimensionless user-specified constant. h_D, $\mathcal{F}_D$ and f_D are functions specific to the type of dissipation that ensure dimensional consistency, detect the steep gradient in a flow property and set the direction normal to the discontinuity surface respectively. $\Delta \boldsymbol{x}_l$ is the local displacement vector along the grid line in the ξ_l direction, defined as $\Delta \boldsymbol{x}_l = [(x_{l+1} - x_{l-1})/2, (y_{l+1} - y_{l-1})/2, (z_{l+1} - z_{l-1})/2]^\intercal$. $\Delta \xi_l$ is the grid spacing in the computational space after transforming the Cartesian coordinate system, x_l, in the physical space to the generalised curvilinear coordinate system, ξ_l. An approximate truncated Gaussian filter is applied to terms beneath the overbar [Cook and Cabot, 2004]:

$$\bar{f}_i = \frac{3565}{10368} f_i + \frac{3091}{12960}(f_{i-1} + f_{i+1}) + \frac{1997}{25920}(f_{i-2} + f_{i+2}) + \frac{149}{12960}(f_{i-3} + f_{i+3}) + \frac{107}{103680}(f_{i-4} + f_{i+4}). \tag{3.1.25}$$

For the artificial bulk viscosity, $C_\mu = 1.0$,

$$h_\mu = \rho, \quad \mathcal{F}_\mu = \sqrt{\mathbf{D} : \mathbf{D}}, \quad f_\mu = \rho.$$

Artificial conductivity, $C_\kappa = 0.01$,

$$h_\kappa = \frac{\rho c_o}{T}, \quad \mathcal{F}_\kappa = e, \quad f_\kappa = e,$$

where c_o is the sound speed and e is the internal energy.

Artificial resistivity, $C_\eta = 10.0$,

$$h_\eta = \frac{1}{\rho c_o}, \quad \mathcal{F}_\eta = \boldsymbol{J} \cdot \boldsymbol{J}, \quad f_\eta = \frac{\boldsymbol{B} \cdot \boldsymbol{B}}{2},$$

where $\boldsymbol{J}$ is the current density vector.

Artificial mass diffusivity, $C_\chi = 0.2$,

$$h_\chi = \frac{c_o}{\rho}, \quad \mathcal{F}_\eta = \rho, \quad f_\eta = \rho.$$

We adopt $r = 4$ in the present study. The fourth derivative of each respective flow property is evaluated using a standard fourth order central difference scheme:

$$\frac{\partial^4 f_i}{\partial \xi_l^4} = \frac{-f_{i+3} + 12f_{i+2} - 39f_{i+1} + 56f_i - 39f_{i-1} + 12f_{i-2} - f_{i-3}}{\Delta \xi_l^4}. \tag{3.1.26}$$

The above technique was deemed suitable for capturing shocklets in compressible MHD turbulence applications as it is able to restrict spurious noise at the shock to around 1% of the pre–shock state. However, with respect to investigating the linear response of an isolated shock to small amplitude disturbances, the spurious oscillations present at shocks captured using the above LAD method will be of a similar magnitude if not higher than that of incident perturbations. As such, an alternative method is employed in which the spurious noise at the shock can be reduced to $< 0.01\%$ of the pre–shock state through a combination of grid refinement and application of constant localised artificial diffusivity at the shock location [Touber and Alferez, 2019]. Grid refinement employed in the region of the shock (separating physical length scales from the computational grid) enables a scale separation between the shock thickness and the characteristic length scale of the incident perturbation. The magnitude of artificial bulk viscosity is computed using the weak shock approximation of the shock structure derived by Salas for an ideal equation of state [Salas, 2009]. The expression for the shock structure defines the relationship between viscosity (assumed constant across the shock), shock thickness, Δ, and pre– and post–shock states:

$$\frac{\mu_a}{\rho_1 u_1 l} = \frac{3}{8} \frac{\gamma + 1}{\gamma} \frac{1 - \sqrt{\vartheta_r}}{1 + \sqrt{\vartheta_r}} \frac{\Delta}{l}, \tag{3.1.27}$$

in which ϑ_r is the shock compression ratio, $\vartheta_r = \rho_1/\rho_2$, and subscript 1(2) denote upstream(downstream) flow properties.

The value of Δ/l, and number of grid points across which it is discretised are modified as appropriate to ensure sufficient length scale separation exists between the incident perturbation and shock. Localised application of the artificial bulk viscosity to the momentum and energy equations is straightforward as the

location of the isolated shock is known a-priori. An artificial thermal conductivity is also added to the energy equation using the relation, $\kappa_a T_1/(\rho_1||\boldsymbol{u}_1||^3 l) = \gamma(\gamma-1)\mu_a/Pr$, assuming a constant Prandtl number (Pr), set equal to 3/4, and $\gamma = 1 + R/c_v$. The formulation given in (3.1.24) is used to prescribe artificial resistivity in MHD validation cases. For shock refraction, artificial bulk viscosity computed via the weak shock approximation reduces spurious noise in the magnetic field variables to a similar amplitude as observed in the hydrodynamic flow properties ($< 0.01\%$).

3.1.4 Characteristic boundary conditions

The flow is modelled as ideal MHD for numerical problems presented in the current study. As shown in section 2.2.2, the set of conservation laws that govern ideal MHD are hyperbolic. Numerical solutions to the hyperbolic systems are obtained over a finite region in space, within which time integrated properties are dependent not only on the interior state but also exterior waves entering through the domain boundaries. To obtain an accurate and stable solution for hyperbolic systems a physically consistent model must be developed to handle the boundary conditions. For each type of wave found in the system there exists a characteristic equation on a path (or curve) in time and space along which the total derivative of some property of the flow is zero (i.e. the property is constant). If the incoming and outgoing waves are known, a system of equations describing the characteristic curves can be applied at the domain boundaries to dynamically solve the flow properties. This method is derived below for a one–dimensional flow but can be generalised to any multi-dimensional hyperbolic system. We first express the governing conservation laws in general divergence form:

$$\frac{\partial \boldsymbol{q}}{\partial t} + \frac{\partial}{\partial x}\boldsymbol{f}(\boldsymbol{q}) = \boldsymbol{0}, \tag{3.1.28}$$

where the conserved variables are represented by $\boldsymbol{q}$, a state vector in $\mathbb{R}^n$ taken to be a function of both time ($t \in \mathbb{R}_{\geq 0}$) and space ($x \in \mathbb{R}$), and $\boldsymbol{f}$, a function $\boldsymbol{q}$.

(3.1.28) can be transformed to the primitive system, in which the conservation laws now take the form of quasi–linear system of PDEs:

$$\frac{\partial \boldsymbol{\mu}}{\partial t} + \mathbf{A}\frac{\partial \boldsymbol{\mu}}{\partial x} = \boldsymbol{0}, \tag{3.1.29}$$

where $\boldsymbol{\mu}$ is a vector of primitive variables in $\mathbb{R}^n$ and matrix $\mathbf{A}$ is a function of $\boldsymbol{\mu}$ in $\mathbb{R}^{n\times n}$.

The primitive system is related to the divergence form through the following definitions:

$$\frac{\partial \boldsymbol{\mu}}{\partial t} = \mathbf{P}\frac{\partial \boldsymbol{q}}{\partial t}, \qquad \frac{\partial \boldsymbol{f}}{\partial x} = \mathbf{Q}\frac{\partial \boldsymbol{\mu}}{\partial x}, \tag{3.1.30}$$

where,

$$P_{ij} = \frac{\partial q_i}{\partial \mu_j}, \qquad Q_{ij} = \frac{\partial f_i}{\partial \mu_j}, \tag{3.1.31}$$

and,

$$\mathbf{A} = \mathbf{P}^{-1}\mathbf{Q}, \tag{3.1.32}$$

in which $\mathbf{P}$ and $\mathbf{Q}$ are both real–valued rank 2 tensors.

We wish to obtain a characteristic path in $x - t$ space along which a property of the flow is constant (i.e. total derivative equal to zero). To do so, we first define the total derivative of $\boldsymbol{\mu}$:

$$\mathrm{d}\boldsymbol{\mu} = \frac{\partial \boldsymbol{\mu}}{\partial x}\mathrm{d}x + \frac{\partial \boldsymbol{\mu}}{\partial t}\mathrm{d}t, \tag{3.1.33}$$

which can be reduced to the following form using (3.1.29):

$$\mathrm{d}\boldsymbol{\mu} = [\mathbf{I}\mathrm{d}x - \mathbf{A}\mathrm{d}t]\frac{\partial \boldsymbol{\mu}}{\partial x}. \tag{3.1.34}$$

By considering the diagonalisation of matrix $\mathbf{A}$:

$$\boldsymbol{\Lambda} = \mathbf{S}^{-1}\mathbf{A}\mathbf{S}, \tag{3.1.35}$$

where the rows of $\mathbf{S}$ are the left eigenvectors, the columns of $\mathbf{S}^{-1}$ are the right eigenvectors and $\boldsymbol{\Lambda}$ is a diagonal matrix of the eigenvalues of $\mathbf{A}$, $\Lambda_{ii} = \lambda_i$, it is possible to show that a relation exists between changes in time and space for which the total derivative of, $\boldsymbol{\xi}$, will be zero:

$$\mathrm{d}\boldsymbol{\xi} = [\mathbf{I}\mathrm{d}x - \boldsymbol{\Lambda}\mathrm{d}t]\mathbf{S}^{-1}\frac{\partial \boldsymbol{\mu}}{\partial x}, \tag{3.1.36}$$

where $\mathrm{d}\boldsymbol{\xi} \equiv \mathbf{S}^{-1}\mathrm{d}\boldsymbol{\mu}$.

From (3.1.36), $\mathrm{d}\boldsymbol{\xi} = \mathbf{0}$, when $\mathbf{I}\mathrm{d}x = \boldsymbol{\Lambda}\mathrm{d}t$. As such, the eigenvalues of $\mathbf{A}$ correspond to a family of curves in $x - t$ space along which $\boldsymbol{\xi}$ is constant. If we imagine $\boldsymbol{\xi}$ to represent the constant amplitude of a wavefront, each eigenvalue can be thought of as the characteristic speed, $\lambda_i = \mathrm{d}x/\mathrm{d}t$, at which the wave propagates through the domain.

For a one–dimensional problem over the domain, $x_1 \leq x \leq x_2$, the waves propagating out of the domain ($\lambda_i \leq 0$ at $x = x_1$ and $\lambda_i \geq 0$ at $x = x_2$), depend only on the flow in the interior and at the boundaries. Therefore, a numerical solution to (3.1.29) will be stable if the spatial derivative, $\partial\boldsymbol{\mu}/\partial x$, is computed using one-sided finite difference stencil involving only interior and boundary points.

Whereas waves propagating into the domain ($\lambda_i \geq 0$ at $x = x_1$ and $\lambda_i \leq 0$ at $x = x_2$) depend on the exterior flow. As such, the exterior solution must be known a-priori in order to compute a stable numerical solution at the boundary. It is common in many problems for the farfield solution (e.g. steady-state aerodynamics) to be known to a good approximation and thus set the boundary points to the appropriate values. However, for unsteady problems (and some steady-state) a type of boundary known as non-reflecting is preferred. First developed by Hedstrom [Hedstrom, 1979] for one–dimensional flows, a non-reflecting boundary condition assumes the amplitudes of the incoming waves are constant in time at the boundaries, $\mathbf{S}^{-1}\partial\boldsymbol{\mu}/\partial t = \mathbf{0}$. As waves are indicated by a changing amplitude in time, this is equivalent to saying there exist no incoming waves. We recast the characteristic equations in (3.1.35) as :

$$\mathbf{S}^{-1}\frac{\partial \boldsymbol{\mu}}{\partial t} + \boldsymbol{L} = \mathbf{0}, \tag{3.1.37}$$

where $\boldsymbol{L}$ is a vector of wave operators, $\mathcal{L}_i$, for which non-reflecting boundary conditions are defined as:

$$\boldsymbol{L} = \begin{cases} \boldsymbol{\Lambda}\mathbf{S}^{-1}\dfrac{\partial \boldsymbol{\mu}}{\partial x}, & \text{outgoing waves,} \\ \mathbf{0}, & \text{incoming waves.} \end{cases} \tag{3.1.38}$$

In order to compute the time evolution of the primitive variables at the boundaries, using the operator, $\mathcal{L}$, we combine (3.1.37) with $\mathbf{S}^{-1}$:

$$\frac{\partial \boldsymbol{\mu}}{\partial t} + \mathbf{S}^{-1}\boldsymbol{L} = \mathbf{0}. \tag{3.1.39}$$

Applying the transformation matrix, $\mathbf{P}$ to (3.1.39), we obtain an equation describing the time evolution of the conservative variables in terms of the wave operators,

$$\frac{\partial \boldsymbol{q}}{\partial t} + \mathbf{P}(\mathbf{S}^{-1}\boldsymbol{L}) = \mathbf{0}. \tag{3.1.40}$$

Characteristic boundary conditions are sought for a one–dimensional ideal MHD flow as obtained previously by Cimino et al. [Cimino et al., 2016]. The state vector of conserved variables, $\boldsymbol{q}$, and flux vector, $\boldsymbol{f}$, (see (3.1.28)) are defined as:

$$\boldsymbol{q} = \begin{bmatrix} \rho \\ \rho u \\ \rho v \\ \rho w \\ \rho e_t \\ B_y \\ B_z \end{bmatrix} \qquad \text{and} \qquad \boldsymbol{f} = \begin{bmatrix} \rho u \\ \rho u^2 + p + B^2/2 - B_x^2 \\ \rho uv - B_x B_y \\ \rho uw - B_x B_z \\ (\rho e_t + p + B^2/2)u + B_x(B_x u + B_y v + B_z w) \\ B_y u - B_x v \\ B_z u - B_x w \end{bmatrix}, \tag{3.1.41}$$

and we note that B_x is constant in both space and time (as a result of applying the divergence-free magnetic field condition to the x-component of the induction equation).

In the primitive form of the ideal MHD equations, the state vector is defined as $\boldsymbol{\mu} = [\rho, u, v, w, p, B_y, B_z]^\intercal$, and the matrix $\mathbf{A}$ (see (3.1.29)), is given by:

$$\mathbf{A} = \begin{bmatrix} u & \rho & 0 & 0 & 0 & 0 & 0 \\ 0 & u & 0 & 0 & \frac{1}{\rho} & \frac{B_y}{\rho} & \frac{B_z}{\rho} \\ 0 & 0 & u & 0 & 0 & -\frac{B_x}{\rho} & 0 \\ 0 & 0 & 0 & u & 0 & 0 & -\frac{B_x}{\rho} \\ 0 & \rho c_o^2 & 0 & 0 & u & 0 & 0 \\ 0 & B_y & -B_x & 0 & 0 & u & 0 \\ 0 & B_z & 0 & -B_x & 0 & 0 & u \end{bmatrix}. \tag{3.1.42}$$

The seven eigenvalues (and corresponding waves) of $\mathbf{A}$ are the same as those given in (2.2.19). Each respective wave corresponds to the following wave operators:

$$\mathcal{L}_1 = (u - c_f)\left\{ \frac{\alpha_s \beta_z c_s S}{2c_o^2}\frac{\partial w}{\partial x} + \frac{\alpha_s \beta_y c_s S}{2c_o^2}\frac{\partial v}{\partial x} - \frac{\alpha_f c_f}{2c_o^2}\frac{\partial u}{\partial x} + \frac{\alpha_f}{2c_o^2\rho}\frac{\partial p}{\partial x} + \frac{\alpha_s \beta_z}{2c_o\sqrt{\rho}}\frac{\partial B_z}{\partial x} + \frac{\alpha_s \beta_y}{2c_o\sqrt{\rho}}\frac{\partial B_y}{\partial x} \right\}, \tag{3.1.43}$$

$$\mathcal{L}_2 = (u - b_x)\left\{ \frac{\beta_y}{2}\frac{\partial w}{\partial x} - \frac{\beta_z}{2}\frac{\partial v}{\partial x} + \frac{\beta_y S}{2\sqrt{\rho}}\frac{\partial B_z}{\partial x} - \frac{\beta_z S}{2\sqrt{\rho}}\frac{\partial B_y}{\partial x} \right\}, \tag{3.1.44}$$

$$\mathcal{L}_3 = (u - c_s)\left\{ -\frac{\alpha_f \beta_z c_f S}{2c_o^2}\frac{\partial w}{\partial x} - \frac{\alpha_f \beta_y c_f S}{2c_o^2}\frac{\partial v}{\partial x} - \frac{\alpha_s c_s}{2c_o^2}\frac{\partial u}{\partial x} + \frac{\alpha_s}{2c_o^2\rho}\frac{\partial p}{\partial x} - \frac{\alpha_f \beta_z}{2c_o\sqrt{\rho}}\frac{\partial B_z}{\partial x} - \frac{\alpha_f \beta_y}{2c_o\sqrt{\rho}}\frac{\partial B_y}{\partial x} \right\}, \tag{3.1.45}$$

$$\mathcal{L}_4 = u\left\{ \frac{\partial \rho}{\partial x} - \frac{1}{c_o^2}\frac{\partial p}{\partial x} \right\}, \tag{3.1.46}$$

$$\mathcal{L}_5 = (u + c_s)\left\{ \frac{\alpha_f \beta_z c_f S}{2c_o^2}\frac{\partial w}{\partial x} + \frac{\alpha_f \beta_y c_f S}{2c_o^2}\frac{\partial v}{\partial x} + \frac{\alpha_s c_s}{2c_o^2}\frac{\partial u}{\partial x} + \frac{\alpha_s}{2c_o^2\rho}\frac{\partial p}{\partial x} - \frac{\alpha_f \beta_z}{2c_o\sqrt{\rho}}\frac{\partial B_z}{\partial x} - \frac{\alpha_f \beta_y}{2c_o\sqrt{\rho}}\frac{\partial B_y}{\partial x} \right\}, \tag{3.1.47}$$

$$\mathcal{L}_6 = (u + b_x)\left\{ -\frac{\beta_y}{2}\frac{\partial w}{\partial x} + \frac{\beta_z}{2}\frac{\partial v}{\partial x} + \frac{\beta_y S}{2\sqrt{\rho}}\frac{\partial B_z}{\partial x} - \frac{\beta_z S}{2\sqrt{\rho}}\frac{\partial B_y}{\partial x} \right\}, \tag{3.1.48}$$

$$\mathcal{L}_7 = (u + c_f)\left\{-\frac{\alpha_s\beta_z c_s S}{2c_o^2}\frac{\partial w}{\partial x} - \frac{\alpha_s\beta_y c_s S}{2c_o^2}\frac{\partial v}{\partial x} + \frac{\alpha_f c_f}{2c_o^2}\frac{\partial u}{\partial x} + \frac{\alpha_f}{2c_o^2\rho}\frac{\partial p}{\partial x} + \frac{\alpha_s\beta_z}{2c_o\sqrt{\rho}}\frac{\partial B_z}{\partial x} + \frac{\alpha_s\beta_y}{2c_o\sqrt{\rho}}\frac{\partial B_y}{\partial x}\right\}, \tag{3.1.49}$$

where,

$$\alpha_f^2 = \frac{c_o^2 - c_s^2}{c_f^2 - c_s^2}, \quad \alpha_s^2 = \frac{c_f^2 - c_o^2}{c_f^2 - c_s^2}, \qquad B_\perp = \sqrt{B_y^2 - B_z^2}, \quad \beta_y = \frac{B_y}{B_\perp}, \quad \beta_z = \frac{B_z}{B_\perp}, \qquad S = sign(B_x).$$

Using (3.1.39) the time derivatives of the primitive variables as functions of the wave operators, $\mathcal{L}_i$, can be computed:

$$\frac{\partial \rho}{\partial t} = -\alpha_f\rho(\mathcal{L}_1 + \mathcal{L}_7) - \alpha_s\rho(\mathcal{L}_3 + \mathcal{L}_5), \tag{3.1.50}$$

$$\frac{\partial u}{\partial t} = -\alpha_f c_f(\mathcal{L}_7 - \mathcal{L}_1) - \alpha_s c_s(\mathcal{L}_5 - \mathcal{L}_3), \tag{3.1.51}$$

$$\frac{\partial v}{\partial t} = -\alpha_s c_s\beta_y S(\mathcal{L}_1 - \mathcal{L}_7) - \alpha_f c_f\beta_y(\mathcal{L}_5 - \mathcal{L}_3) - \beta_z(\mathcal{L}_6 - \mathcal{L}_2), \tag{3.1.52}$$

$$\frac{\partial w}{\partial t} = -\alpha_s c_s\beta_z S(\mathcal{L}_1 - \mathcal{L}_7) - \alpha_f c_f\beta_z(\mathcal{L}_5 - \mathcal{L}_3) + \beta_y(\mathcal{L}_6 - \mathcal{L}_2), \tag{3.1.53}$$

$$\frac{\partial B_y}{\partial t} = -\sqrt{\rho}\beta_y\alpha_s c_o(\mathcal{L}_1 + \mathcal{L}_7) + \sqrt{\rho}\beta_y\alpha_f c_o(\mathcal{L}_3 + \mathcal{L}_5) + \sqrt{\rho}\beta_z S(\mathcal{L}_2 + \mathcal{L}_6), \tag{3.1.54}$$

$$\frac{\partial B_z}{\partial t} = -\sqrt{\rho}\beta_z\alpha_s c_o(\mathcal{L}_1 + \mathcal{L}_7) + \sqrt{\rho}\beta_z\alpha_f c_o(\mathcal{L}_3 + \mathcal{L}_5) - \sqrt{\rho}\beta_z S(\mathcal{L}_2 + \mathcal{L}_6), \tag{3.1.55}$$

$$\frac{\partial p}{\partial t} = -\alpha_f\rho c_o^2(\mathcal{L}_1 + \mathcal{L}_7) + \alpha_s\rho c_o^2(\mathcal{L}_3 + \mathcal{L}_5). \tag{3.1.56}$$

The relations below can be applied to transform the above system of equations into the time derivatives of the conserved momentum and total energy variables (for a perfect gas):

$$\frac{\partial(\rho u)}{\partial t} = u\frac{\partial \rho}{\partial t} + \rho\frac{\partial u}{\partial t}, \tag{3.1.57}$$

$$\frac{\partial(\rho v)}{\partial t} = v\frac{\partial \rho}{\partial t} + \rho\frac{\partial v}{\partial t}, \tag{3.1.58}$$

$$\frac{\partial(\rho w)}{\partial t} = w\frac{\partial \rho}{\partial t} + \rho\frac{\partial w}{\partial t}, \tag{3.1.59}$$

$$\frac{\partial(\rho e_t)}{\partial t} = \frac{1}{\gamma - 1}\frac{\partial p}{\partial t} + u\left(\frac{u}{2}\frac{\partial \rho}{\partial t} + \rho\frac{\partial u}{\partial t}\right) + v\left(\frac{v}{2}\frac{\partial \rho}{\partial t} + \rho\frac{\partial v}{\partial t}\right) + w\left(\frac{w}{2}\frac{\partial \rho}{\partial t} + \rho\frac{\partial w}{\partial t}\right) + B_x\frac{\partial B_x}{\partial t} + B_y\frac{\partial B_y}{\partial t} + B_z\frac{\partial B_z}{\partial t}. \tag{3.1.60}$$

In the present study, non-reflecting boundary conditions are prescribed to solve for the set of conserved variables given in (3.1.41) at the domain boundaries.

3.2 The $\nabla \cdot \boldsymbol{B} = 0$ constraint

In addition to the hyperbolic system of conservation laws describing a single-fluid ideal MHD flow there is an additional constraint on the divergence of the magnetic field:

$$\nabla \cdot \boldsymbol{B} = 0. \tag{3.2.1}$$

In order to maintain numerical stability and avoid the generation of spurious forces in MHD codes, the divergence error must be kept reasonably small and not be allowed to accumulate in any part of the solution domain. It has been shown that a non–zero magnetic field divergence can lead to non–physical plasma transport orthogonal to the direction of the magnetic field [Brackbill and Barnes, 1980].

The strategies for handling (3.2.1) in MHD codes are categorised as either divergence cleaning or divergence-free. Divergence cleaning methods include the 8-wave scheme devised by Powell [Powell, 1994], in which the governing ideal MHD equations are derived without the assumption of zero magnetic field divergence. An eigen–decomposition of the resulting system of equations reveals an additional eighth eigenvalue relating to a divergence wave, propagating $\nabla \cdot \boldsymbol{B}$ at the local flow speed, thus avoiding accumulation of divergence errors at the source of generation. This method was found to improve stability, however, the set of governing equations cannot be written in divergence form due to the source term, $\partial \boldsymbol{q}/\partial t + \boldsymbol{\nabla} \cdot F = \boldsymbol{f}(\nabla \cdot \boldsymbol{B})$. As such, the volume integral of the discretised equations no longer conserves mass, momentum, energy and magnetic flux leading to incorrect shock jump conditions [Tóth, 2000]. Additionally, this method does not actively reduce the divergence error meaning sizeable spurious magnetic forces may still be generated within the flow. An extension of this method was developed by Dedner et al. [Dedner et al., 2002], in which the divergence of error is coupled to a generalised Lagrangian multiplier (GLM) which is evolved in time and space via an advection-diffusion equation thereby damping the divergence error as it is propagated through the domain. Unlike the 8-wave technique, in the GLM method the mass, momentum, energy and magnetic flux equations can be written in divergence form. Both the 8-wave and GLM methods are straightforward to implement using any base scheme and are computationally inexpensive. The clear downside is their inability to guarantee divergence errors are reduced to machine precision.

The projection method [Crockett et al., 2005], [Yang et al., 2016], another divergence cleaning technique, is able to eliminate divergence errors by solving a Poisson equation after each time step, $\nabla^2\phi + \nabla \cdot \boldsymbol{B} = 0$, and projecting the magnetic field onto the corrected zero-divergence field, $\boldsymbol{B}^{corr} = \boldsymbol{B} - \nabla\phi$. This method can also be coupled with any base scheme, however, solving the additional Poisson equation can be very computationally expensive. In divergence-free techniques, constraint (3.2.1) is maintained numerically to machine precision using the base scheme itself [Tóth, 2000]. Constrained transport (CT) is a commonly-

used method of this type in which a staggered or unstaggered grid representation of $\boldsymbol{B}$ or the electric field, $\boldsymbol{\Omega} = \boldsymbol{u} \times \boldsymbol{B}$, is used to ensure $(\nabla \cdot \boldsymbol{B})^{n+1} = (\nabla \cdot \boldsymbol{B})^{n}$ [Lee and Deane, 2009], [Gardiner and Stone, 2005], [Ziegler, 2004], [Helzel et al., 2011]. Therefore, if the initial magnetic field is divergence-free, it shall remain free of divergence errors (greater than machine precision) as it is evolved in time. However, CT methods restrict the type of base scheme involved in discretising the magnetic flux equation. As such, certain benefits of the main base scheme (e.g. low dispersion and dissipation errors in DRP schemes) will not be experienced by the magnetic field. Consequently, due to flexibility in base scheme selection and computational speed, the mixed GLM divergence cleaning method is implemented in CompReal. The GLM, denoted by the scalar, ψ, is coupled to both the induction equation and the divergence error, $\nabla \cdot \boldsymbol{B}$:

$$\frac{\partial \boldsymbol{B}}{\partial t} + \boldsymbol{\nabla} \cdot \{\boldsymbol{uB} - \boldsymbol{Bu} + \psi \mathbf{I}\} = 0, \tag{3.2.2}$$

$$D(\psi) + \nabla \cdot \boldsymbol{B} = 0, \tag{3.2.3}$$

where D is a differential linear operator which is chosen along with the initial boundary conditions for ψ in such a way that the numerical approximation to the GLM MHD equations is physically consistent with the original MHD system. Through combining (3.2.2) and (3.2.3), it can be shown that the magnetic field divergence and scalar, ψ, satisfy the same evolution equation. Therefore, setting the linear operator as an advection-diffusion of ψ also leads to the advection and diffusion of the divergence error. We define $D(\psi)$ as the following:

$$D(\psi) \equiv \frac{1}{c_h^2}\frac{\partial \psi}{\partial t} + \frac{1}{c_p^2}\psi, \tag{3.2.4}$$

where c_h is the propagation speed and c_p is the damping rate. We can now recast (3.2.3) as:

$$\frac{\partial \psi}{\partial t} + c_h^2(\nabla \cdot \boldsymbol{B}) = -\frac{c_h^2}{c_p^2}\psi. \tag{3.2.5}$$

We fix the propagation speed, c_h, using the maximum physical propagation speed within the flow - i.e. forward fast magneto–acoustic wave speed [Dedner et al., 2002]:

$$c_h = max(|u| + c_{f,x}, |v| + c_{f,y}, |w| + c_{f,z}). \tag{3.2.6}$$

From numerical tests, Dedner et al. found the optimal value of the damping constant, c_p, highly dependent on the grid spacings [Dedner et al., 2002]. As such, it was proposed that c_p is fixed as a function of c_h via the introduction of a new constant, $c_r = c_p^2/c_h$. The constant c_r effectively represents the ratio between convective and diffusive effects. Through keeping c_r constant, the proportion of decay to transport can be fixed. Dedner et al. found the optimal value of c_r to be independent of grid resolution [Dedner et al., 2002].

Following from (3.2.5), the solution vector of conserved variables is now defined in the GLM MHD system as $\boldsymbol{q} = [\rho, \rho\boldsymbol{u}^{\intercal}, \rho e_t, \boldsymbol{B}^{\intercal}, \psi]^{\intercal}$. ψ is set to zero in the initial flowfield of all simulations presented in the current study.

3.3 Validation of MHD solver

In this section, the results of 2d and quasi–1d/2d numerical validation cases are presented. Quasi-dimensionality refers to flows in which all three components of the respective velocity and magnetic vector fields are initialised and evolve in time on a set number of spatial dimensions. These test problems aim to test the proficiency of the code at handling the range of complex and dynamic structures that may emerge in compressible MHD flows. We numerically solve the non–dimensional formulation of the ideal MHD equations derived in section 2.2.1 for all tests. All results presented in this section are computed for flows with the ratio of specific heats set as, $\gamma = 5/3$, on a uniformly spaced grid, using a 13-point stencil, 4^{th}-order DRP scheme in conjunction with a 13-point stencil, 8^{th}-order, selective filter, filtering all primitive variables at a weighting of 10% each time-step (unless specified) to remove under-resolved structures from the flowfield [Bogey and Bailly, 2004].

3.3.1 Slow shock-wave

For the first test case, a slow switch–off shock wave is propagated through a quasi–1d domain. In [Kawai, 2013], this problem is used to identify the optimum value for the user-defined coefficient, C_η, in the formulation of the localised artificial resistivity. For the initial condition, the left- and right-hand side flow properties are given as:

$$\begin{aligned}(\rho, u, v, w, p, B_x, B_y, B_z)_L &= (1.368, 0.269, 1.000, 0.000, 1.769, 1.000, 0.000, 0.000),\\ (\rho, u, v, w, p, B_x, B_y, B_z)_R &= (1.000, 0.000, 0.000, 0.000, 1.000, 1.000, 1.000, 0.000),\end{aligned} \tag{3.3.1}$$

on the domain, $x \in [0, 1]$ consisting of 496 grid points, in which the left- and right-hand states are initialised on the regions: $0 \leq x \leq 0.5$ and $0.5 \leq x \leq 1.0$ respectively. Non-reflecting characteristic boundary conditions are implemented at both the inlet and outlet.

Figure 3.1 shows qualitatively the reduction of wiggle amplitude in B_y at the shock location as the user–defined artificial resistivity constant, C_η, is increased. Additional wiggles seen in both the right– and left–hand states at $x/L \approx 0.4$ and $x/L \approx 0.85$ respectively, are start-up errors, a consequence of imposing the discontinuity over a single grid point in the initial condition. These errors persist for relatively long times in non-dissipative schemes such as the DRP scheme presented in the current study and the 6^{th}-order compact scheme applied in [Kawai, 2013].

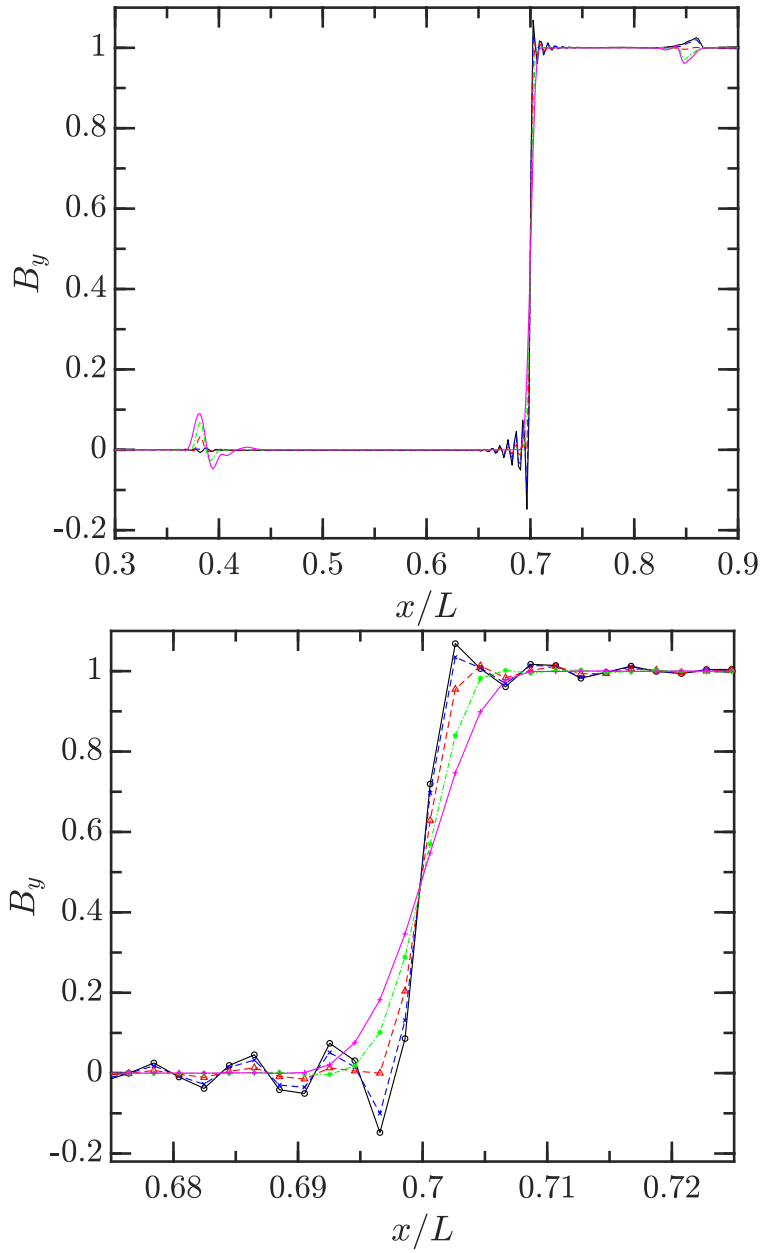


Fig. 3.1: Slow switch–off shock profiles of B_y at a non–dimensional time, $t = 0.2$, for different values of the user defined artificial resistivity constant; $C_\eta = 0.0$ (black circles), $C_\eta = 0.1$ (blue crosses), $C_\eta = 1.0$ (red triangles), $C_\eta = 10.0$ (green asterisk), $C_\eta = 100.0$ (pink crosses).

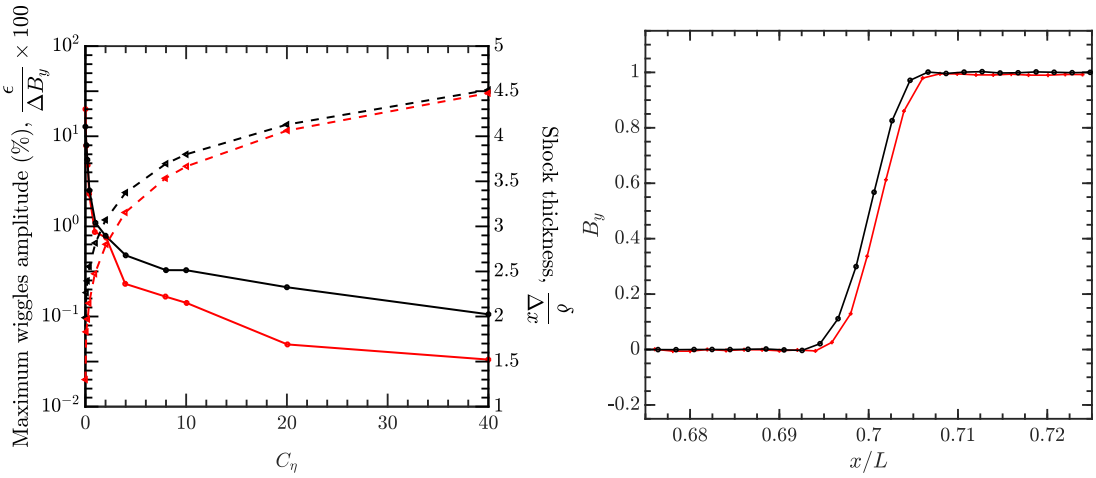


Fig. 3.2: (Left) Maximum relative spurious noise (%) in semi-logarithmic scale on the left-axis (circles) for B_y and non–dimensional numerical shock thickness on right axis (triangles) at a non–dimensional time, $t = 0.2$, for different values of , artificial resistivity constant, C_η. (Right) Slow switch–off shock B_y profiles at non–dimensional time, $t = 0.2$, for $C_\eta = 10.0$. CompReal data (black) and data from [Kawai, 2013] (red crosses) both shown.

Figure 3.2 shows the influence of C_η on the shock thickness and amplitude of spurious noise, ϵ, at the shock with respect to the jump in the magnetic field y-component, ΔB_y. The non–dimensional numerical shock thickness, $\delta/\Delta x$, is defined as:

$$\frac{\delta}{\Delta x} = \frac{\Delta B_y}{\Delta x \left.\frac{\partial B_y}{\partial x}\right|_{max}}, \tag{3.3.2}$$

where Δx is the grid spacing.

Comparing results to those shown in [Kawai, 2013] we find there exists a relatively small difference in $\delta/\Delta x$ across all values of C_η, with both data sets converging to $\delta/\Delta x = 4.5$ at $C_\eta = 40.0$, However, a difference equivalent to roughly half an order of magnitude is observed in $\epsilon/\Delta B_y$, indicating for a shock of equal thickness in the computational domain, CompReal produces higher amplitude spurious oscillations at the shock. The difference between wiggle amplitudes in the present study and [Kawai, 2013], could be a result of several factors including, the definition of wiggle amplitude (3.3.2) in regards to where the maximum gradient of B_y was computed. For the recommended C_η value of 10.0 [Kawai, 2013], which shows a wiggle amplitude of approximately 3 times that of the data in [Kawai, 2013] in figure 3.2, the non–dimensional shock thickness is roughly 4 computational grid points.

Following on from the above results, all MHD simulations involving the formulation of artificial resistivity proposed by the author in [Kawai, 2013] employed a C_η value of 10.0.

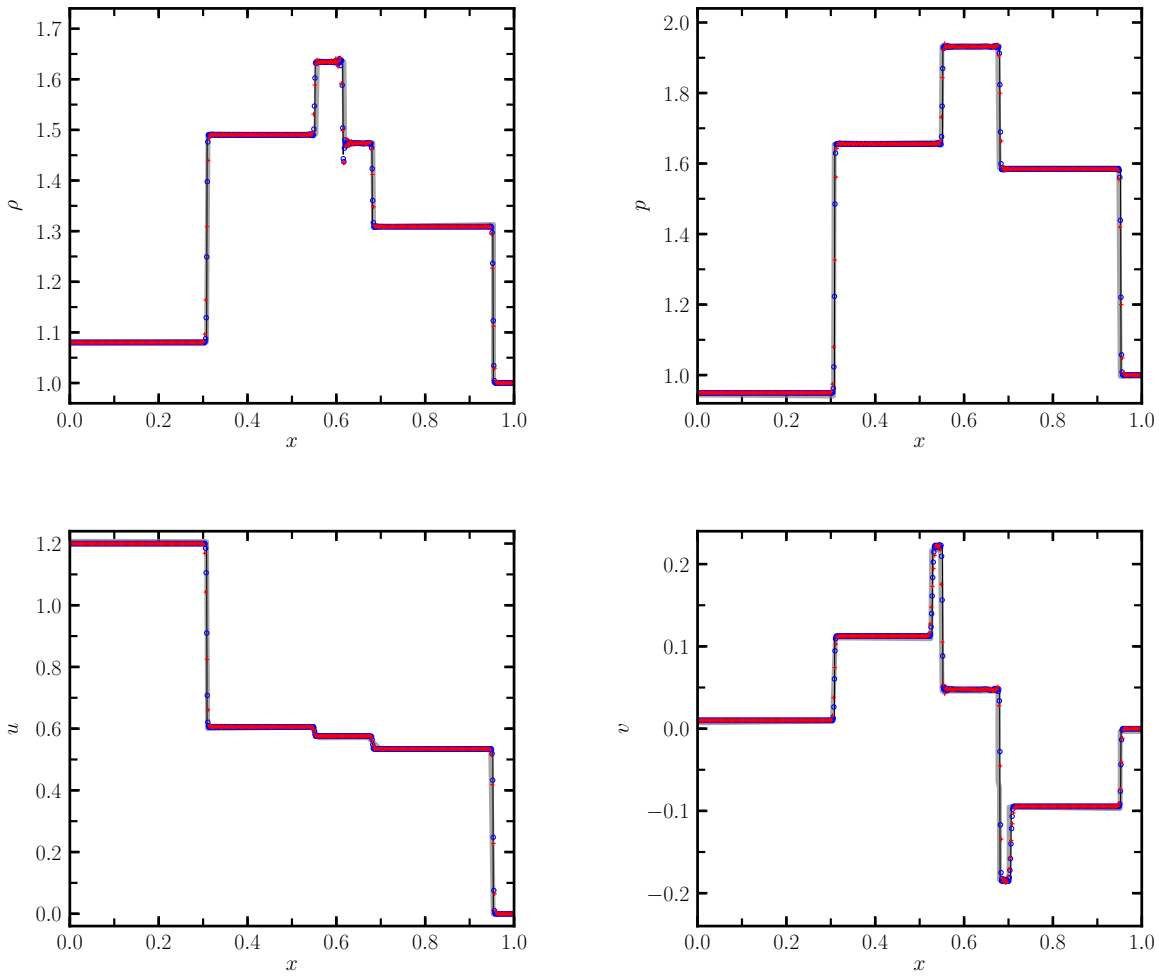


Fig. 3.3: Dai-Woodward shock problem profiles of thermodynamic and flow properties, at a non–dimensional time, $t = 0.2$, for different grid sizes; $N = 4000$ (solid black line), $N = 800$ (blue circles), $N = 400$ (red crosses). Reference data (grey line) extracted from [Ryu and Jones, 1995].

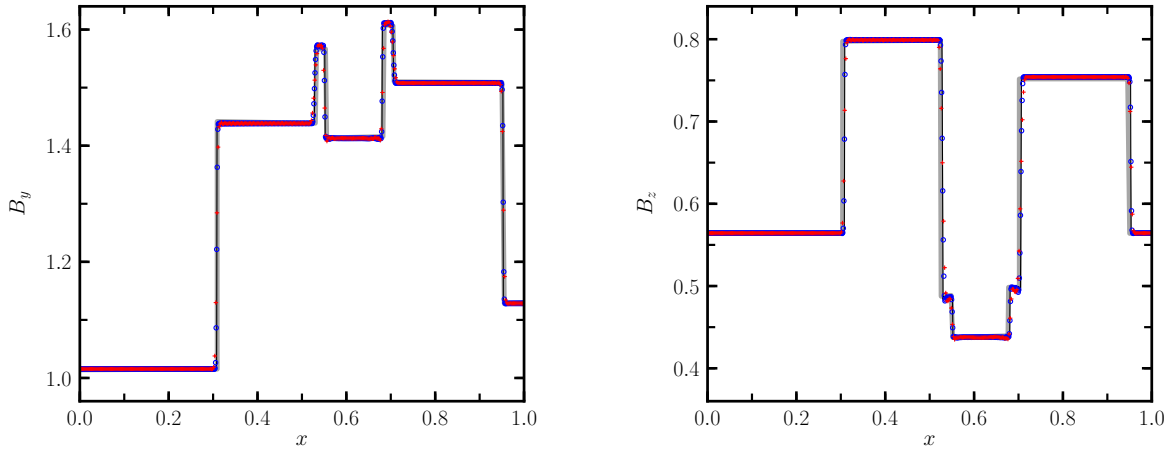


Fig. 3.4: Dai-Woodward shock problem profiles of magnetic field components at a non–dimensional time, $t = 0.2$, for different grid sizes; $N = 4000$ (solid black line), $N = 800$ (blue circles), $N = 400$ (red crosses). Reference data (grey line) extracted from [Ryu and Jones, 1995].

3.3.2 Dai and Woodward shock problem

The second test case is a MHD Riemann problem initially proposed in [Dai and Woodward, 1994], within which various ideal MHD discontinuities emerge from the discontinuity between the initial left and right states. We initialise the flow on a quasi–1d domain, for which the left- and right-hand flow properties are given as:

$$(\rho, u, v, w, p, B_x, B_y, B_z)_L = (1.08, 1.20, 0.01, 0.50, 0.95, 2.00/\sqrt{4.00\pi}, 3.60/\sqrt{4.00\pi}, 2.00/\sqrt{4.00\pi}),$$
$$(\rho, u, v, w, p, B_x, B_y, B_z)_R = (1.00, 0.00, 0.00, 0.00, 1.00, 2.00/\sqrt{4.00\pi}, 4.00/\sqrt{4.00\pi}, 2.00/\sqrt{4.00\pi}), \quad (3.3.3)$$

on the domain, $x \in [0, 1]$, in which the left- and right-hand states are initialised on the regions: $0 \leq x \leq 0.5$ and $0.5 \leq x \leq 1.0$ respectively. Non-reflecting characteristic boundary conditions are implemented at both the inlet and outlet. To show grid convergence, results in [Ryu and Jones, 1995] are compared to the flow computed on grids of size $N = 400$, $N = 800$ and $N = 4000$ for a time step of $\Delta t = 1.0\times10^{-4}$, $\Delta t = 5.0\times10^{-5}$ and $\Delta t = 2.5 \times 10^{-5}$ respectively - corresponding to an inviscid $CFL_{max} \leq 0.13$. Figures 3.3 and 3.4 show profiles for the thermodynamic, velocity and magnetic fields at $t = 0.2$. Results in the present study appear to compare well with those in [Ryu and Jones, 1995]. We observe two fast shocks, two slow shocks, two rotational discontinuities and a contact discontinuity captured using artificial dissipation for bulk viscosity, resistivity and mass diffusivity without significant spurious oscillations at any grid size. Additionally, each discontinuity is captured on roughly $3 - 4$ grid points as specified by the respective dissipation schemes for the given coefficient values.

3.3.3 Magnetic Sod shock problem

The magnetic Sod shock problem (figure 3.5) is a modification on a gasdynamic shock test [Sod, 1978], first suggested by Brio and Wu [Brio and Wu, 1988]. The initial left and right-hand states in this Riemann problem are given as:

$$\begin{aligned}(\rho, u, v, w, p, B_x, B_y, B_z)_L &= (1.000, 0.000, 0.000, 0.000, 1.000, 0.750, 1.000, 0.000),\\ (\rho, u, v, w, p, B_x, B_y, B_z)_R &= (0.125, 0.000, 0.000, 0.000, 0.100, 0.750, -1.000, 0.000),\end{aligned} \tag{3.3.4}$$

on a domain with non-reflecting boundary conditions. To show grid convergence, we compare a reference solution provided in [Ryu and Jones, 1995] with the flow at non–dimensional time, $t = 0.1$, computed on grids of size $N = 400$, $N = 800$ and $N = 4000$, for a time step of $\Delta t = 5.0 \times 10^{-5}$, $\Delta t = 2.5 \times 10^{-5}$ and $\Delta t = 5.0 \times 10^{-6}$ respectively - corresponding to an inviscid $CFL_{max} \leq 0.08$. In figure 3.5, we compare a reference solution at time, $t = 0.2$, for thermodynamic, velocity and magnetic fields to simulations with a reduced number of grid points. Within this Riemann problem we observe the emergence of a fast rarefaction wave, slow compound wave, contact discontinuity, slow shock and slow intermediate shock where B_y changes sign. As noted by Brio and Wu, by certain conventions, intermediate shocks are considered not admissible [Kunkel, 1966], however, the presence of resistivity (artificial in the present case) can enable the existence of admissible intermediate shock solutions [Wu, 1987].

Figure 3.6 shows the $x-t$ contours of each flow property given in figure 3.5 on a grid of resolution, $N = 800$. As a result of the non–reflecting boundary conditions, discontinuities emerging from the Riemann problem and passing through the domain boundaries experience minimal reflection despite their large amplitude ($\sim 50\%$ initial state value). This represents a more than adequate performance for the present study, considering the domain boundary will be expected to minimise reflections for the passage disturbances of much smaller amplitudes ($\sim 1\%$ initial state)

3.3.4 Advection of B_x

The 2d advection of B_x is a test case, first proposed by Dedner et al. [Dedner et al., 2002], used to evaluate the robustness of $\nabla \cdot \boldsymbol{B}$ cleaning schemes employed in MHD solvers. In this problem, a non–physical divergence in the magnetic field is introduced in the initial condition by imposing a perturbation in B_x while keeping all other magnetic field components uniform. If left untreated, the divergence error can grow in time and eventually lead to simulation blow up.

The initial perturbation in B_x is given by:

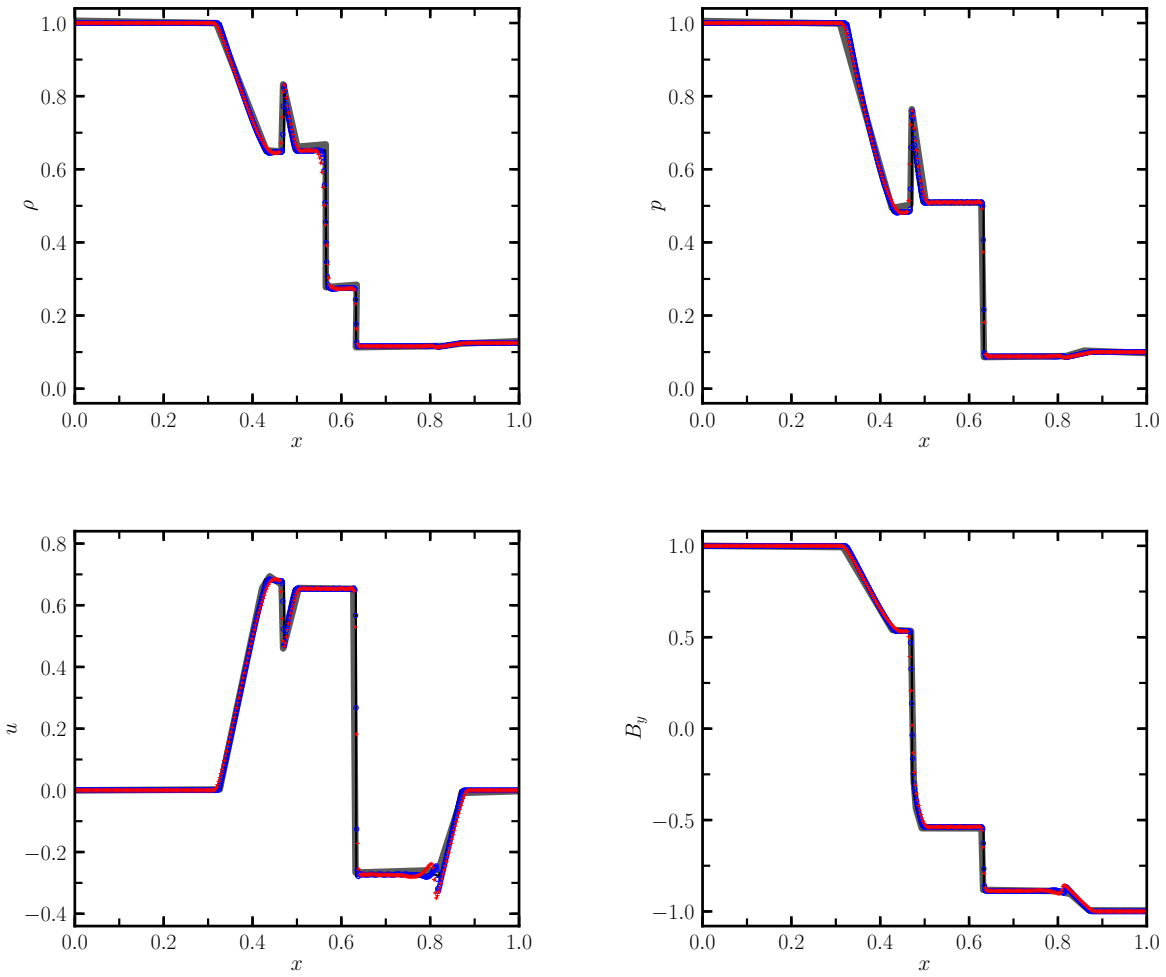
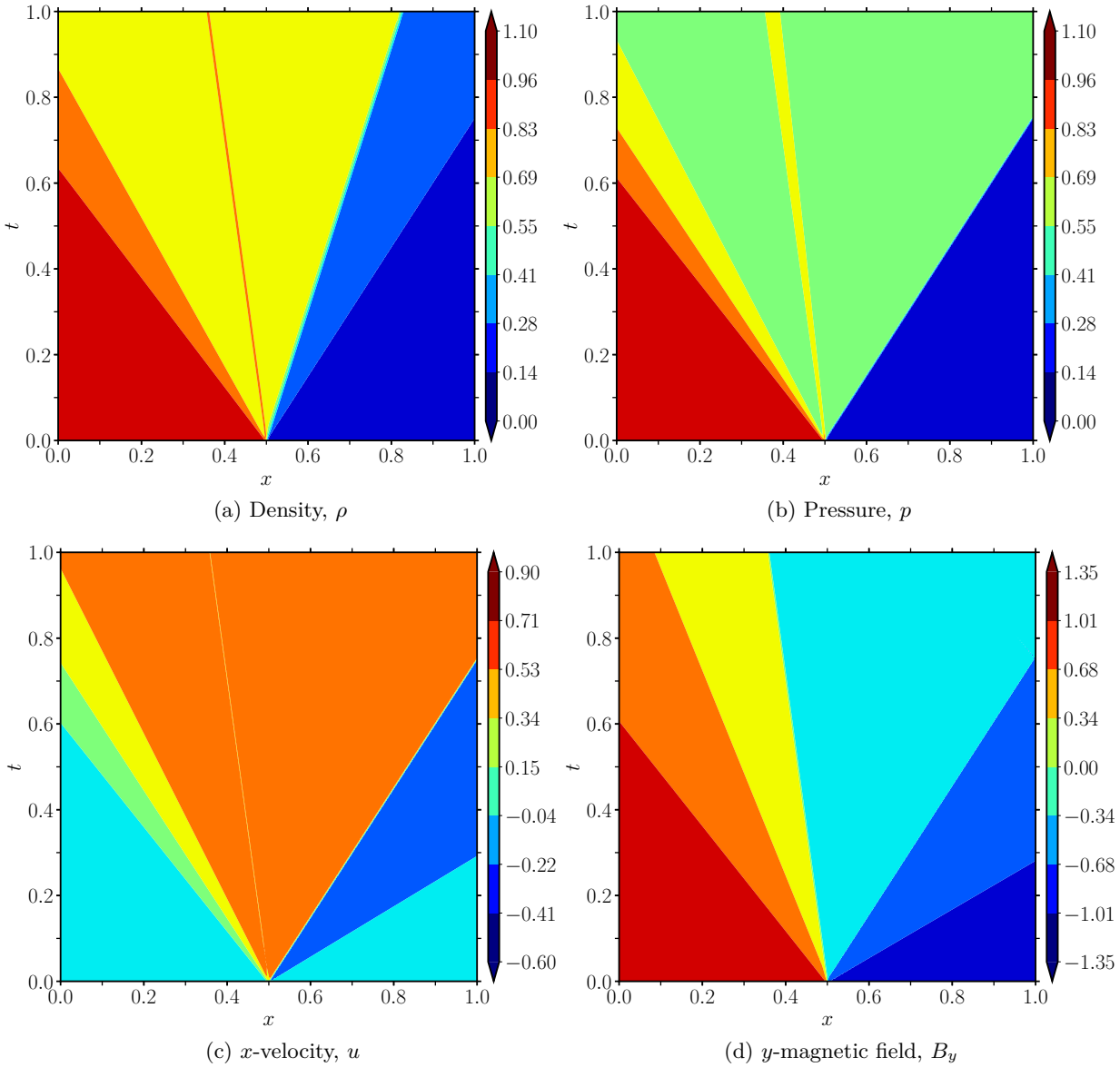


Fig. 3.5: 1.5d Magnetic Sod shock problem flow property profiles at a non–dimensional time, $t = 0.1$, for different grid sizes; $N = 4000$ (solid black line), $N = 800$ (blue circles), $N = 400$ (red crosses). Reference data (grey line) extracted from [Ryu and Jones, 1995].



(a) Density, ρ

(b) Pressure, p

(c) x-velocity, u

(d) y-magnetic field, B_y

Fig. 3.6: $x-t$ contours of 1.5d magnetic Sod shock problem with non-reflecting boundary conditions. 8 equally-spaced contours of density, pressure, x-velocity and y-magnetic field plotted for $N = 800$.

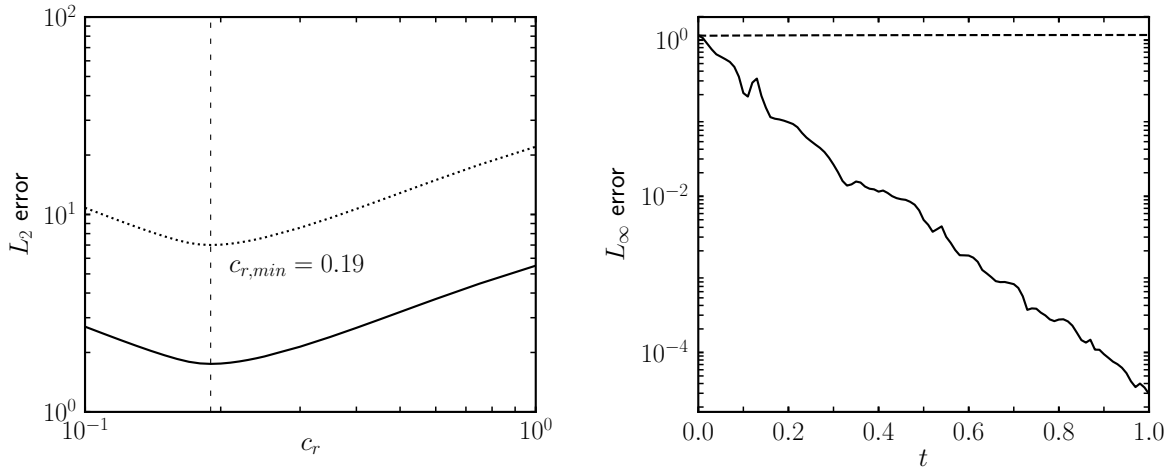


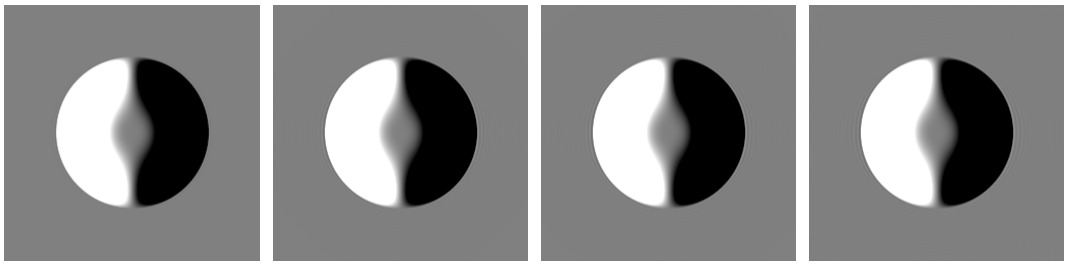
Fig. 3.7: 2d advection of B_x. (Left) Time integral of L_2-error in $\nabla \cdot \boldsymbol{B}$ within the time interval, $0 \leq t \leq 1$. Results shown for different c_r values on $N \times N$ grid of resolution $N = 64$ (solid line) and $N = 256$ (dashed line). (Right) Time evolution of maximum $\nabla \cdot \boldsymbol{B}$ error on $N \times N$ grid of resolution $N = 64$ - no divergence–cleaning (dashed line) and mixed–correction GLM cleaning for $c_r = 0.19$ (solid line) shown.

$$B_x = \begin{cases} \dfrac{1}{\sqrt{4\pi}} \left[\left(\dfrac{r}{r_0} \right)^8 - 2 \left(\dfrac{r}{r_0} \right)^4 + 1 \right], & \text{if } r \leq r_0, \\ 0, & \text{otherwise,} \end{cases} \tag{3.3.5}$$

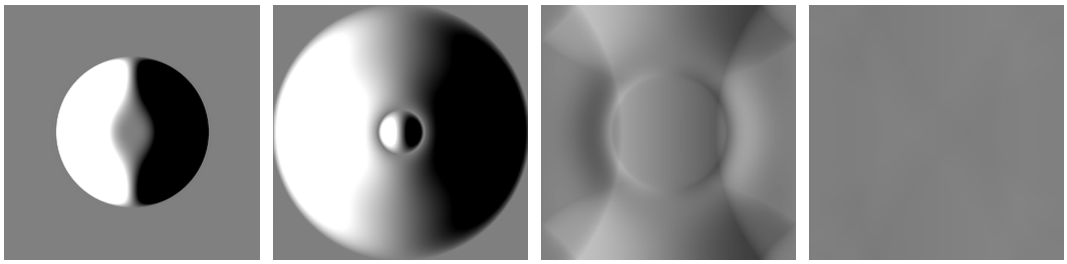
where we define $r = \sqrt{x^2 + y^2}$, and set $r_0 = 1/\sqrt{8}$. The remaining flow properties are initialised as; $\rho = 1.0$, $u = 1.0$, $v = 1.0$, $p = 6.0$ and $B_y = 0.0$. The flow is computed on the domain, $x, y \in [0, 2]^2$ with periodic boundary conditions imposed in both x and y directions. Simulations are performed on uniformly-spaced $N \times N$ grids with resolutions of $N = 64$ and $N = 256$ respectively.

Figure 3.7 shows the influence of c_r on the time–integrated L_2-error of $\nabla \cdot \boldsymbol{B}$, $||\nabla \cdot \boldsymbol{B}||_2$, in the range $0.0 \leq t \leq 1.0$. The optimum value of c_r - corresponding to the minimum $||\nabla \cdot \boldsymbol{B}||_2$ - is given as $c_r = 0.19$ rather than $c_r = 0.18$ as specified by the previous author [Dedner et al., 2002]. Although the value of c_r is grid–size independent ($c_r = 0.19$ is the optimal value for grids $N = 64$ and $N = 256$ in figure 3.7), a finite volume method is utilised in [Dedner et al., 2002] as opposed to the spectral–like finite difference scheme employed in the present study. As such, it is possible the dissipation of $\nabla \cdot \boldsymbol{B}$ errors using the GLM method may be influenced by the type of numerical scheme.

Also in figure 3.7 is the time history (for $0 \leq t \leq 1.0$) of the L_∞-error for the mixed–correction GLM scheme at the $c_r = 0.19$ compared to no divergence cleaning. The dissipating effect of the mixed–correction GLM method is seen clearly as the maximum $\nabla \cdot \boldsymbol{B}$ error reduces by 4 orders of magnitude within 1 time unit. A time–lapse of $\nabla \cdot \boldsymbol{B}$ contours given in figure 3.8 shows the hyperbolic content of the mixed-correction GLM method. As the $\nabla \cdot \boldsymbol{B}$ error is damped, it also propagates outwards from the centre of the flowfield as a wave. Without $\nabla \cdot \boldsymbol{B}$ cleaning, the error remains stationary and undamped.



(a) No $\nabla \cdot \boldsymbol{B}$ cleaning



(b) Mixed–correction GLM $\nabla \cdot \boldsymbol{B}$ cleaning

Fig. 3.8: 2d advection of B_x. $\nabla \cdot \boldsymbol{B}$ contours shown in the range, $-0.3 \leq \nabla \cdot \boldsymbol{B} \leq 0.3$ at $t = 0.0$, 0.1, 0.25, 0.5 (left to right) for $N = 256$.

Following on from the above results, all MHD simulations involving the formulation of mixed–correction GLM divergence cleaning proposed by the author in [Dedner et al., 2002] employed a c_r value of 0.19.

3.3.5 Circularly-polarised Alfvén wave

The incompressible circularly-polarised (c–p) Alfvén waves are an exact nonlinear solution to the ideal compressible MHD equations [Del Zanna et al., 2001]. A test case involving the propagation of these waves at constant speed was first introduced by Toth [Tóth, 2000]. As wave propagation is sensitive to both numerical dissipation and dissipation errors, the c–p Alfvén wave case provides an effective test to validate numerical schemes for smooth flows. However, for large amplitudes the c–p Alfvén wave solution has been shown to be unstable and undergo parametric decay in compressible flow solvers [Del Zanna et al., 2001]. As a result, small amplitudes are prescribed to prevent any significant nonlinear distortion of the wave for at least several passages of the wave through the flow domain. Similar to previous authors, in order to test the oblique propagation of plane waves by the numerical scheme, we rotate the c–p Alfvén wave solution with respect to the computational domain [Tóth, 2000] [Kawai, 2013]. We define vectors for velocity, $\boldsymbol{u}' = [u_{\parallel}, u_{\perp}]^{\intercal}$, the magnetic field, $\boldsymbol{B}' = [B_{\parallel}, B_{\perp}]^{\intercal}$, and spatial coordinates, $\boldsymbol{x}' = [x_{\parallel}, x_{\perp}]^{\intercal}$, in a coordinate system orthogonal to the c–p Alfvén wave vector basis, where ($\parallel$) and ($\perp$) denote the directions parallel and perpendicular to the wavevector. The transformation to the computational domain coordinate system for a counter–clockwise rotation of α about the x-direction is given by, $\boldsymbol{u} = \mathbf{R}_{\alpha}\boldsymbol{u}'$, $\boldsymbol{B} = \mathbf{R}_{\alpha}\boldsymbol{B}'$ and $\boldsymbol{x} = \mathbf{R}_{\alpha}\boldsymbol{x}'$, where $\mathbf{R}_{\alpha}$, is a two–dimensional rotation matrix is defined as:

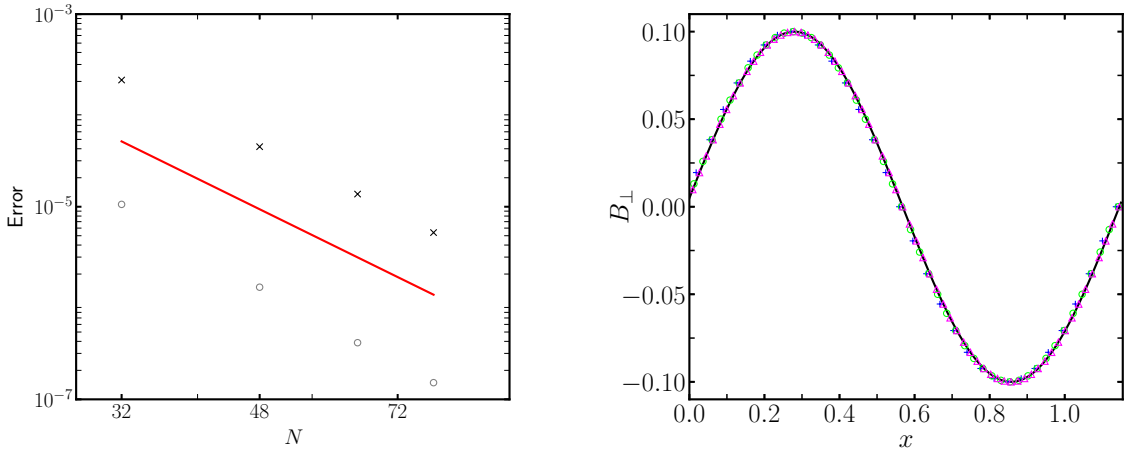


Fig. 3.9: (Left) Grid size ($N \times N$) dependency of L_2 (crosses) and L_∞ (circles) errors in the perpendicular component of the magnetic field in the orthogonal wavevector basis, $B_\perp$, after 5 passages through the computational domain of a circularly–polarised Alfvén wave propagating at 30° with respect to the x-axis. Slope, error $\propto N^{-4}$, also shown (solid red line). (Right) $B_\perp$ of c–p Alfvén wave at $y = 1/(2\sin 30°)$, for non–dimensional time, $t = 5.0$, equivalent to 5 wave passages through the domain. Profiles shown for exact solution (black line) and different grid sizes: $N = 32$ (blue crosses), $N = 48$ (green circles) and $N = 64$ (pink triangles).

$$\mathbf{R}_\alpha = \begin{pmatrix} \cos\alpha & -\sin\alpha \\ \\ \sin\alpha & \cos\alpha \end{pmatrix}. \tag{3.3.6}$$

We compute the error in $B_\perp$, which can be obtained from $\boldsymbol{B}$ through the transformation $\boldsymbol{B'} = \mathbf{R}_\alpha^{-1}\boldsymbol{B}$, where $\mathbf{R}_\alpha^{-1}$, the inverse of the rotation matrix, is given by:

$$\mathbf{R}_\alpha^{-1} = \begin{pmatrix} \cos\alpha & \sin\alpha \\ \\ -\sin\alpha & \cos\alpha \end{pmatrix}. \tag{3.3.7}$$

We define orthogonal wavevector basis velocity and magnetic field components; $u_\parallel = 0.0$, $B_\parallel = 1.0$, $u_\perp = B_\perp = 0.1\sin x_\parallel$, $u_z = B_z = 0.1\cos x_\parallel$. The density and pressure are initialised as uniform fields, $\rho = 1.0$ and $p = 1.0$. The flow is computed for $\alpha = 30°$ on a uniformly-spaced two–dimensional grid with N grid points in x and y directions respectively and periodic boundary conditions. To enforce periodicity of the plane wave on the computational domain we set, $0 \leq x \leq 1/\cos\alpha$, and, $0 \leq y \leq 1/\sin\alpha$, corresponding to the limits, $0 \leq x_\parallel \leq 1$, in the orthogonal wavevector basis. As in [Kawai, 2013], a time–step, $\Delta t = (1/N^3)$, is chosen to ensure time–integration errors are smaller than those introduced by the localised artificial dissipation and DRP finite difference scheme.

Figure 3.9 shows the L_2 and L_∞ errors in $B_\perp$ after five passages of the wave through computational domains of size $N = 32$, $N = 48$, $N = 64$ and $N = 80$ (where each grid contains $N \times N$ points). Both error trends

show reasonably good agreement with the ideal slope, $\propto N^{-4}$, for the $4th$-order DRP schemes. As opposed to several MHD shock–capturing codes evaluated by Toth for the same test problem [Tóth, 2000], at grid resolution $N = 32$, no dissipation or distortion is visible in the $B_\perp$ profile when compared against the exact solution. Toth tests the accuracy of several divergence–free numerical schemes (8-wave, projection method, constrained–transport/central–difference) in conjunction with a Godunov–type base scheme [Tóth, 2000]. All numerical strategies evaluated by the author show some level of distortion for $N = 32$. Compressible MHD problems are expected to have wave content - in the case of turbulence (or any flowfield with broadband fluctuations) at a wide range of scales. Thus results in figure 3.9 suggest the code utilised in the present study may be at an advantage for such problems compared to commonly–used MHD solvers (as those presented in [Tóth, 2000]).

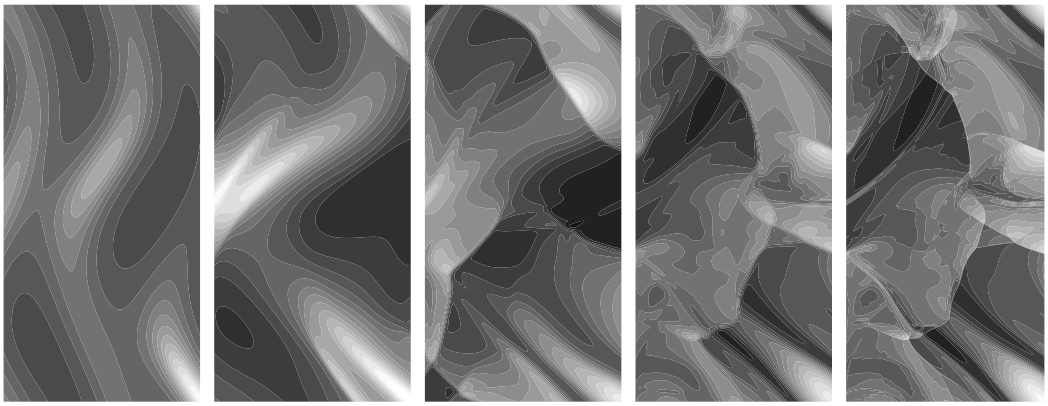
3.3.6 Orszag-Tang vortex

The Orszag-Tang vortex is a quasi–2d compressible MHD problem first introduced by Orszag and Tang [Orszag and Tang, 1979] in order to study the emergence of discontinuities from an initially smooth flowfield. It tests the capability of the code to accurately model complex interactions between shocks and vortices similar to those observed in compressible turbulent flows. Parameters selected match those used by several authors previously [Helzel et al., 2011] [Kawai, 2013], [Yang et al., 2016]. The initial state is given by:

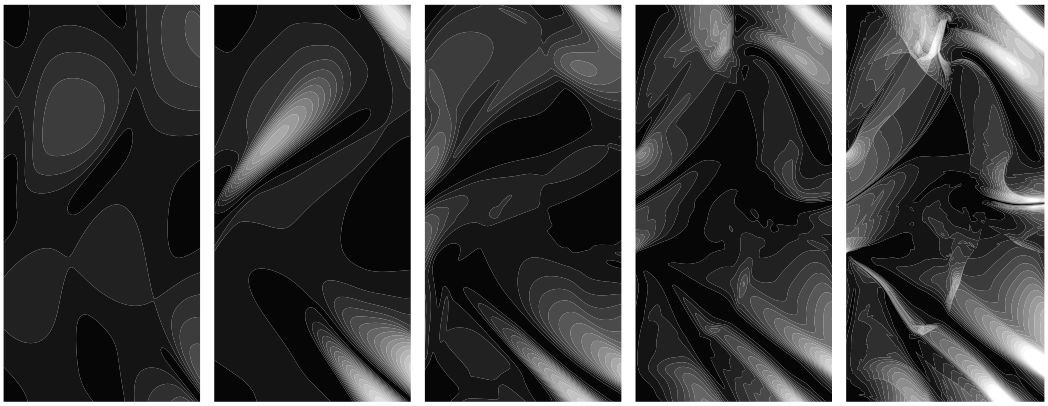
$$(\rho, u, v, w, p, B_x, B_y, B_z) = (\gamma^2, -\sin y, \sin x, 0, -\sin y, \sin 2x, 0, \gamma), \tag{3.3.8}$$

on the domain, $x, y \in [0, 2\pi]^2$, with periodic boundary conditions imposed in both x and y directions. Simulations are performed on a uniformly-spaced grid with $N = 200, 400, 800, 1600$ points respectively in both x and y directions.

In figure 3.10, a time–lapse of density, magnetic pressure and artificial resistivity contours show the evolution of the Orszag–Tang problem from an initially smooth flowfield to one of discontinuities (in both thermodynamic and magnetic quantities) and complex shock–shock interactions for a $N \times N$ grid of size $N = 400$. Contours at the final time for a higher resolution grid of $N = 1600$ display structures to higher level of refinement, however, in figure 3.11, grid resolutions $N = 200$, $N = 400$, $N = 800$ and $N = 1600$ are all shown to capture discontinuities on $3 - 4$ grid points, indicating the artificial dissipation terms are working as expected, comparing reasonably well with results in [Kawai, 2013]. In terms of values of normalised artificial resistivity, compared to results in [Kawai, 2013], the relative peak is higher by 0.3 in the present work. Regarding grid convergence within this study, for each grid resolution, peaks in the normalised artificial resistivity occur for a similar relative magnitude at the three main shock structures visible.



(a) $0.8 \leq \rho \leq 6.8$

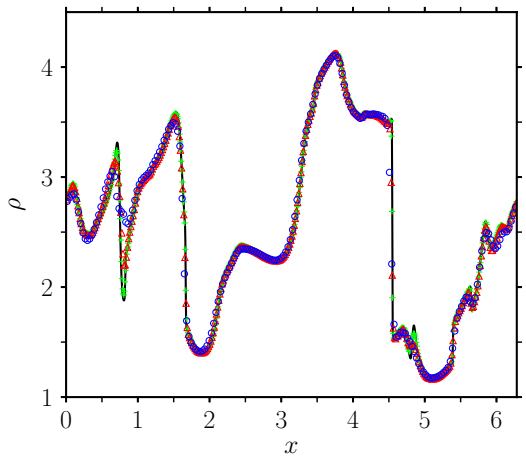


(b) $0.0001 \leq p_b \leq 4.4$

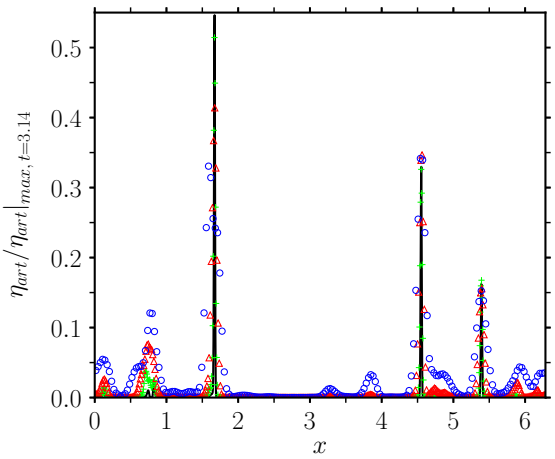


(c) $0 \leq \eta_{art}/\eta_{art}|_{\text{max. at } t=3.14} \leq 1$

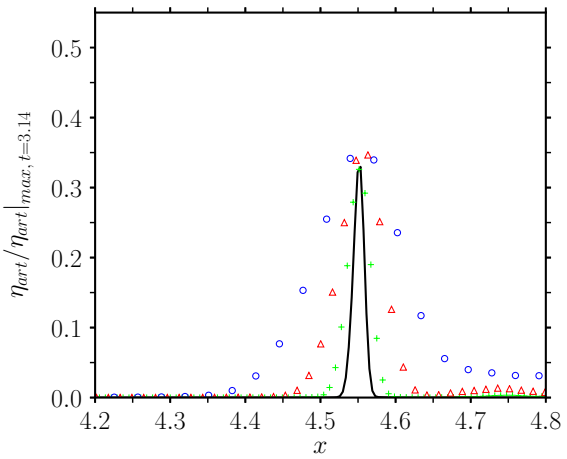
Fig. 3.10: 2.5d numerical simulation of Orszag-Tang vortex. 20 equally-spaced contours of density, ρ, magnetic pressure, $p_b = ||\boldsymbol{B}||^2/2$, and artificial resistivity, η_{art}, plotted for (from left-to-right) $N = 200$ result at $t = 0.5$, 1.0, 2.0, 3.14 and $N = 1600$ result at $t = 3.14$. Domain is restricted to $x \in [0, \pi]$, $y \in [0, 2\pi]$.



(a) ρ

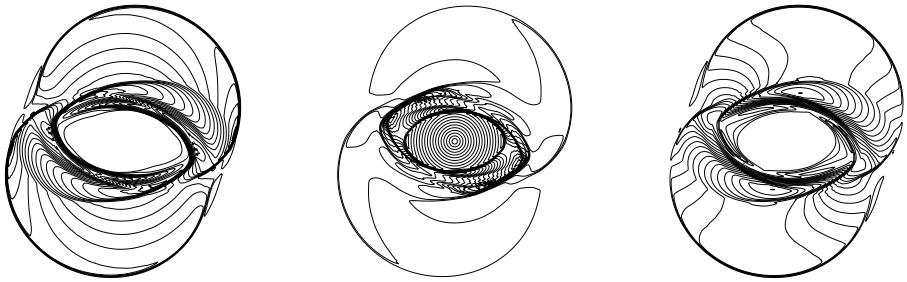


(b) Normalised artificial resistivity: overview

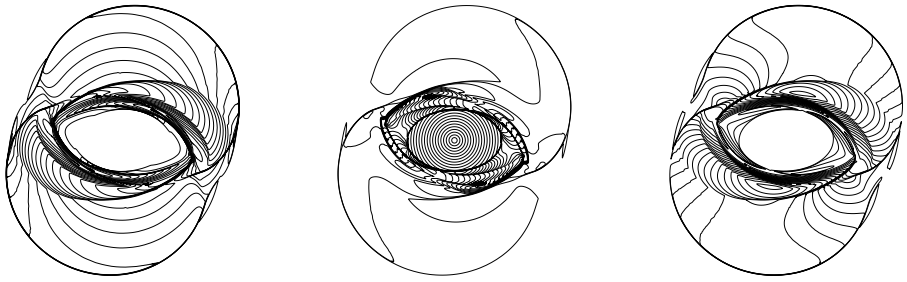


(c) Normalised artificial resistivity: close-up

Fig. 3.11: Density and normalised artificial resistivity profiles for 2.5d numerical simulation of Orszag-Tang vortex. Results plotted for $t = 3.14$ at $y = 0.5\pi$ on different grid sizes; $N = 200$ (blue circles), $N = 400$ (red triangles), $N = 800$ (green crosses), $N = 1600$ (black line).



(a) $N = 400$



(b) $N = 1600$

Fig. 3.12: 2.5d numerical simulation of rotor problem. 20 equally-spaced contours plotted for pressure, $0.03 \leq p \leq 1.98$, Mach number, $0.0 \leq M = ||\boldsymbol{u}||/c \leq 4.0$, and magnetic pressure, $0.0018 \leq p_b = ||\boldsymbol{B}||^2/2 \leq 2.6$, at $t = 0.15$ on $N = 400, 1600$ grids ($N \times N$ grid points)

3.3.7 Rotor problem

The rotor problem is a quasi–2d compressible MHD numerical test first studied by Balasara and Spicer [Balsara and Spicer, 1999] in order to investigate the propagation of strong torsional Alfvén waves. Within the flowfield there exists a very low pressure region at the centre of the rotor surrounded by a large pressure jump. Consequently, it provides a good test for a numerical scheme's robustness. The flow is initialised as a dense rotating disk enclosed by an ambient fluid of uniform density and velocity:

$$(\rho,\, u,\, v) = \begin{cases} (10.0,\, -u_0(y-0.5)/r_0,\, u_0(x-0.5)/r_0), & \text{for} \quad r \leq r_0, \\ (1.0 + 9.0f(r),\, -u_0(y-0.5)f(r)/r,\, u_0(x-0.5)f(r)/r), & \text{for} \quad r_0 < r < r_1, \\ (1.0,\, 0,\, 0), & \text{for} \quad r \geq r_1, \end{cases} \tag{3.3.9}$$

where we define, $r = \{(x-0.5)^2 + (y-0.5)^2\}^{1/2}$, $f(r) = (r_1 - r)/(r_1 - r_0)$, $r_0 = 0.115$, $r_1 = 0.1$, $u_0 = 2.0$. The remaining flow properties are initialised as $p = 1.0$, $w = 0.0$, $B_x = 5.0/(4.0\pi)$, $B_y = B_z = 0.0$. The flow is computed on the domain, $x, y \in [0, 1]^2$, with periodic boundary conditions imposed in both x and y directions. Simulations are performed on a uniformly-spaced $N \times N$ grid with $N = 400, 1600$ points respectively.

Figure 3.12 shows pressure, Mach number and magnetic pressure contours for the rotor problem computed

on $N \times N$ grids of resolution $N = 400$ and $N = 1600$ for a time–step of $\Delta t = 2 \times 10^{-4}$ and $\Delta t = 5 \times 10^{-5}$ respectively (inviscid $CFL_{max} \leq 0.35$). The highly pressurised region surrounding the central rotor is well–captured by the scheme, in addition to the rotor rotation. The closely–spaced contours of magnetic pressure also indicate a high intensity in the magnetic quantities occurs within the flow - and again, well–captured by the artificial resistivity term. Additionally, $\nabla \cdot \boldsymbol{B}$ remains of the order $\sim 10^{-12}$, for both $N = 400$ and $N = 1600$ grid resolutions, indicating the divergence–free constraint is reasonably well maintained by the mixed–correction GLM scheme. Small wiggles are also visible in contours for $N = 400$ are smoothed in the $N = 1600$, indicating better resolution of small–scale structures. However, contours for both grid sizes show good agreement with those present by [Kawai, 2013] and [Yang et al., 2016].

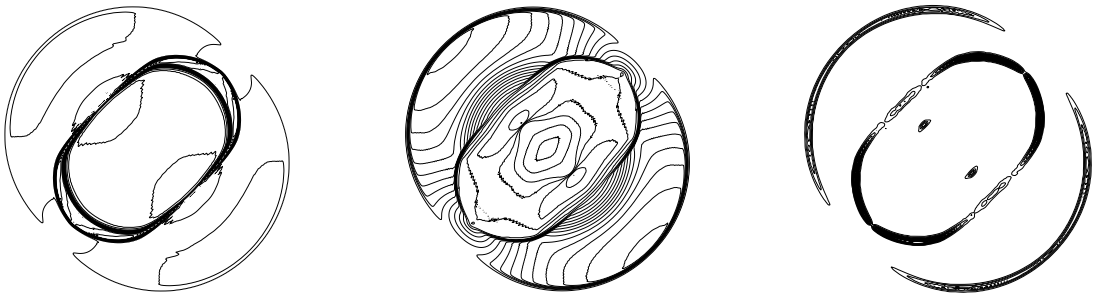
3.3.8 Blast wave problem

The final test case is the quasi–2d blast wave problem, in which we test the solver's ability to model strong shockwaves as they propagate outwards from a central over-pressurised region into the surrounding low pressure and plasma beta ambient medium. Parameters provided for this test case match those given previously by several other authors [Londrillo and Del Zanna, 2000], [Gardiner and Stone, 2005], [Kawai, 2013]. Similar to the set–up of the dense central disc in the rotor problem we initialise the over-pressurised region in the centre with a linear taper to avoid start up errors:

$$p = \begin{cases} 100.0, & \text{for} \quad r \leq r_0, \\ 1.0 + 99.0 f(r), & \text{for} \quad r_0 < r < r_1, \\ 1.0, & \text{for} \quad r \geq r_1, \end{cases} \tag{3.3.10}$$

where we define, $r = \{(x - 0.5)^2 + (y - 0.5)^2\}^{1/2}$, $f(r) = (r_1 - r)/(r_1 - r_0)$, $r_0 = 0.115$, $r_1 = 0.125$, $u_0 = 2.0$. The remaining flow properties are initialised as $\rho = 1.0$, $u = v = w = 0.0$, $B_x = B_y = 10.0\sqrt{2.0}$ and $= B_z = 0.0$. The flow is computed on the domain, $x, y \in [0, 1]^2$, with periodic boundary conditions imposed in both x and y directions. Simulations are performed on a uniformly-spaced grid with $N = 400$ points in both x and y directions respectively. A time step, $\Delta t = 4 \times 10^{-5}$ (inviscid $CFL_{max} \leq 0.46$) with filtering applied every 10 steps.

In figure 3.13, contours for the density, magnetic pressure and normalised artificial resistivity at $t = 0.02$ are shown for the blast wave problem . Symmetry of the blast wave is well maintained by the scheme. Strong MHD shocks, indicated by both the magnetic pressure and artificial resitivity contours, are well captured. Furthermore, similar to the rotor problem, $\nabla \cdot \boldsymbol{B}$ is maintained on the order of $\sim 10^{-12}$, throughout the simulation, confirming the divergence–free constraint is again reasonably upheld. Contours for all flow



(a) $0.17 \leq \rho \leq 3.34$ (b) $25.00 \leq p_b \leq 74.00$ (c) $0.00 \leq \eta_{art}/\eta_{art}|_{\text{max. at } t=0.02} \leq 1.00$

Fig. 3.13: 2.5d numerical simulation of blast wave problem. 20 equally-spaced contours of density, ρ, magnetic pressure, $p_b = ||\boldsymbol{B}||^2/2$, and artificial resistivity, η_{art}, plotted for $N = 400$ ($N \times N$ grid points) at $t = 0.02$.

properties match well with those presented in [Kawai, 2013]. Both show artificial resistivity to be restricted primarily to inner and outer rings of blast wave.

Chapter 4

Shock Refraction Problem

In this chapter we investigate small disturbances propagating through a fluid undergoing steady and uniform motion either side of an isolated planar shockwave. The first section concerns the piece–wise uniform base flow, in which there exists an MHD shock. Hugoniot curves are derived from the shock jump conditions in order to study the downstream flow in both thermodynamic and magnetic field-based phase spaces for a range of pre–shock states. Upstream conditions required for downstream high/low plasma beta flow and the "magnetosonic" condition are identified. Specific shock solutions are obtained by solving a cubic of the density ratio. In the second section a linear interaction analysis of the shock refraction problem is carried out. First, an eigen–decomposition is performed to derive the set of linear waves present in an ideal MHD flow and study their dependency on the mean magnetic field strength and direction. Subsequently the shock jump conditions are linearised and the shock refraction problem defined for an entropy mode impinging on a fast shock. The modal response of vorticity production by a refracted normal entropy mode is investigated for a range of base flow configurations through both linear and numerical studies. Analysis is extended to a Gaussian-distributed entropy mode for which a linear reconstruction of the downstream flow is performed and compared to the DNS result. The influence of magnetic field angle on post–shock vorticity strength and distribution is studied for a range of plasma beta regimes to investigate conditions required for maximum production.

4.1 Base flow: MHD shocks

The solution to the perturbed flowfield and shock surface deformation are found by solving a set of conservation equations given at the steady–shock location. We consider a fluid in which the motion is governed by the following system of conservation laws:

$$\frac{\partial \boldsymbol{q}}{\partial t} + \frac{\partial \boldsymbol{f}}{\partial x} + \frac{\partial \boldsymbol{g}}{\partial y} + \frac{\partial \boldsymbol{h}}{\partial z} = \mathbf{0}, \tag{4.1.1}$$

in which $\boldsymbol{q}$ is a vector of conserved variables, $\boldsymbol{q} = [q_1, \ldots, q_n]^\intercal$, and $\boldsymbol{f}$, $\boldsymbol{g}$, $\boldsymbol{h}$, are flux functions of $\boldsymbol{q}$ in $\mathbb{R}^n$.

Ideal MHD, which can be expressed in the above system of equations, permits the formation of shocks. Unlike the perturbations, the shock within the base flow is an inherently nonlinear phenomena and represents a discontinuity in the flowfield properties. As such, the base-flow is only piece–wise uniform.

Within a mathematical context, in ideal gas dynamics (Euler flows), shocks occur when two distinct acoustic wave fronts or "characteristics" of the same family - i.e. forward propagating or backward propagating - converge. A property known as the Riemann invariant - a function of flow velocity, speed of sound and ratio of specific heats (unique for each family) - is constant along each respective characteristic. As such, the intersection represents a point in time and space at which the same Riemann invariant is multi-valued. This is only possible if we consider the flow discontinuous. In the case of ideal MHD, there exists three types of propagating waves in the form of Alfvén, fast magneto–acoustic and slow magneto–acoustic modes. As such, a wider range of shocks satisfying the conservation laws are permitted to form within an MHD flow.

4.1.1 Rankine–Hugoniot jump conditions

Across a shock, mass, energy and magnetic flux are conserved and momentum is balanced. First we consider a one–dimensional flow in which we define the conservative variables by $\boldsymbol{q}(x,t)$, a vector in $\mathbb{R}^n$, a function of both space ($x \in \mathbb{R}$) and time ($\mathbb{R}_{\geq 0}$), and define f as a function of $\boldsymbol{q}$. If we then consider the solution to the field $\boldsymbol{q}$ in the approach of the shock (from either side) in which we assume $\boldsymbol{q}$ to be continuous and differentiable, we are able to write the conservation equation in divergence form:

$$\frac{\partial \boldsymbol{q}}{\partial t} + \frac{\partial}{\partial x} f(\boldsymbol{q}) = \mathbf{0}, \tag{4.1.2}$$

which denotes a classical solution to the conserved vector field, $\boldsymbol{q} = [\rho, \rho u, \rho e_t, B_x]^\intercal$.

Clearly, at a shock, (4.1.2) is no longer a valid method of solving for $\boldsymbol{q}$ as the discontinuous nature of the flow variables prevents evaluating spatial derivatives of $\boldsymbol{q}$. However, we can integrate (4.1.2) across the shock in time, $t \in \mathbb{R}_{\geq 0}$, and space, $x \in \mathbb{R}$, using a test function, φ, with compact support inside the rectangle $0 \leq t \leq \tau$, $a \leq x \leq b$, to find a solution to $\boldsymbol{q}$:

$$\int_{t=0}^{+\infty} \int_{x=-\infty}^{+\infty} \left[\frac{\partial \boldsymbol{q}}{\partial t} + \frac{\partial}{\partial x} f(\boldsymbol{q}) \right] \varphi(x,t) \mathrm{d}x\mathrm{d}t = \mathbf{0}. \tag{4.1.3}$$

Integrating by parts gives:

$$\int_{t=0}^{+\infty} \int_{x=-\infty}^{+\infty} \left[\boldsymbol{q} \frac{\partial \varphi}{\partial t} + f(\boldsymbol{q}) \frac{\partial \varphi}{\partial x} \right] \mathrm{d}x\mathrm{d}t + \int_{x=-\infty}^{+\infty} \boldsymbol{q}(x,0)\varphi(x,0)\mathrm{d}x = \mathbf{0}. \tag{4.1.4}$$

Thus, providing $\boldsymbol{q}$ is Lebesgue measurable and the test function is well-behaved on the compact support - in this context meaning continuous and differentiable - (4.1.4) opens up a class of solutions to $\boldsymbol{q}$ known as weak solutions.

To select a solution to $\boldsymbol{q}$ we now define an area, ∂S, on the $x-t$ plane around the discontinuity and consider only a non-intersecting shock segment, $\partial\Sigma$, defined by the shock position $x_s(t)$, which is continuous and differentiable within ∂S. If we then integrate (4.1.4) within ∂S we find that the classical solutions of $\boldsymbol{q}$ within ∂S separated by the discontinuity at $x = x_s(t)$, can be related through the following jump conditions:

$$-\dot{x_s}[\![\boldsymbol{q}]\!] + [\![f(\boldsymbol{q})]\!] = \boldsymbol{0}, \tag{4.1.5}$$

where $[\![\boldsymbol{q}]\!] \equiv \boldsymbol{q}_2 - \boldsymbol{q}_1$, $[\![f(\boldsymbol{q})]\!] \equiv f(\boldsymbol{q}_2) - f(\boldsymbol{q}_1)$ with $\boldsymbol{q}_1 = \boldsymbol{q}(x_s^-(t), t)$ and $\boldsymbol{q}_2 = \boldsymbol{q}(x_s^+(t), t)$. x_s^+ and x_s^- define approaches towards the shock from the positive (post–shock) and negative (pre–shock) directions respectively.

We can generalise (4.1.5) to three dimensions in the form:

$$-u_s[\![\boldsymbol{q}]\!] + [\![\mathbf{F}(\boldsymbol{q})]\!] \cdot \boldsymbol{n} = \boldsymbol{0}, \tag{4.1.6}$$

where $\boldsymbol{n}$ denotes the unit vector normal to the shock surface in the positive x-direction, u_s is the speed of the shock parallel to the normal and $\mathbf{F}$ is the flux function for a three–dimensional flow.

We can apply (4.1.6) to the ideal MHD conservation equations to derive jump conditions for mass, momentum, total energy and magnetic flux (where vacuum permeability, μ_m has been absorbed into the units of $\boldsymbol{B}$):

$$-u_s[\![\rho]\!] + \boldsymbol{n} \cdot [\![\rho\boldsymbol{u}]\!] = 0, \tag{4.1.7}$$

$$-u_s[\![\rho\boldsymbol{u}]\!] + \boldsymbol{n} \cdot [\![\rho\boldsymbol{u}\boldsymbol{u}^\intercal + (p + \boldsymbol{B}\cdot\boldsymbol{B}/2)\mathbf{I} - \boldsymbol{B}\boldsymbol{B}^\intercal]\!] = \boldsymbol{0}, \tag{4.1.8}$$

$$-u_s[\![\rho\boldsymbol{u}\cdot\boldsymbol{u}/2 + \rho e_i + \boldsymbol{B}\cdot\boldsymbol{B}/2]\!] + \boldsymbol{n} \cdot [\![(\rho\boldsymbol{u}\cdot\boldsymbol{u}/2 + \rho e_i + p + \boldsymbol{B}\cdot\boldsymbol{B})\boldsymbol{u} - (\boldsymbol{u}\cdot\boldsymbol{B})\boldsymbol{B}]\!] = 0, \tag{4.1.9}$$

$$-u_s[\![\boldsymbol{B}]\!] + \boldsymbol{n} \cdot [\![\boldsymbol{u}\boldsymbol{B} - \boldsymbol{B}\boldsymbol{u}]\!] = \boldsymbol{0}, \tag{4.1.10}$$

also noting, $\boldsymbol{n} \cdot [\![\boldsymbol{B}]\!] = 0$, as a result of Gauss' law of magnetism.

If we now redefine the shock jump conditions in the frame of the shock, $\boldsymbol{u'} = \boldsymbol{u} - u_s\boldsymbol{n}$, in which we define the shock normal, $\boldsymbol{n} = [1,\, 0,\, 0]^\intercal$:

$$[\![\rho u_n]\!] = 0, \tag{4.1.11}$$

$$\rho u_n[\![\boldsymbol{u}_t]\!] = B_n[\![\boldsymbol{B}_t]\!], \tag{4.1.12}$$

$$[\![\rho u_n^2 + p + B_t^2/2]\!] = 0, \qquad , \tag{4.1.13}$$

$$\rho u_n[\![(u_n^2 + \boldsymbol{u}_t\cdot\boldsymbol{u}_t)/2 + \rho e_i + p + \boldsymbol{B}_t\cdot\boldsymbol{B}_t/\rho]\!] = B_n[\![\boldsymbol{u}_t\cdot\boldsymbol{B}_t]\!], \tag{4.1.14}$$

$$\rho u_n [\![\boldsymbol{B}_t/\rho]\!] = B_n [\![\boldsymbol{u}_t]\!], \tag{4.1.15}$$

$$[\![B_n]\!] = 0, \tag{4.1.16}$$

where $u_n = \boldsymbol{u}' \cdot \boldsymbol{n}$, $\boldsymbol{u}_t = \boldsymbol{u}' - u_n \boldsymbol{n}$, $B_n = \boldsymbol{B} \cdot \boldsymbol{n}$ and $\boldsymbol{B}_t = \boldsymbol{B} - B_n \boldsymbol{n}$.

In ideal MHD there exist a range of discontinuities for which the conservation equations can be satisfied, however, in the present study we restrict our analysis to those containing a mass flow - **MHD shocks**. Unlike other MHD discontinuities, MHD shocks involve jumps in all thermodynamic quantities, velocities and the tangential magnetic field:

$$\begin{aligned} &[\![\rho]\!] \neq 0, \qquad [\![p]\!] \neq 0, \qquad [\![\boldsymbol{B}_t \cdot \boldsymbol{B}_t]\!] \neq 0, \\ &[\![u_n]\!] \neq 0, \qquad [\![\boldsymbol{u}_t]\!] \neq \boldsymbol{0}, \qquad [\![\boldsymbol{B}_t]\!] \neq \boldsymbol{0}. \end{aligned} \tag{4.1.17}$$

An MHD shock has three degrees of freedom in the upstream flow through which to fix the post–shock state, the Mach number, M_1, ratio of normal magnetic and thermodynamic pressures (plasma beta), $\beta_n = 2p_1/B_n^2$, and the magnetic field angle, φ. Special cases include parallel and perpendicular shocks in which the alignment of the upstream and downstream magnetic fields with respect to shock normal direction is parallel, $\varphi_1 = \varphi_2 = 0°$, and perpendicular, $\varphi_1 = \varphi_2 = 90°$, respectively. An oblique shock refers to cases in which the upstream and/or downstream magnetic field is not aligned to the parallel and perpendicular shock normal directions.

In the context of the shock refraction problem, only two types of MHD shocks (slow and fast) satisfy the conditions necessary for linear stability [Akhiezer et al., 1959]. With respect to the piece–wise base flow solution, fast and slow shocks are given by conditions (4.1.18) and (4.1.19) respectively:

$$u_{n,1} > c_{f,1}, \quad b_{n,2} < u_{n,2} < c_{f,2}, \tag{4.1.18}$$

$$b_{n,1} > u_{n,1} > c_{s,1}, \quad u_{n,2} < c_{s,2}, \tag{4.1.19}$$

in which the slow, fast and Alfvén wave speeds are defined as in (2.2.19) - (2.2.20), with the x-direction taken as the normal direction.

4.1.2 Hugoniot curves

In gas dynamics, the "Hugoniot curve" represents the locus in the $p - \vartheta$ phase plane of all allowable thermodynamic states a fluid may attain on passage through a normal shock. The equation for the curve is independent of shock speed and can be obtained from a combination of mass conservation and momentum and energy balance across a shock. A solution of the post–shock state is given by the intersection of this

curve with the Rayleigh line (a straight line in $p-\vartheta$ space, derived from conservation of mass and balance of momentum, whose slope is given by the negative squared mass flux). In MHD, an additional degree of freedom involving the magnetic field must be fixed in order to express the downstream state in the $p-\vartheta$ plane. In order to draw out comparisons between gasdynamic and MHD shocks, we derive analogous Hugoniot curve and Rayleigh line equations through which to aid visualisations of the magnetic field contribution to the post–shock state.

We consider a form of the Rankine–Hugoniot equations in which the jump in transversal velocity has been eliminated [Torrilhon, 2002]:

$$j^2[\![\vartheta]\!] + [\![p]\!] + \frac{1}{2}[\![B_t^2]\!] = 0, \tag{4.1.20}$$

$$j^2[\![\vartheta B_t]\!] - B_n^2[\![B_t]\!] = 0, \tag{4.1.21}$$

$$\frac{1}{\gamma-1}[\![p\vartheta]\!] + \frac{1}{2}(p_1+p_2)[\![\vartheta]\!] + \frac{1}{4}[\![\vartheta]\!][\![B_t]\!]^2 = 0, \tag{4.1.22}$$

where ϑ is the specific volume, j is the mass flow, $j = u_n/\vartheta$ and subscripts "n" and "t" denote components in the directions normal and tangential to the shock surface.

We eliminate the jump in the tangential magnetic field from (4.1.20)-(4.1.22) and derive expressions for the pressure ratio, $Y = p_2/p_1$, in terms of $X = \vartheta_2/\vartheta_1$ and non–dimensional parameters in front of the shock:

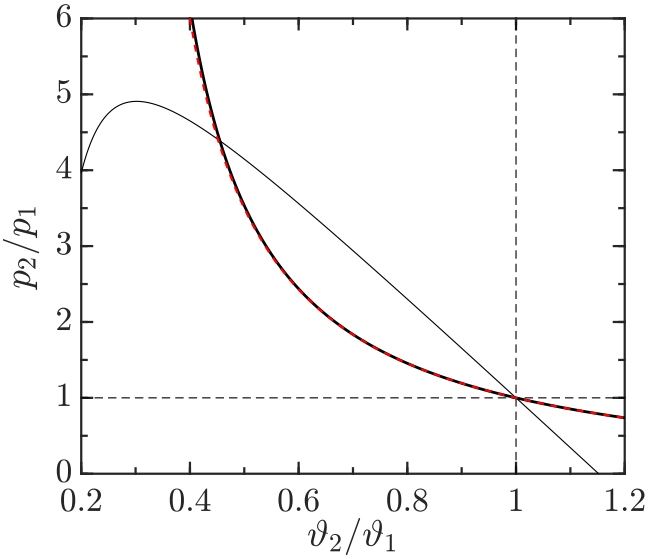
$$Y = 1 + \gamma M_1^2(1-X) - \frac{1}{2}\left\{\frac{(M_1^2 - r_{n,1}^2)^2}{(XM_1^2 - r_{n,1}^2)^2} - 1\right\}\hat{B}_{t,1}^2, \tag{4.1.23}$$

which represents the MHD equivalent of the Rayleigh line, and:

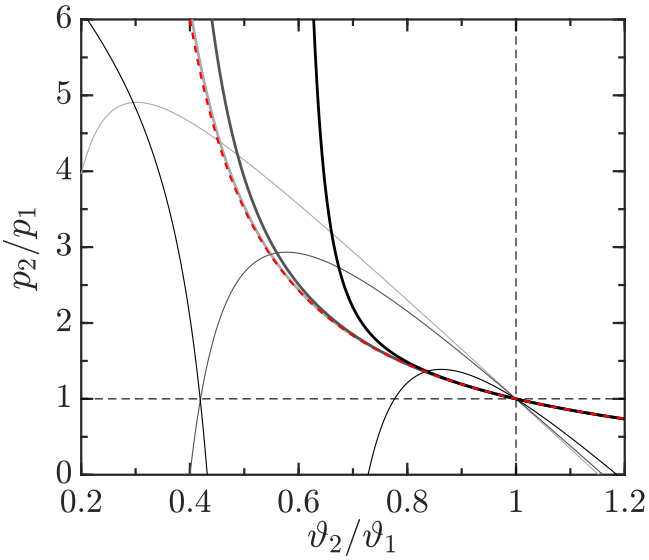
$$Y = \frac{A-X}{AX-1} - \frac{1}{2}\frac{X-1}{AX-1}\left\{\frac{M_1^2 - r_{n,1}^2}{XM_1^2 - r_{n,1}^2} - 1\right\}^2\hat{B}_{t,1}^2, \tag{4.1.24}$$

representing the Hugoniot curve, in which, $A = (\gamma+1)/(\gamma-1)$, and we define the upstream normal Mach number, $M = u_{n,1}/c_{o,1}$, where $c_{o,1}$ is the sound speed, $c_{o,1}^2 = (\partial p/\partial\rho)_s|_{\rho_1,p_1}$, the ratio between the normal Alfvén speed and sound speed, $r_{n,1} = b_{n,1}/c_{o,1}$, and the non–dimensional tangential magnetic field, $\hat{B}_{t,1} = B_{t,1}/\sqrt{p_1}$. It is trivial to show that (4.1.23) and (4.1.24) reduce to their gasdynamic form for shocks in which the upstream tangential magnetic field is zero, $\hat{B}_t = 0$.

Figures 4.1a and 4.1b show the "Rayleigh" lines and "Hugoniot" curves for an upstream state in which $M_1 = 2.0$, $\varphi = 26.56505°$ while the magnetic field strength is varied via the $r_{n,1}$ parameter. The shock solutions given by the intersections between curves of identical shading indicate an increase in magnetic field strength decreases both the pressure and density ratio (inverse of $\vartheta_2/\vartheta 1$) for a fixed M_1 and φ_1. The rapidly increasing divergence of the MHD "Hugoniot" curve from that of the gasdynamic corresponds to an increasing significance of the transversal magnetic energy jump within the energy balance given by (4.1.22)



(a) $r_{n,1} = 0.5$



(b) $r_{n,1} = 0.5,\ 1.0,\ 1.5$

Fig. 4.1: Intersections between "Hugoniot" curves in MHD (thick solid line) and gas dynamics (red dashed line) and MHD "Rankine" line (thin solid line) shown for Mach number, $M_1 = 2.0$, and magnetic field incidence angle, $\varphi_1 = 26.56505°$ at a range of normal magnetic field strengths, $r_{n,1} = b_{n,1}/c_{o,1} = B_n/\sqrt{\gamma p_1}$. In (b), solid lines become lighter with decreasing $r_{n,1}$. Only intersections between thin and thick solid lines of identical lightness (i.e. identical upstream state) indicate a shock solution.

involving internal energy and pressure work. We also find that the Rayleigh line, which has a constant slope in gas dynamics, is given by a curve in MHD. The influence of increasing magnetic field strength is less clear on the "Rayleigh" line, however, from figure 4.1b it is apparent the maximum slope increases. The curve can also exhibit multiple peaks in positive phase space (visible for $r_{n,1} = 1.5$). As mentioned previously, the $p - \vartheta$ phase plane provides a view of only the post–shock thermodynamic state in MHD, of which we can extract the sound wave speed as a useful parameter. In the context of the refraction problem, our interest also lies in MHD waves, most pertinently that of the magneto–acoustic wave which is present in both the two- and three–dimensional interaction. The importance of the magnetic field on the dynamics of the post–shock state lie within evaluation of the β parameter, $\beta = 2p/||\boldsymbol{B}||^2$. In very high β ($\beta \gg 1$) flows the thermodynamic pressure dominates that of the magnetic field and waves behave similar to those found in gas dynamics [Roe and Balsara, 1996]. In regards to the base flow, at very high β_1 we can be infer from both (4.1.23) and (4.1.24) that the pressure and density jump will approach that of a gasdynamic shock. We make the substitution $\hat{B}_{t,1} \equiv \sqrt{\gamma}\varepsilon_1 r_{n,1}$, where $\varepsilon_1 = B_{\perp,1}/B_n$. Noting that $r_{n,1} = \sqrt{2/(\gamma\beta_1(1+\varepsilon_1^2))}$, as $\beta_1 \to \infty$, $r_{n,1} \to 0$ (for finite ε_1). As such, it is clear that the magnetic field contribution in both (4.1.23) and (4.1.24) disappears in the high β_1 limit. In very low β flows ($\beta \ll 1$), the magnetic field dominates, and it is expected the magnetic field strength and direction will play a key role in post–shock phenomena. Therefore, to better quantify the effectiveness of a potential MHD flow control device, it is desirable to switch to an alternate phase space for the post–shock state in which the nature of the downstream magnetic field is more easily visualised.

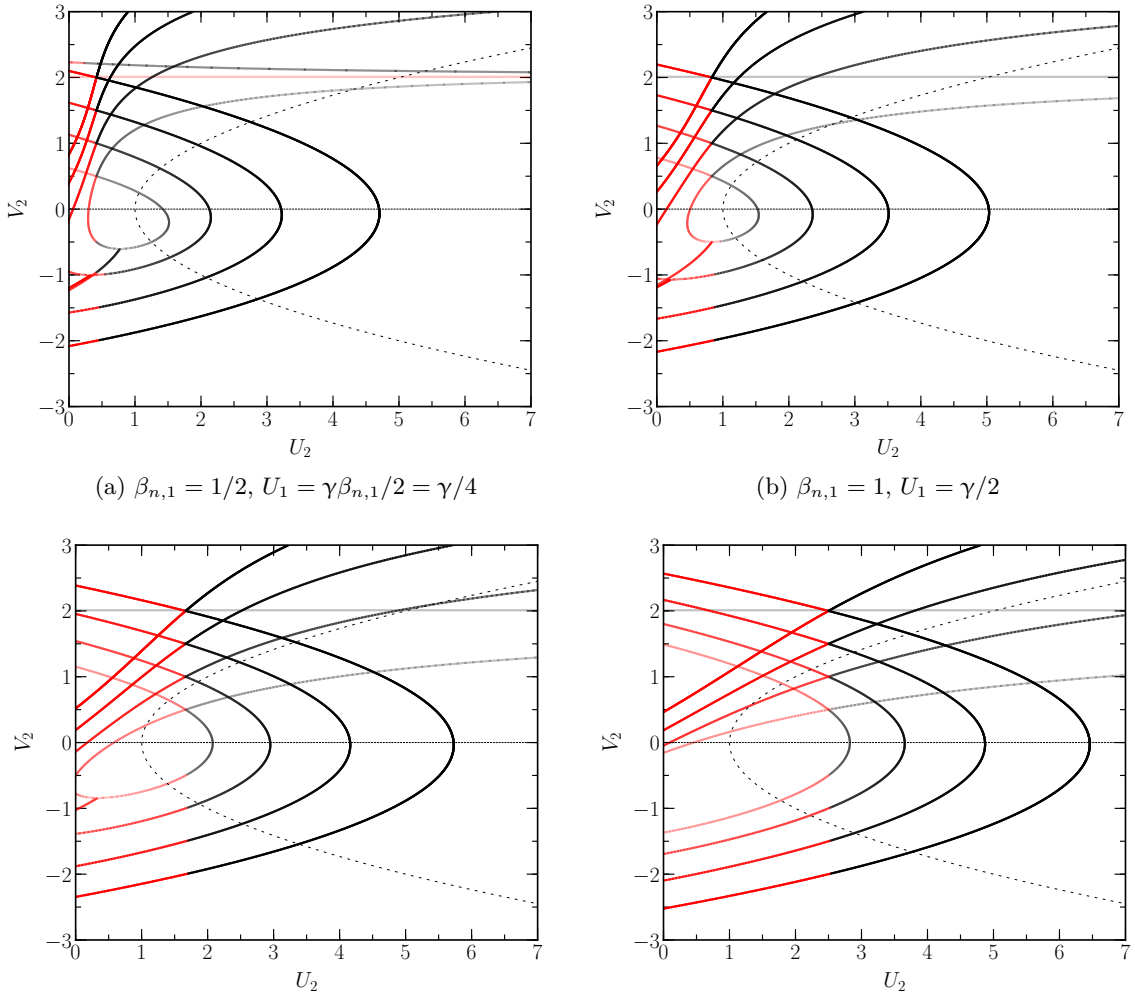
If non–zero B_n is assumed, it is possible derive an expression from (4.1.20)-(4.1.22) relating the pre– and post–shock states in terms of the magnetic field strength (with respect to the thermodynamic pressure) and its tangential component within non–dimensional phase space, $\boldsymbol{U} = (U, V)$ phase space, where $U = \gamma p/B_n^2$ and $V = B_\perp/B_n$ [Myong and Roe, 1997]:

$$([\![U]\!] + \gamma\bar{V}[\![V]\!])\{\gamma(\gamma-1)[\![V]\!]^3 + 4\gamma\bar{U}[\![V]\!] - 4\bar{V}[\![U]\!]\} - 4\gamma[\![U]\!][\![V]\!] = 0, \tag{4.1.25}$$

in which the overbar denotes the average of the pre– and post–shock states, $\bar{Q} = (Q_1 + Q_2)/2$.

Figures 4.2a - 4.2d show the Hugoniot curves for MHD shock in $\boldsymbol{U}$ phase space at a range of fixed upstream, $\beta_{n,1}$ (related to $\beta_{n,1} = 2\gamma/U_1$) for a range of magnetic field incidence angles, (given by V). No sign change occurs in $B_\perp$ across slow and fast shocks, as such, they are located in the upper plane of each plot ($V_2 > 0$) as V_1 is positive for all cases. Conversely, intermediate shocks are found in the bottom plane as the sign of $B_\perp$ does change across the discontinuity. We identify compressive shocks ($p_2/p_1 > 1$) in black and expansive ($p_2/p_1 < 1$) in red.

Consideration of the shock refraction problem with respect to expansive shocks is out of the scope of this present study, as such, subsequent analysis involves only compressive shocks. Additionally, as mentioned



(a) $\beta_{n,1} = 1/2$, $U_1 = \gamma\beta_{n,1}/2 = \gamma/4$

(b) $\beta_{n,1} = 1$, $U_1 = \gamma/2$

(c) $\beta_{n,1} = 2$, $U_1 = \gamma$

(d) $\beta_{n,1} = 3$, $U_1 = 3\gamma/2$

Fig. 4.2: Myong MHD Hugoniot curves in $\boldsymbol{U} = (U, V)$ phase space, where $U = \gamma p/B_n^2$ and $V = B_\perp/B_n$, for a fixed upstream U_1 and $V_1 \in [0.5, 2.0]$ (equivalent to range of magnetic field incidence angles, $\varphi_1 \in [26.56505°, 63.43494°]$). Solid lines become lighter with decreasing V_1. Shocks where $p_2/p_1 > 1$ indicated by black, and red otherwise. Fast and slow shocks located above horizontal line, $V_2 = 0$, intermediate shocks located below. Curved dashed line corresponds to unity ratio between post–shock Alfvén and sound speeds, $U_2 = 1 + V_2^2$.

previously, intermediate shocks do not fulfil the evolutionary condition, and will therefore also be ignored, leaving fast and slow shocks to be the focus of the discussion henceforth. Fast shocks can be identified by the relation, $V_2 > V_1$ (i.e. the downstream magnetic field angle is greater than the upstream value). The intersection of like curves within the upper plane in figures 4.2a - 4.2d occurs at the value of V_2 where $V_2 = V_1$. As such, fast shocks are only located above this intersection point.

We also note the interesting downstream state where $U_2 = (1 + V_2^2)$ - indicating the downstream ratio of Alfvén and sound speeds is unity, $r_2 = b_2/c_{o,2} = B_2/\sqrt{\gamma p_2} = 1$. $r_2 = 1$ equates to a plasma beta, $\beta_2 = 2/\gamma$. In flows where the Alfvén speed exceeds the sound speed, $r > 1$, the wave dynamics are said to be primarily influenced by the magnetic pressure as opposed to the thermodynamic pressure. For flows where the Alfvén speed is lower than the sound speed, $r < 1$, we find that wave behaviour is dominated by the thermodynamic pressure. Therefore $r = 1$ corresponds to a flow in which the influence of the magnetic and thermodynamic pressures are equal. These flows are also known as "magnetosonic" [Roe and Balsara, 1996] as the fast and slow magneto–acoustic wave speeds degenerate to the Alfvén/sound speeds. With respect to (U, V) phase space, if $V = 0$, a unity ratio between the Alfvén and sound speeds satisfies the "triple umbilic condition" (see section 2.2.2). In figures 4.2a - 4.2d (within which V_2 can be non–zero), at a given V_1, the value of V_2 at which a curve intersects the magnetosonic line, $(1 + V_2^2)/U_2 = 1$, increases with increasing $\beta_{n,1}$. For the given values of $\beta_{n,1}$, an increase in V_1 reduces the V_2 value at intersection of $(1 + V_2^2)/U_2 = 1$. In the fast shock regime we find that intersections for which the shock is compressive is visible only for $\beta_{n,1}$ values ≤ 2. However, decreasing $\beta_{n,1}$ reduces the locus of points found in the high U_2 regime for the range of V_1 values. In the present study we wish to observe downstream flows dominated by magnetic pressure (low β) and thermodynamic pressure (high β) respectively. Noting that $\beta \equiv 2U/(\gamma(1 + V^2))$, in the upper plane of figures 4.2a - 4.2d, Hugoniot curves below the dashed line represent thermodynamic pressure–dominated downstream base flow regimes, $\beta_2 > 2/\gamma$, and curves above denote base flow regimes dominated by magnetic pressure, $\beta_2 < 2/\gamma$. From figures 4.2c we see that when $\beta_{n,1} = 2$ both regimes and the "magnetosonic" condition can be studied for fast shocks. As such, we select a base flow configuration for which $\beta_{n,1} = 2$.

4.1.3 Solutions to MHD shocks in terms of density ratio

To obtain the post–shock state for a given pre–shock state it is possible to combine the Rayleigh and Hugoniot equations, eliminate the pressure ratio and derive a polynomial in terms of the shock density ratio [Lynn, 1966], $\eta_c = \rho_2/\rho_1$, to solve:

$$a\eta_c^3 + b\eta_c^2 + c\eta_c + d = 0, \tag{4.1.26}$$

where,

$$a = r_{n,1}^4\{2 + M_1^2(\gamma - 1)(\varepsilon_1^2 + 1)\},$$
$$b = (r_{n,1}M_1)^2\{M_1^2[\varepsilon_1^2(2 - \gamma) + 2(1 - \gamma)] - 4 - r_{n,1}^2(\gamma + 1)(\varepsilon_1^2 + 1)\},$$
$$c = M_1^4\{2 + r_{n,1}^2[\gamma\varepsilon_1^2 + 2(\gamma + 1)] + M_1^2(\gamma - 1)\},$$
$$d = -M_1^6(\gamma + 1),$$

in which we have assumed a non–zero normal magnetic field component.

From (4.1.26) we obtain three potential solutions for the shock density ratio. From Lax's condition we know there exists the additional condition of increasing entropy across a physical shock. Work by Lust [Lüst, 1955] showed that for an MHD shock in an ideal gas, this is satisfied for $\eta_c > 1$.

Once the density ratio for a given upstream state is known, it is possible to use the following equations to compute the respective flow property jumps across the shock:

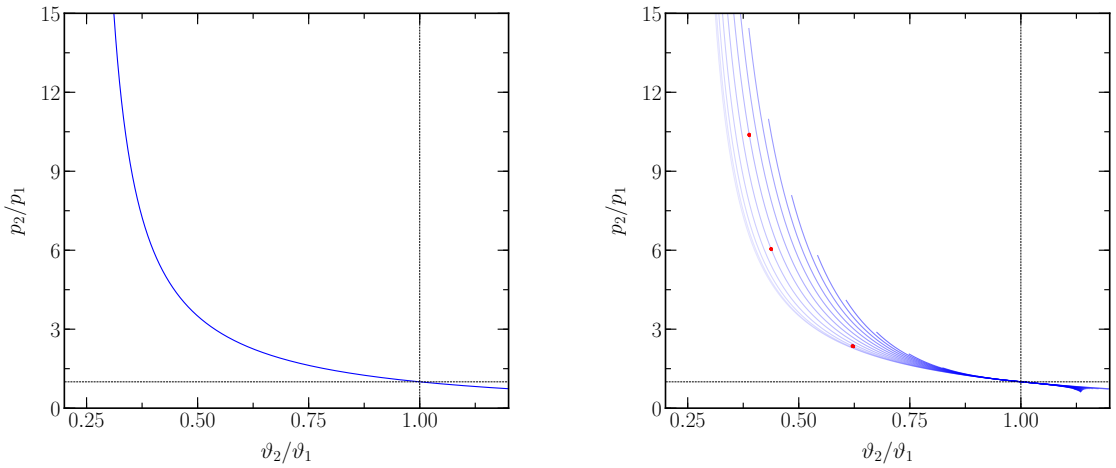
$$\frac{p_2}{p_1} = 1 + \frac{\gamma M_1^2(\eta_c - 1)}{\eta_c}\left\{1 + \frac{\eta_c r_{n,1}^2\varepsilon_1^2}{2}\frac{2\eta_c r_{n,1}^2 - (\eta_c + 1)M_1^2}{(M_1^2 - \eta_c r_{n,1}^2)^2}\right\}, \tag{4.1.27}$$

$$\varepsilon_2 = \varepsilon_1\eta_c\frac{M_1^2 - r_{n,1}^2}{M_1^2 - \eta_c r_{n,1}^2}, \tag{4.1.28}$$

$$\delta_2 = \eta_c r_{n,1}^2\varepsilon_1\left\{\frac{\eta_c - 1}{M_1^2 - \eta_c r_{n,1}^2}\right\}, \tag{4.1.29}$$

where δ_2 is the ratio between the downstream tangential and normal velocities, $\delta_2 = v_2/u_2$.

In figure 4.3 the fast shock solutions in the $p - \vartheta$ plane are shown for a range of $r_{n,1}$ at different fixed values of φ_1. For a parallel MHD shock, $\varphi_1 = 0.0°$, we see that the shock solutions are independent of the magnetic field strength (as shown in (4.1.23) and (4.1.24)). For non–zero φ_1 a reduction in the maximum pressure and density ratio is observed (density ratio is inverse of ϑ_2/ϑ_1) for increasing values of $r_{n,1}$. With respect to the magnetosonic condition (indicated by red dots) we also see that its incidence for the range of M_1 computed reduces with increasing φ_1.



(a) $\varphi_1 = 0.00000°$ (b) $\varphi_1 = 26.56505°$

(c) $\varphi_1 = 43.50912°$ (d) $\varphi_1 = 56.30993°$

Fig. 4.3: Fast shock solutions at fixed upstream magnetic field incidence angle, φ_1, for upstream normal Alfvén to sound speed ratio in the range, $r_{n,1} \in [10^{-6}, 8/\sqrt{\gamma}]$, where $r_{n,1} = b_{n,1}/c_{o,1} = B_n/\sqrt{\gamma p_1}$ and $\gamma = 5/3$. Lines become lighter with decreasing $r_{n,1}$. Red dots corresponds to shocks where the ratio between downstream Alfvén and sound speeds is unity.

4.2 Linear interaction analysis

4.2.1 Eigen-decomposition of ideal MHD Equations

A perturbation ($\boldsymbol{\mu}'$) is added to a homogeneous plasma flow, ($\bar{\boldsymbol{\mu}}$):

$$\boldsymbol{\mu} = \bar{\boldsymbol{\mu}} + \epsilon \boldsymbol{\mu}', \tag{4.2.1}$$

where $\boldsymbol{\mu} \equiv [\rho, \boldsymbol{u}^\intercal, p, \boldsymbol{B}^\intercal]^\intercal$, $\bar{\boldsymbol{\mu}} \equiv [\bar{\rho}, \bar{\boldsymbol{u}}^\intercal, \bar{p}, \bar{\boldsymbol{B}}^\intercal]^\intercal$, $\boldsymbol{\mu}' \equiv [\rho', \boldsymbol{u}'^\intercal, p', \boldsymbol{B}'^\intercal]^\intercal$ are the vectors of dimensionless primitive variables respectively of the perturbed flow, the base flow and an unsteady and inhomogeneous perturbation. The constant ϵ is a control parameter set arbitrarily small, $\epsilon \ll 1$.

To ensure there is not excessive notation, from this section onwards, the sound speed, c_o, Alfvén velocity, $\boldsymbol{b}$, and plasma beta, β, will be defined with respect to the base flow properties, $c_o^2 = (\partial p/\partial \rho)_s|_{\bar{\rho},\bar{p})}$, $\boldsymbol{b} = \bar{\boldsymbol{B}}/\sqrt{\bar{\rho}}$ and $\beta = 2\bar{p}/||\bar{\boldsymbol{B}}||^2$.

We use (4.2.1) to derive a linear approximation of the single-fluid compressible ideal MHD equations:

$$\frac{\partial \rho'}{\partial t} + (\bar{\boldsymbol{u}} \cdot \nabla)\rho' + \bar{\rho}(\nabla \cdot \boldsymbol{u}') = 0, \tag{4.2.2}$$

$$\frac{\partial \boldsymbol{u}'}{\partial t} + (\bar{\boldsymbol{u}} \cdot \nabla)\boldsymbol{u}' + \frac{\boldsymbol{\nabla} p'}{\bar{\rho}} + \frac{(\boldsymbol{\nabla} \boldsymbol{B}') \cdot \bar{\boldsymbol{B}}}{\bar{\rho}} + \frac{(\bar{\boldsymbol{B}} \cdot \nabla)\boldsymbol{B}'}{\bar{\rho}} = \boldsymbol{0}, \tag{4.2.3}$$

$$\frac{\partial p'}{\partial t} + (\bar{\boldsymbol{u}} \cdot \nabla)p' + \bar{\rho} c_o^2 (\nabla \cdot \boldsymbol{u}') = 0, \tag{4.2.4}$$

$$\frac{\partial \boldsymbol{B}'}{\partial t} + (\bar{\boldsymbol{u}} \cdot \nabla)\boldsymbol{B}' + \bar{\boldsymbol{B}}(\nabla \cdot \boldsymbol{u}') - (\bar{\boldsymbol{B}} \cdot \nabla)\boldsymbol{u}' = \boldsymbol{0}, \tag{4.2.5}$$

where we have assumed the base flow is uniform and steady, $\partial \bar{\boldsymbol{\mu}}/\partial t = \partial \bar{\boldsymbol{\mu}}/\partial x = \partial \bar{\boldsymbol{\mu}}/\partial y = \partial \bar{\boldsymbol{\mu}}/\partial z = \boldsymbol{0}$.

We now consider plane wave solutions of the perturbation:

$$\boldsymbol{\mu}' = \boldsymbol{\xi} \exp[\mathrm{i}(\boldsymbol{k} \cdot \boldsymbol{x} - \omega t)], \tag{4.2.6}$$

where $\boldsymbol{k} = [k_x, k_y, k_z]^\intercal$ is a complex-valued vector of wave numbers in the $\boldsymbol{e}_x$, $\boldsymbol{e}_y$ and $\boldsymbol{e}_z$ directions and ω is the real-valued angular frequency. $\boldsymbol{\xi}$ is a vector containing the wave amplitudes of the primitive variables, $\boldsymbol{\xi} \equiv [\xi^\rho, \xi^u, \xi^v, \xi^w, \xi^p, \xi^{B_x}, \xi^{B_y}, \xi^{B_z}]^\intercal$.

Substituting (4.2.6) into (4.2.2) - (4.2.5), produces the ideal MHD eigenvalue problem, the solutions of which give the dispersion relation for each respective ideal MHD wave mode:

$$-\omega_0 \rho' + \bar{\rho}(\boldsymbol{k} \cdot \boldsymbol{u}') = 0, \tag{4.2.7}$$

$$-\omega_0 \boldsymbol{u}' + \frac{\boldsymbol{k} p'}{\bar{\rho}} + \left(\frac{\boldsymbol{k}\bar{\boldsymbol{B}}^t}{\bar{\rho}}\right) \cdot \boldsymbol{B}' - \left(\frac{\boldsymbol{k} \cdot \bar{\boldsymbol{B}}}{\bar{\rho}}\right) \boldsymbol{B}' = \boldsymbol{0}, \tag{4.2.8}$$

$$-\omega_0 p' + \bar{\rho} c_o^2 (\boldsymbol{k} \cdot \boldsymbol{u}') = 0, \tag{4.2.9}$$

$$-\omega_0 \boldsymbol{B}' - (\bar{\boldsymbol{B}} \cdot \boldsymbol{k})\boldsymbol{u}' + \bar{\boldsymbol{B}}(\boldsymbol{k} \cdot \boldsymbol{u}') = \boldsymbol{0}, \tag{4.2.10}$$

where ω_0 is the angular frequency taken in the reference frame in which the fluid is at rest:

$$\omega_0 = \omega - \boldsymbol{k} \cdot \bar{\boldsymbol{u}}. \tag{4.2.11}$$

Without loss of generality, we move to a coordinate system in which $\boldsymbol{k} = [k_\perp,\, 0,\, k_\parallel]^\intercal$, and $\bar{\boldsymbol{B}} = [0,\, 0,\, \bar{B}]^\intercal$. Consequently, we can reduce (4.2.7) - (4.2.10), to a compact vector form:

$$\mathbf{A} \cdot \boldsymbol{\mu}' = \boldsymbol{0}, \tag{4.2.12}$$

where $\mathbf{A} \equiv \mathbf{M} - \omega_0 \mathbf{I}$,

$$\mathbf{M} = \begin{bmatrix}
0 & \bar{\rho}k_\perp & 0 & \bar{\rho}k_\parallel & 0 & 0 & 0 & 0 \\
0 & 0 & 0 & 0 & \dfrac{k_\perp}{\bar{\rho}} & -\dfrac{k_\parallel \bar{B}}{\bar{\rho}} & 0 & \dfrac{k_\perp \bar{B}}{\bar{\rho}} \\
0 & 0 & 0 & 0 & 0 & 0 & -\dfrac{k_\parallel \bar{B}}{\bar{\rho}} & 0 \\
0 & 0 & 0 & 0 & \dfrac{k_\parallel}{\bar{\rho}} & 0 & 0 & 0 \\
0 & \bar{\rho}c_o^2 k_\perp & 0 & \bar{\rho}c_o^2 k_\parallel & 0 & 0 & 0 & 0 \\
0 & -k_\parallel \bar{B} & 0 & 0 & 0 & 0 & 0 & 0 \\
0 & 0 & -k_\parallel \bar{B} & 0 & 0 & 0 & 0 & 0 \\
0 & k_\perp \bar{B} & 0 & 0 & 0 & 0 & 0 & 0
\end{bmatrix}$$

For a non-trivial solution to $\boldsymbol{\mu}'$ to exist ($\boldsymbol{\mu}' \neq \boldsymbol{0}$), $\boldsymbol{A}$ must be non-invertible - i.e. the determinant must be equal to zero, $\det \mathbf{A} = \det(\mathbf{M} - \omega_0 \mathbf{I}) = 0$. Computing the determinant results in a 8^{th} degree polynomial of ω_0, the roots of which denote the eigenvalues of $\mathbf{M}$:

$$\omega_0^8 - \omega_0^6[k^2(b^2 + c_o^2) + b^2 k_\parallel^2] + \omega_0^4[b^4 k^2 k_\parallel^2 + 2c_o^2 b^2 k^2 k_\parallel^2] - \omega_0^2[c_o^2 b^4 k^2 k_\parallel^4] = 0, \tag{4.2.13}$$

where $k = (k_\perp^2 + k_\parallel^2)^{1/2}$, for which the principal root is taken as the square root, and b is the magnitude of the Alfvén velocity, $b = ||\boldsymbol{b}||$.

Each root of (4.2.13) (and therefore eigenvalue of $\mathbf{M}$) gives the dispersion relationship of each respective ideal MHD "wave mode". The eigenvector corresponding to each eigenvalue denotes fluctuations in the

primitive variables transported by the respective wave. Where the dispersion relationship is given in terms of $\omega_{0\beta}^2$, the positive (negative) root denotes the forward (backward) modes and has the subscript + (−), $\omega_{0\beta\pm} = \pm\omega_{0\beta}$.

We define one eigenvalue root (or eigenfrequency) of (4.2.13), $\omega_{0E} = 0$, and its corresponding eigenvector, $\boldsymbol{e}_E$, as the **entropy mode**, denoting constant pressure density fluctuations convected at the flow speed:

$$\boldsymbol{e}_E = [1,\, 0,\, 0,\, 0,\, 0,\, 0,\, 0,\, 0]^\intercal. \tag{4.2.14}$$

The second "zero" root of (4.2.13), $\omega_{02} = 0$, corresponds to the $\nabla \cdot \boldsymbol{B}$ mode and denotes non–physical transport of perturbations in $\nabla \cdot \boldsymbol{B}$. This is typically regarded as a spurious eigenvalue solution of the ideal MHD equations as it can be removed by coupling the magnetic field perturbations through Gauss' law, $\boldsymbol{k} \cdot \boldsymbol{B}' = 0$, thereby reducing the size of $\mathbf{M}$ by one and the determinant in (4.2.13) to a 7^{th} degree polynomial in ω_0.

Two additional roots of (4.2.13) represent incompressible, isentropic waves called **Alfvén modes**:

$$\omega_{0A}^2 = (\boldsymbol{k} \cdot \boldsymbol{b})^2 = (k_\parallel b)^2, \tag{4.2.15}$$

carrying perturbations in velocity and magnetic field components only in the direction perpendicular to the plane containing the wavevector and mean magnetic field:

$$\boldsymbol{e}_{A\pm} = [0,\, \boldsymbol{u}_A'^\intercal,\, 0,\, \boldsymbol{B}_{A\pm}'^\intercal]^\intercal, \tag{4.2.16}$$

where, $\boldsymbol{u}'_{A\pm} = (\boldsymbol{k} \times \boldsymbol{b})/(kb \sin\alpha)$ and $\boldsymbol{B}'_{A\pm} \equiv \mp\sqrt{\bar{\rho}}\boldsymbol{u}'_{A\pm}$, in which α is the angle between the wavevector and the mean magnetic field, $\boldsymbol{k} \cdot \boldsymbol{b} = kb\cos\alpha$.

An Alfvén wave therefore constitutes a purely transverse wave (velocity field is solenoidal, $\nabla \cdot \boldsymbol{u}' = 0$). It can be physically interpreted as the elastic bending of mean magnetic field lines via the action of magnetic tension. This restoring force induces oscillations between kinetic and magnetic energy as the wave propagates through the fluid.

The four remaining roots of (4.2.13) correspond to the eigenfrequencies of compressible, isentropic waves known as the **fast/slow magneto–acoustic modes**, $\omega_{0f,s\pm}$:

$$\omega_{0f,s}^2 = \frac{k^2}{2}\left((b^2 + c_o^2) \pm \sqrt{(b^2 + c_o^2)^2 - 4\frac{(\boldsymbol{k} \cdot \boldsymbol{b})^2}{k^2}c_o^2}\right), \tag{4.2.17}$$

In magneto–acoustic waves, three separate restoring forces (thermodynamic pressure, magnetic pressure and magnetic tension) enable transfers between the kinetic, magnetic and internal energies. These transfers

are represented as fluctuations transported with the wave in the thermodynamic quantities and velocity and magnetic field components in the plane parallel to the wavevector and mean magnetic field:

$$\boldsymbol{e}_{f,s\pm} = [\rho'_{f,s\pm},\, \boldsymbol{u}'^{\intercal}_{f,s\pm},\, c_o^2\rho'_{f,s\pm},\, \boldsymbol{B}'^{\intercal}_{f,s\pm}]^{\intercal}, \tag{4.2.18}$$

where,

$$\begin{aligned}
\rho'_{f,s\pm} &= \{1 - (\boldsymbol{k}\cdot\boldsymbol{b})^2/\omega^2_{0f,s\pm}\},\\
\boldsymbol{u}'_{f\pm} &= \{(\omega_{0f\pm}/k^2)\boldsymbol{k} - (\boldsymbol{k}\cdot\boldsymbol{b}/\omega_{0f\pm})\boldsymbol{b}\}/\bar{\rho},\\
\boldsymbol{u}'_{s\pm} &= sign(\boldsymbol{k}\cdot\boldsymbol{B})\{(\omega_{0s\pm}/k^2)\boldsymbol{k} - (\boldsymbol{k}\cdot\boldsymbol{b}/\omega_{0s\pm})\boldsymbol{b}\}/\bar{\rho},\\
\boldsymbol{B}'_{f,s\pm} &= \{\boldsymbol{b} - (\boldsymbol{k}\cdot\boldsymbol{b})\boldsymbol{k}/k^2\}/\sqrt{\bar{\rho}}.
\end{aligned}$$

Magneto-acoustic waves induce a combination of solenoidal and irrotational ($\boldsymbol{\nabla}\times\boldsymbol{u}' = \boldsymbol{0}$) fluid motion if the wavevector is not aligned parallel or perpendicular to the mean magnetic field [Goedbloed et al., 2004], [Somov, 2012]. The "intensity" of solenoidal/irrotational fluid motions transported by magneto–acoustic modes at a given wavevector direction and ratio of Alfvén and sound speeds, $r = b/c_o$, is shown in figure 4.4, through the re–scaled magnitude of vorticity fluctuation $\hat{\omega} = ||\hat{\boldsymbol{k}}\times\boldsymbol{u}'||/u'$, (where $\hat{\boldsymbol{k}}$ is the unit wavevector, $\hat{\boldsymbol{k}} \equiv \boldsymbol{k}/k$, and $u' = ||\boldsymbol{u}'||$). $\hat{\omega} = 0$ indicates purely irrotational fluid motion (i.e. the wave is longitudinal) and $\hat{\omega} = 1$ corresponds to fully solenoidal fluid motion.

In the case of parallel alignment of the wavevector and mean magnetic field, $\hat{k}_\perp = 0$, where the base flow is magnetic–pressure dominated, $r > 1$, figure 4.4 shows the fast magneto–acoustic mode will induce only solenoidal fluid motions (see appendix A.1 for eigenvector definition), $\hat{\omega} = 1$. Additionally, applying the following relation at parallel alignment, $\boldsymbol{k}\cdot\boldsymbol{b} = kb$, to (4.2.17), we find that the eigenfrequency of a fast magneto–acoustic mode transporting solenoidal fluid motions reduces to $\omega^2_{0f} = k^2b^2$. This results in a fast magneto–acoustic phase speed, $V_\mu = \omega_{0\mu}/||\boldsymbol{k}||$, equal to the Alfvén speed, $V_{f\pm} = \pm b$. For the same base flow, figure 4.4 shows the slow magneto–acoustic mode produces irrotational fluid motions, $\hat{\omega} = 0$. Analogous to the gasdynamic acoustic mode, the slow magneto–acoustic eigenfrequency reduces to, $\omega^2_{0s} = k^2c_o^2$, resulting in a phase speed equal to the sound speed, $V_{s\pm} = \pm c_o$. For base flows that are thermodynamic pressure–dominated, $r < 1$, the fast and slow magneto–acoustic mode wave behaviours at parallel alignment are reversed.

At perpendicular alignment between the wavevector and mean magnetic field, $|\hat{k}_\perp| = 1$, in both magnetic and thermodynamic pressure–dominated regimes, in figure 4.4 we see that the fast magneto–acoustic mode exhibits irrotational fluid motions, $\hat{\omega} = 0$. From substituting $\boldsymbol{k}\cdot\boldsymbol{b} = 0$ into (4.2.17), it is trivial to also show, $\omega^2_{0f} = k^2(b^2 + c_o^2)$, which corresponds to the maximum phase speed of the fast magneto–acoustic

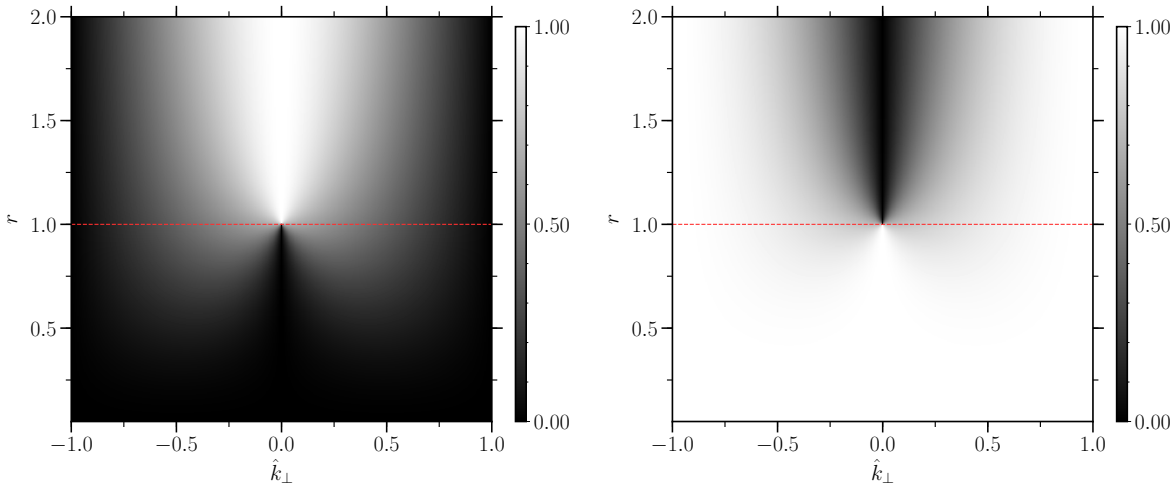


Fig. 4.4: Re–scaled magnitude of magneto–acoustic mode vorticity fluctuation, $\hat{\omega} = ||\hat{\boldsymbol{k}} \times \boldsymbol{u}'||/||\boldsymbol{u}'||$, where $\hat{\boldsymbol{k}}$ is the unit wavevector, $\hat{\boldsymbol{k}} = \boldsymbol{k}/||\boldsymbol{k}||$. $\hat{\omega}$ for fast magneto–acoustic (left) and slow magneto–acoustic (right) modes shown to vary with $\hat{k}_\perp$ (perpendicular unit wavevector component in a coordinate system orthogonal to the mean magnetic field), and ratio between Alfvén and sound speeds, $r = b/c_o$. Magnetosonic condition (Alfvén speed equal to sound speed, $b = c_o$) indicated on plots, $r = 1.0$ (red dashed line).

mode. Figure 4.4 shows the slow magneto–acoustic induces only solenoidal fluid motions (see appendix A.2 for eigenvector definition), $\hat{\omega} = 1$. Using (4.2.17), we find that the slow magneto–acoustic eigenfrequency and phase speed reduce to zero, $V_{s\pm} = \omega_{0s} = 0$ (i.e. it is convected with the flow).

The group velocity, $\boldsymbol{V}^g$, provides a physically meaningful description of a wave's propagation through space:

$$\boldsymbol{V}^g = \frac{\partial \omega}{\partial \boldsymbol{k}} = \bar{\boldsymbol{u}} + V_\mu \boldsymbol{k} + \frac{\partial V_\mu}{\partial \boldsymbol{k}} |\boldsymbol{k}|. \tag{4.2.19}$$

The group velocity is independent of wavevector direction for the entropy mode:

$$\boldsymbol{V}^g_E = \boldsymbol{u}, \tag{4.2.20}$$

and the Alfvén modes:

$$\boldsymbol{V}^g_{A\pm} = \boldsymbol{u} \pm \boldsymbol{b}. \tag{4.2.21}$$

However, the respective magneto–acoustic mode group velocities exhibit a dependency on wavevector direction via the second and third terms on the right–hand–side of (4.2.19), for which we define $\partial V_\mu/\partial \boldsymbol{k}$ for the fast magneto–acoustic modes:

$$\frac{\partial V_{f\pm}}{\partial \boldsymbol{k}} = -\frac{b(\hat{\boldsymbol{k}} \cdot \boldsymbol{b})}{\omega_{0f\pm}[(b^2 + c_o^2)^2 - 4c_o^2(\hat{\boldsymbol{k}} \cdot \boldsymbol{b})^2]^{1/2}} [\hat{\boldsymbol{k}} \times (\boldsymbol{b} \times \hat{\boldsymbol{k}})], \tag{4.2.22}$$

and the slow magneto–acoustic modes,

$$\frac{\partial V_{s\pm}}{\partial \boldsymbol{k}} = \frac{b(\hat{\boldsymbol{k}} \cdot \boldsymbol{b})}{\omega_{0s\pm}[(b^2 + c_o^2)^2 - 4c_o^2(\hat{\boldsymbol{k}} \cdot \boldsymbol{b})^2]^{1/2}}[\hat{\boldsymbol{k}} \times (\boldsymbol{b} \times \hat{\boldsymbol{k}})], \tag{4.2.23}$$

where $\hat{\boldsymbol{k}}$ is the unit wavevector, $\hat{\boldsymbol{k}} = \boldsymbol{k}/||\boldsymbol{k}||$, for which $||\boldsymbol{k}||$ is taken as the principal square root of $\boldsymbol{k} \cdot \boldsymbol{k}$, $||\boldsymbol{k}|| \equiv (\boldsymbol{k} \cdot \boldsymbol{k})^{1/2}$.

4.2.2 Linearised Rankine–Hugoniot jump conditions

In the linear limit, we have derived a set of seven waves in an eigenvector basis to represent perturbations propagating through a multi-dimensional ideal MHD flow. Within the field of gas dynamics, an analogous decomposition of the Euler equations has been shown to provide a good approximation of weak turbulent fluctuations and their interactions in 3D supersonic flows [Kovasznay, 1953]. In the context of MHD, a similar type of analysis has been pursued in order to explore the much more extensive range of fluctuating modes present in electrically conductive turbulent flows [Cho and Lazarian, 2005]. If the flow field is also discontinuous, we find that the perturbed flow, and thus superposition of linear waves, must satisfy algebraic relations - known as the Rankine–Hugoniot jump conditions - given at the surface of the discontinuity. The perturbed shock system therefore becomes a boundary value problem, in which the amplitudes of waves diverging from the shock are obtained by solving a linearised form of the Rankine–Hugoniot jump conditions at the shock front. For a solution to be attainable the number of boundary conditions must match the number of unknowns in the system - if this condition is satisfied, the shock is stable with respect to shock-splitting, or "evolutionary". In MHD, we find that only the slow and fast shocks fulfill the evolutionary condition [Akhiezer et al., 1959], in which the unknown amplitudes of six waves diverging from the discontinuity and shock displacement match the seven boundary conditions given by MHD Rankine–Hugoniot relations.

If we define the upstream and downstream flows under the subscripts 1 and 2 respectively, the following inequalities denote fast:

$$V_{fn,1} < \bar{u}_{n,1}, \qquad V_{An,2} < \bar{u}_{n,2} < V_{fn,2}, \tag{4.2.24}$$

and slow shocks:

$$V_{sn,1} < \bar{u}_{n,1} < V_{An,1}, \qquad \bar{u}_{n,2} < V_{sn,2}, \tag{4.2.25}$$

where $\bar{u}_n$, is the mean fluid velocity normal to the shock surface, and V_{An}, V_{fn}, V_{sn}, denote the wave phase speeds for a wavevector aligned parallel to the shock normal direction for the Alfvén mode, $V_{An} = b_n = \bar{B}_n/\sqrt{\bar{\rho}}$, and fast and slow magneto–acoustic modes:

$$V_{fn,sn} = \left(\frac{1}{2}\left[(b^2 + c_o^2) \pm \sqrt{(b^2 + c_o^2)^2 - 4(b_n c_o)^2}\right]\right)^{1/2}. \tag{4.2.26}$$

In the absence of a perturbation, the planar shock travels at constant velocity, $\bar{\boldsymbol{u}}_s$, as a result of the base flow choice (steady and piece–wise uniform). Without loss of generality, we define a Cartesian coordinate system in which the origin, ($x = 0$, $y = 0$, $z = 0$), is tracking the unperturbed shock front and the shock normal is aligned with the x-axis, $\bar{\boldsymbol{u}}_s = \bar{u}_s \boldsymbol{e}_x$. Consequently, we can express the displacement of the shock surface in x due to an incident linear perturbation as $x_s = \epsilon x'_s$, where x'_s takes the form of a plane wave:

$$x'_s = x'_s(y, z, t) = \delta_s \exp\left[\mathrm{i}(k_y y + k_z z - \omega t)\right], \tag{4.2.27}$$

where δ_s is the unknown amplitude of displacement to be found.

As such, we can derive the unit normal vector to the perturbed shock surface as:

$$\hat{\boldsymbol{n}} = \frac{\boldsymbol{\nabla}\psi}{\|\boldsymbol{\nabla}\psi\|} = \left[1, -\mathrm{i}k_y x_s, -\mathrm{i}k_z x_s\right]^\intercal, \tag{4.2.28}$$

where ψ is a function describing the surface of the discontinuity, $\psi(x_s, y, t, z) = x_s - \epsilon x'_s(y, z, t) = 0$.

We define the perturbed shock velocity, $\boldsymbol{u}_s$, as:

$$\boldsymbol{u}_s = \frac{\partial \boldsymbol{x}_s}{\partial t} = \left[-\mathrm{i}\omega x_s, \dot{y}, \dot{z}\right]^\intercal, \tag{4.2.29}$$

where $\boldsymbol{x}_s$ is the instantaneous shock position, $\boldsymbol{x}_s = [x_s,\, y,\, z]$.

The instantaneous fluid velocity relative to the perturbed shock is now given as, $\tilde{\boldsymbol{u}} = \bar{\boldsymbol{u}} + \epsilon \boldsymbol{u}' - \boldsymbol{u}_s$. Consequently, we define the normal component of the fluid velocity relative to the shock as:

$$u_n = \bar{u}_n + \epsilon u'_n = (\bar{\boldsymbol{u}} + \epsilon \boldsymbol{u}' - \boldsymbol{u}_s) \cdot \hat{\boldsymbol{n}}, \tag{4.2.30}$$

and the tangential velocity component,

$$\boldsymbol{u}_t = \bar{\boldsymbol{u}}_t + \epsilon \boldsymbol{u}'_t = (\bar{\boldsymbol{u}} + \epsilon \boldsymbol{u}' - \boldsymbol{u}_s) - (\bar{u}_n + \epsilon u'_n)\hat{\boldsymbol{n}}. \tag{4.2.31}$$

Analogously, we define the normal component of the magnetic field as:

$$B_n = \bar{B}_n + \epsilon B'_n = (\bar{\boldsymbol{B}} + \epsilon \boldsymbol{B}') \cdot \hat{\boldsymbol{n}}, \tag{4.2.32}$$

and the tangential magnetic field component,

$$\boldsymbol{B}_t = \bar{\boldsymbol{B}}_t + \epsilon \boldsymbol{B}'_t = (\bar{\boldsymbol{B}} + \epsilon \boldsymbol{B}') - (\bar{B}_n + \epsilon B'_n)\hat{\boldsymbol{n}}. \tag{4.2.33}$$

Applying (4.2.30) - (4.2.33) to (4.1.11)-(4.1.15) and retaining only first order perturbations in ϵ, we find the mass, momentum, energy and induction equations in the Rankine–Hugoniot jump conditions reduce to the following form (assuming a perfect gas) :

$$[\![\bar{\rho}u'_n + \bar{u}_n\rho']\!] = 0, \tag{4.2.34}$$

$$[\![p' + 2\bar{\rho}\bar{u}_n u'_n + \bar{u}_n^2\rho' + \bar{\boldsymbol{B}}_t \cdot \boldsymbol{B}'_t]\!] = 0, \tag{4.2.35}$$

$$[\![\bar{\rho}\bar{u}_n \boldsymbol{u}'_t + \bar{\boldsymbol{u}}_t(\bar{\rho}u'_n + \bar{u}_n\rho') - (\bar{B}_n\boldsymbol{B}'_t + \bar{\boldsymbol{B}}_t B'_n)]\!] = \boldsymbol{0}, \tag{4.2.36}$$

$$[\![(\gamma/(\gamma-1))\{p'/\bar{\rho} - \bar{p}\rho'/\bar{\rho}^2\}]\!] + [\![\bar{u}_n u'_n]\!] -$$
$$[\![(\bar{u}_n^2\bar{B}_t^2/\bar{B}_n^3)B'_n - (\bar{u}_n\bar{B}_t^2/\bar{B}_n^2)u'_n - \bar{u}_n^2\bar{\boldsymbol{B}}_t \cdot \boldsymbol{B}'_t/\bar{B}_n^2]\!] = 0, \tag{4.2.37}$$

$$[\![\bar{u}_n\boldsymbol{B}'_t + \bar{\boldsymbol{B}}_t u'_n - \bar{B}_n\boldsymbol{u}'_t - \bar{\boldsymbol{u}}_t B'_n]\!] = \boldsymbol{0}. \tag{4.2.38}$$

From the theory of co–planarity, it is possible to show that any shock wave can be reduced to two dimensions on a plane containing both the upstream and downstream velocity and magnetic fields [Landau and Lifschitz, 1984]. Without loss of generality, we consider a case in which the mean velocity and magnetic fields are located in the $x-y$ plane, $\bar{\boldsymbol{u}} = [\bar{u},\, \bar{v},\, 0]^\intercal$ and $\bar{\boldsymbol{B}} = [\bar{B}_x,\, \bar{B}_y,\, 0]^\intercal$. Consequently, the normal and tangential components of the mean velocity and magnetic field are defined as:

$$\bar{u}_n = \bar{u}, \qquad \bar{\boldsymbol{u}}_t = [0,\, \bar{v},\, 0]^\intercal, \tag{4.2.39}$$
$$\bar{B}_n = \bar{B}_x, \qquad \bar{\boldsymbol{B}}_t = [0,\, \bar{B}_y,\, 0]^\intercal,$$

and the perturbations to the base flow:

$$u'_n = u' - u'_s\left(1 - \frac{k_y\bar{v}}{\omega}\right), \quad \boldsymbol{u}'_t = \left[-u'_s\frac{k_y\bar{v}}{\omega},\, v' - \dot{y} - u'_s\frac{k_y\bar{u}}{\omega},\, w' - \dot{z} - u'_s\frac{k_z\bar{u}}{\omega}\right]^\intercal, \tag{4.2.40}$$

$$B'_n = B'_x + u'_s\frac{k_y\bar{B}_y}{\omega}, \qquad \boldsymbol{B}'_t = \left[-u'_s\frac{\bar{B}_y k_y}{\omega},\, B'_y - u'_s\frac{k_y\bar{B}_x}{\omega},\, B'_z - u'_s\frac{k_z\bar{B}_x}{\omega}\right]^\intercal, \tag{4.2.41}$$

where u'_s is the x-component of the perturbation to the shock velocity, $u'_s = -\mathrm{i}\omega x'_s$.

Note the following relations, $\beta_n = 2\bar{p}/\bar{B}_x^2$ and $r_n \equiv r_x = b_x/c_o = \bar{B}_x/\sqrt{\gamma\bar{p}}$.

Using (4.2.39), (4.2.40) and (4.2.41), we reduce the linearised Rankine–Hugoniot conditions in the $x-y$ plane to the following compact vector form:

$$\mathbf{T}_2\boldsymbol{\mu}'_2 + \boldsymbol{R}\delta_s = \mathbf{T}_1\boldsymbol{\mu}'_1, \tag{4.2.42}$$

where,

$$\mathbf{T} = \begin{bmatrix} \bar{u} & \bar{\rho} & 0 & 0 & 0 & 0 & 0 & 0 \\ \bar{u}^2 & 2\bar{\rho}\bar{u} & 0 & 0 & 1 & 0 & \bar{B}_y & 0 \\ \bar{v}/\bar{\rho} & \bar{v}/\bar{u} & 1 & 0 & 0 & -\bar{B}_y/(\bar{\rho}\bar{u}) & -\bar{B}_x/(\bar{\rho}\bar{u}) & 0 \\ 0 & 0 & 0 & 1 & 0 & 0 & 0 & -\bar{B}_x/(\bar{\rho}\bar{u}) \\ -c_o^2/\bar{\rho}(\gamma-1) & \bar{u}\bar{B}^2/\bar{B}_x^2 & 0 & 0 & \gamma/\bar{\rho}(\gamma-1) & -\bar{u}^2\bar{B}_y^2/\bar{B}_x^3 & \bar{u}^2\bar{B}_y/\bar{B}_x^2 & 0 \\ 0 & \bar{B}_y & -\bar{B}_x & 0 & 0 & -\bar{v} & \bar{u} & 0 \\ 0 & 0 & 0 & -\bar{B}_x & 0 & 0 & 0 & \bar{u} \end{bmatrix},$$

$$\boldsymbol{R} = \begin{bmatrix} \mathrm{i}[\![\bar{\rho}(\omega - \bar{v}k_y)]\!] \\ -\mathrm{i}\bar{\rho}\bar{u}[\![\bar{v}k_y]\!] \\ \mathrm{i}[\![\omega\bar{v}/\bar{u}]\!] + \mathrm{i}[\![k_y(\bar{u} - \bar{v}^2/\bar{u} + \bar{B}_y^2/(\bar{\rho}\bar{u}))]\!] \\ \mathrm{i}[\![k_z\bar{u}]\!] \\ \mathrm{i}(1/\bar{B}_x^2)[\![\omega\bar{B}^2\bar{u}]\!] - \mathrm{i}[\![k_y(\bar{u}\bar{B}^2/\bar{B}_x^3)(\bar{v}\bar{B}_x - \bar{u}\bar{B}_y)]\!] \\ \mathrm{i}[\![\omega\bar{B}_y]\!] \\ 0 \end{bmatrix}.$$

4.2.3 Fast shock linear interaction problem

In the present study we will restrict the refraction problem to the interaction of an entropy disturbance with a fast MHD shock. Similar to the gasdynamic shock refraction problem, all refracted eigenmodes propagate on the downstream side of the shock. In three dimensions, the refracted modes consist of the forward/backward slow, forward/backward Alfvén, forward fast and entropy modes. If we also assume no upstream propagating eigenmodes impinge on the downstream side of the shock, the refraction problem is defined by:

(i) The continuous forcing of a unitary entropy mode at a prescribed frequency on the upstream side of the shock (i.e. $x < x_s$):

$$\boldsymbol{\mu}_1' = \boldsymbol{\xi}_1 \mathrm{e}^{\mathrm{i}[\boldsymbol{k}_1 \cdot \boldsymbol{x} - \omega t]}, \tag{4.2.43}$$

in which $\boldsymbol{\xi}_1 \equiv \boldsymbol{e}_1$ (where $\boldsymbol{e}_1$ is the entropy eigenvector) and $\boldsymbol{k}_1 \equiv [k_{x,1},\, k_y,\, k_z]^\intercal$ is such that $\boldsymbol{k}_1 \cdot \bar{\boldsymbol{u}}_1 = \omega$.

(ii) Perturbations on the downstream side ($x > x_s$) decomposed into eigenmodes leaving the shock:

$$\begin{aligned} \boldsymbol{\mu}_2' = \boldsymbol{\xi}_E \mathrm{e}^{[\mathrm{i}(\boldsymbol{k}_E \cdot \boldsymbol{x} - \omega t)]} \quad + \quad \boldsymbol{\xi}_{f+} \mathrm{e}^{[\mathrm{i}(\boldsymbol{k}_{f+} \cdot \boldsymbol{x} - \omega t)]} \quad + \\ + \quad \boldsymbol{\xi}_{s+} \mathrm{e}^{[\mathrm{i}(\boldsymbol{k}_{s+} \cdot \boldsymbol{x} - \omega t)]} \quad + \quad \boldsymbol{\xi}_{s-} \mathrm{e}^{[\mathrm{i}(\boldsymbol{k}_{s-} \cdot \boldsymbol{x} - \omega t)]} + \\ + \quad \boldsymbol{\xi}_{A+} \mathrm{e}^{[\mathrm{i}(\boldsymbol{k}_{A+} \cdot \boldsymbol{x} - \omega t)]} \quad + \quad \boldsymbol{\xi}_{A-} \mathrm{e}^{[\mathrm{i}(\boldsymbol{k}_{A-} \cdot \boldsymbol{x} - \omega t)]}, \end{aligned} \tag{4.2.44}$$

where $\boldsymbol{k}_\mu \equiv [k_{x,\mu},\, k_y,\, k_z]^\intercal$, such that $\boldsymbol{k}_\mu \cdot \bar{\boldsymbol{u}} = \omega - \omega_{0\mu}$ and $\boldsymbol{\xi}_\mu \equiv \chi_\mu \boldsymbol{e}_\mu$, in which χ_μ is the unknown refraction coefficient and $\boldsymbol{e}_\mu$ is the eigenvector of a given mode, computed as a function of the respective refracted wavevector and downstream base flow ($\bar{\boldsymbol{\mu}}_2$).

We relate the unknown refraction coefficients, χ_μ, to the base flow properties and impinging entropy mode by injecting equations (4.2.43) and (4.2.44) into the linearised Rankine–Hugoniot jump conditions, (4.2.42), given at the shock location. Consequently, it is possible to then reduce the system of equations that define the shock refraction problem into the following compact form:

$$\mathbf{L} \cdot \boldsymbol{Y} = \boldsymbol{X}, \tag{4.2.45}$$

where vector $\boldsymbol{Y}$ is a complex–valued function of the six unknown complex refraction coefficients and shock displacement amplitude in $\mathbb{Z}^7$, the scattering matrix, $\mathbf{L}$, is a complex–valued function of the base flow properties, angular frequency and refracted wave vectors in $\mathbb{Z}^{7\times 7}$, and the input vector, $\boldsymbol{X}$, is a real–valued function of the base flow properties in $\mathbb{R}^7$. $\mathbf{L}$ is the result of a linear mapping process from primitive variable to eigenmode space via the eigenvector of each respective mode (see appendix B.1 for full derivation). With respect to the Alfvén and magneto–acoustic modes, each eigenvector is a function of the base flow properties and wavevector direction. The base flow is known a-priori, as such, to compute $\mathbf{L}$, only the wavevector of each refracted mode is to be found. The above system, (4.2.45), is then inverted, provided that $\det(\mathbf{L}) \neq 0$.

4.2.3.1 Decoupled entropy/magneto–acoustic mode excitation

If analysis is restricted to a flow configuration in which the incident disturbance wavevector is co–planar with the mean velocity and magnetic fields in the $x-y$ plane, $\boldsymbol{k} = [k_x, k_y, 0]$, the refraction problem decouples into in–plane (x, y) magneto–acoustic/entropy (see figure 4.5) and out–of–plane (z) Alfvén mode excitations respectively. In this configuration, the mean normal and tangential components of the velocity and magnetic fields remain the same as given in (4.2.33), however, the perturbations to the base flow reduce to the form:

$$u'_n = u' - u'_s\left(1 - \frac{k_y \bar{v}}{\omega}\right), \quad \boldsymbol{u}'_t = \left[-u'_s \frac{k_y \bar{v}}{\omega},\, v' - \dot{y} - u'_s \frac{k_y \bar{u}}{\omega},\, w' - \dot{z}\right]^\intercal, \tag{4.2.46}$$

$$B'_n = B'_x + u'_s \frac{k_y \bar{B}_y}{\omega}, \qquad \boldsymbol{B}'_t = \left[-u'_s \frac{\bar{B}_y k_y}{\omega},\, B'_y - u'_s \frac{k_y \bar{B}_x}{\omega},\, B'_z\right]^\intercal. \tag{4.2.47}$$

The boundary conditions governing the entropy/magneto–acoustic mode excitation are given by the linearised Rankine–Hugoniot jump conditions in the $x-y$ plane:

$$\mathbf{T}_2 \boldsymbol{\mu}'_{xy,2} + \boldsymbol{R}\delta_s = \mathbf{T}_1 \boldsymbol{\mu}'_{xy,1}, \tag{4.2.48}$$

where $\boldsymbol{\mu}'_{xy} = [\rho',\, u',\, v',\, p',\, B'_x,\, B'_y]^\intercal$,

$$\mathbf{T} = \begin{bmatrix} \bar{u} & \bar{\rho} & 0 & 0 & 0 & 0 \\ \bar{u}^2 & 2\bar{\rho}\bar{u} & 0 & 1 & 0 & \bar{B}_y \\ \bar{v}/\bar{\rho} & \bar{v}/\bar{u} & 1 & 0 & -\bar{B}_y/(\bar{\rho}\bar{u}) & -\bar{B}_x/(\bar{\rho}\bar{u}) \\ -c_o^2/\bar{\rho}(\gamma-1) & \bar{u}\bar{B}^2/\bar{B}_x^2 & 0 & \gamma/\bar{\rho}(\gamma-1) & -\bar{u}^2\bar{B}_y^2/\bar{B}_x^3 & \bar{u}^2\bar{B}_y/\bar{B}_x^2 \\ 0 & \bar{B}_y & -\bar{B}_x & 0 & -\bar{v} & \bar{u} \end{bmatrix},$$

$$\boldsymbol{R} = \begin{bmatrix} \mathrm{i}[\![\bar{\rho}(\omega - \bar{v}k_y)]\!] \\ -\mathrm{i}\bar{\rho}\bar{u}[\![\bar{v}k_y]\!] \\ \mathrm{i}[\![\omega\bar{v}/\bar{u}]\!] + \mathrm{i}[\![k_y(\bar{u} - \bar{u}_y^2/\bar{u} + \bar{B}_y^2/(\bar{\rho}\bar{u}))]\!] \\ \mathrm{i}(1/\bar{B}_x^2)[\![\omega\bar{B}^2\bar{u}]\!] - [\![k_y(\bar{u}\bar{B}^2/\bar{B}_x^3)(\bar{v}\bar{B}_x - \bar{u}\bar{B}_y)]\!] \\ \mathrm{i}[\![\omega\bar{B}_y]\!] \end{bmatrix}.$$

The refraction problem is now effectively two–dimensional and is defined by:

(i) The displacement of the shock surface, $x_s = \epsilon x_s'$, where x_s' takes the form:

$$x_s' = x_s'(y,t) = \delta_s \exp\left[\mathrm{i}(k_y y - \omega t)\right], \tag{4.2.49}$$

where, δ_s, is the unknown amplitude of shock displacement.

(ii) The continuous forcing by a unitary entropy mode at a prescribed frequency on the upstream side of the shock (i.e. $x < x_s$):

$$\boldsymbol{\mu}_{xy,1}' = \boldsymbol{\xi}_1^{xy} \mathrm{e}^{\mathrm{i}[\boldsymbol{k}_1 \cdot \boldsymbol{x} - \omega t]}, \tag{4.2.50}$$

in which $\boldsymbol{\xi}_1^{xy} = [1,\, 0,\, 0,\, 0,\, 0,\, 0]^\intercal$ and $\boldsymbol{k}_1 \equiv [k_{x,1},\, k_y,\, 0]^\intercal$ is such that $\boldsymbol{k}_1 \cdot \bar{\boldsymbol{u}}_1 = \omega$.

(iii) Perturbations on the downstream side ($x > x_s$) decomposed into entropy/magneto–acoustic eigenmodes leaving the shock:

$$\begin{aligned} \boldsymbol{\mu}_{xy,2}' = \boldsymbol{\xi}_E^{xy} \mathrm{e}^{[\mathrm{i}(\boldsymbol{k}_E \cdot \boldsymbol{x} - \omega t)]} \quad + \quad \boldsymbol{\xi}_{f+}^{xy} \mathrm{e}^{[\mathrm{i}(\boldsymbol{k}_{f+} \cdot \boldsymbol{x} - \omega t)]} \quad + \\ + \quad \boldsymbol{\xi}_{s+}^{xy} \mathrm{e}^{[\mathrm{i}(\boldsymbol{k}_{s+} \cdot \boldsymbol{x} - \omega t)]} \quad + \quad \boldsymbol{\xi}_{s-}^{xy} \mathrm{e}^{[\mathrm{i}(\boldsymbol{k}_{s-} \cdot \boldsymbol{x} - \omega t)]}, \end{aligned} \tag{4.2.51}$$

where $\boldsymbol{k}_\mu \equiv [k_{x,\mu},\, k_y,\, 0]^\intercal$, such that $\boldsymbol{k}_\mu \cdot \bar{\boldsymbol{u}} = \omega - \omega_{0\mu}$ and $\boldsymbol{\xi}_\mu^{xy} \equiv \chi_\mu \boldsymbol{e}_\mu^{xy}$, in which $\boldsymbol{\xi}_\mu^{xy}$ is a vector of wave amplitudes of the primitive variables in the $x-y$ plane, χ_μ is the unknown refraction coefficient and $\boldsymbol{e}_\mu^{xy}$ is the eigenvector of a given mode, redefined in the $x-y$ plane, for the entropy mode, $\boldsymbol{e}_E^{xy} = [1,\, 0,\, 0,\, 0,\, 0,\, 0]^\intercal$, and the magneto–acoustic modes, $\boldsymbol{e}_{f,s\pm}^{xy} = [\rho_{f,s\pm}',\, u_{f,s\pm}',\, v_{f,s\pm}',\, p_{f,s\pm}',\, B_{x,f,s\pm}',\, B_{y,f,s\pm}']^\intercal$, in which $u_{f,s\pm}'$, $v_{f,s\pm}'$, $p_{f,s\pm}'$, $B_{x,f,s\pm}'$, $B_{y,f,s\pm}'$ have been extracted from the magneto–acoustic eigenvector definition in (4.2.18) and are computed as a function of the respective refracted wavevector and downstream base flow ($\bar{\boldsymbol{\mu}}_2$).

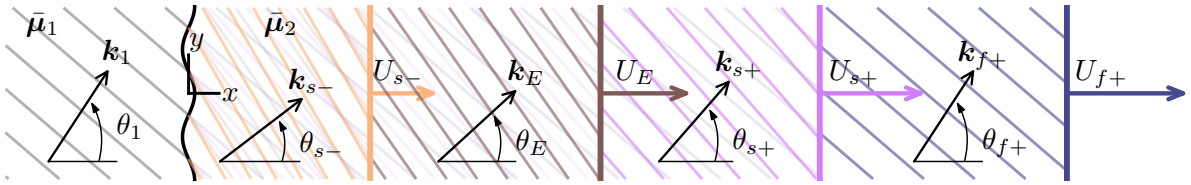


Fig. 4.5: Unitary entropy mode prescribed with ($\boldsymbol{k}_1$, θ_1) refracted at fast MHD shock in decoupled system generating backward slow mode (orange), ($\boldsymbol{k}_{s-}$, θ_{s-}); entropy mode (brown), ($\boldsymbol{k}_E$, θ_E); forward slow mode (purple), ($\boldsymbol{k}_{s+}$, θ_{s+}); forward fast mode (blue), ($\boldsymbol{k}_{f+}$, θ_{f+}). Normal wave speeds, U_μ, defined as, $U_{s-} = \bar{u}_2 - V_{sn,2}$, $U_E = \bar{u}_2$, $U_{s+} = \bar{u}_2 + V_{sn,2}$, $U_{s-} = \bar{u}_2 + V_{fn,2}$.

Analogous to (4.2.45) we relate the unknown refraction coefficients, χ_μ, to the base flow properties and impinging entropy mode by injecting equations (4.2.50) and (4.2.51) into the two–dimensional linearised Rankine–Hugoniot jump conditions, (4.2.48), given at the shock location:

$$\mathbf{L} \cdot \boldsymbol{Y} = \boldsymbol{X}, \tag{4.2.52}$$

where vector $\boldsymbol{Y}$ is a complex–valued function of the four unknown complex refraction coefficients and shock displacement amplitude in $\mathbb{Z}^5$, the scattering matrix, $\mathbf{L}$, is a complex–valued function of the base flow properties, angular frequency and refracted wave vectors in $\mathbb{Z}^{5\times5}$, and the input vector, $\boldsymbol{X}$, is a real–valued function of the base flow properties in $\mathbb{R}^5$ (see appendix B.2 for full derivation). As in three dimensions, the normal components of the refracted wavevectors must be found in order to compute $\mathbf{L}$ and thus solve system, (4.2.52).

4.2.3.2 Dispersion relations in a discontinuous medium

To solve the three–dimensional and decoupled shock refraction problem for the unknown refraction coefficients and shock displacement amplitude, as defined in (4.2.45) and (4.2.52) respectively, the refracted wavevector components must be fully defined. If we consider the refraction of a single plane wave across a discontinuity, from Snell's laws [Barton, 1939], we can set the angular frequency and wavevector components tangential to the (unperturbed) shock surface, $\boldsymbol{k}_t$, as continuous. Consequently, to fully describe the refracted wavevector, only the normal component is left to be found. In the present configuration, the unperturbed shock surface is located at $x = 0$, as such, the normal wavevector component is given by k_x, and the tangential components by $\boldsymbol{k}_t = [0,\, k_y,\, k_z]^\intercal$ and $\boldsymbol{k}_t = [0,\, k_y,\, 0]^\intercal$ in the three–dimensional and decoupled perturbed shock systems respectively. The normal and tangential components of the incident wavevector, $\boldsymbol{k}_1$, are defined with respect to the incident wavevector magnitude, k_1, and angles of incidence, θ_1 (positive in the anti–clockwise direction about $\mathbf{e}_z$), and Φ_1 (positive in the anti–clockwise direction about $\mathbf{e}_y$); $k_{x,1} \equiv k_1 \cos\theta_1$ and $\boldsymbol{k}_t \equiv k_1[0,\, \sin\theta_1 \cos\Phi_1,\, \sin\theta_1 \sin\Phi_1]^\intercal$ respectively ($\Phi_1 = 0$ in the decoupled system), where $k_1 \equiv ||\boldsymbol{k}_1||$. To compute the normal wavevector component of a downstream refracted mode, $k_{x,\mu}$, we solve the dispersion

relations (section 4.2.1) in the post–shock flow for a given $(\omega, \boldsymbol{k}_t)$ pair. From the plane wave definition given in (4.2.6), we find that if $k_{x,\mu}$ is complex-valued, the imaginary normal wavevector component represents the decay/growth rate of a disturbance as it propagates in the x-direction whereas the real component contributes to the phase:

$$\boldsymbol{\mu}' = \boldsymbol{\xi}\left(\mathrm{e}^{\mathrm{i}[\mathrm{Re}[k_{x,\mu}]x+\boldsymbol{k}_t\cdot\boldsymbol{x}-\omega t]}\right)\left(\mathrm{e}^{-\mathrm{Im}[k_{x,\mu}]x}\right). \tag{4.2.53}$$

However, a condition of evolutionary MHD shocks is the assumption that the amplitude of all waves transmitted by the perturbed shock must be finite at infinity - i.e. no transport of "infinite" energy. As such, only solutions which satisfy this boundary condition ($\mathrm{Im}\left[k_{x,\mu}\right] \geq 0$) may be permitted into the system of equations given in (4.2.34) - (4.2.38). Analogous to acoustic modes in gas dynamics, we find that the solutions to the dispersion relations of the magneto–acoustic modes in a discontinuous medium can exist in complex space. The effect of a complex solution on the evolutionarity of an MHD shock and the linear interaction problem was first broached by Kontorovich [Kontorovich, 1959]. Kontorovich noted that for incident waves above a "critical" incidence angle there existed complex conjugate solutions for the fast magneto–acoustic modes. One of the solutions is always discarded as it disobeys boundary condition at $x = +\infty$ whereas the other solution - corresponding to the forward fast magneto–acoustic mode - represents a "surface wave" that decays as it penetrates the downstream flow. For an incidence angle exactly equal to the critical value ($(\theta_1, \Phi_1) = (\theta^{c+}, \Phi^{c+})$ for $\theta_1, \Phi_1 \geq 0$ and $(\theta_1, \Phi_1) = (\theta^{c-}, \Phi^{c-})$ for $\theta_1, \Phi_1 < 0$), the normal component of the forward fast magneto–acosutic mode group velocity reduces to zero, $V^g_{x,f+} = 0$. Additionally, Kontorovich noted that regardless of the incidence angle (and emergence of surface waves), the number of refracted waves and thus evolutionarity of the shock is maintained as long as condition (4.2.24) or (4.2.25) is satisfied [Kontorovich, 1959].

Using (4.2.11), we find that the normal component of the downstream entropy wavevector is always real:

$$k_{x,E} = \frac{\omega}{\bar{u}_2} - k_y\delta_2, \tag{4.2.54}$$

where δ_2 is the ratio between the downstream tangential and normal mean velocity components, $\delta_2 = \bar{v}_2/\bar{u}_2$.

We substitute (4.2.15) into (4.2.11) to expand the dispersion relationship for Alfvén waves into a quadratic in terms of normal component of the Alfvén wavevector, $k_{x,A}$:

$$[\bar{u}_2^2 - b_{x,2}^2]k_{x,A}^2 - 2\left[\bar{u}_2(\omega - k_y\bar{v}_2) + k_y b_{x,2}b_{y,2}\right]k_{x,A} + \left[(\omega - k_y\bar{v}_2)^2 - k_y^2 b_{y,2}^2\right] = 0. \tag{4.2.55}$$

We obtain two real solutions to (4.2.55):

$$k_{x,A(1,2)} = \frac{M_2 k_{x,E} \pm r_{x,2}\varepsilon_2 k_y}{M_2 \mp r_{x,2}}, \tag{4.2.56}$$

where ε_2 is the ratio between the downstream tangential and normal mean magnetic field components, $\varepsilon_2 = \bar{B}_{y,2}/\bar{B}_x$, and $r_{x,2}$ is the $x-$component of the ratio between the downstream Alfvén velocity and sound speed, $\boldsymbol{r}_2 = \boldsymbol{b}_2/c_{o,2}$.

To find the normal component of the downstream magneto–acoustic wavevectors, $k_{x,m}$, we substitute (4.2.17) into (4.2.11) which produces a quartic in terms of $k_{x,m}$:

$$A_4 k_{x,m}^4 + A_3 k_{x,m}^3 + A_2 k_{x,m}^2 + A_1 k_{x,m} + A_o = 0, \tag{4.2.57}$$

where the coefficients, A_i, are:

$$A_4 = \bar{u}_2^4 - \bar{u}_2^2(c_{o,2}^2 + b_2^2) + c_{o,2}^2 b_{x,2}^2, \tag{4.2.58}$$

$$A_3 = -4\bar{u}_2^3(\omega - k_y\bar{v}_2) + 2\bar{u}_2(\omega - k_y\bar{v}_2)(c_{o,2}^2 + b_2^2) + 2k_y c_{o,2}^2 b_{x,2} b_{y,2}, \tag{4.2.59}$$

$$A_2 = 6\bar{u}_2^2(\omega - k_y\bar{v}_2)^2 - (\omega - k_y\bar{v}_2)^2(c_{o,2}^2 + b_2^2) - \bar{u}_2^2 k_t^2(c_{o,2}^2 + b_2^2) + k_y^2 c_{o,2}^2 b_{y,2}^2 + k_t^2 c_{o,2}^2 b_{x,2}^2, \tag{4.2.60}$$

$$A_1 = -4\bar{u}_2(\omega - k_y\bar{v}_2)^3 + 2\bar{u}_2 k_t^2(\omega - k_y\bar{v}_2)(c_{o,2}^2 + b_2^2) + 2k_y k_t^2 c_{o,2}^2 b_{x,2} b_{y,2}, \tag{4.2.61}$$

$$A_0 = (\omega - k_y\bar{v}_2)^4 - k_t^2(\omega - k_y\bar{v}_2)^2(c_{o,2}^2 + b_2^2) + k_y^2 k_t^2 c_{o,2}^2 b_{y,2}^2, \tag{4.2.62}$$

in which k_t is the magnitude of the tangential wavevector, $k_t = ||\boldsymbol{k}_t||$.

We can simplify the above formula to:

$$F_m(k_{x,m}) = \tilde{A}_4 k_{x,m}^4 + \tilde{A}_3 k_{x,m}^3 + \tilde{A}_2 k_{x,m}^2 + \tilde{A}_1 k_{x,m} + \tilde{A}_o = 0, \tag{4.2.63}$$

where the normalised coefficients, $\tilde{A} = A/c_{o,2}^4$, are computed as

$$\tilde{A}_4 = M_2^4 - M_2^2(1 + r_2^2) + r_{x,2}^2, \tag{4.2.64}$$

$$\tilde{A}_3 = -4M_2^4 k_{x,E} + 2M_2^2(1 + r_2^2)k_{x,E} + 2k_y r_{x,2}^2 \varepsilon_2^2, \tag{4.2.65}$$

$$\tilde{A}_2 = 6M_2^4 k_{x,E}^2 - M_2^2 k_{x,E}^2(1 + r_2^2) - M_2^2 k_t^2(1 + r_2^2) + k_y^2 r_{x,2}^2 \varepsilon_2^2 + k_t^2 r_{x,2}^2, \tag{4.2.66}$$

$$\tilde{A}_1 = -4M_2^4 k_{x,E}^3 + 2M_2^2 k_{x,E} k_t^2(1 + r_2^2) + 2k_y k_t^2 r_{x,2}^2 \varepsilon_2, \tag{4.2.67}$$

$$\tilde{A}_0 = M_2^4 k_{x,E}^4 - M_2^2 k_{x,E}^2 k_t^2(1 + r_2^2) + k_y^2 k_t^2 r_{x,2}^2 \varepsilon_2^2. \tag{4.2.68}$$

To determine the nature of the roots of the above quartic, we first note that its behaviour at the extremes of $k_{x,m}$; $k_{x,m} \in \{-\infty, +\infty\}$ - is governed by the coefficient $\tilde{A}_4$. It is possible to show that $\tilde{A}_4$ is always negative downstream of a fast shock, $\hat{V}_{fn,2} > M_2 > \hat{V}_{sn,2}$:

$$\tilde{A}_4 = (\hat{V}_{fn,2}^2 - M_2^2) \cdot (\hat{V}_{sn,2}^2 - M_2^2) < 0, \tag{4.2.69}$$

where $\hat{V}_{fn,2}$ and $\hat{V}_{sn,2}$ refer to the normalised downstream normal fast and slow magneto–acoustic wave speeds,

$$\hat{V}^2_{fn,sn} = \left(\frac{V_{fn,sn}}{c_o}\right)^2 = \frac{1}{2}(r^2 + 1 \pm \sqrt{(r^2+1)^2 - 4r_x^2}). \tag{4.2.70}$$

As such, we find that $F_m(k_{x,m})$ is negative for the values $k_{x,m} = \pm\infty$. Consequently, if we consider solutions for which $k_{x,E}$ is finite - we can compute $F_m(k_{x,E})$ and check for changes in sign in the range $-\infty < k_{x,m} < +\infty$.

We find that $F_m(k_{x,E})$ is always positive,

$$F_m(k_{x,E}) = r^2_{x,2}[k_{x,E} + \varepsilon_2 k_y]^2 \cdot (k^2_{x,E} + k^2_t) > 0. \tag{4.2.71}$$

Combining the above result with (4.2.69), we conclude that there must be two changes of sign in the finite set of $k_{x,m}$. As such, the quartic, F_m, must have at least two real solutions. The two remaining roots of F_m are either real or complex conjugates.

Two methods exist to match each solution of (4.2.63) with the corresponding magneto–acoustic mode. For the first method we define the expression for the normalised tangential wavevector component:

$$\tilde{k}_{y,i} = \frac{k_y}{\omega/c_{o,i}} = \frac{\hat{k}_y}{\hat{V}_\mu + M_i[\hat{k}_x + \hat{k}_y\delta_i]}, \quad i = 1, 2, \tag{4.2.72}$$

where $\hat{k}_x$ and $\hat{k}_y$ are the unit wavevector components, $\hat{k}_x \equiv k_x/||\boldsymbol{k}||$, and, $\hat{k}_y \equiv k_y/||\boldsymbol{k}||$, respectively and $\hat{V}_\mu$ is the normalised phase speed, $\hat{V}_\mu = \omega_{0\mu}/(c_o||\boldsymbol{k}||)$. For an entropy mode incident on a normal shock, $\tilde{k}_{y,1}$ reduces to:

$$\tilde{k}_{y,1} = \frac{\tan\theta_1}{M_1}. \tag{4.2.73}$$

Therefore, if we note that, $\tilde{k}_{y,2} = R\tilde{k}_{y,1}$, it is possible to substitute solutions of $k_{x,m}$ into (4.2.72) for $\hat{V}_\mu = \hat{V}_{f+}$, $\hat{V}_\mu = \hat{V}_{s+}$ and $\hat{V}_\mu = \hat{V}_{s-}$, and find which expression of V_μ provides the correct value of $\tilde{k}_{y,1}$ for a given $k_{x,m}$.

In the second method the property of well–orderedness of the ideal MHD eigenvalues - $|\omega_{0f}| \geq |\omega_{0A}| \geq |\omega_{0s}| \geq |\omega_{0E}|$ - is applied to the dispersion relationship in the form:

$$k_{x,\mu} = \frac{\omega - k_y\bar{v}_2 - \omega_{0\mu}}{\bar{u}_2}. \tag{4.2.74}$$

Consequently, it is possible to show that if $\boldsymbol{k}_1 \cdot \bar{\boldsymbol{B}}_1 \geq 0$ and all four solutions to (4.2.52) are real:

$$k_{x,A-} \geq k_{x,s-} \geq k_{x,E} \geq k_{x,s+} \geq k_{x,A+} \geq k_{x,f+} \geq k_{x,f-}, \tag{4.2.75}$$

(note: $k_{x,A-} \equiv k_{x,A1}$ and $k_{x,A+} \equiv k_{x,A2}$) and if only two solutions are real:

$$k_{x,A-} \geq k_{x,s-} \geq k_{x,E} \geq k_{x,s+} \geq k_{x,A+}, \tag{4.2.76}$$

with $k_{x,f+}$ and $k_{x,f-}$ corresponding to the complex conjugate solutions of (4.2.52).

If $\boldsymbol{k}_1 \cdot \bar{\boldsymbol{B}}_1 \leq 0$, where all four solutions to (4.2.52) are real:

$$k_{x,A+} \geq k_{x,s+} \geq k_{x,E} \geq k_{x,s-} \geq k_{x,A-} \geq k_{x,f+} \geq k_{x,f-}, \tag{4.2.77}$$

and if only two solutions are real:

$$k_{x,A+} \geq k_{x,s+} \geq k_{x,E} \geq k_{x,s-} \geq k_{x,A-}, \tag{4.2.78}$$

with $k_{x,f+}$ and $k_{x,f-}$ corresponding to the complex conjugate solutions of (4.2.52).

The relations given in (4.2.75) - (4.2.78) can be used to order and subsequently match the four solutions of (4.2.52) to their respective magneto–acoustic modes.

4.2.4 Refraction coefficients: comparison with Westphal & McKenzie

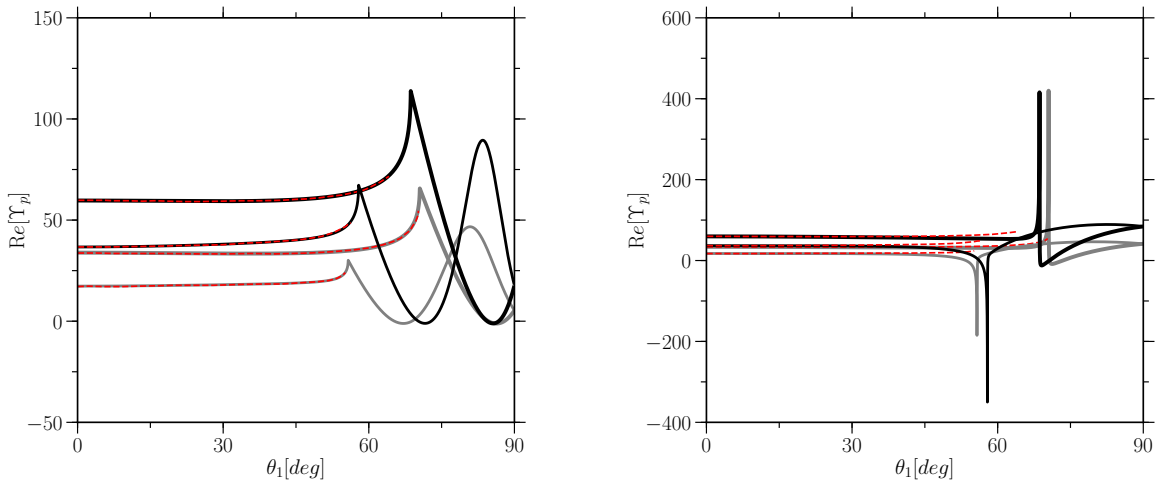
We define the pressure amplification factor, Υ_p, for a magneto–acoustic mode impinging on the upstream side of a shock in the decoupled system (see appendix B.2) as the ratio between the summed pressure fluctuation amplitudes of the incident and refracted modes:

$$\Upsilon_p = \xi_2^p / \xi_1^p = \frac{1}{p'_{in}} \left\{ \chi_{f+} p'_{f+} + \chi_{s+} p'_{s+} + \chi_{s-} p'_{s-} \right\}, \tag{4.2.79}$$

where subscript "in" corresponds to the incident magneto–acoustic mode (i.e. "$f+$", "$f-$","$s+$" or "$s-$").

Figure 4.6 shows the real part of Υ_p for the case of upstream fast magneto–acoustic waves incident on a parallel fast MHD shock at incidence angles above and below the critical value. Results from the LIA formulation derived in the present study are compared with those given in [Westphal and McKenzie, 1969]. The difference between results in figures 4.6a and 4.6b is a result of an error in the scattering matrix derived by the authors of [Westphal and McKenzie, 1969]. It was found that the shock velocity's contribution to the tangential momentum is missing a factor equal to the ratio of the pre– and post–shock speed of sounds, $R = c_{o,2}/c_{o,1}$. Further confirmation of this mistake is given in section 4.3 in which the corrected linear theory result is shown to match well with DNS results of entropy plane waves interacting with parallel MHD shocks. In approach of the critical angle, from figure 4.6 we observe the real part of the pressure amplification to increase/decrease for incident backward/forward fast magneto–acoustic waves. For incidence angles above the critical value, this effect reverses with the pressure amplification decreasing/increasing for

incident backward/forward fast magneto–acoustic waves until $\theta_1 = 90°$ at which the values coincide for the respective upstream Mach numbers.



(a) Incorrect LIA formulation

(b) Corrected LIA formulation

Fig. 4.6: Validating incidence angle, θ_1, dependency of real component of pressure amplification factor, Υ_p, for backward (thin line) and forward (thick line) fast magneto–acoustic waves incident on a parallel fast MHD shock at upstream Mach number, $M_1 = 8$ (grey) and, $M_1 = 11$ (black). LIA data from present study using the formulation in [Westphal and McKenzie, 1969] (a) and corrected (b). LIA data extracted from [Westphal and McKenzie, 1969] is also shown (red dashed line). [$r_1 = 5/8$, $\gamma = 5/3$].

4.2.5 Modal response of magneto–acoustic vorticity transport

Refraction coefficients for the decoupled entropy mode–fast shock interaction were derived in section 4.2.3.1. The coefficients are obtained from the base flow properties and mode of the impinging entropy disturbance. Consequently, for a given pre–shock state, the downstream perturbed flow can be fully described by computing the refraction coefficients for a full range of incident modes. In this section, we model the incident entropy disturbance as a two–dimensional plane wave and investigate the modal response of magneto–acoustic mode vorticity generation in the post–shock flowfield. We define the real part of the (z-component) vorticity transported by each respective magneto–acoustic wave, ω'_μ:

$$\begin{aligned}
\mathrm{Re}\left[\omega'_\mu\right] &= \mathrm{Re}\left[\frac{\partial(\xi^v_\mu \mathrm{e}^{[\mathrm{i}(\boldsymbol{k}_\mu\cdot\boldsymbol{x}-\omega t)]})}{\partial x} - \frac{\partial(\xi^u_\mu \mathrm{e}^{[\mathrm{i}(\boldsymbol{k}_\mu\cdot\boldsymbol{x}-\omega t)]})}{\partial y}\right], \\
&= \mathrm{Re}\left[\omega\Omega_\mu(\mathrm{i}\cos\left(\boldsymbol{k}^r_\mu\cdot\boldsymbol{x}-\omega t\right) - \sin\left(\boldsymbol{k}^r_\mu\cdot\boldsymbol{x}-\omega t\right))\right]\mathrm{e}^{-k^i_{x,\mu}x}, \\
&= -\omega\Big(\mathrm{Im}\left[\Omega_\mu\right]\cos\left(\boldsymbol{k}^r_\mu\cdot\boldsymbol{x}-\omega t\right) + \mathrm{Re}\left[\Omega_\mu\right]\sin\left(\boldsymbol{k}^r_\mu\cdot\boldsymbol{x}-\omega t\right)\Big)\mathrm{e}^{-k^i_{x,\mu}x}, \qquad (4.2.80)
\end{aligned}$$

where $\boldsymbol{k}^r_\mu \equiv \mathrm{Re}[\boldsymbol{k}_\mu]$, $k^i_{x,\mu} \equiv \mathrm{Im}[k_{x,\mu}]$, Ω_μ is the vorticity coefficient, $\Omega_\mu = \chi_\mu(\tilde{k}_{x,\mu}v'_\mu/c_{o,2} - \tilde{k}_y u'_\mu/c_{o,2})$, in which we also define the normalised normal wavenumber, $\tilde{k}_{x,\mu} = k_{x,\mu}/(\omega/c_o)$.

From (4.2.80) we find that the real and imaginary components of Ω_μ describe the out-of-phase and in-phase magneto–acoustic mode contributions to the post–shock vorticity field. As Ω_μ is a function of χ_μ and $\boldsymbol{e}_\mu$, we find that the modal response of magneto–acoustic vorticity generation exists in a parametric space fully described by the base flow and incidence angle of the impinging disturbance.

In section 4.1 we investigated steady–state MHD shocks and the three dimensionless degrees of freedom that exist in the upstream base flow (M_1, φ_1, $\beta_{n,1}$) through which to control the downstream state. The importance of the downstream flow in terms of magneto–acoustic vorticity transport lies primarily in the magnitude and direction of the mean magnetic field. Section 4.2.1 showed that the presence of solenoidal and irrotational fluctuating fluid motions (within the magneto–acoustic modes) is dependent on the both the ratio between Alfvén and sound speeds, r, as well as the alignment between the mean magnetic field and wavevector directions. It was shown that while Alfvén modes always carry vorticity regardless of the base flow, slow and fast magneto–acoustic modes exhibit maximum solenoidal fluid motions (and thus vorticity transport) in opposite flow regimes. In $r < 1$ ($\beta > 2/\gamma$) flows - i.e. the thermodynamic pressure is more influential than the magnetic pressure on wave behaviour - as the wavevector direction was varied with respect to the mean magnetic field, the slow mode was primarily transverse in nature (and fully transverse when wavevector and mean magnetic field were aligned) whereas the fast mode was mainly longitudinal (degenerating to a fully longitudinal mode at alignment). This flow regime can be thought as analogous to gas dynamics in which there exists the longitudinal acoustic mode (represented by the fast mode) propagating at faster speeds than the transverse vortical mode (represented by the slow modes) which is convected at the local flow speed. For the $r > 1$ ($\beta < 2/\gamma$) regime - i.e. mean magnetic field pressure dominates wave behaviour - transverse and longitudinal behaviour in the fast and slow magneto–acoustic modes was reversed for wavevector directions close to that of the mean magnetic field vector. From the Hugoniot curves displayed in section 4.1, it was found that through selecting $\beta_{n,1} = 2$, a compressive fast shock could be utilised to attain a wide range of low and high β_2 regimes if φ_1 was varied. Most notably, at $\beta_{n,1} = 2.0$, it was possible to select a compressive fast shock for which $r_2 = 1$ ($\beta = 2/\gamma$) - i.e. influence of magnetic and thermodynamic pressures on wave behaviour is similar. In the context of wave propagation, from 4.2.1, for flows where $r_2 = 1$, if a wavevector is aligned with the mean magnetic field, the system is "magnetosonic" as the slow, fast, Alfvén and sound speeds coincide. This presents an interesting case as both the slow and fast modes will exhibit longitudinal and transverse wave behaviour [Roe and Balsara, 1996]. The wavevector directions of the refracted modes were determined in section 4.2.3.2 by solving the dispersion relations for a given base flow and $(\omega, \boldsymbol{k}_t)$ pair. Through exploring the (M_1, φ_1, $\beta_{n,1}$, θ_1) parametric space, we can gain full insight into how a magnetic field may be utilised to control the strength and distribution of vorticity transported by magneto–acoustic modes generated in the interaction of broadband disturbances with a fast shock, thus aiding potential future studies

into predictions of post–shock turbulent kinetic energy and magnetic field amplification in MHD SWTIs.

To quantify the contribution to vorticity across all incident modes, it is convenient to define an integrated value for the vorticity coefficient. First, assuming an incident entropy mode, we define in complex space the non–dimensional vorticity fluctuation transported by a refracted mode, "μ":

$$\frac{\omega'_\mu}{\mathrm{i}k_1\bar{u}_1} = \hat{\Omega}_\mu \exp[\mathrm{i}(\boldsymbol{k}_\mu \cdot \boldsymbol{x} - \omega t)], \tag{4.2.81}$$

where $\hat{\Omega}_\mu$ is the complex-valued amplitude of the non–dimensional vorticity, given by $\hat{\Omega}_\mu \equiv \Omega_\mu \cos\theta_1$.

The magnitude of $\hat{\Omega}_\mu$ is then integrated in θ_1-space for a given pre–shock state:

$$\mathcal{I}_\mu = \int_{-90}^{+90} |\hat{\Omega}_\mu| \mathrm{d}\theta_1, \tag{4.2.82}$$

in which $|\hat{\Omega}_\mu|$ is defined $|\hat{\Omega}_\mu| = \{(\mathrm{Re}[\hat{\Omega}_\mu])^2 + (\mathrm{Im}[\hat{\Omega}_\mu])^2\}^{1/2}$.

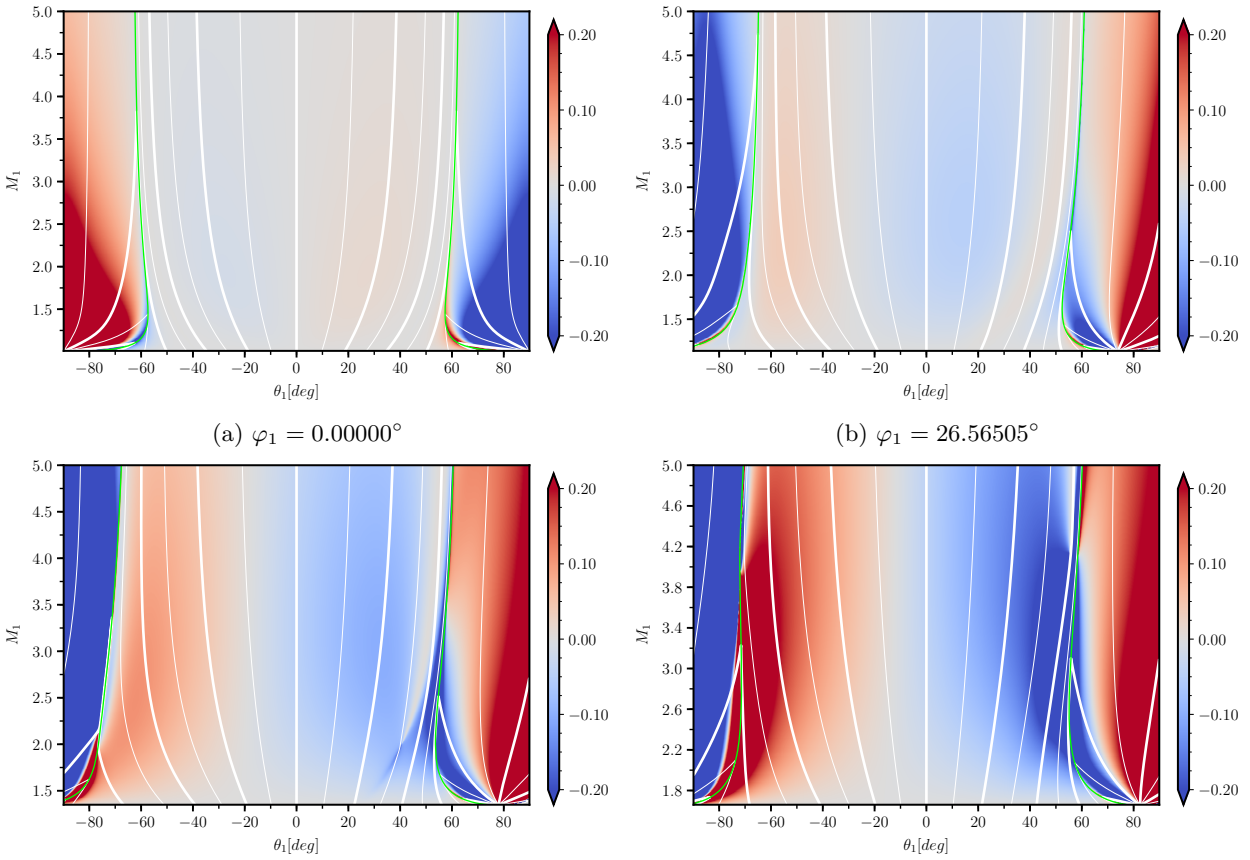
With respect to the forward fast magneto–acoustic mode, whose amplitude rapidly decays in the non–propagative regime for normal mode disturbances incident on the shock above a critical angle, it is useful to define the integrated quantity, $\mathcal{I}_\mu$, between different limits:

$$\mathcal{I}_{f+} = \int_{\theta^{c-}}^{\theta^{c+}} |\hat{\Omega}_{f+}| \mathrm{d}\theta_1, \tag{4.2.83}$$

where θ^{c+} (θ^{c-}) refers to the critical incidence angle for positive (negative) angles of incidence.

In the context of shock refraction problems involving broadband disturbances, $\mathcal{I}_\mu$, provides a measure of the expected total vorticity production by each refracted mode for a given base flow configuration. However, when defining vorticity production for an actual impinging disturbance, the integrated quantity would involve the integral of the product of the non–dimensional vorticity and disturbance amplitudes, $\mathcal{I}_{\epsilon,\mu} = \int_{-90^\circ}^{+90^\circ} \epsilon|\hat{\Omega}_\mu| \mathrm{d}\theta_1$, where ϵ is the disturbance amplitude. Consequently, care must be taken when attempting to draw definitive conclusions for the actual post–shock vorticity production from $\mathcal{I}_\mu$, as the non–dimensional complex vorticity amplitude is dependent on θ_1, therefore, if the incident disturbance amplitude also exhibits a dependency on θ_1, we find that $\mathcal{I}_{\epsilon,\mu} \neq \epsilon\mathcal{I}_\mu$. Only in cases for which the impinging disturbance has an amplitude independent of wavevector direction (i.e. it is isotropic), is it possible to take I_μ as a reliable measure of actual post–shock vorticity production (i.e. $\mathcal{I}_{\epsilon,\mu} = \epsilon\mathcal{I}_\mu$). This is a particularly noteworthy distinction to make with regards to MHD turbulence, for which anisotopy is an indelible feature of flowfields permeated by a strong mean magnetic field. Indeed, it may be found that certain angles of alignment of an anisotropic turbulent flow with respect to the shock will significantly amplify or reduce the post–shock vorticity contribution of a refracted mode.

In figures 4.7a - 4.11d we study maps of both the real and imaginary components of $\hat{\Omega}_\mu$ for a set of



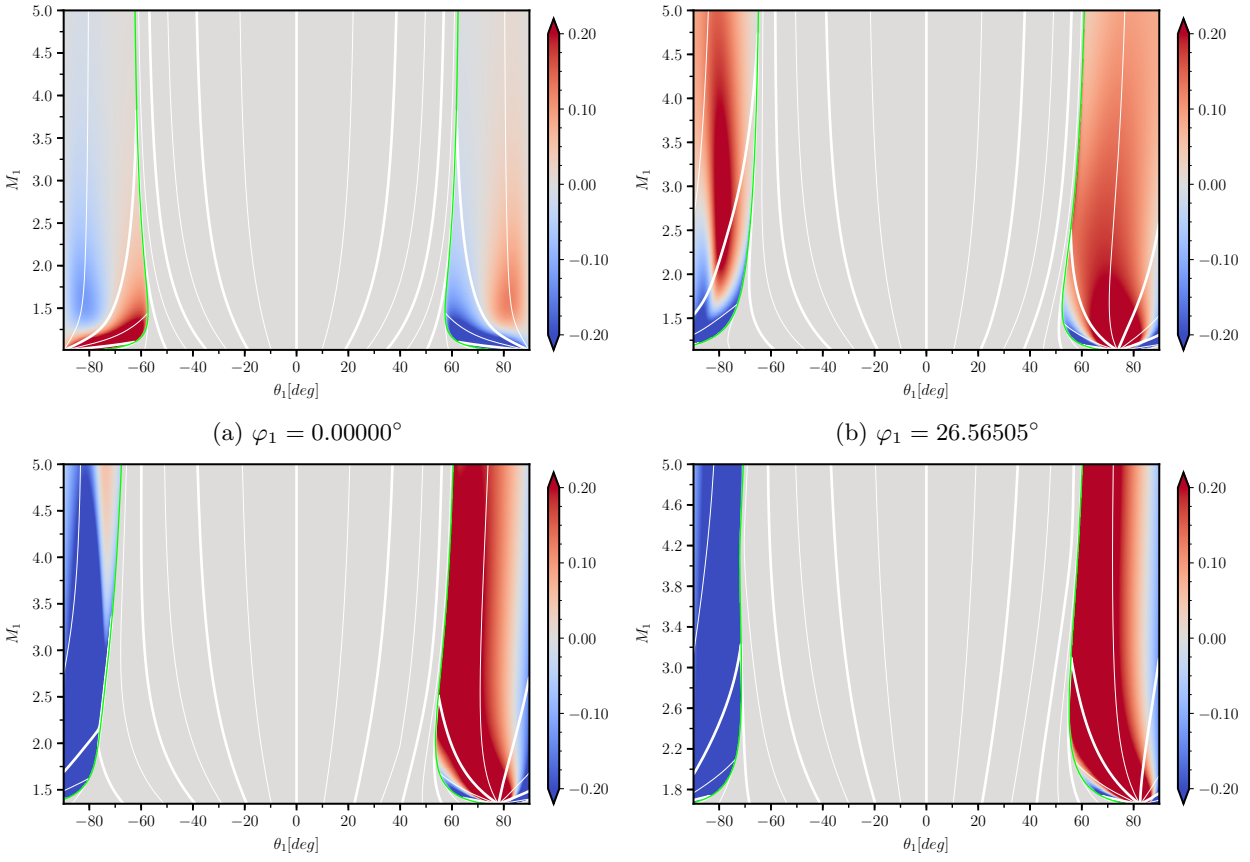
(a) $\varphi_1 = 0.00000°$ (b) $\varphi_1 = 26.56505°$

(c) $\varphi_1 = 43.50912°$ (d) $\varphi_1 = 56.30993°$

Fig. 4.7: Influence of magnetic field orientation on vorticity distribution of refracted forward fast mode generated by an entropy mode-fast shock interaction. Real component of non–dimensional complex vorticity amplitude computed in the $M_1 - \theta_1$ plane for multiple upstream magnetic field angles, φ_1. Forward fast refraction angle (white line) shown, with 40.0° separation between thick lines, and critical incidence angle (green line) are projected on plot. Note that minimum allowable upstream (sound) Mach number, M_1, for an admissible fast shock increases with mean magnetic field angle, φ_1. $\beta_{n,1} = 2$ and $\gamma = 5/3$ for all plots.

four magnetic field configurations in (M_1, θ_1)–space in the range $\theta_1 \in (-90°, +90°)$ and $M_1 \in (M_{min}, 5.0]$, where M_{min} is the minimum allowable upstream Mach number for an admissible fast shock at a given φ_1 and $\beta_{n,1}$. For each case, $\beta_{n,1}$ is kept fixed, $\beta_{n,1} = 2.0$, while the magnetic field angle is varied, $\varphi_1 = 0.00000°, 26.56505°, 43.50912°, 56.30993°$, which correspond to ratios of between the upstream tangential and normal magnetic field strengths of, $\varepsilon_1 = B_{y,1}/B_x = 0.000000, 0.500000, 0.949267, 1.500000$. For $\beta_{n,1} = 2$, it was found that for a reference $M_1 = 2.0$, $\varphi_1 \approx 43.50912°$, results in a post–shock magnetosonic flow, $\beta_2 = 2/\gamma$. For $\varphi_1 < 43.50912°$ and $\varphi_1 > 43.50912$ we find that $\beta_2 > 2/\gamma$ and $\beta_2 < 2/\gamma$ respectively, at the reference $M_1 = 2.0$. As such, the base flow configurations presented in this section provide a view of both high and low β_2 regimes.

Figures 4.7a - 4.8d show the modal response of the real and imaginary forward fast magneto–acoustic mode non–dimensional complex vorticity amplitude, $\mathrm{Re}[\hat{\Omega}_{f+}]$ and $\mathrm{Im}[\hat{\Omega}_{f+}]$. The distribution of $\hat{\Omega}_{f+}$ in the



(a) $\varphi_1 = 0.00000°$

(b) $\varphi_1 = 26.56505°$

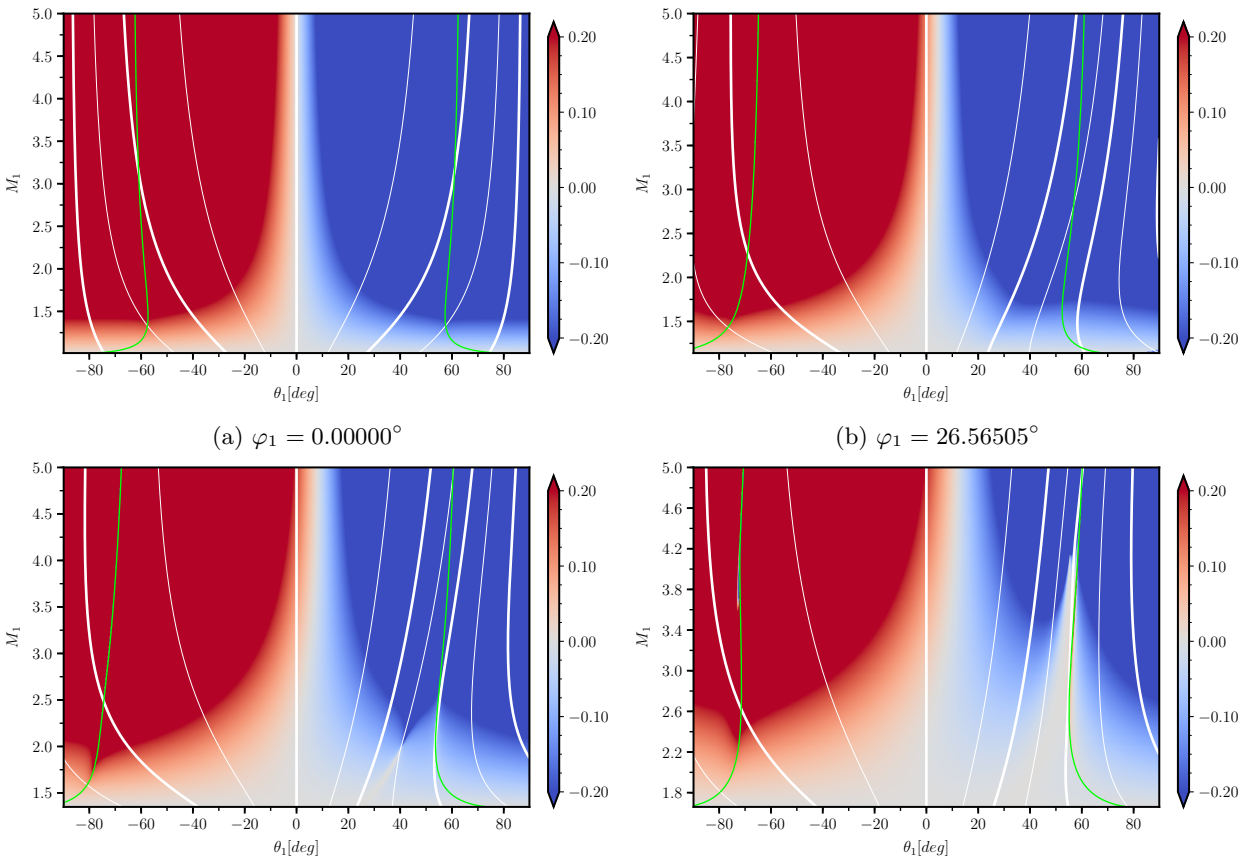
(c) $\varphi_1 = 43.50912°$

(d) $\varphi_1 = 56.30993°$

Fig. 4.8: Imaginary component of forward fast mode non–dimensional complex vorticity amplitude computed in the $M_1 - \theta_1$ plane for multiple upstream magnetic field angles, φ_1, at $\beta_{n,1} = 2$ and $\gamma = 5/3$. See figure 4.7 for additional details.

refracted field wavespace is indicated by the forward fast mode refraction angle, θ_{f+}, provided in the maps. Similar to the forward acoustic mode in gas dynamics [McKenzie and Westphal, 1968], the magnitude of θ_{f+} increases with incidence angle magnitude, reaching a maximum in the ranges $\theta_1 > 0$ and $\theta_1 < 0$ at $\theta_1 = \theta^{c+}$ and $\theta_1 = \theta^{c-}$ respectively, at which we find the critical forward fast refraction angle satisfies, $|\theta^{c\pm}_{f+}| > 90°$ for all values of M_1 and φ_1 shown. For increasing $|\theta_1|$ in the non–propagative regime, $\theta_1 \leq \theta^{c-}$ and $\theta_1 \geq \theta^{c+}$, $|\theta_{f+}|$ reduces. From figures 4.8a - 4.8d we see that $\hat{\Omega}_{f+}$ becomes complex in the non–propagative regime ($\mathrm{Im}[\hat{\Omega}_{f+}]$ is non–zero). With respect to $\mathrm{Re}[\hat{\Omega}_{f+}]$, for $\varphi_1 = 0.0°$ and $\varphi_1 \approx 26.6°$, in which $\beta_2 > 2/\gamma$ for all values of M_1, a relatively high increase in the magnitude of $\mathrm{Re}[\hat{\Omega}_{f+}]$ is observed in the non–propagative regime. Additionally, figures 4.8a - 4.8d, show $\mathrm{Im}[\hat{\Omega}_{f+}]$ increases in magnitude as φ_1 is increased. However, as the forward fast magneto–acoustic mode amplitude in the non–propagative regime is rapidly damped as it penetrates the downstream flow (decay $\propto e^{-\mathrm{Im}[k_{x,f+}]x}$), the respective contributions of $\mathrm{Re}[\hat{\Omega}_{f+}]$ and $\mathrm{Im}[\hat{\Omega}_{f+}]$ to downstream vorticity will be restricted to the near–shock region. Furthermore, at a given M_1, $\mathrm{Re}[\hat{\Omega}_{f+}]$ appears to increase in the propagative regime, $\theta_1 \in [\theta^{c-}, \theta^{c+}]$, with increases in φ_1. This indicates the relative contributions by $\mathrm{Re}[\hat{\Omega}_{f+}]$ and $\mathrm{Im}[\hat{\Omega}_{f+}]$ from non–propagative incident modes ($\theta_1 < \theta^{c-}$ and $\theta_1 > \theta^{c+}$) to the near–shock vorticity field will also diminish with increases in φ_1. The $\varphi_1 = 0.0°$ case, representing a parallel MHD shock, displays symmetry in both $\mathrm{Re}[\hat{\Omega}_{f+}]$ and $\mathrm{Im}[\hat{\Omega}_{f+}]$ (with the signs flipped about $\theta_1 = 0$). As expected for a $\beta_2 > 2/\gamma$ flow, quiet regions are observed for the refraction angles $\theta_{f+} = 0.0°$ and $\theta_{f+} = 90.0°$, representing the directions parallel and perpendicular to the mean magnetic field. Quiet regions shown in figure 4.7b, for the $\varphi_1 \approx 26.6°$ case are asymmetric about $\theta_1 = 0.0°$ as the magnetic field is no longer aligned with the shock normal. In figure 4.7c, the transition between solenoidal and irrotational velocity fluctuations of a fast mode propagating parallel to the magnetic field can be seen clearly at $M_1 = 2.00$ (where $\beta_2 = 2/\gamma$) and $\theta_1 \approx 40.0°$. For $M_1 > 2.00$ (where $\beta_2 > 2/\gamma$) and quiet regions are again observed. In figure 4.7d, for $M_1 \lessapprox 4.14$ (where $\beta_2 < 2/\gamma$) we observe forward fast modes aligned with the magnetic field maintaining solenoidal velocity fluctuations.

In figures 4.9a - 4.12d, we find that the non–dimensional complex vorticity amplitude of both the backward ($\hat{\Omega}_{s-}$) and forward ($\hat{\Omega}_{s+}$) slow modes decreases with increasing φ_1. Additionally, quiet regions (across the full range of θ_1) are observed at low M_1 for all four values of φ_1. The extent of this quiet region in M_1 increases as φ_1 is increased. Additionally, in figure 4.9c for $M_1 < 2.00$ (i.e. below the magnetosonic condition, $\beta_2 < 2/\gamma$) for $\varphi_1 \approx 43.5°$ a narrow band of low $\mathrm{Re}[\hat{\Omega}_{s+}]$ extends from $\theta_1 = 40.00°$ to lower values of M_1 and θ_1. In figure 4.9d this quiet band widens and extends from $M_1 \approx 4.14$ (i.e. the value of M_1 at which $\beta_2 = 2/\gamma$ for $\varphi_1 \approx 56.3°$). These respective bands of low $\mathrm{Re}[\hat{\Omega}_{s+}]$ correspond to the foward slow mode degenerating to longitudinal behaviour for θ_{s+} close to φ_2 in the magnetic–pressure dominated flow, $\beta_2 < 2/\gamma$. For $\theta_1 < 0$, θ_{s+} remains significantly below φ_2, as a result, quiet regions are not observed in this range. The positioning



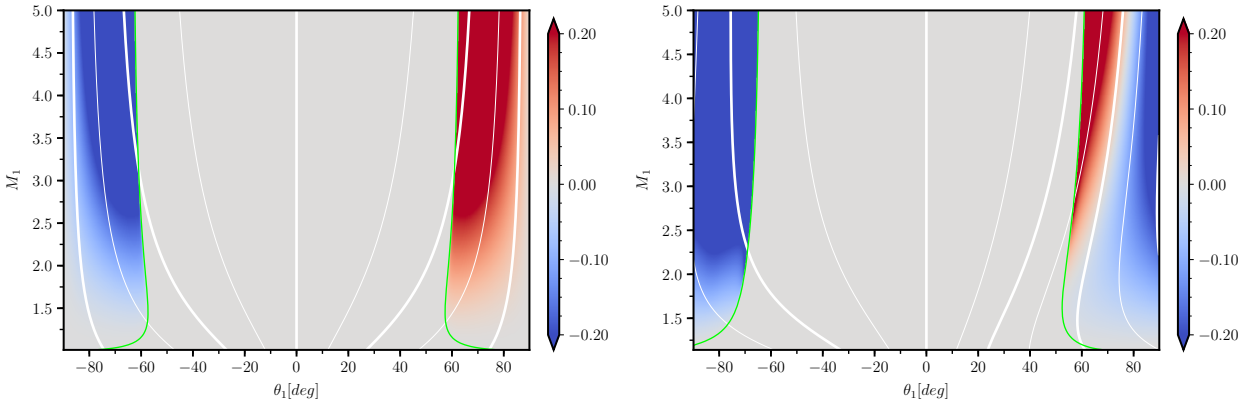
(a) $\varphi_1 = 0.00000°$

(b) $\varphi_1 = 26.56505°$

(c) $\varphi_1 = 43.50912°$

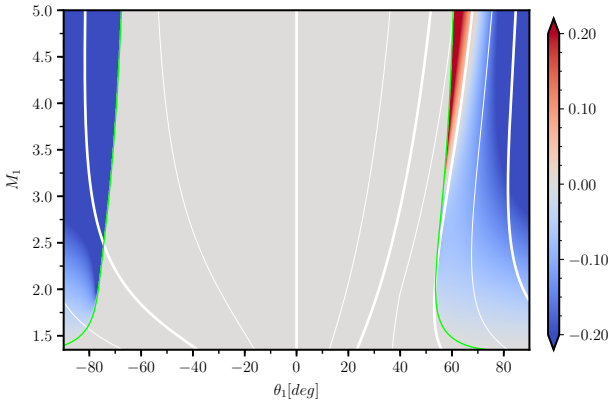
(d) $\varphi_1 = 56.30993°$

Fig. 4.9: Influence of magnetic field orientation on vorticity distribution of refracted forward slow mode generated by an entropy mode-fast shock interaction. Real component of non–dimensional complex vorticity amplitude computed in the $M_1 - \theta_1$ plane for multiple upstream magnetic field angles, φ_1. Forward slow refraction angle (white line) shown, with $40.0°$ separation between thick lines, and critical incidence angle (green line) are projected on plot. Note that minimum allowable upstream (sound) Mach number, M_1, for an admissible fast shock increases with mean magnetic field angle, φ_1. $\beta_{n,1} = 2$ and $\gamma = 5/3$ for all plots.

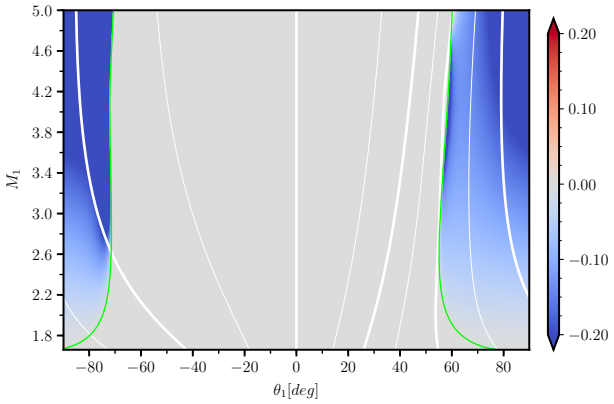


(a) $\varphi_1 = 0.00000°$

(b) $\varphi_1 = 26.56505°$

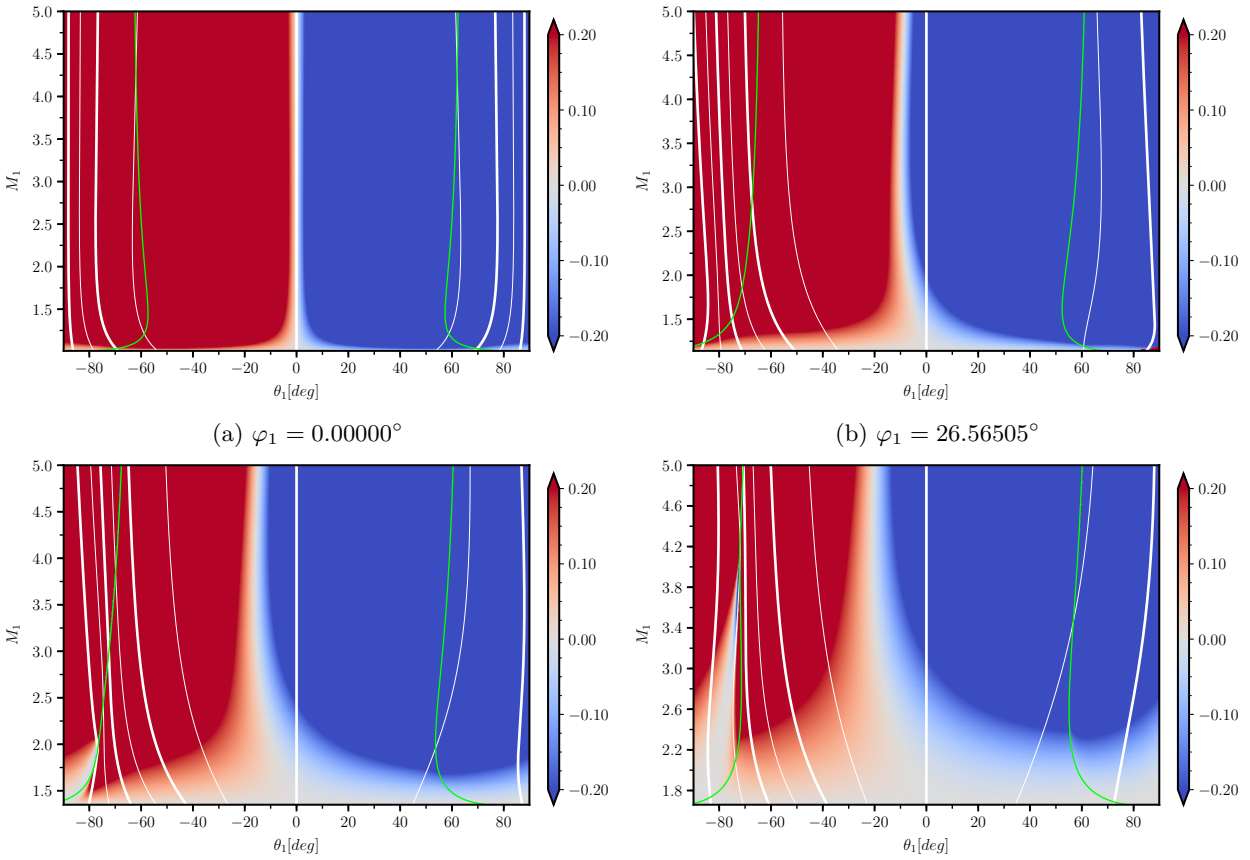


(c) $\varphi_1 = 43.50912°$



(d) $\varphi_1 = 56.30993°$

Fig. 4.10: Imaginary component of forward slow mode non–dimensional complex vorticity amplitude computed in the $M_1 - \theta_1$ plane for multiple upstream magnetic field angles, φ_1, at $\beta_{n,1} = 2$ and $\gamma = 5/3$. See figure 4.9 for additional details.



(a) $\varphi_1 = 0.00000°$

(b) $\varphi_1 = 26.56505°$

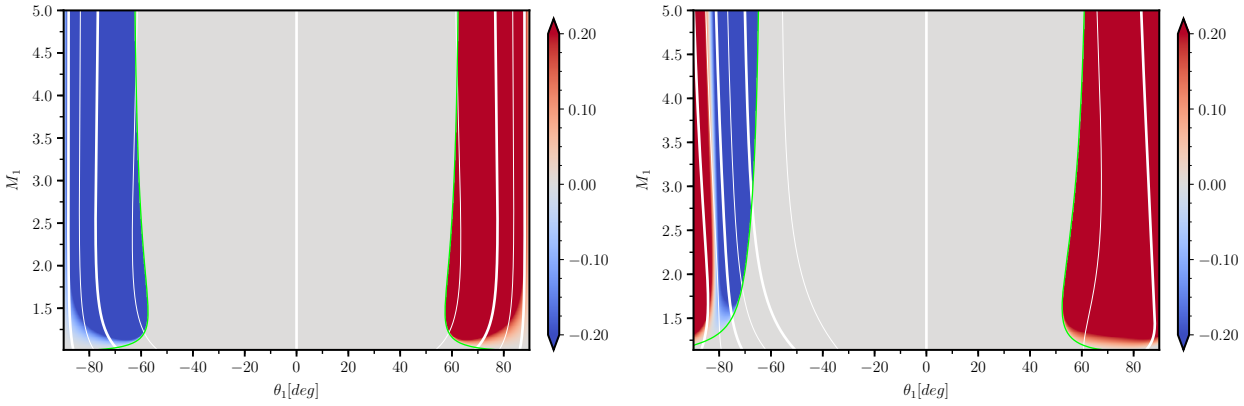
(c) $\varphi_1 = 43.50912°$

(d) $\varphi_1 = 56.30993°$

Fig. 4.11: Influence of magnetic field orientation on vorticity distribution of refracted backward slow mode generated by an entropy mode-fast shock interaction. Real component of non–dimensional complex vorticity amplitude computed in the $M_1 - \theta_1$ plane for multiple upstream magnetic field angles, φ_1. Backward slow refraction angle (white line) shown, with $40.0°$ separation between thick lines, and critical incidence angle (green line) are projected on plot. Note that minimum allowable upstream (sound) Mach number, M_1, for an admissible fast shock increases with mean magnetic field angle, φ_1. $\beta_{n,1} = 2$ and $\gamma = 5/3$ for all plots.

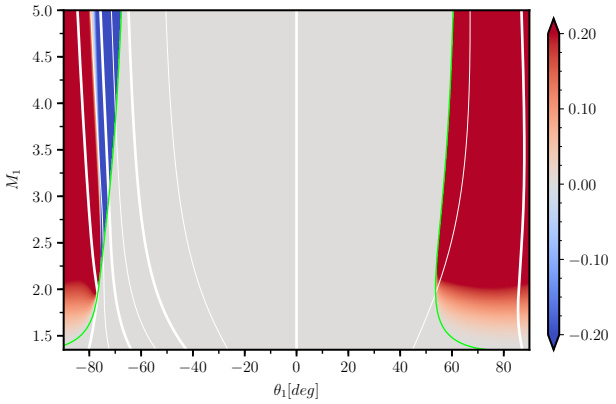
of the quiet regions is reversed to $\theta_1 < 0$ for the backward slow mode, extending from $\theta_1 \approx -80°$ and $\theta_1 \approx -75°$ for $\varphi_1 \approx 43.5°$ and $\varphi_1 \approx 56.3°$ respectively (see figures 4.11c and 4.11d) thereby occurring in the non–propagative regime.

Figures 4.13a - 4.13d show the influence of both M_1 and φ_1 on $\mathcal{I}_\mu$ for the respective fast and slow magneto–acoustic modes. However, notably, there exists relatively large noise for both $\varphi_1 \approx 43.5°$ and $\varphi_1 \approx 56.3°$ (an order of magnitude higher than the given $\mathcal{I}_\mu$ value) in the ranges $M_1 \gtrapprox 2.2$ and $M_1 \gtrapprox 3.9$ respectively. The noisy regions result from singular behaviour of the refraction coefficient near the critical incidence angle above the aforementioned values of M_1. In figures 4.14a - 4.14d, results are presented for the integrated value of $|\hat{\Omega}_\mu|$ in the range, $\theta_1 \in [\theta^{c-} + 1.0°, \theta^{c+} - 1.0°]$, inside propagative regime for all modes. Despite this restriction, a similar trend as in figures 4.13a - 4.13d in $\mathcal{I}_\mu$ is maintained for all modes. The forward fast mode, $\mathcal{I}_{f+}$, exhibits a small peak at low M_1 for $\varphi_1 = 0.0°$, that exceeds the forward slow mode, $\mathcal{I}_{s+}$, at low

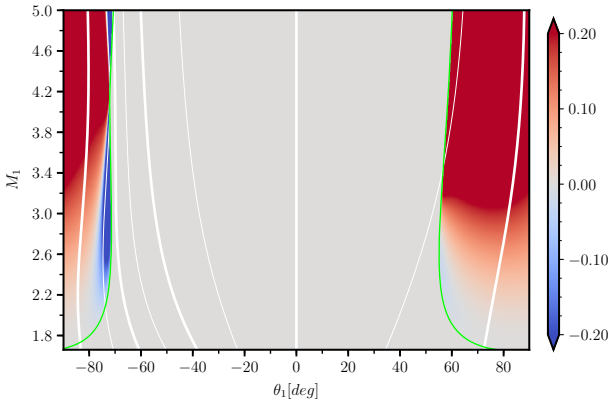


(a) $\varphi_1 = 0.00000°$

(b) $\varphi_1 = 26.56505°$

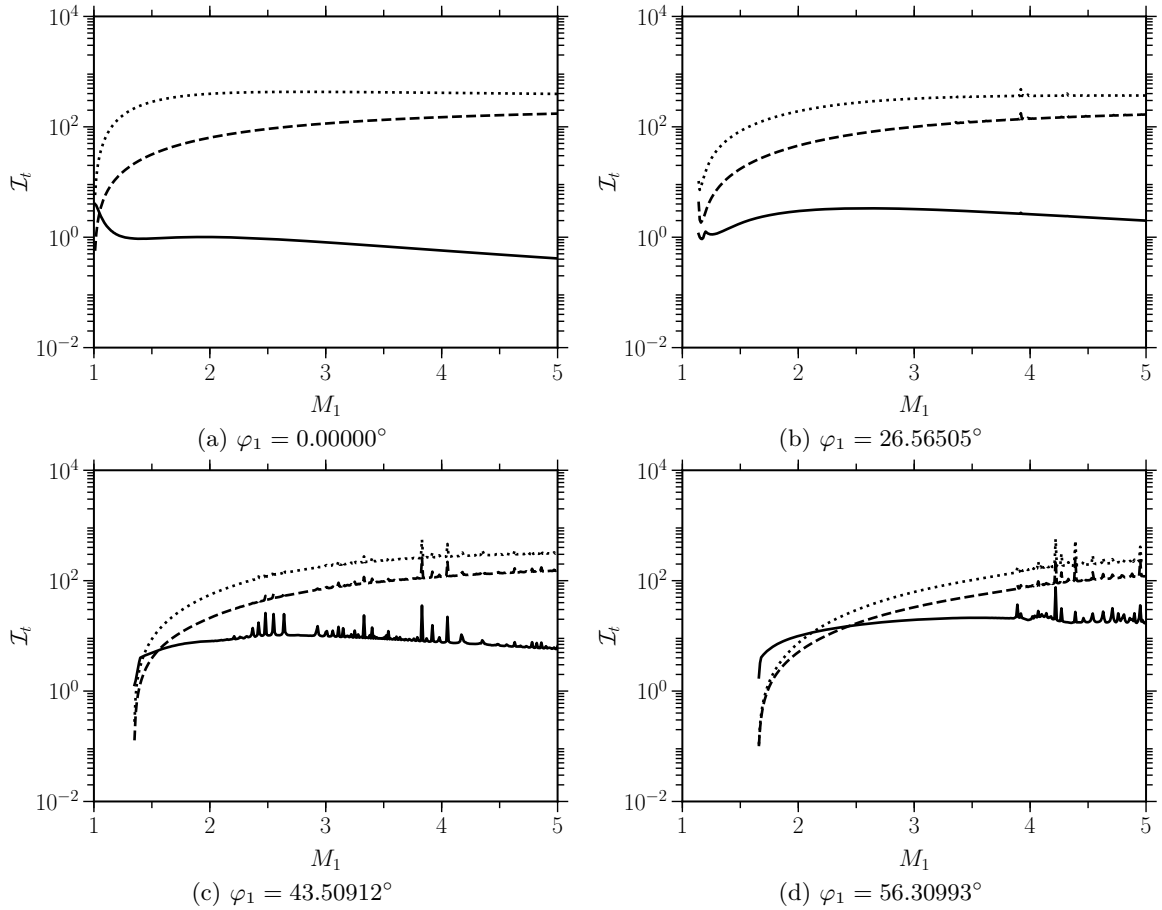


(c) $\varphi_1 = 43.50912°$



(d) $\varphi_1 = 56.30993°$

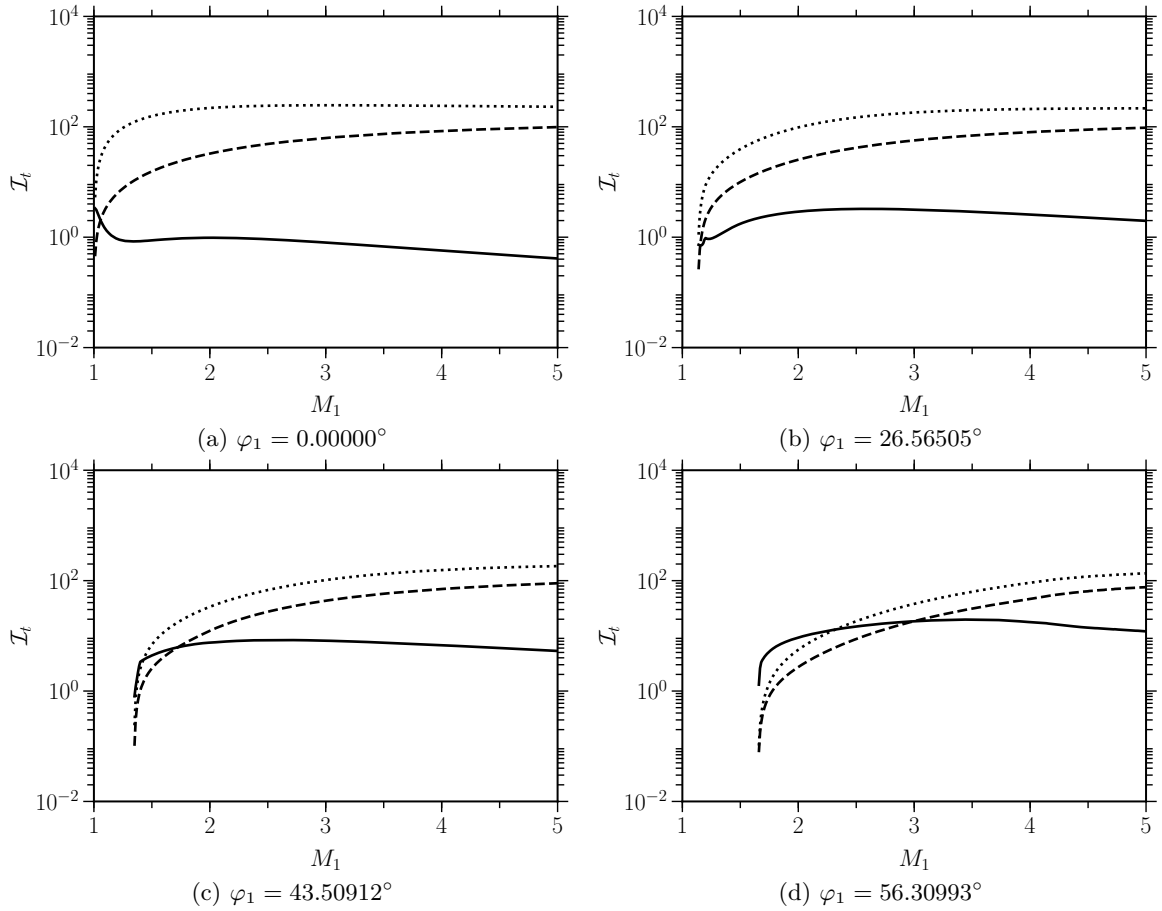
Fig. 4.12: Imaginary component of backward slow mode non–dimensional complex vorticity amplitude computed in the $M_1 - \theta_1$ plane for multiple upstream magnetic field angles, φ_1, at $\beta_{n,1} = 2$ and $\gamma = 5/3$. See figure 4.11 for additional details.



(a) $\varphi_1 = 0.00000°$ (b) $\varphi_1 = 26.56505°$

(c) $\varphi_1 = 43.50912°$ (d) $\varphi_1 = 56.30993°$

Fig. 4.13: Mach number dependency of integrated non–dimensional complex vorticity amplitude (in θ_1-space) for downstream magneto–acoustic modes generated in refraction of a normal entropy mode across a fast MHD shock. Forward fast (solid), forward slow (dashed) and backward slow (dotted) modes shown [$\beta_{n,1} = 2$, $\gamma = 5/3$].



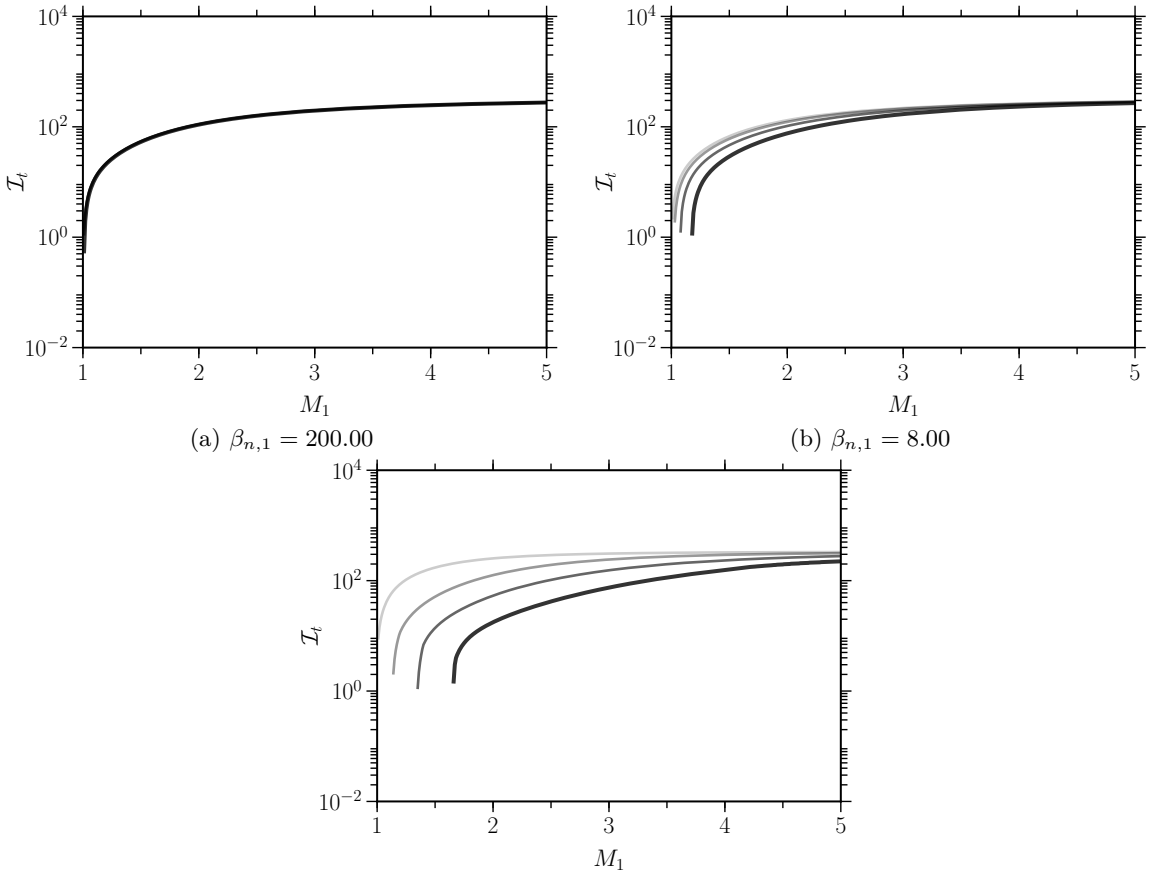
(a) $\varphi_1 = 0.00000°$ (b) $\varphi_1 = 26.56505°$

(c) $\varphi_1 = 43.50912°$ (d) $\varphi_1 = 56.30993°$

Fig. 4.14: Mach number dependency of integrated non–dimensional complex vorticity amplitude (in θ_1-space for range within critical angle for all modes) for downstream magneto–acoustic modes generated in refraction of a normal entropy mode across a fast MHD shock. Forward fast (solid), forward slow (dashed) and backward slow (dotted) modes shown [$\beta_{n,1} = 2$, $\gamma = 5/3$].

M_1 values. For $\varphi_1 \approx 43.5°$ and $\varphi_1 \approx 56.3°$, $\mathcal{I}_{f+}$ exhibits a rapid increase at low M_1 and exceeds both $\mathcal{I}_{s+}$ and $\mathcal{I}_{s-}$. As M_1 is increased, the rate of increase of $\mathcal{I}_{f+}$ rapidly drops and $\mathcal{I}_{f+}$ approaches a limiting value before gradually decreasing. Both $\mathcal{I}_{s+}$ and $\mathcal{I}_{s-}$ also appear to approach a maximum value as M_1 increases. However, this occurs at faster rate of change than $\mathcal{I}_{f+}$, leading both $\mathcal{I}_{s+}$ and $\mathcal{I}_{s-}$ to exceed $\mathcal{I}_{f+}$ by $M_1 \approx 1.9$ and $M_1 \approx 3.2$ for $\varphi_1 \approx 43.5°$ and $\varphi_1 \approx 56.3°$ respectively. With respect to increases in φ_1, the maximum of $\mathcal{I}_{f+}$ at $M_1 = 5.0$ also increases by more than an order of magnitude between $\varphi_1 = 0.0°$ and $\varphi_1 \approx 56.3°$. $\mathcal{I}_{s+}$ and $\mathcal{I}_{s-}$ display the opposite trend, with the maxmimum at $M_1 = 5.0$ roughly half their respective values at $\varphi_1 \approx 56.3°$ compared to $\varphi_1 = 0.0°$.

The amplification/suppression of the superposition of fast and slow modes is shown by the total integrated non–dimensional vorticity coeficient, $\mathcal{I}_t = \mathcal{I}_{f+} + \mathcal{I}_{s+} + \mathcal{I}_{s-}$, plotted in figures 4.16a - 4.16c at different values of $\beta_{n,1}$. For $\beta_{n,1} = 200$, increases in φ_1 appear to have an insignificant effect on $\mathcal{I}_t$. With respect to the post–shock flow, the lowest β_2 observed (across all M_1 and φ_1 values) is, $\beta_2 \approx 37.0/\gamma$ (at $\varphi_1 \approx 56.3°$ for $M_1 = 1.01$).



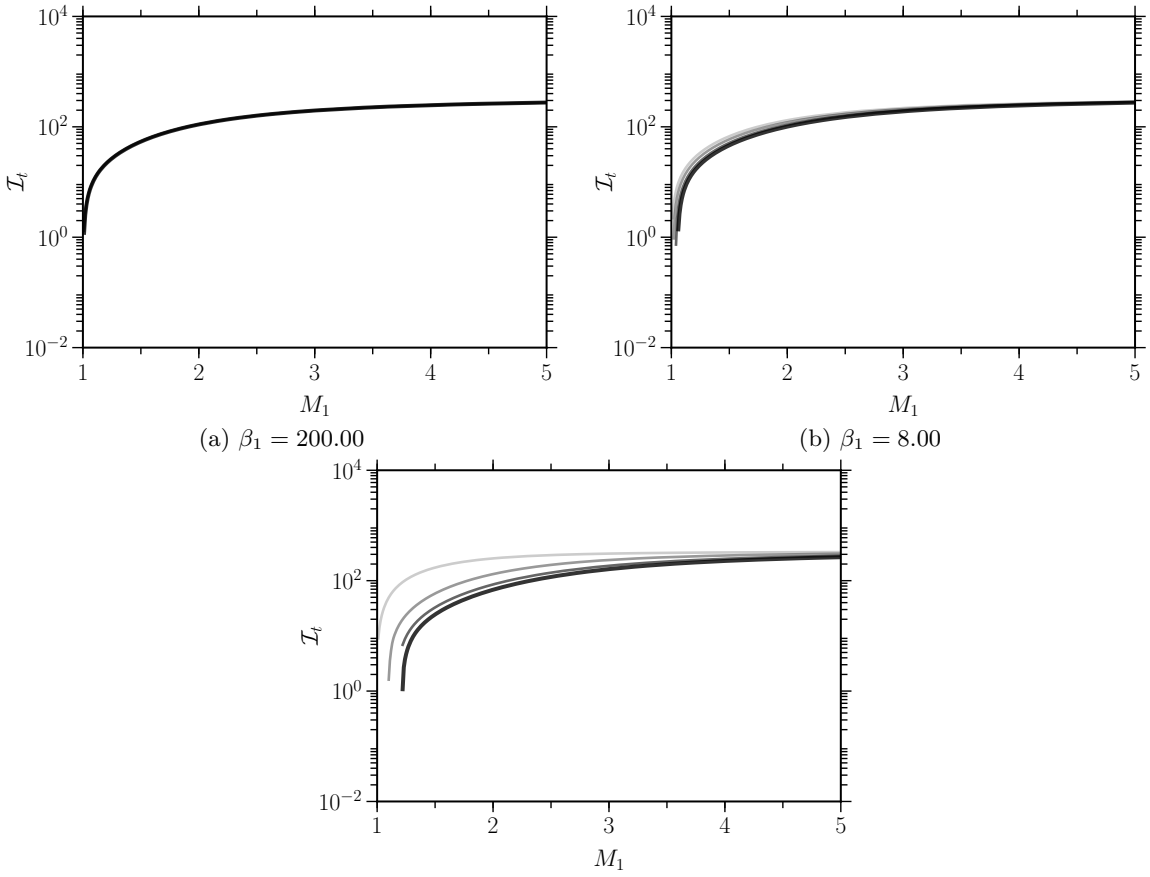
(a) $\beta_{n,1} = 200.00$ (b) $\beta_{n,1} = 8.00$

(c) $\beta_{n,1} = 2.00$

Fig. 4.15: Mach number dependency of integrated non–dimensional complex vorticity amplitude (in θ_1-space for range within critical angle for all modes) summed across all downstream magneto–acoustic modes. Results shown for different $\beta_{n,1}$ regimes for $\varphi_1 \in [0.0°, 56.30993°]$ - line becomes lighter with decreasing φ_1. [$\gamma = 5/3$].

The high β_2 regime indicates wave dynamics close to the gasdynamic limit - the fast mode behaves similar to acoustic waves and slow modes to vortical waves - with minimal influence from the magnetic field direction. As $\beta_{n,1}$ is reduced, increases in φ_1 have a suppressing effect on the total vorticity production. However, for a given $\beta_{n,1}$, this suppression effect also appears to reduce as the shock strength is increased.

At fixed $\beta_{n,1}$, increasing φ_1 corresponds with a decrease in β_1 ($\beta_1 = \beta_{n,1}/(1 + \tan^2 \varphi_1)$) and β_2 (see figures 4.2a - 4.2d). However, when β_1 is fixed (i.e. the upstream magnetic field strength is kept the same if the upstream pressure is also kept constant), increases in φ_1 result in a lesser suppression effect (at β_1 values in figure 4.16 equivalent to $\beta_{n,1}$ values in figure 4.15). It may also be seen as a point of interest for flow control configurations that although the total vorticity production reduces with increases of φ_1, in an upstream flow regime where thermodynamic pressure dominates ($\beta_1 > 2/\gamma$), vorticity transported by the "fastest mode" (forward fast magneto–acoustic) can be amplified (as observed in figures 4.14a - 4.14d). Additionally, the suppression of total vorticity production will be more prominent in relatively low speed flow control applications ($M_1 < 5$) than at higher speeds.



(a) $\beta_1 = 200.00$ (b) $\beta_1 = 8.00$

(c) $\beta_1 = 2.00$

Fig. 4.16: Mach number dependency of integrated non–dimensional complex vorticity amplitude (in θ_1-space for range within critical angle for all modes) summed across all downstream magneto–acoustic modes. Results shown for different β_1 regimes for $\varphi_1 \in [0.0°, 56.30993°]$ - line becomes lighter with decreasing φ_1. [$\gamma = 5/3$].

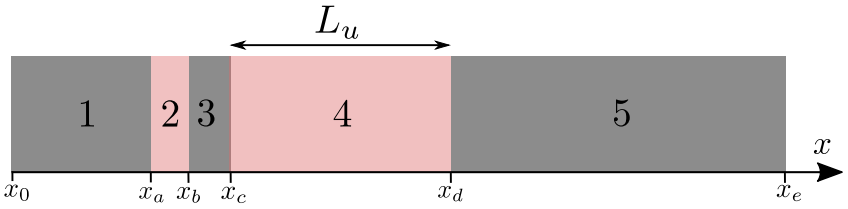


Fig. 4.17: Five–block grid stretching configuration in x-direction. Uniform (non-uniform) regions represented by pink (gray) shading. Centre–line of shock, x_{sh}, located in region 2 at $x_{sh} = (x_a + x_b)/2$. Sampling region for errors between DNS and LIA results located within region 4, in $x_c \leq x \leq x_d$. Length of sampling region, L_u, selected such that $L_u > \lambda_x$, where λ_x is the normal component of the incident disturbance wavelength. x_0 and x_e indicate the limits of the computational domain, $x_0 \leq x \leq x_e$.

4.3 Plane wave interaction with a fast shock

In this section we compare linear theory and DNS results for an entropy disturbance modelled as a normal mode, continuously forced at the inlet of a two–dimensional flowfield, refracted through a parallel and oblique fast MHD shock respectively. Incident disturbances are 1% the upstream base flow density and are studied for a range of incidence angles in both the propagative and non–propagative regimes. The error between the linear and DNS result is computed in physical space.

4.3.1 Numerical method

For all simulations presented in this section a 13-point stencil, 4^{th}-order DRP scheme (see section 3.1.1 is used in conjunction with a 13-point stencil, 8^{th}-order discrete filter (see section 3.1.2). A $N_x \times N_y$ grid of resolution $N_x = 1024$ and $N_y = 128$ is used for all simulations. We apply non-reflecting characteristic boundary conditions in the x-direction (see section 3.1.4). Periodic boundary conditions are applied in the y-direction. To enforce periodicity of the incident waves, the domain length in the y-direction is set equal to a multiple of two of the tangential wavelength component, $l_y = 2\lambda_y = 2\lambda/\sin\theta_1$. Simulations are solved on a stretched grid, refined in the x-direction in the shock region, to maintain scale separation between the shock thickness and the incident wavelength. The normal component of the wavelength, $\lambda_x = \lambda/\cos\theta_1$, is kept fixed for all incidence angles, $\lambda_x = 10.0$. The ratio between the thickness of the shock (captured over 20 grid points) and the normal component of the incident wavelength adheres to the following constraint, $\lambda_x/\Delta > 325$ (unless specified).

4.3.1.1 Baseflow initialisation

To generate a two–dimensional base flow (uniform either side of a shock) the flowfield is extruded from the one–dimensional numerical solution, computed on a 1024 point, five–block, stretched grid configuration (see figure 4.17), in which $X_1 \in [x_0, x_a]$, $X_2 \in [x_a, x_b]$, $X_3 \in [x_b, x_c]$, $X_4 \in [x_c, x_d]$ and $X_5 \in [x_d, x_e]$, where X_i

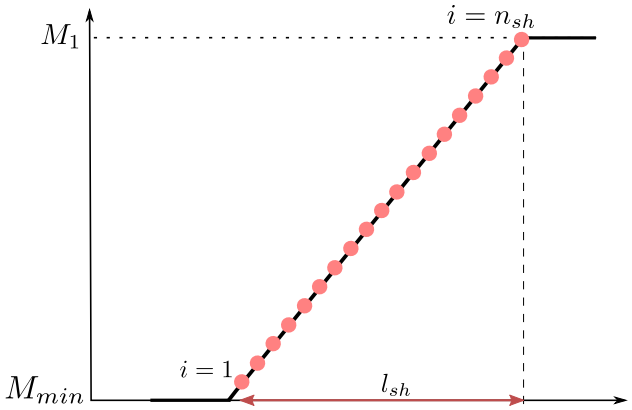


Fig. 4.18: Seeding of flow within shock between prescribed upstream Mach number, M_1, and M_{min}, for which $\bar{\rho}_2 = \bar{\rho}_1 = 1.0$.

denotes a given spatial region. x_0 and x_e represent the upper and lower bounds of the computational domain, $x \in [0, L]$, where L is the length of the domain. Regions X_2 and X_4 consist of uniform grids. X_1, X_3 and X_5 are non–uniform. The non–uniform regions are generated with a polynomial grid for which the function between block interfaces is class C^9. The shock is located in X_2 and error analysis on the refracted wave modes is conducted in X_4. Values for x_a, x_b, x_c and x_d correspond to x_{lo} for regions X_2, X_3, X_4 and X_5 respectively, given in table 4.1. Although non–reflecting boundary conditions have been applied, to reduce the amplitude of waves leaving the domain (and thus minimise reflections) we prescribe a relatively long domain of length, $L = 100$, so that waves are damped in the coarse non–uniform grid region, X_5, prior to impinging on the domain boundaries. For the value of L given, X_2 has a uniform grid spacing of $\Delta/L = 0.1538 \times 10^{-4}$ which corresponds to a ratio $\lambda_x/\Delta \approx 325$ with 20 points within the shock. The length of the X_3 region in the computational domain is $L_u/L = 0.13$, satisfying $L_u > \lambda_x$.

The one–dimensional base flow is computed for an upstream Mach number, $M_1 = 2.0$, and normal plasma beta, $\beta_{n,1} = 2.0$. We wish to evaluate the shock refraction problem for both parallel and oblique fast MHD shock cases. As such, the downstream state was computed for two different values of the upstream

Region	Nbpts	x_{lo}/L	x_{up}/L	$\Delta x_{lo}/L$	$\Delta x_{up}/L$
X_1	195	0.0000	0.0990	0.1000×10^{-2}	0.1538×10^{-4}
X_2	65	0.0990	0.1000	0.1538×10^{-4}	0.1538×10^{-4}
X_3	153	0.1000	0.1200	0.1538×10^{-4}	0.2461×10^{-3}
X_4	528	0.1200	0.2499	0.2461×10^{-3}	0.2461×10^{-3}
X_5	83	0.2499	1.0000	0.2461×10^{-3}	0.1783×10^{-1}

Table 4.1: Five–block grid stretching configuration for the plane wave-fast MHD shock interaction. L is the reference length of the computational domain. Number of points ($Nbpts$), upper/lower bounds in x (x_{up}/x_{lo}) and grid spacing ($\Delta x_{up}/\Delta x_{lo}$) given for each region of stretched grid. Regions X_2 and X_4 are uniform. X_1, X_3, X_5 are non–uniform and utilise a x^{th} grid.

.

magnetic field angle, $\varphi_1 = 0.0^\circ$ (parallel fast MHD shock), and $\varphi_1 = 26.56505^\circ$ (oblique fast MHD shock). The downstream state is obtained using (4.1.26) - (4.1.29) (however the gasdynamic normal shock solutions can also be used). The pre– and post–shock states were initialised in the regions $x < x_{sh} - l_{sh}/2$ and $x > x_{sh} + l_{sh}/2$ respectively. To seed flow properties at the i-th point within the shock (see figure 4.18), $x_{sh} - l_{sh}/2 \leq x \leq x_{sh} + l_{sh}/2$, the shock jump is computed for a linear function of the grid position:

$$M_{1,i} = M_{min} + \frac{M_1 - M_{min}}{n_{sh}}(i), \tag{4.3.1}$$

where M_{min} is the value of M_1 for which $\bar{\rho}_2/\bar{\rho}_1 = 1$. This can be obtained by rearranging (4.1.26) in terms of a cubic in M_1 to be solved for $\eta_c = 1$:

$$aM_1^3 + bM_1^2 + cM_1 + d = 0, \tag{4.3.2}$$

where,

$$\begin{aligned}
a &= (\gamma - 1)\eta_c - (\gamma + 1), \\
b &= ((2 - \gamma)\varepsilon_1^2 - 2(\gamma - 1))\eta_c^2 r_{n,1}^2 + (2 + r_{n,1}^2(\gamma\varepsilon_1^2 + 2(\gamma + 1)))\eta_c, \\
c &= (\gamma - 1)(1 + \varepsilon_1^2)r_{n,1}^4\eta_c^3 - (4r_{n,1}^2 + r_{n,1}^4(\varepsilon_1^2 + 1)(\gamma + 1))\eta_c^2, \\
d &= 2\eta_c^3 r_{n,1}^4.
\end{aligned}$$

In the case parallel fast MHD shock case, $\varepsilon_1 = 0$, from which we computed $M_{min} = 1.00000$. In the oblique fast MHD shock case we set $\varepsilon_1 = 0.5$ (which corresponds to $\varphi_1 \approx 26.56505^\circ$) and subsequently computed $M_{min} \approx 1.13224$. In the computational domain the normal and tangential magnetic fields are B_x and B_y respectively. For both parallel and oblique shock cases we set $\rho_1 = p_1 = B_x = 1.0$ (note: B_x is constant throughout the domain) and $v_1 = 0$. $B_{y,1} = 0.0$ and $B_{y,1} = 0.5$ in the parallel and oblique shock cases respectively.

The "post–shock" state at each grid point, $\bar{\boldsymbol{q}}_{2,i}$, can be computed for the corresponding value of $M_{1,i}$.

The maximum fast magneto–acoustic wave speed, $c_{f,max} = \sqrt{B^2/\rho + c_o^2}$, is only 10% higher in the oblique case compared to the parallel. As such, the same time–step was used to compute both flows, $\Delta t = 4 \times 10^{-5}$. This corresponds to an inviscid maximum CFL numbers, $CFL_{max} = 0.100$, and, $CFL_{max} = 0.110$, for the parallel and oblique shock cases respectively.

For both shock cases, the one–dimensional base flow is run until all initial transients have left the domain. Figure 4.19 shows the density profile of the parallel MHD shock case after steady–state conditions have been reached. The LAD strategy implemented involves constant artificial bulk viscosity and conductivity (computed from the bulk viscosity) applied in the shock region. Spurious noise has been minimised to a small

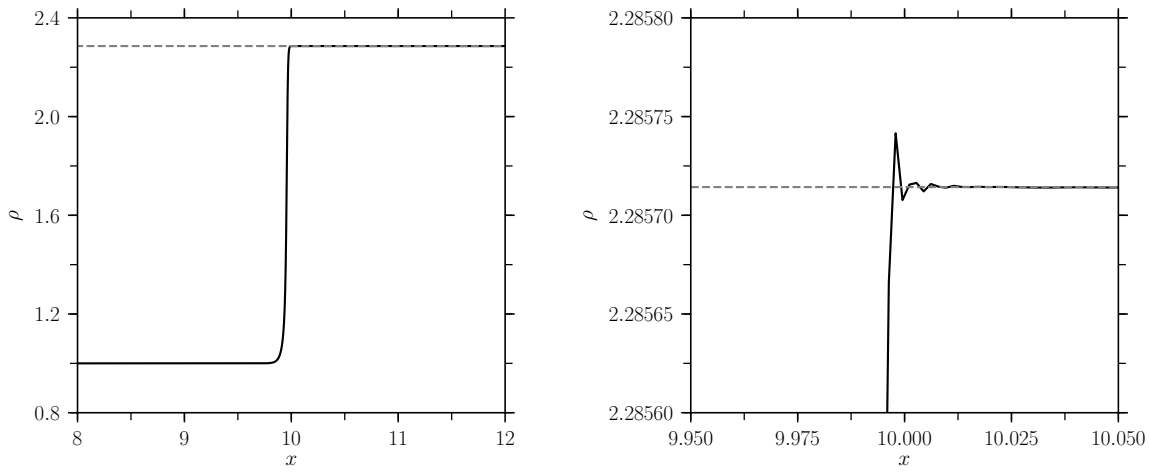


Fig. 4.19: DNS density profiles for parallel fast shock captured using constant artificial bulk viscosity. Theoretical post–shock value given by dashed line. Close–up of profile shown on the right–hand–side.

fraction of the jump, $< 0.01\%$. In figures 4.20 and 4.21, accurate capture of the oblique shock is observed despite the constant LAD method being derived for a gasdynamic shock (as such no dissipation is applied to the magnetic field variables). Discontinuities in both thermodynamic and magnetic components are smeared over the same length. The relative errors for the parallel and oblique case are shown in figure 4.22. The initial DNS flow (with the theoretical shock solution) is subtracted from the steady–state DNS solution and the result divided by a relevant upstream quantity; ρ_1, for ρ, p_1 for p, u_1 for u_2 and v_2, B_n for $B_{y,2}$. The relatively large error before the shock, $x < 9.95$, originates from smoothing of pre–shock profile (visible in figures 4.19 and 4.20). Immediately after the shock centre–line there is a steep decrease in the error values to the order of 10^{-7} (after which they fluctuate). As such, errors in the base flow solution will scale significantly smaller than the amplitude of the incident perturbation, $\epsilon = 0.01$.

4.3.1.2 Entropy plane wave initialisation

A constant–pressure density (i.e. entropy mode) perturbation, in the form of a plane wave, is imposed on the upstream flow (to be forced continuously only at the inlet throughout the duration of each simulation). To avoid start–up errors, we assign a Gaussian-taper to the upstream perturbation in the initial field:

$$\rho_1' = \begin{cases} f(x)\bar{\rho}_1\epsilon\cos\left[k_x x + k_y y\right] & \text{for} \quad x_0 \leq x \leq x_{sh},\, t = 0, \\ \bar{\rho}_1\epsilon\cos\left[k_x x + k_y y\right] & \text{for} \quad 0 \leq x < x_0,\, t = 0, \\ \bar{\rho}_1\epsilon\cos\left[k_x x + k_y y - \omega t\right] & \text{for} \quad -x_h \leq x < 0,\, \forall t, \end{cases} \tag{4.3.3}$$

in which x_{sh} is the shock centre–line, $x_0 = x_{sh}/2$, x_h is the length of the extra ghost cells at the boundary

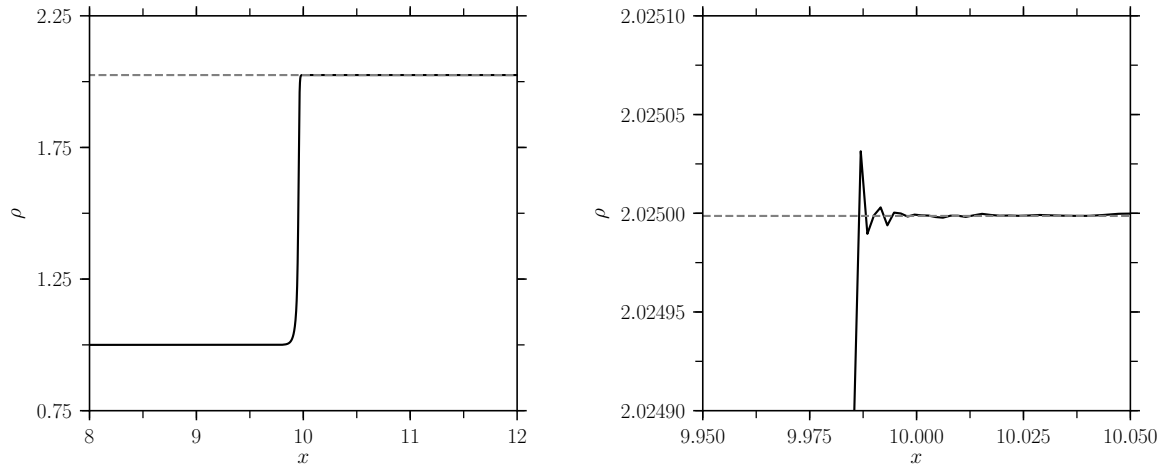


Fig. 4.20: DNS density profiles for oblique fast shock captured using constant artificial bulk viscosity. Theoretical post–shock value given by dashed line. Close–up of profile shown on the right–hand–side.

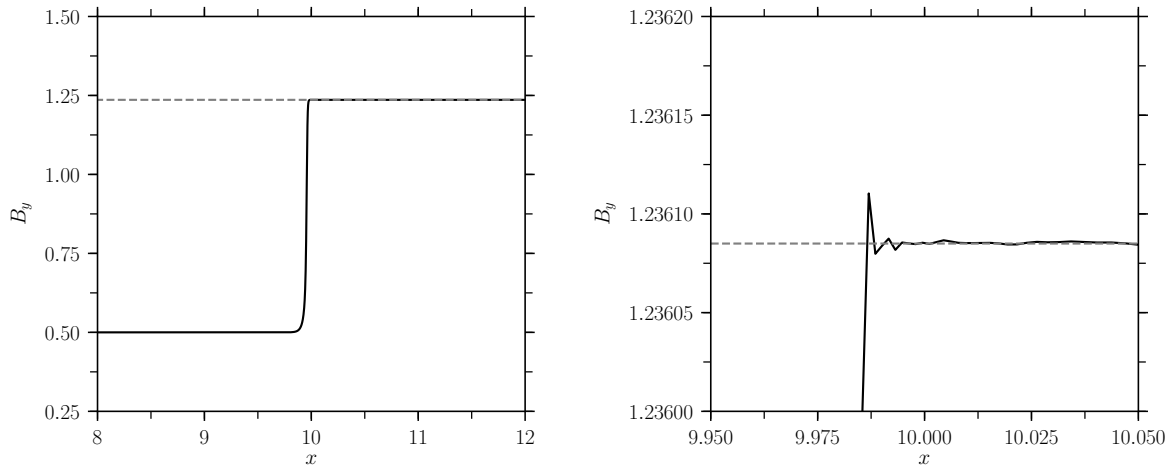
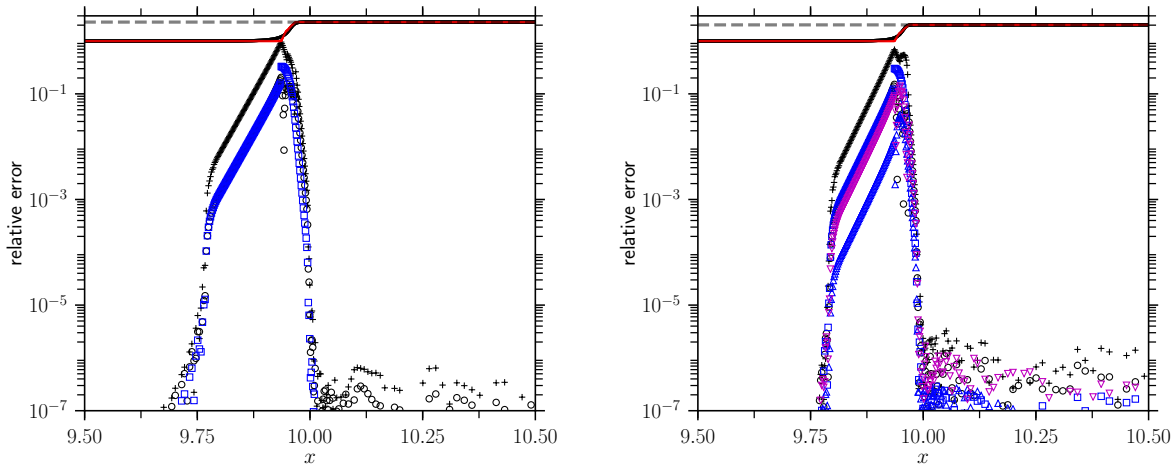


Fig. 4.21: DNS y-magnetic field profiles for oblique fast shock captured using constant artificial bulk viscosity. Theoretical post–shock value given by dashed line. Close–up of profile shown on the right–hand–side.



(a) $\varphi_1 = 0.00000°$ (b) $\varphi_1 = 26.56505°$

Fig. 4.22: Relative error between theoretical and DNS values for parallel (a) and oblique (b) fast MHD shocks captured using constant artificial bulk and conductivity computed from the weak shock approximation [Salas, 2009]. Upstream magnetic field angle given by φ_1. Error computed by subtracting initial solution from DNS flowfield at steady state for ρ (black circles), p (black crosses), u (blue square), v (blue triangle) and B_y field (pink triangles). Errors normalised by upstream theoretical value (normal component of velocity and magnetic field used for velocity and magnetic field errors respectively). DNS density profiles for steady–state initial flow (red) and steady–state (black) shown. Theoretical post–shock density (dashed line) shown as reference for shock location (centre-line of shock is at $x = 9.95$).

of the domain inlet and we define the Gaussian function, $f(x)$, fitted to the density perturbation as:

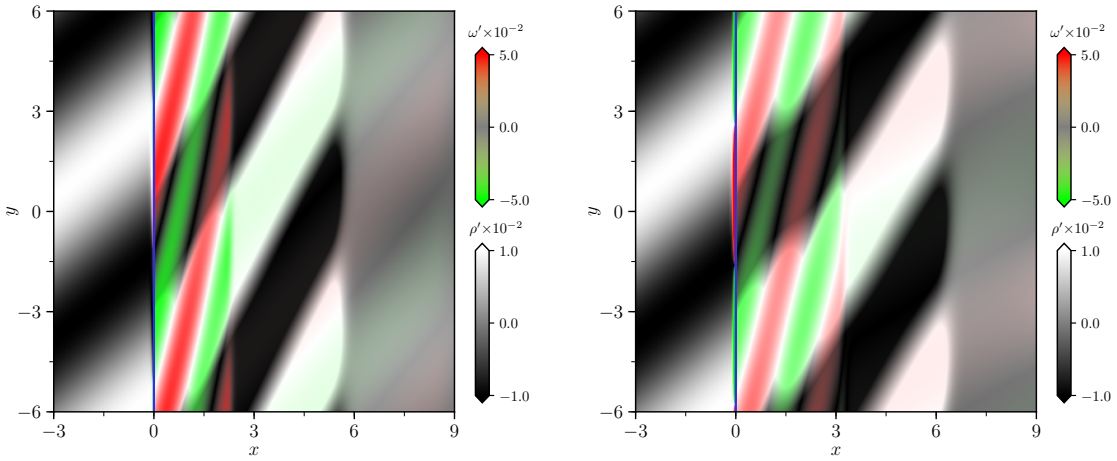
$$f(x) = \exp\left\{-\frac{(x - x_0)^2}{2r_0^2}\right\}, \tag{4.3.4}$$

where $r_0 = 1/(2\sqrt{2\log 2})$.

Note that in all plots shown after figure 4.22 the steady–state shock position, x_{sh}, is re–centered to $x = 0.00$.

4.3.2 Perturbed field contours

Figure 4.23 shows the downstream vorticity transport of multiple wave modes generated in the refraction of an entropy mode through parallel and oblique fast MHD shocks respectively. The incidence angle of the impinging entropy mode is $\theta_1 = 50.00°$, as such, both flowfields are in the propagative regime (critical angles for parallel and oblique shock cases are $|\theta^{c\pm}| \approx 58.63$, and $\theta^{c+} \approx 53.51$ and $\theta^{c-} \approx -75.00$ respectively). The most intense vorticity transport is observed in the backward slow mode, as predicted by the linear theory in section 4.2.5. Figure 4.24 shows the separation with respect to time of each refracted mode along the centre–line in the y-direction, $y = \lambda_y$. In figures 4.23b and 4.24b, a reduction in vorticity intensity for $\varphi_1 \approx 26.6°$ is apparent in the backward slow mode. This represents the suppression effect of increasing the magnetic field angle as noted in section 4.2.5. The propagation speed and wavelength of the backward slow mode increases with φ_1. Increasing φ_1 has a similar effect on the entropy mode, in which a slight wavelength increase is

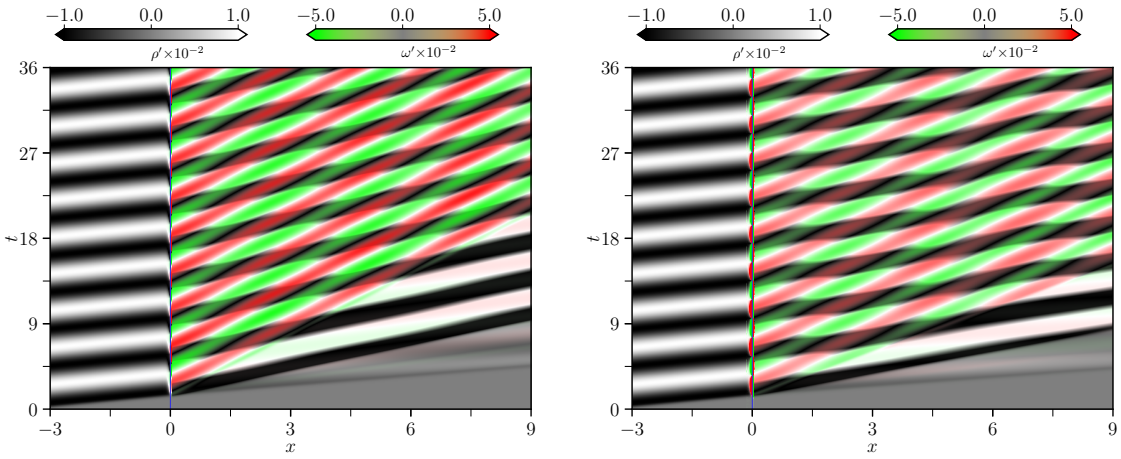


(a) $\varphi_1 = 0.00000°$ (b) $\varphi_1 = 26.56505°$

Fig. 4.23: Density (white/black), ρ', and vorticity (green/red), $\omega' = [\boldsymbol{\nabla} \times \boldsymbol{u}']_z$, contours of normal entropy mode refraction (incident below critical angle at $\theta_1 = 50.00°$) across parallel and oblique fast MHD shocks respectively. Upstream mean magnetic field angle, φ_1, shown. Steady–state shock located at $x = 0$ (blue line). Snapshot taken at early time for which separation between refracted modes still visible in selected domain. Intense vorticity transport corresponds with backward slow mode. Entropy mode indicated by strong post–shock density fluctuations. Weak vorticity and density transport visible for forward slow mode.

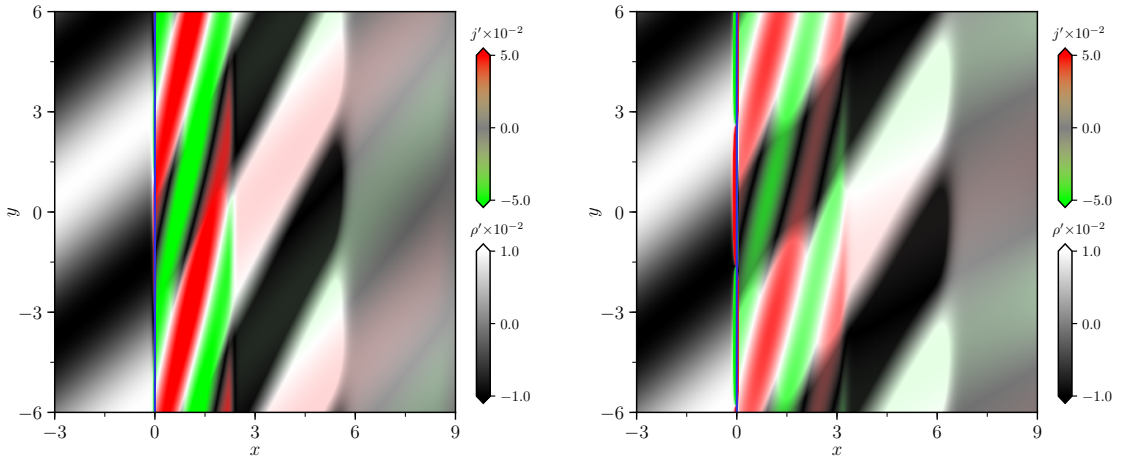
observed. In figure 4.23, the forward slow mode is characterised by weak density and vorticity fluctuations, of which vorticity appears slightly more intense in the parallel shock case.

The close link between current density and vorticity evolution in MHD is highlighted by contours of the former shown in figure 4.25. As seen in figure 4.23 for vorticity, the backward slow mode is responsible for high amplitude fluctuations of current density, whereas the forward slow mode is only a weak transporter. Dilatation rate contours provided in figure 4.26 indicate that slow mode irrotational velocity fluctuations are weak compared to the solenoidal contributions represented by vorticity transport. This is to be expected as $\beta_2 \approx 15.83/\gamma$ and $\beta_2 \approx 4.93/\gamma$ for the parallel and oblique shock cases respectively, as such, slow mode velocity fluctuations will be more solenoidal than irrotational (see section 4.2.1). Weak transport is once again observed in the forward slow mode. For the backward backward slow mode, an increase in φ_1 corresponds with an increase the dilatation rate magnitude.



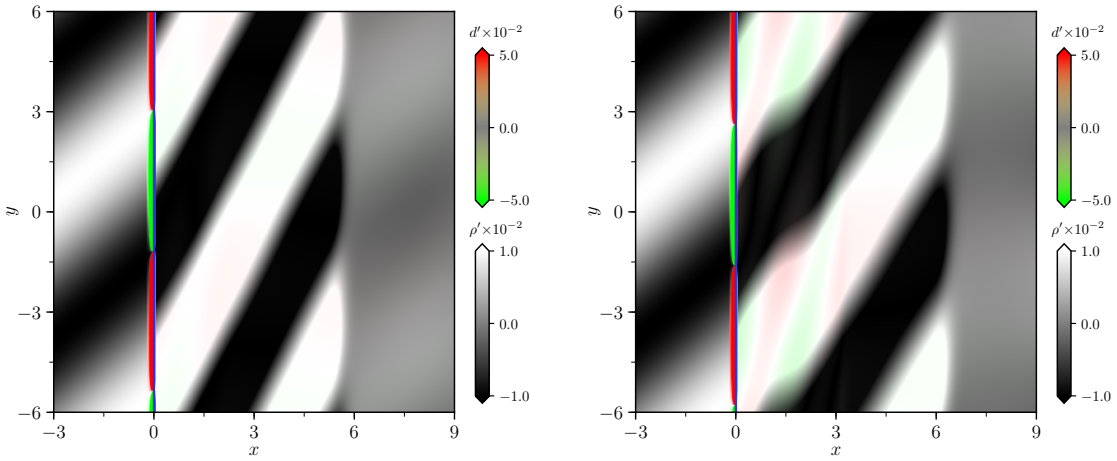
(a) $\varphi_1 = 0.000000°$ (b) $\varphi_1 = 26.56505°$

Fig. 4.24: Density (white/black), ρ', and vorticity (green/red), $\omega' = [\boldsymbol{\nabla} \times \boldsymbol{u}']_z$, contours in $x-t$ space (along centre–line, $y = \lambda_y = 10.0/\tan\theta_1$) of normal entropy mode refraction (incident below critical angle at $\theta_1 = 50.00°$) across parallel and oblique fast MHD shocks respectively. Upstream mean magnetic field angle, φ_1, shown. Steady–state shock located at $x = 0$ (blue line). Modes visibly separate in time as a result of differing normal speeds. Intense vorticity transport corresponds with backward slow mode (which propagates faster in oblique MHD shock case). Entropy mode indicated by strong post–shock density fluctuations. Weak vorticity and density transport visible for forward slow mode.



(a) $\varphi_1 = 0.00000°$ (b) $\varphi_1 = 26.56505°$

Fig. 4.25: Density (white/black), ρ', and current density (green/red), $j' = [\boldsymbol{\nabla} \times \boldsymbol{B}']_z$, contours of normal entropy mode refraction (incident below critical angle at $\theta_1 = 50.00°$) across parallel and oblique fast MHD shocks respectively. Upstream mean magnetic field angle, φ_1, shown. Steady–state shock located at $x = 0$ (blue line). Snapshot taken at early time for which separation between refracted modes still visible in selected domain. Current density fluctuations highest in backward slow mode (like–signed with vorticity fluctuations - see figure 4.23). Entropy mode indicated by strong post–shock density fluctuations. Weak current density and density transport visible for forward slow mode.



(a) $\varphi_1 = 0.00000°$ (b) $\varphi_1 = 26.56505°$

Fig. 4.26: Density (white/black), ρ', and dilatation rate (green/red), $d' = \nabla \cdot \boldsymbol{u}'$, contours of normal entropy mode refraction (incident below critical angle, $\theta_1 = 50.00°$) across parallel and oblique fast MHD shocks respectively. Upstream mean magnetic field angle, φ_1, shown. Steady–state shock located at $x = 0$ (blue line). Snapshot taken at early time for which separation between refracted modes still visible in selected domain. Dilatation rate contours visible for $x < 0$ indicate displacement of shock from steady–state position. Weak dilatation rate production in both slow modes.

4.3.3 Error analysis in physical space

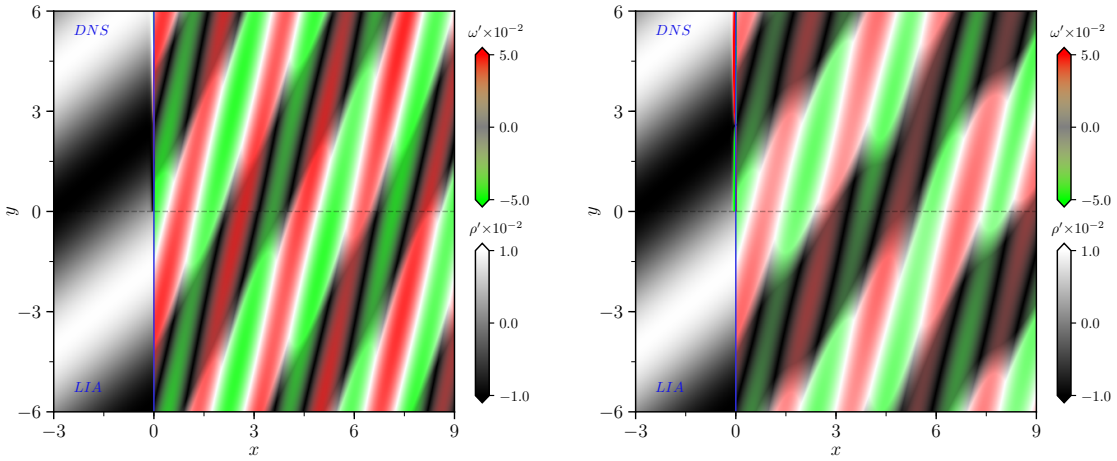
The error in the density and vorticity fields between DNS data and LIA data projected onto physical space are computed. The sample distance within which the LIA and DNS fields are subtracted from one another, L_{s1}, was set within a distance an incident disturbance normal wavelength, $L_{s1} = \lambda_x = 10.0$, away from the shock. From LIA theory, the instantaneous shock location is a function of both time and space, $x_s = \bar{x}_s + x'_s$, where $x'_s = \delta_s \exp[\mathrm{i}(k_y y - \omega t)]$. However, the DNS data for the fluctuating field is obtained by subtracting the initial base flow (for which the shock is fixed at $x_s = x_{sh}$) from the solution at a given sample time, as such, according to theory, in the region, $x \in [x_{sh}, x_{sh} + \delta_s]$, the extracted field will potentially include an error related to the difference in the shock jump at the initial shock location and that of the instantaneous field. δ_s can be computed from (4.2.52). This value of δ_s corresponds to a shock of zero–thickness, responding instantaneously to the forcing mode. However, in the simulation, an artificial dissipation term is added to capture the shock, giving it a finite width, scaling larger than δ_s. Therefore motion of the shock (and thus the perturbed field obtained by subtracting the initial base flow from the instantaneous flow) is likely to diverge from the linear theory result and have a dependency on the artificial dissipation term. Consequently, as a precautionary measure against errors resulting from "numerical" shock motion, the sampling region of the linear theory projection was placed an offset distance of $\lambda_x/50.0$ away from the shock location. We select a sample space spanning the entirety of the tangential direction, $y \in [0, 2\lambda_y]$, and restricted to $x_1 \leq x \leq x_2$, where $x_1 = x_{sh} + \lambda_x/50.0$ and $x_2 = x_{sh} + \lambda_x]$. The grid point index at x_1 and x_2 are given as n_1 and n_2 respectively.

The LIA projection of the post–shock flow is computed by summing the real part of (4.2.51) across all contributing modes. For the density field this corresponds to:

$$\begin{aligned}\rho'_{LIA} = \epsilon\Big[&\mathrm{Re}\left[\chi_E\right]\cos\left(\boldsymbol{k}_E\cdot\boldsymbol{x}-\omega t\right) - \mathrm{Im}\left[\chi_E\right]\sin\left(\boldsymbol{k}_E\cdot\boldsymbol{x}-\omega t\right)+ \\ &+\Big\{\mathrm{Re}\left[\chi_{f+}\rho'_{f+}\right]\cos\left(\boldsymbol{k}^r_{f+}\cdot\boldsymbol{x}-\omega t\right) - \mathrm{Im}\left[\chi_{f+}\rho'_{f+}\right]\sin\left(\boldsymbol{k}^r_{f+}\cdot\boldsymbol{x}-\omega t\right)\Big\}\mathrm{e}^{-k^i_{x,f+}x}+ \\ &+\mathrm{Re}\left[\chi_{s+}\rho'_{s+}\right]\cos\left(\boldsymbol{k}_{s+}\cdot\boldsymbol{x}-\omega t\right) - \mathrm{Im}\left[\chi_{s+}\rho'_{s+}\right]\sin\left(\boldsymbol{k}_{s+}\cdot\boldsymbol{x}-\omega t\right)+ \\ &+\mathrm{Re}\left[\chi_{s-}\rho'_{s-}\right]\cos\left(\boldsymbol{k}_{s-}\cdot\boldsymbol{x}-\omega t\right) - \mathrm{Im}\left[\chi_{s-}\rho'_{s-}\right]\sin\left(\boldsymbol{k}_{s-}\cdot\boldsymbol{x}-\omega t\right)\Big],\end{aligned} \tag{4.3.5}$$

in which $\boldsymbol{k}^r_{f+} = [k^r_{x,f+},\, k_y,\, 0]^\intercal$, $k^r_{x,f+} \equiv \mathrm{Re}[k_{x,f+}]$ and $k^i_{x,f+} \equiv \mathrm{Im}[k_{x,f+}]$. The vorticity field is computed from:

$$\begin{aligned}\omega'_{LIA} = -\epsilon\omega\Big[&\Big\{\mathrm{Im}\left[\Omega_{f+}\right]\cos\left(\boldsymbol{k}^r_{f+}\cdot\boldsymbol{x}-\omega t\right) + \mathrm{Re}\left[\Omega_{f+}\right]\sin\left(\boldsymbol{k}^r_{f+}\cdot\boldsymbol{x}-\omega t\right)\Big\}e^{-k^i_{x,f+}x}+ \\ &+\mathrm{Im}\left[\Omega_{s+}\right]\cos\left(\boldsymbol{k}_{s+}\cdot\boldsymbol{x}-\omega t\right) + \mathrm{Re}\left[\Omega_{s+}\right]\sin\left(\boldsymbol{k}_{s+}\cdot\boldsymbol{x}-\omega t\right)+\end{aligned} \tag{4.3.6}$$



(a) $\varphi_1 = 0.00000°$ (b) $\varphi_1 = 26.56505°$

Fig. 4.27: Comparison between DNS (top plane in both plots) and LIA projection (bottom plane in both plots) density (black/white) and vorticity contours (green/red) for entropy mode refracted incident at $\theta_1 = 50.00°$ on parallel and obliquefast MHD shocks respectively. Upstream mean magnetic field angle, φ_1, shown. Shock located at $x = 0$ (blue line). Displacement of shock from steady–state position visible in DNS result. Snapshot taken after propagation of backward slow mode through selected domain, $t = 28$.

$$+\mathrm{Im}\left[\Omega_{s-}\right]\cos\left(\boldsymbol{k}_{s-}\cdot\boldsymbol{x}-\omega t\right)+\mathrm{Re}\left[\Omega_{s-}\right]\sin\left(\boldsymbol{k}_{s-}\cdot\boldsymbol{x}-\omega t\right)\Big].$$

The relative root–mean–squared and maximum error between the DNS and LIA projections are computed. To normalise the errors we compute the magnitude of the complex amplitude of each refracted wave mode (contributing to a given flow property, "ϕ"), $|\xi^{\phi}_{\mu}| = (\mathrm{Re}[\xi^{\phi}_{\mu}]+\mathrm{Im}[\xi^{\phi}_{\mu}])^{1/2}$, and divide the error by the maximum magnitude, ξ^{ϕ}_{max}:

$$\xi^{\phi}_{max} = max(|\xi^{\phi}_{E}|,\, |\xi^{\phi}_{f+}|,\, |\xi^{\phi}_{s+}|,\, |\xi^{\phi}_{s-}|), \tag{4.3.7}$$

at each respective incidence angle (note that the following substitution is used, $\xi^{\omega}_{\mu} \equiv \Omega_{\mu}$). As such, the relative error can be contextualised as the margin of confidence in a given post–shock flow property value with respect to the amplitude of the largest contributing wave mode.

The relative root–mean–squared error, L^{ϕ}_{rms}:

$$L^{\phi}_{rms} = \left(\frac{1}{n_s \times n_y}\sum_{i=n_1}^{n_2}\sum_{j=1}^{n_y}\left(\frac{\phi'_{LIA}(i,j)-\phi'_{DNS}(i,j)}{\epsilon\xi^{\phi}_{max}}\right)^2\right)^{1/2}, \tag{4.3.8}$$

where $n_s = (n_2 - n_1 + 1)$.

The relative maximum error, L^{ϕ}_{∞}:

$$L^{\phi}_{\infty} = max\left(\frac{|\phi'_{LIA}(i,j)-\phi'_{DNS}(i,j)|}{\epsilon\xi^{\phi}_{max}}\right), \quad \text{for} \quad i \in \{n_1,\dots n_2\}, \quad j \in \{1,\dots,n_y\}. \tag{4.3.9}$$

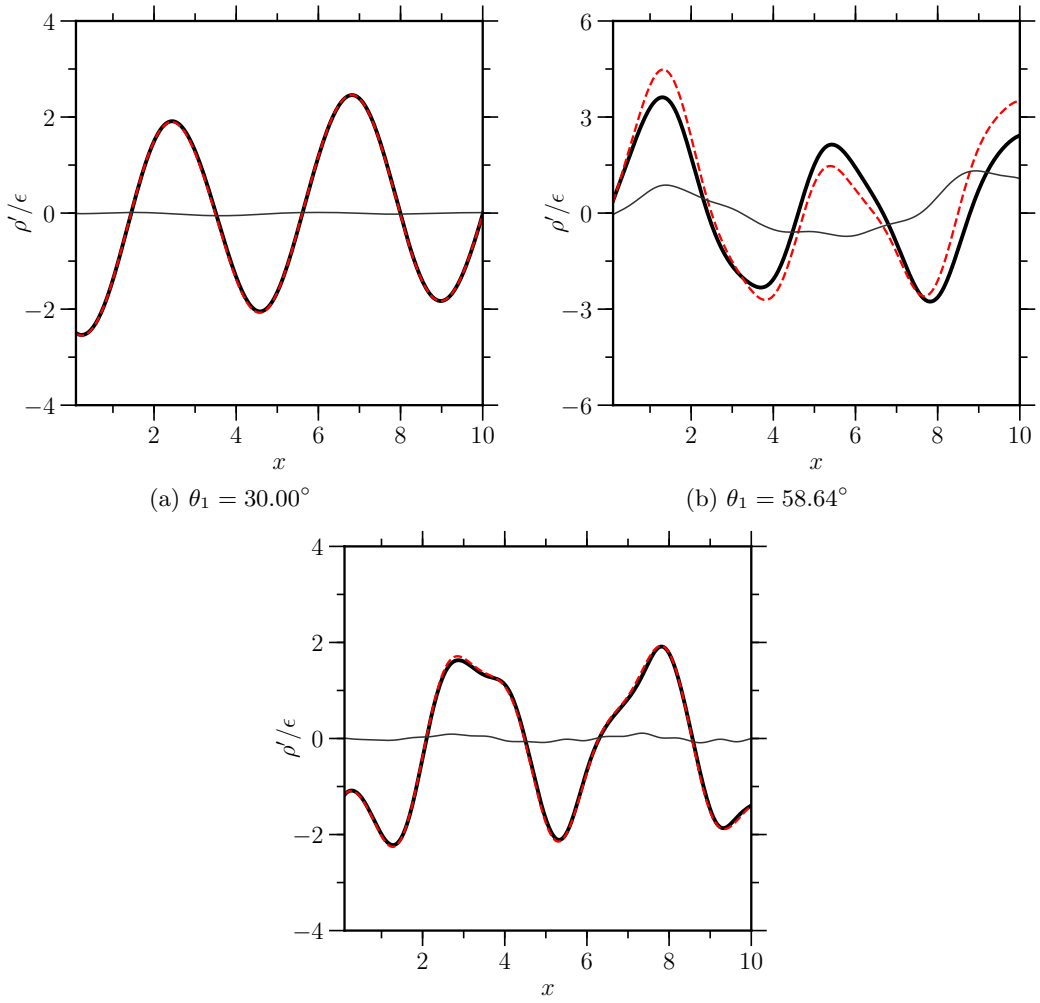
In figure 4.27, an example of the LIA projection onto the density and vorticity fields for an entropy mode incident at $\theta_1 = 50.00°$, refracted through parallel and oblique fast MHD shocks respectively is compared to the DNS result at $t = 28$ (corresponding to the backward slow mode propagating a distance $> \lambda_x$ away from the shock for both cases). To compensate for the time–lag introduced by the non–zero shock thickness in the DNS result, a small phase shift is added to the LIA projection in (4.3.5) - (4.3.6). Figure 4.27 represents the phase shift added for which the maximum error in the density field is at a minimum. Qualitatively, the DNS and LIA fields compare well with each other, there exists no noticeable discrepancy between the alignment or amplitude at the centre–line of the domain ($y = \lambda_y$).

4.3.3.1 Parallel MHD shock

The density and vorticity profiles at the y position containing the maximum error at $t = 28$ are shown for the parallel MHD shock case in figures 4.28 and 4.29 for a selection of incidence angles in the propagative regime away from the critical value, $\theta_1 = 30.00°$, and in the non–propagative regime close to and away from the critical angle, $\theta_1 = 58.64°$ and $\theta_1 = 75.00°$ respectively. For all incidence angles, density fluctuations are dominated by the relatively large wavelength entropy mode whereas vorticity fluctuations are primarily transported by the backward slow mode which has a smaller wavelength.

In the propagative regime, $\theta_1 = 30.00°$, very good agreement between LIA and DNS results is observed in both the density (figure 4.28a) and vorticity (figure 4.29a) fields. In the non–propagative regime, $\theta_1 = 75.00°$, a relatively small discrepancy between DNS and LIA results is apparent in the density field (figure 4.28c) whereas the vorticity field (figure 4.30d) displays a noticeable error that grows with distance away from the shock. Near the critical angle (in the non–propagative regime), $\theta_1 = 58.64°$, larger discrepancies are observed between the DNS and LIA results in both the density (figure 4.28b) and vorticity (figure 4.30b) field, in which it appears the predicted LIA wave amplitudes overshoot those computed in the DNS.

Assuming the LIA theory is accurate, discrepancies between DNS and LIA projections will result from either the imposed boundary conditions or the discretisation of the continuous flowfield. Regarding the latter, the grid employed in the present study captures the tangential wavelength of the incident and refracted modes on 64 grid points due to an enforced periodicity of 2 in the y-direction ($N_y = 128$ grid points) and the normal wavelength of the incident mode and refracted backward slow mode (i.e. smallest refracted normal wavelength) on 100 and > 73 grid points respectively for all incidence angles computed. In section 3.3.5, it was shown the DRP finite difference scheme employed in the present study accurately captured the propagation of a circularly–polarised Alfvén wave on 32 grid points (which exceeds the theoretical minimum of 4 points–per–wavelength for well–resolved structures captured using a DRP scheme). As such, insufficient grid resolution is unlikely the source of error in the non–propagative regime results - in particular when it is noted that



(a) $\theta_1 = 30.00^\circ$

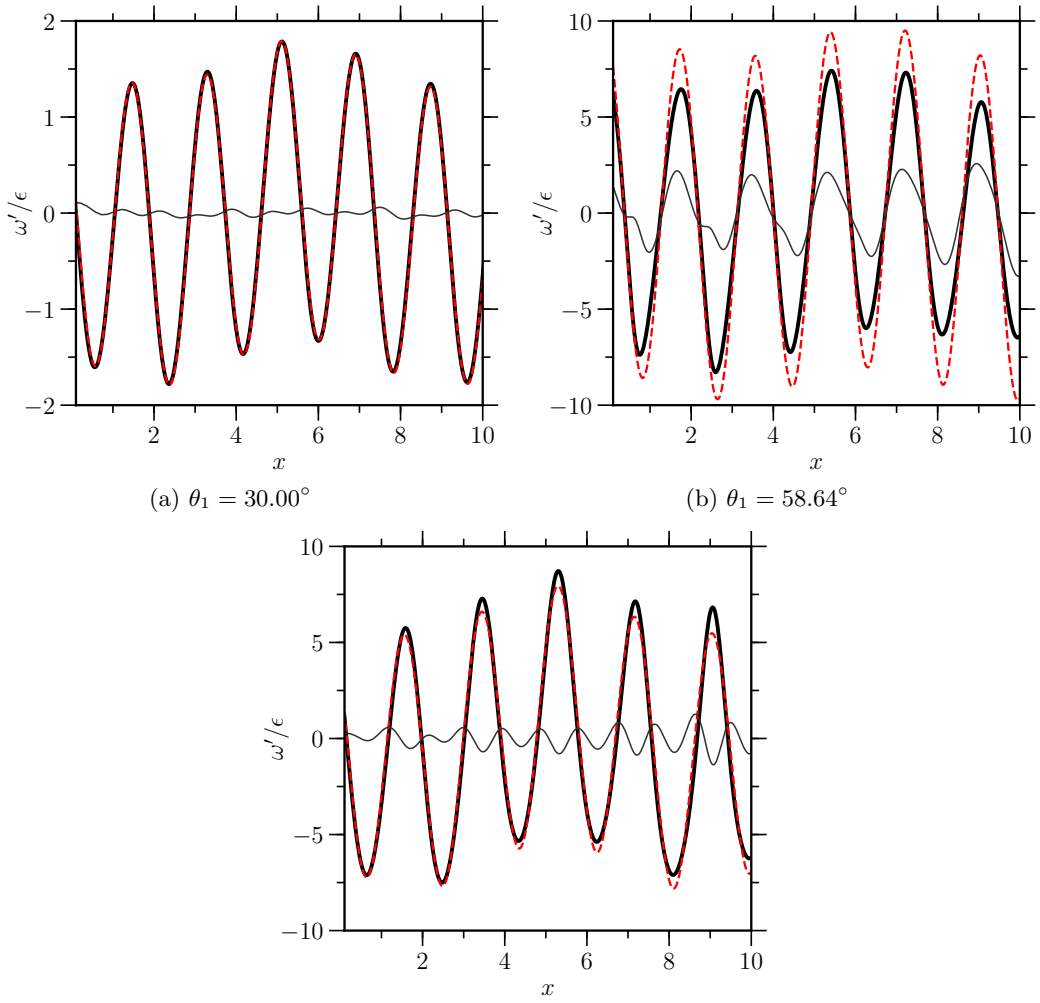
(b) $\theta_1 = 58.64^\circ$

(c) $\theta_1 = 75.00^\circ$

Fig. 4.28: Fluctuating post–shock density, ρ' at $t = 28$ shown for refraction of two–dimensional entropy plane waves (amplitude, $\epsilon = 0.01$, and incidence angle, θ_1) across a parallel ($\varphi_1 = 0.0^\circ$) fast MHD shock (located at $x = 0$). DNS data (black solid line), LIA projection (dashed red line) and error between DNS and LIA (thin grey line). Slice through domain taken along y position at which maximum error between DNS and LIA projection computed. Plots shown for incidence angles above, close to and below critical angle, $\theta^{c\pm} \approx \pm 58.63^\circ$. Propagative regime in the range, $\theta^{c-} < \theta_1 < \theta^{c+}$.

the resolution of the refracted backward slow mode normal wavelength for an entropy wave incident in the propagative regime (in which DNS and LIA compare well) is similar or lower than that of the non–propagative regime cases; $\lambda_{x,s+}^{\theta_1=30.00^\circ}/\Delta x_4 \approx 74$, $\lambda_{x,s+}^{\theta_1=58.64^\circ}/\Delta x_4 \approx 74$, $\lambda_{x,s+}^{\theta_1=75.00^\circ}/\Delta x_4 \approx 76$ (Δx_4 denotes grid spacing in region $x \in [x_c, x_d]$, see figure 4.17).

In terms of boundary conditions, shock refraction theory assumes a continuously forced entropy mode of amplitude, $\epsilon \to 0$ (i.e. interaction is linear), impinging on a shock of thickness, $\Delta \to 0$, at an incidence angle θ_1, generates all post–shock modes (i.e. there are no reflections from domain boundaries). However, the incident entropy mode in the DNS has a finite amplitude, $\epsilon = 0.01$, and impinges on a shock of finite thickness, for which $\lambda_x/\Delta \approx 325$ ($\lambda_x/\Delta \to \infty$ in LIA theory). Additionally, the Gaussian–fit smoothing



(a) $\theta_1 = 30.00°$

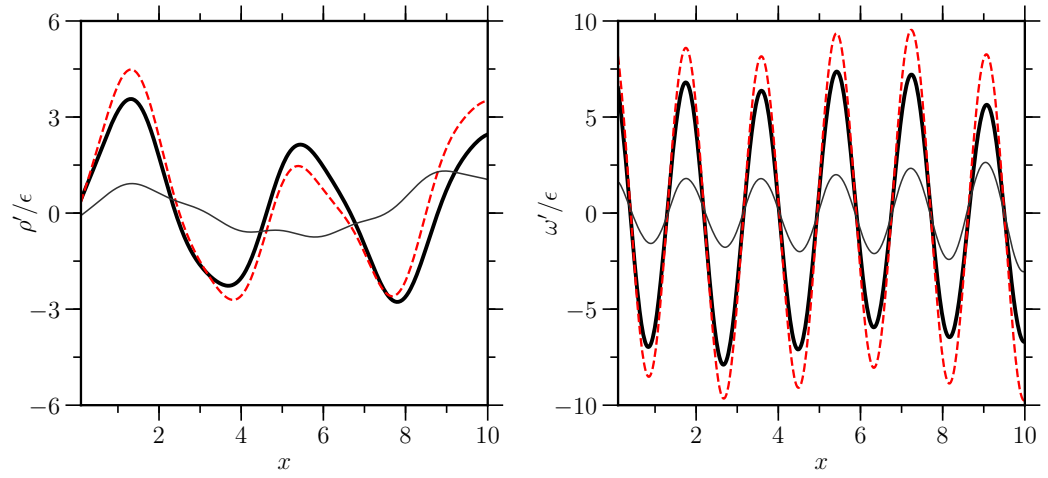
(b) $\theta_1 = 58.64°$

(c) $\theta_1 = 75.00°$

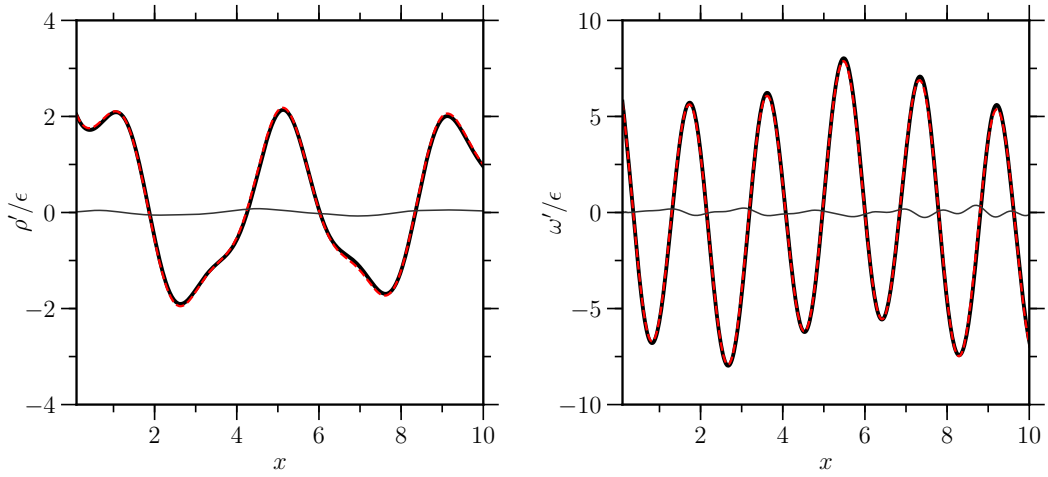
Fig. 4.29: Fluctuating post–shock vorticity, ω' at $t = 28$ shown for refraction of two–dimensional entropy plane waves (amplitude, $\epsilon = 0.01$, and incidence angle, θ_1) across a parallel ($\varphi_1 = 0.0°$) fast MHD shock. See figure 4.28 for additional information.

applied to the incident entropy mode in the initial pre–shock field introduces additional modes which are then refracted through the shock. Furthermore, reflections of the refracted modes and initial transient modes in the uniform–sponge region boundary ($x = x_d$) and the outlet ($x = x_e$) may also contribute to the post–shock field. Theoretically, as the DNS set–up approaches the exact LIA theory conditions ($\epsilon \to 0$ and $\lambda_x/\Delta \to \infty$) the DNS result should also approach an exact fit with the LIA projection. However, contributions to the post–shock field by the initial transients and reflections may cause a discrepancy between DNS and LIA results that is independent of both ϵ and λ_x/Δ.

To discern whether nonlinear effects are the source of errors for $\theta_1 = 58.64°$ and $\theta_1 = 75.00°$, in figure 4.30, we show the post–shock density and vorticity fields for a continuously forced entropy mode of reduced amplitude, $\epsilon = 0.001$. For $\theta_1 = 75.00°$, the vorticity field error has reduced to a similar magnitude to that of the density field (which remains relatively unchanged compared to $\epsilon = 0.01$) suggesting magneto–acoustic



(a) $\theta_1 = 58.64°$ (b) $\theta_1 = 58.64°$

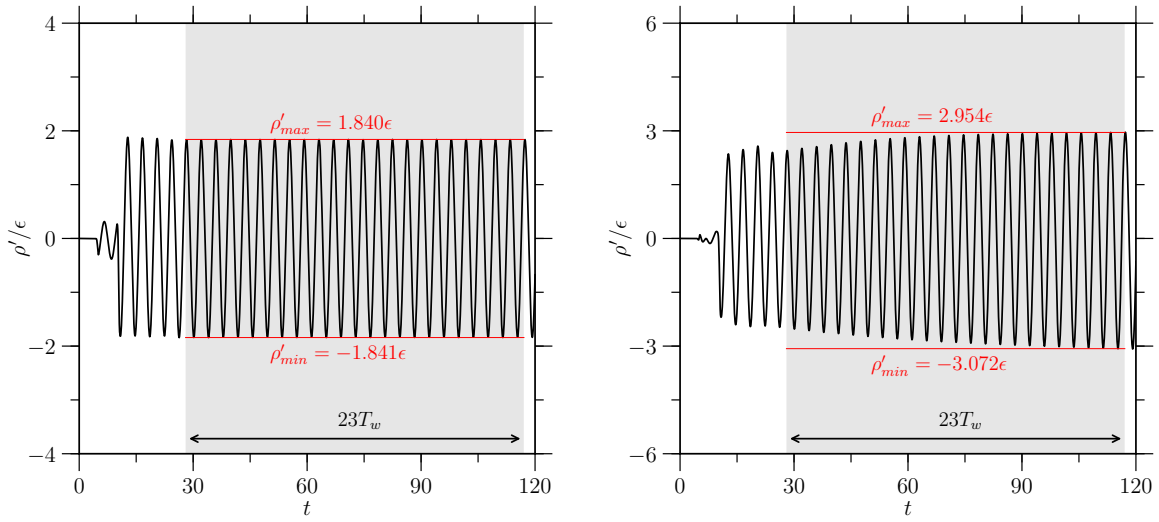


(c) $\theta_1 = 75.00°$ (d) $\theta_1 = 75.00°$

Fig. 4.30: Fluctuating post–shock density, ρ', and vorticity, ω', at $t = 28$ shown for refraction of two–dimensional entropy plane waves (amplitude, $\epsilon = 0.001$, and incidence angle, θ_1) across a parallel ($\varphi_1 = 0.0°$) fast MHD shock. See figure 4.28 for additional information.

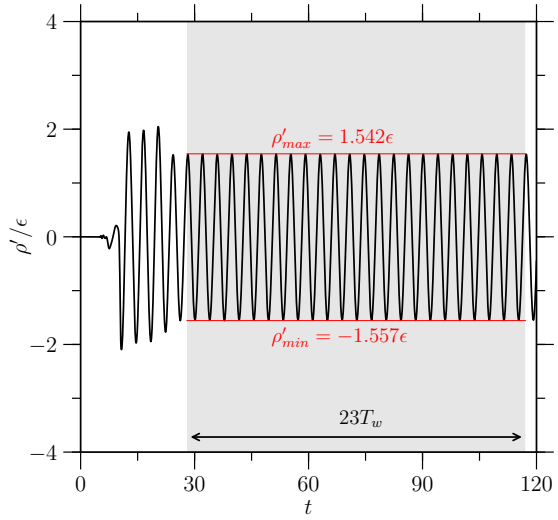
modes (transporting vorticity) are particularly sensitive to nonlinear behaviour. However, for $\theta_1 = 58.64°$, neither the density nor vorticity field error show significant reduction compared to $\epsilon = 0.01$ (in figures 4.28 and 4.29) indicating issues unrelated to nonlinear effects are also of importance for incidence angles close to the critical value.

The presence of transients is observed in figure 4.31 where the fluctuating density value at λ_x away from the shock front along the centre–line, $y = \lambda_y$, is plotted with respect to time for $\theta_1 = 30.00°$, $\theta_1 = 58.64°$ and $\theta_1 = 75.00°$. In the absence of a transient, it is expected the amplitude of a time signal at the fixed sample position will be constant for $t > x_{sh}/\bar{u}_1 + \lambda_x/(\bar{u}_2 - V_{sn,2})$ - i.e. the time taken for the backward slow mode (generated by an entropy mode forced at the domain inlet at $t = 0$) to pass through the sample position. For the given base flow, $x_{sh}/\bar{u}_1 + \lambda_x/(\bar{u}_2 - V_{sn,2}) \approx 25.1$.



(a) $\theta_1 = 30.00°$

(b) $\theta_1 = 58.64°$



(c) $\theta_1 = 75.00°$

Fig. 4.31: Transient behaviour of post–shock fluctuating density flowfield at an incident normal wavelength distance away from the shock, $x = \lambda_x = 10.0$ (shock located at $x = 0.0$), along the centre–line, $y = \lambda_y = 10.0/\tan\theta_1$, for refraction of two–dimensional entropy plane waves (amplitude, $\epsilon = 0.01$, and incidence angle, θ_1) across a parallel ($\varphi_1 = 0.0°$) fast MHD shock. Maximum and minimum values of density fluctuation (ρ'_{max} and ρ'_{min} respectively, indicated by solid red lines) extracted from shaded region which spans peak–to–peak in the range, $28 < t < 28{+}23T_w = 117$, where T_w is the time period of the refracted waves.

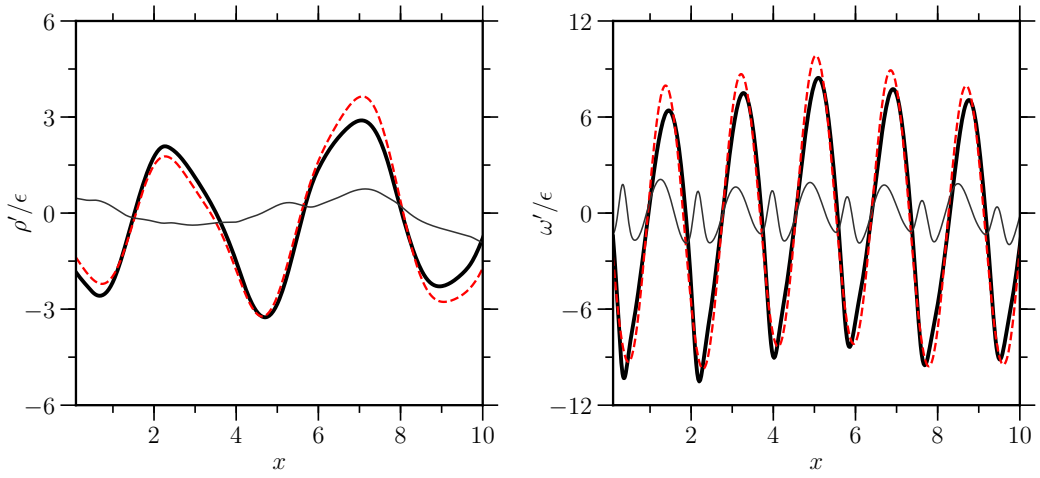


Fig. 4.32: Fluctuating post–shock density (left) and vorticity (right) at $t = 110$ shown for refraction of a two–dimensional entropy plane wave (amplitude, $\epsilon = 0.01$, and incidence angle, $\theta_1 = 58.64°$) across a parallel ($\varphi_1 = 0.0°$) fast MHD shock. See figure 4.28 for additional information.

From figures 4.31a and 4.31c, we find that transient behaviour, with respect to changing amplitude, is insignificant at the sample time, $T_s = 28$, for $\theta_1 = 30.00°$ and $\theta_1 = 75.00°$ respectively. For $\theta_1 = 58.64°$, transient behaviour is apparent in figure 4.31b for $t < 105$. Possible origins of the prolonged transient behaviour are refracted waves (and their resulting reflections in the domain boundaries) generated by additional modes (close to the critical angle) introduced upstream by the Gaussian–fit smoothing. The longer characteristic length of decay for forward fast waves produced by entropy modes incident near the critical angle (compared to further along the non–propagative regime) may also play a role in the size of contribution of these initial transients (and their reflections) to the post–shock field.

Figure 4.33 shows the density and vorticity field for $\theta_1 = 58.64°$ and $\epsilon = 0.01$ at $t = 110$ (i.e. after the passage of transients). Agreement between DNS and LIA projection appears to have improved compared to $t = 28$ in figures 4.28 and 4.29. However, there appears to be a noticeable "steepening" of vorticity fluctuations. With respect to the density field, the reduced error is still relatively large compared to both $\theta_1 = 30.00°$ and $\theta_1 = 75.00°$ but does not show any clear signs of a steepening wave. Two possible causes of "steepening" in the vorticity field could be nonlinear behaviour (primarily affecting the magneto–acoustic modes) or the superposition of reflected magneto–acoustic waves (originating from the domain boundary) adding to the post–shock field. Figure 4.30, showing lower amplitude post–shock vorticity fluctuations for a reduced amplitude incident entropy wave ($\epsilon = 0.001$) indicates the steepening of vorticity–carrying waves is possibly the result of nonlinear behaviour. However, compared to $\theta_1 = 30.00°$ and $\theta_1 = 75.00°$, a significant discrepancy remains between the DNS and LIA results for both vorticity and density (which shows only a relatively small error difference between $\epsilon = 0.001$ and $\epsilon = 0.01$) suggesting the presence of issues unrelated to nonlinear effects.

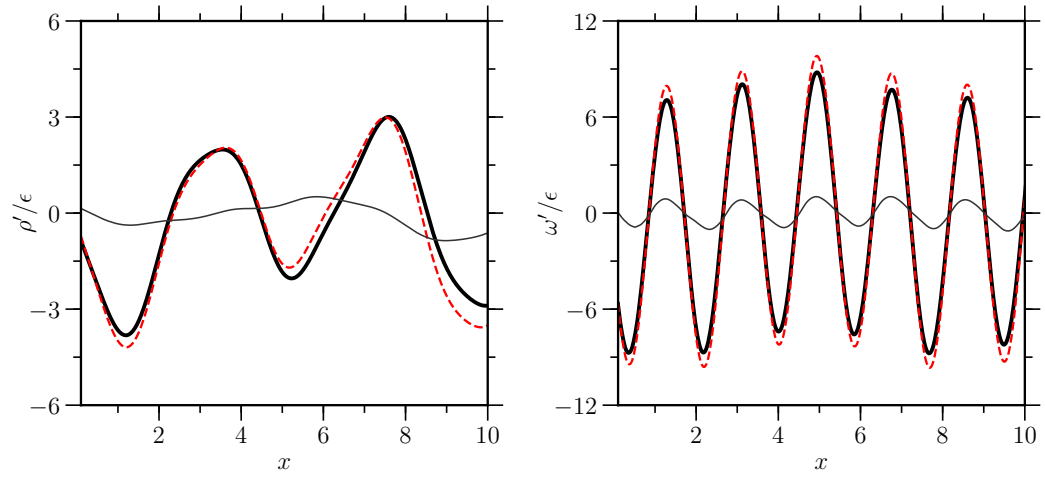


Fig. 4.33: Fluctuating post–shock density (left) and vorticity (right) at $t = 110$ shown for refraction of a two–dimensional entropy plane wave (amplitude, $\epsilon = 0.001$, and incidence angle, $\theta_1 = 58.64°$) across a parallel ($\varphi_1 = 0.0°$) fast MHD shock. See figure 4.28 for additional information.

If we consider the signal at the sampling point after all transients have passed through, in addition to a constant amplitude, it is expected that the magnitude of the minimum and maximum density fluctuations are equal (i.e. the perturbations are centred on zero), $|\rho'_{max}| = |\rho'_{min}|$ for which we define ρ' at $(x, y) = (\lambda_x, \lambda_y)$ and t:

$$\rho' = \mathrm{Re}\left[A\mathrm{e}^{-\mathrm{i}\omega t}\right], \tag{4.3.10}$$

where A is a constant,

$$A = \{[\chi_E]\mathrm{e}^{\mathrm{i}(k_{x,E}\lambda_x)} + [\chi_{f+}e^{\rho}_{f+}]\mathrm{e}^{\mathrm{i}(k_{x,f+}\lambda_x)} + [\chi_{s+}e^{\rho}_{s+}]\mathrm{e}^{\mathrm{i}(k_{x,s+}\lambda_x)} + [\chi_{s-}e^{\rho}_{s-}]\mathrm{e}^{\mathrm{i}(k_{x,s-}\lambda_x)}\}\mathrm{e}^{\mathrm{i}k_y\lambda_y}.$$

For time, $28 < t < 28 + 23T_w$, (where T_w is the time period of the refracted waves, $T_w = 2\pi/\omega = \lambda_x/\bar{u}_1$, if we define the density perturbation amplitude difference, $D = |\rho'_{max}| - |\rho'_{min}|$, figure 4.31a shows $D = -0.001 \times 10^{-2}$, $D = -0.118 \times 10^{-2}$, and $D = -0.015 \times 10^{-2}$ for $\theta_1 = 30.00°$, $\theta_1 = 58.64°$ and $\theta_1 = 75.00°$ respectively. These values of D indicate there has been a small shift in the underlying base flow for all three θ_1 values. Applying these respective shifts in post–shock density to the upstream Mach number we obtain the following values for $\theta_1 = 30.00°$, $\theta_1 = 58.64°$ and $\theta_1 = 75.00°$; $M_1 = 2.0000$, $M_1 = 1.9999$ and $M_1 = 2.0000$ respectively. From the shift in M_1 for $\theta_1 = 58.64°$, we compute a maximum change in amplitude of density and vorticity fluctuations for the refracted modes (ξ^{ρ}_{μ} and Ω_{μ} respectively) of $< 1\%$ compared to $M_1 = 2.0000$. From table 4.2, we find that the maximum relative vorticity error for $\theta_1 = 58.64°$ and $\epsilon = 0.001$ at $t = 110$ is around double the value of $\theta_1 = 30.00°$ for $\epsilon = 0.01$ and $\theta_1 = 75.00°$ for $\epsilon = 0.001$ at $t = 28$. The maximum relative density error is several times larger for the former case compared to the latter two cases. As the shift in base flow will only produces a relative change in the post–shock fields of $< 1\%$, it is not credible to

θ_1	ϵ	T_s	L^{ρ}_{∞}	L^{ω}_{∞}
30.00°	0.01	28	0.0254	0.0671
58.64°	0.01	28	0.4779	0.3690
58.64°	0.001	28	0.4762	0.3431
58.64°	0.01	110	0.3374	0.2366
58.64°	0.001	110	0.3121	0.1258
75.00°	0.01	28	0.0578	0.2055
75.00°	0.001	28	0.0415	0.0560

Table 4.2: Maximum relative error between DNS and LIA projection in post–shock fluctuating density, L^{ρ}_{∞}, and vorticity, L^{ω}_{∞}, (see (4.4.2) for definition of L^{ϕ}_{∞}) for the refraction of two–dimensional entropy plane waves of amplitude, ϵ, incident at θ_1, across a parallel ($\varphi_1 = 0.0°$) fast MHD shock. Sample time, T_s, given in time units.

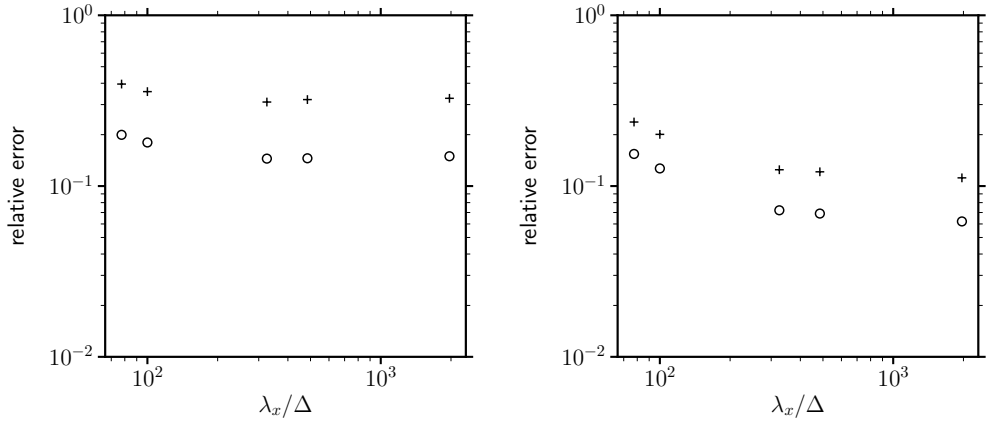


Fig. 4.34: Convergence of relative error between DNS data and LIA projection for post–shock density (left) and vorticity (right). Relative error computed at time, $t = 110$, for entropy mode of normal wavelength, λ_x, and amplitude, $\epsilon = 0.001$, incident at $\theta_1 = 58.64°$, on a parallel shock of thickness, Δ. Relative root–mean–squared error (circles) and maximum error (crosses) shown.

attribute it to the discrepancy in DNS and LIA density and vorticity fields for $\theta_1 = 58.64°$.

In figure 4.34 the shock thickness, Δ, is explored as a potential source of error between DNS and LIA post–shock fields at $t = 110$ for an entropy mode of amplitude, $\epsilon = 0.001$, incident at $\theta_1 = 58.64°$ on a parallel MHD shock. In both the density and vorticity fields we observe a reduction in the maximum relative error as the ratio between the normal incident mode wavelength, λ_x, and Δ, is increased from ~ 77 to ~ 325. However, for $\lambda_x/\Delta > 325$, no significant reduction in error is observed indicating there is potentially another more dominant error source contributing to the post–shock field.

Further study is necessary in order to identify the reason for the lack of expected convergence between the DNS result and LIA projection for $\epsilon \to 0$ and $\lambda_x/\Delta \to \infty$ for an incident angle close to the critical value. A closer examination of the potential contribution of reflected modes to the post–shock field presents an additional avenue of investigation. This will likely involve evaluating the influence of the domain length and difference in resolution between the uniform and sponge regions (as both represent types of boundaries in the post–shock field). The refraction of entropy modes for lower ϵ and higher λ_x/Δ values could also

be computed. However, for lower ϵ values care must be taken with respect to the numerical shock capture strategy to ensure wiggle amplitude does not scale on ϵ. Additionally, higher λ_x/Δ values will necessitate reductions in time steps which may make it considerably computationally expensive to run simulations for sufficiently long times such that transients have exited the sample region. The expensiveness of simulations may also be increased further when smaller time steps are applied in conjunction with aforementioned changes to the domain boundaries (which will likely necessitate a larger grid).

In the present study, it has been shown that entropy modes incident on a parallel MHD shock in the propagative and non–propagative regime away from the critical angle show good agreement between DNS and LIA post–shock density and vorticity fields. LIA theory for propagative and non–propagative regimes involve the computation of real and complex–valued refraction coefficients respectively. It is thought that relatively large discrepancies in DNS and LIA post–shock fields for an incident angle close to the critical value are numerical in origin rather than a failure of the LIA theory to compute complex–valued refraction coefficients. As such, it can be considered that the exact identification of these numerical issues are somewhat outside the scope of the current study. Several avenues of investigation have been suggested, however, they are computationally expensive and will therefore be left to the efforts of further studies.

4.3.3.2 Oblique MHD shock

Figures 4.35 - 4.37 show density and vorticity profiles of entropy mode refraction through an oblique shock, $\varphi_1 \approx 26.6°$, at a selection of incidence angles away from the critical value in the propagative and non–propagative regimes, $\theta_1 = -30.00°$ and $\theta_1 = 75.00°$ respectively, and close to the critical value in the propagative regime, $\theta_1 = 53.50°$. The significance of selecting a negative incidence angle in the propagative regime, $\theta_1 = -30.00°$, is that shock refraction is no longer symmetric, $\chi_\mu(\theta_1) \neq \chi_\mu(-\theta_1)$, for an oblique shock. As such, errors computed for θ_1 are no longer expected to mirror those computed for $-\theta_1$. For $\theta_1 = -30.00\circ$ and $\epsilon = 0.01$, from figure 4.35 we find that qualitatively, there exists good agreement between the DNS and LIA density and vorticity fields. The error appears similar in magnitude to that computed for the interaction of a parallel shock and entropy mode, of amplitude $\epsilon = 0.01$, incident in the propagative regime away from the critical angle ($\theta_1 = 30.00°$, figures 4.28a and 4.29a).

At a reduced amplitude, $\epsilon = 0.001$, an entropy mode incident at $\theta_1 = 53.50°$ on an oblique shock shows agreement between DNS and LIA density and vorticity fields at $t = 110$ (figure 4.36) that is visibly worse than that of $\theta_1 = 75.00°$ at $t = 28$ (figure 4.37). Similar to the parallel shock cases (see table 4.2) we find that for an oblique shock (see table 4.3), the relative error in both the density and vorticity field is lower for $\epsilon = 0.001$ compared to $\epsilon = 0.01$ for an incidence angle close to the critical angle ($\theta_1 = 53.50°$) or in the non–propagative regime ($\theta_1 = 75.00°$). However, a significant reduction in the relative error occurs for

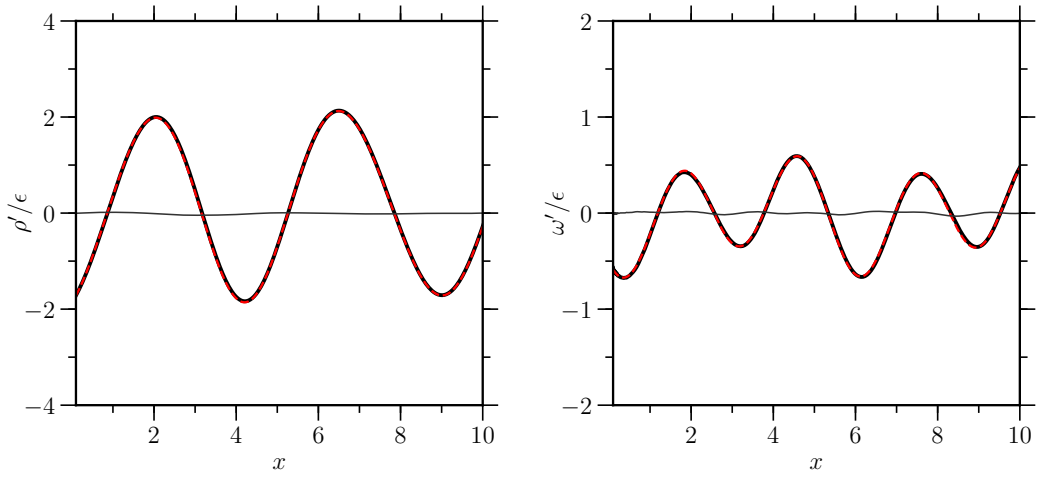


Fig. 4.35: Fluctuating post–shock density (left) and vorticity (right) at $t = 28$ shown for refraction of a two–dimensional entropy plane wave (amplitude, $\epsilon = 0.01$, and incidence angle, $\theta_1 = -30.00°$) across an oblique ($\varphi_1 = 26.56505°$) fast MHD shock. DNS data (black solid line), LIA projection (dashed red line) and error between DNS and LIA (thin grey line). Slice through domain taken along y position at which maximum error between DNS and LIA projection computed. Critical angles for $\theta_1 > 0$ and $\theta_1 < 0$ are $\theta_1^{c+} \approx 53.51°$ and $\theta_1^{c-} \approx -75.00°$ respectively. Propagative regime in the range, $\theta_1^{c-} < \theta_1 < \theta_1^{c+}$.

θ_1	ϵ	T_s	L^{ρ}_{∞}	L^{ω}_{∞}
$-30.00°$	0.01	28	0.0235	0.0639
$53.50°$	0.01	28	0.9941	0.4225
$53.50°$	0.001	28	0.9783	0.3140
$53.50°$	0.01	110	0.7520	0.7380
$53.50°$	0.001	110	0.5673	0.1350
$75.00°$	0.01	28	0.0607	0.3084
$75.00°$	0.001	28	0.0398	0.0673

Table 4.3: Maximum relative error between DNS and LIA projection in post–shock fluctuating density, L^{ρ}_{∞}, and vorticity, L^{ω}_{∞}, (see (4.4.2) for definition of L^{ϕ}_{∞}) for the refraction of two–dimensional entropy plane waves of amplitude, ϵ, incident at θ_1, across an oblique ($\varphi_1 = 26.56505°$) fast MHD shock. Sample time, T_s, given in time units.

$\theta_1 = 53.50°$ only at a later time (i.e. after the passage of transients). Additionally, even at a low amplitude and late time, the relative density error for $\theta_1 = 53.50°$ remains considerably higher than $\theta_1 = -30.00°$ and $\theta_1 = 75.00°$.

4.3.3.3 Dependency of relative errors on θ_1

Relative post–shock density and vorticity errors between DNS and LIA projections at $t = 28$ for an entropy mode, of amplitude $\epsilon = 0.01$, incident at a range of angles, $0.00° \leq \theta_1 \leq 75.00°$, on a parallel MHD shock, are shown in figures 4.38 and 4.39. The maximum and root–mean–squared relative errors in the propagative regime are reasonably independent of incidence angle and remain < 0.03 and < 0.10 for the density and vorticity fields respectively in the range, $\theta_1 \lessapprox 55°$. However, in approach of the critical incidence angle, $\theta^{c\pm} \approx \pm 58.63°$, both relative errors in the density and increase to around > 0.1. Past the critical angle, in the non–propagative, there exists a rapid decrease in both relative errors, the maximum value remaining

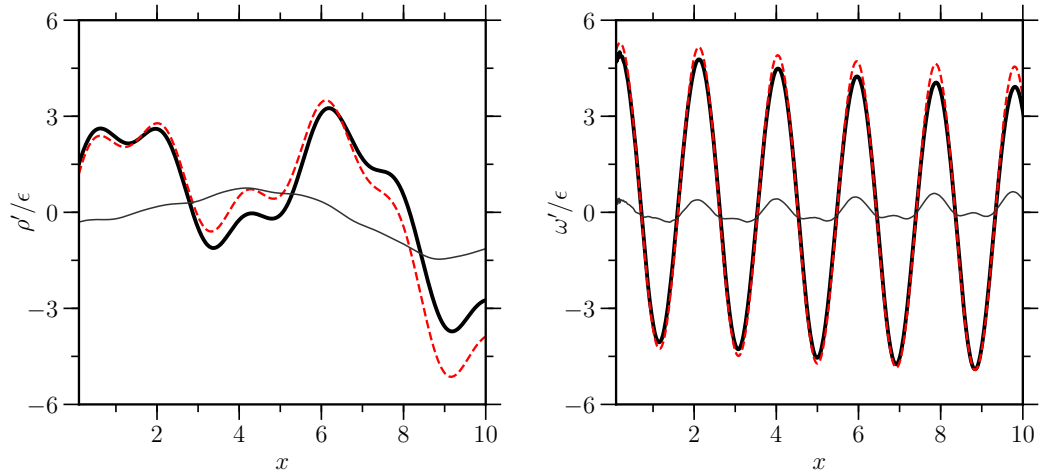


Fig. 4.36: Fluctuating post–shock density (left) and vorticity (right) at $t = 110$ shown for refraction of a two–dimensional entropy plane wave (amplitude, $\epsilon = 0.001$, and incidence angle, $\theta_1 = 53.50°$) across an oblique ($\varphi_1 = 26.56505°$) fast MHD shock. See figure 4.35 for additional information.

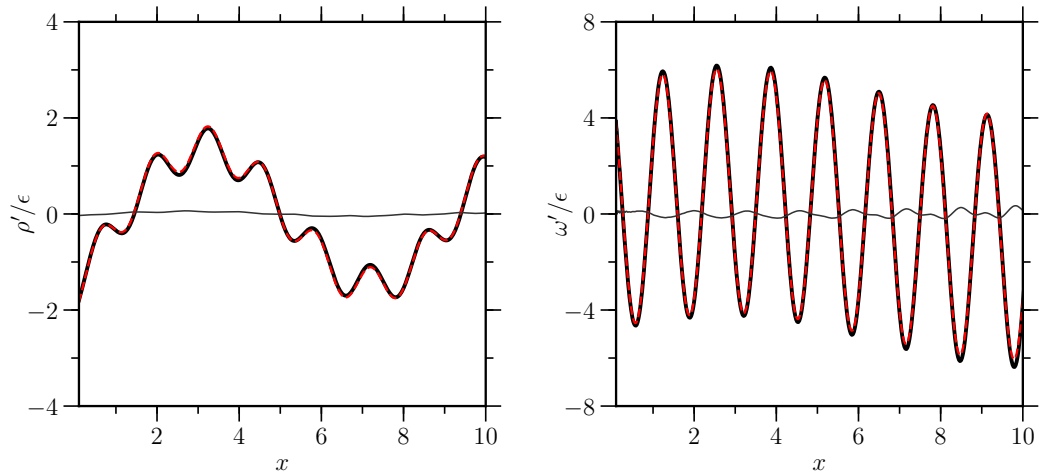


Fig. 4.37: Fluctuating post–shock density (left) and vorticity (right) at $t = 28$ shown for refraction of a two–dimensional entropy plane wave (amplitude, $\epsilon = 0.001$, and incidence angle, $\theta_1 = 75.00°$) across an oblique ($\varphi_1 = 26.56505°$) fast MHD shock. See figure 4.35 for additional information.

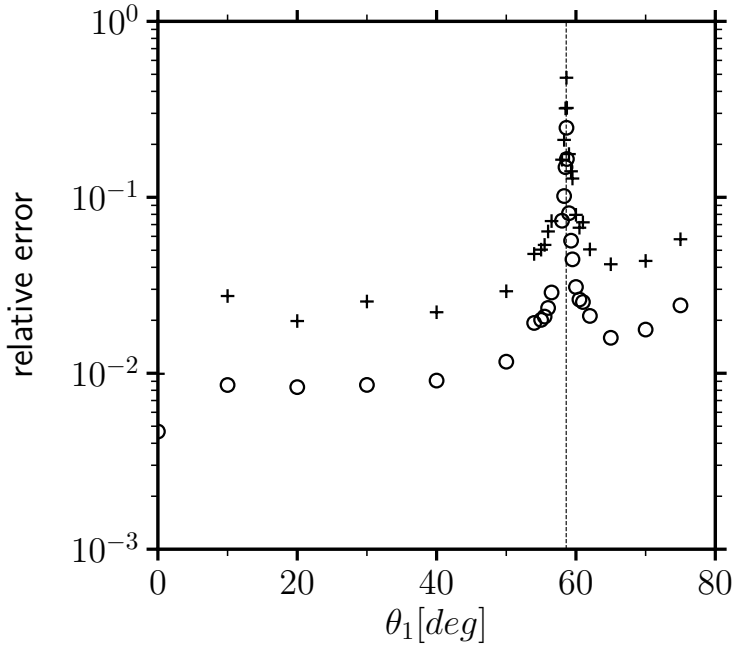


Fig. 4.38: Relative density field error between DNS data and projection of LIA onto physical space for the interaction of two–dimensional entropy plane waves (incidence angle, θ_1, and amplitude, $\epsilon = 0.01$) with a parallel ($\varphi_1 = 0.0°$) MHD shock. Relative root–mean–squared error (circles), and maximum error (crosses). Vertical dashed line indicates the critical incidence angle.

around ~ 0.1 and the root–mean–squared value, < 0.1. Both errors appear to gradually increase with increasing θ_1.

In figures 4.40 and 4.41 the relative density and vorticity errors are shown for the oblique shock case at a range of incidence angles, $-85.00° \leq \theta_1 \leq 75.00°$. In the propagative regime away from the critical angles, $\theta^{c-} \approx -75.00°$ and $\theta^{c+} \approx 53.51°$, like the parallel shock case, the relative error remains largely independent of incidence angle (and thus maximum fluctuation amplitude) for both density and vorticity fields, taking values of < 0.02 and < 0.1 respectively. Similar to the parallel shock case, in approach of the critical angle, both fields show a significant increase in relative errors before rapidly reducing in the non–propagative regime. As mentioned previously, the increase in relative error near the critical angle and in the non–propagative regime is likely the result of numerical sensitivity of the post–shock field. Relative vorticity errors shown in figure 4.39 are around ~ 3 times higher than those found in the density field. From section 4.3.3.2 we can infer this is a result of the vorticity field being more sensitive to nonlinear behaviour that was suggested as being present for $\epsilon = 0.01$.

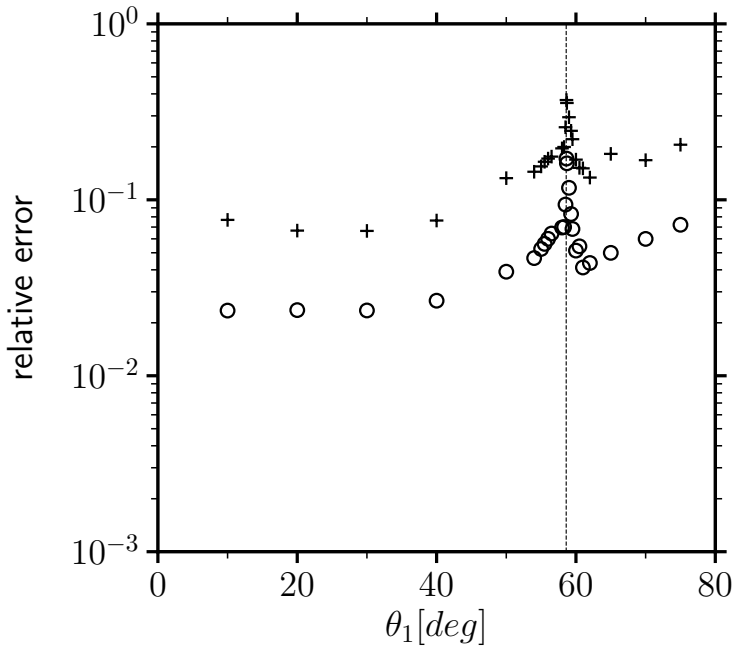


Fig. 4.39: Relative vorticity field error between DNS data and projection of LIA onto physical space for the interaction of two–dimensional entropy plane waves (incidence angle, θ_1, and amplitude, $\epsilon = 0.01$) with a parallel ($\varphi_1 = 0.0°$) MHD shock. Relative root–mean–squared error (circles), and maximum error (crosses). Vertical dashed line indicates the critical incidence angle.

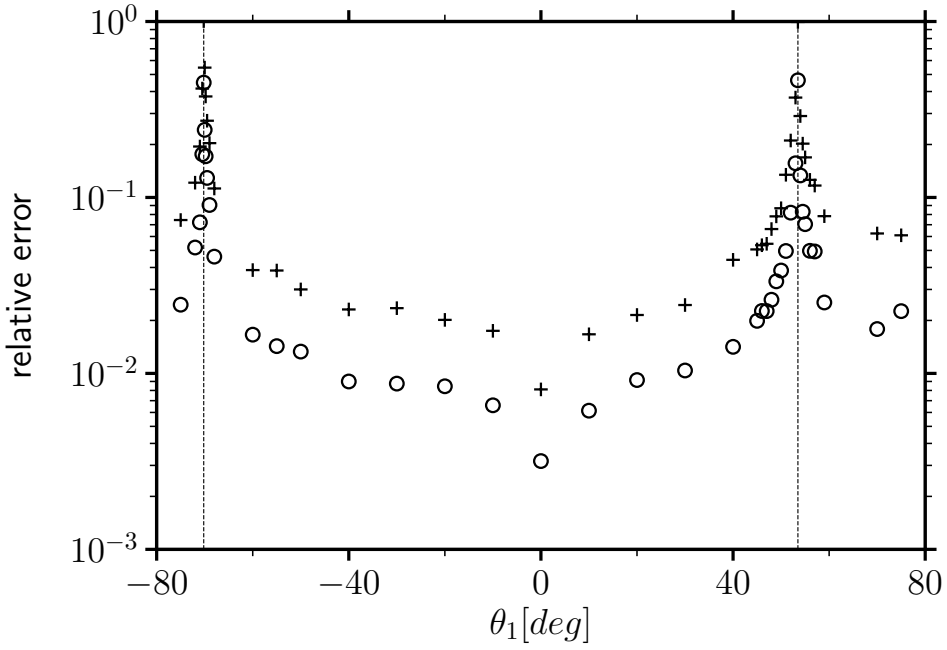


Fig. 4.40: Relative density field error between DNS data and projection of LIA onto physical space for the interaction of two–dimensional entropy plane waves (incidence angle, θ_1, and amplitude, $\epsilon = 0.01$) with an oblique ($\varphi_1 = 26.56505°$) MHD shock. Relative root–mean–squared error (circles), and maximum error (crosses). Vertical dashed line indicates critical incidence angles.

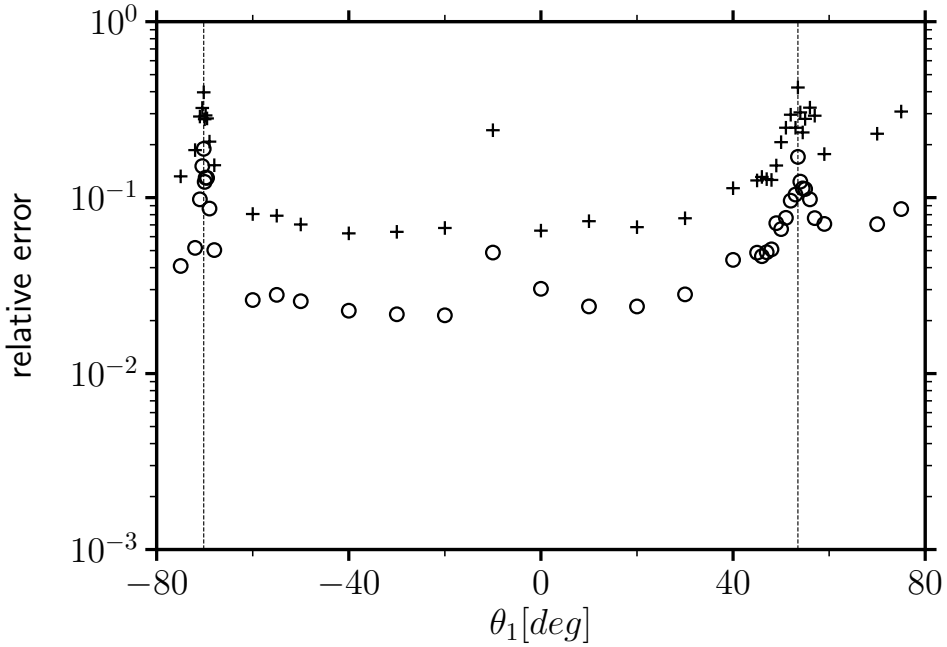


Fig. 4.41: Relative vorticity field error between DNS data and projection of LIA onto physical space for the interaction of two–dimensional entropy plane waves (incidence angle, θ_1, and amplitude, $\epsilon = 0.01$) with a oblique ($\varphi_1 = 26.56505°$) MHD shock. Relative root–mean–squared error (circles), and maximum error (crosses). Vertical dashed line indicates critical incidence angles.

4.4 Gaussian-distributed entropy spot interaction with a fast shock

In this section we study the refraction of a small negative density perturbation with uniform pressure, velocity and magnetic field (i.e. entropy mode) across a fast MHD shock in both two– and three–dimensions. The influence of the upstream magnetic field angle on the generation of vorticity in the post–shock flow is investigated at constant upstream normal plasma beta, $\beta_{n,1} = 2.0$. Both the intensity and distribution of vorticity across the refracted magneto–acoustic modes is of interest. Studies involve numerical simulations on a fully nonlinear code as well as a linear reconstruction of the post–shock field. The predictive capability of the linear theory is evaluated for perturbations 1% and 10% of the upstream mean density. Additionally, comparisons are made between the two–dimensional and three–dimensional interactions with respect to the in–plane vorticity generation.

4.4.1 Numerical method

The numerical strategy implemented in this section is similar to that of section 4.3. For all simulations presented in this section a 13-point stencil, 4^{th}-order DRP scheme (see section 3.1.1) is used in conjunction with a 13-point stencil, 8^{th}-order discrete filter (see section 3.1.2). We apply non-reflecting characteristic boundary conditions in the x-direction (see section 3.1.4). Periodic boundary conditions are applied in the y-direction. As in section 4.3, a five–block stretched grid strategy is employed in the x-direction to maintain scale separation between the shock thickness (captured on 20 points) and the incident perturbation. For two–dimensional grids implemented in this section, the following constraint is maintained - $l_{pert}/\Delta > 150$, where l_{pert} is the characteristic length scale of the perturbation which assumes a Gaussian shape with unitary mid–high width. For three–dimensional grids implemented in this section, $l_{pert}/\Delta > 25$, due to computational constraints.

In two–dimensions, the upstream entropy perturbation assumes a Gaussian in the form:

$$\mu_1' = \begin{bmatrix} \rho' \\ \boldsymbol{u}' \\ p' \\ \boldsymbol{B}' \end{bmatrix} = \begin{bmatrix} -\exp\left\{-\frac{1}{2}\left[\left(\frac{x-x_0}{r_0}\right)^2 + \left(\frac{y-y_0}{r_0}\right)^2\right]\right\} \\ \mathbf{0} \\ 0 \\ \mathbf{0} \end{bmatrix}, \tag{4.4.1}$$

and three–dimensions:

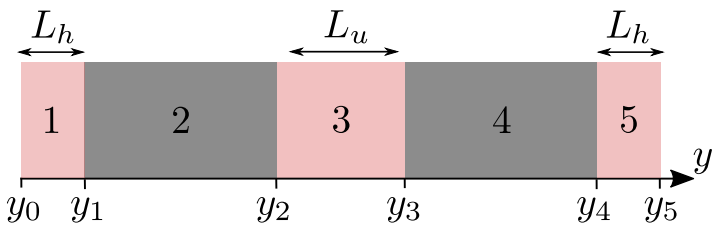


Fig. 4.42: Five–block grid stretching configuration in transverse directions (z direction stretching is equivalent). Uniform (non-uniform) regions represented by pink (grey) shading. Entropy spot–shock interaction studied in uniform region 3. Uniform regions 1 and 5 are the length of ghost cells at domain boundaries to enable periodicity to be enforced.

$$\mu_1' = \begin{bmatrix} \rho' \\ \boldsymbol{u}' \\ p' \\ \boldsymbol{B}' \end{bmatrix} = \begin{bmatrix} -\exp\left\{-\frac{1}{2}\left[\left(\frac{x-x_0}{r_0}\right)^2 + \left(\frac{y-y_0}{r_0}\right)^2 + \left(\frac{z-z_0}{r_0}\right)^2\right]\right\} \\ \mathbf{0} \\ 0 \\ \mathbf{0} \end{bmatrix}, \tag{4.4.2}$$

where $r_0 = 1/(2\sqrt{2\ln 2})$ and (x_0, y_0) and (x_0, y_0, z_0) are the central coordinates of the two–dimensional and three–dimensional Gaussian spots respectively. For each case presented in this section, $x_0/L_x = 0.07$, $y_0/L_t = 0.50$ and $z_0/L_t = 0.50$ (in three–dimensions only), where L_x is the length of the domain in the (streamwise) x-direction and L_t in the (transverse) y and z directions.

Six two–dimensional cases and two three–dimensional cases were run to investigate the entropy spot–shock interaction for parallel and oblique fast MHD shocks. In all simulations we initialise the upstream flow with $M_1 = 2.0$, $\rho_1 = p_1 = B_x = 1.0$ and $v_1 = 0$ (note: B_x is initialised as constant throughout the domain). These upstream conditions correspond to $\beta_{n,1} = 2.0$. Initialisation of the base flow in both two– and three–dimensional interactions involved the extrusion of the one–dimensional numerical solution in a method identical to that described in section 4.3. In the interaction the Gaussian-distributed entropy spot excites a large range of scales which are subsequently compressed across a fully–resolved shock. Consequently, a high grid resolution was necessary to capture all physical scales. Additionally, asymmetry in the entropy spot–oblique shock interaction was a factor in selection of transverse boundaries. The fast magneto–acoustic wave speed along the positive axis in one transverse direction can exceed that along the negative axis ($V_{fast,max}$ is in the direction perpendicular to the magnetic field which is no longer aligned with the shock normal). Furthermore, evolution of the flow in an upper plane of the flow (e.g. $x > x_{sh}$, $y \geq 0$) can differ significantly from the lower plane (e.g. $x > x_{sh}$, $y \leq 0$). The combination of these factors leaves an oblique shock case more susceptible to the effects of wave reflections in the periodic transverse boundaries. As such, a stretched grid is implemented in the transverse directions for oblique MHD shock cases. A five–block configuration

is used in which a central uniform region is bounded by two stretched, more coarse regions, in which waves are damped prior to impinging on the boundaries (see figure 4.42 for full description). Note that in the two–dimensional interaction, central uniform region, $y_2 \leq y \leq y_3$, contains same number of points as entire y direction in parallel shock case, $N_y = 672$. The central uniform region in the three–dimensional oblique shock case contains 850 grid points in y and z directions respectively. For all simulations the uniform region has a length, $L_{t,u} = 20.0$, in the transverse direction ($L_t = L_{t,u}$ in parallel shock case). In the x-direction for two– and three–dimensional cases the five–block configuration outlined in section 4.3 is utilised (see tables 4.4 and 4.5 for respective two– and three–dimensional grid parameters).

Region	$Nbpts$	x_{lo}/L	x_{up}/L	$\Delta x_{lo}/L$	$\Delta x_{up}/L$
X_1	270	0.0000	0.0990	0.7300×10^{-3}	0.3333×10^{-5}
X_2	299	0.0990	0.1000	0.3333×10^{-5}	0.3333×10^{-5}
X_3	241	0.1000	0.1200	0.3333×10^{-5}	0.1627×10^{-3}
X_4	983	0.1200	0.2799	0.1627×10^{-3}	0.1627×10^{-3}
X_5	223	0.2799	1.0000	0.1627×10^{-3}	0.6296×10^{-2}

Table 4.4: Five–block stretched grid configuration in the x-direction for the two–dimensional entropy spot–fast MHD shock interaction. Total number of grid points in x- direction is 2016. L is the reference length of the computational domain, $L = 100$. Number of points ($Nbpts$), upper/lower bounds in x (x_{up}/x_{lo}) and grid spacing ($\Delta x_{up}/\Delta x_{lo}$) given for each region of stretched grid. Regions X_2 and X_4 are uniform. X_1, X_3, X_5 are non–uniform and utilise a polynomial grid.

.

Region	$Nbpts$	x_{lo}/L	x_{up}/L	$\Delta x_{lo}/L$	$\Delta x_{up}/L$
X_1	382	0.0000	0.0990	0.5000×10^{-3}	0.1832×10^{-4}
X_2	54	0.0990	0.1000	0.1832×10^{-4}	0.1832×10^{-4}
X_3	201	0.1000	0.1200	0.1832×10^{-4}	0.1808×10^{-3}
X_4	885	0.1200	0.2799	0.1808×10^{-3}	0.1808×10^{-3}
X_5	158	0.2799	1.0000	0.1808×10^{-3}	0.8933×10^{-2}

Table 4.5: Five–block stretched grid configuration in the x-direction for the three–dimensional entropy spot–fast MHD shock interaction. Total number of grid points in x- direction is 1680. L is the reference length of the computational domain, $L = 100$. Number of points ($Nbpts$), upper/lower bounds in x (x_{up}/x_{lo}) and grid spacing ($\Delta x_{up}/\Delta x_{lo}$) given for each region of stretched grid. Regions X_2 and X_4 are uniform. X_1, X_3, X_5 are non–uniform and utilise a polynomial grid.

.

To investigate the topology of each refracted mode, it was necessary to run each simulation for a sufficient length of physical time such that modes were properly separated (if separation were possible). Initial coarse grid runs indicated this equated to approximately $t = 5$. For the two–dimensional numerical cases studies, it was feasible to run full–scale simulations on a workstation (Dell Z840), while still fulfilling the spatio-temporal grid resolution and physical run–time constraints. The six two–dimensional flow cases involved varying the parameters, φ_1 and ϵ (see table 4.6 for full description of test cases). However, the two three–dimensional cases considered (see table 4.7 for more details) required additional computing resources. Case B1 was run on the Imperial College high performance computing (HPC) facility, CX2, on 4704 cores. Case B1 was run

on the national supercomputer facility, Archer, on 6000 cores. Both runs were completed over the course of several months.

4.4.2 LIA reconstruction

The post–shock flowfield in the entropy–spot/shock–wave interaction problem is reconstructed using linear theory. The refraction of individual modes excited upstream by the entropy–spot is computed and their superposition integrated in spectral space (via an inverse Fourier transform) to rebuild the full refracted field. The methodology for the two–dimensional entropy spot reconstruction is outlined, however, extension to the three–dimensional refraction problem is trivial. Unlike the procedure described by authors in [Fabre et al., 2001] and used by authors [Touber and Alferez, 2019], the method used in the current study does not require the analytical solution to the Fourier transform of the impinging perturbation to be known and can be applied to a disturbance of any general form.

A density perturbation in the form of a Gaussian is initialised on a uniform square grid on the domain $x, y \in [-L/2, L/2]^2$, with 1401 grid points in the x and y directions respectively:

$$f(x,y) = -\exp\left\{-\frac{1}{2}\left(\frac{x^2+y^2}{r_0^2}\right)\right\}, \tag{4.4.3}$$

where $r_0 = 1/(2\sqrt{2\ln 2})$.

We then compute a Fourier transform of (4.4.3), between the finite limits at a phase shift in time equivalent to the time elapsed after the centre–line of the incident entropy spot has passed through the shock, t_p:

$$\hat{F}(k_m, k_n) = \frac{1}{L^2}\int_{-L/2}^{+L/2}\int_{-L/2}^{+L/2} f(x,y)\exp[-\mathrm{i}(\boldsymbol{k}\cdot\boldsymbol{x} - \omega t_p)]\,\mathrm{d}x\mathrm{d}y, \tag{4.4.4}$$

where $\boldsymbol{k} = [k_m,\, k_n,\, 0]^\intercal$ are grid coordinates in (Cartesian) Fourier space, defined on the domain $k_m, k_n \in [-k, +k]^2$ containing M and N modes in k_m and k_n respectively.

The integral for the Fourier transform in (4.4.4) can be computed numerically (Simpsons rule is utilised in the present study).

Case	φ_1	ϵ	M_{min}	N_y	Δt	CFL_{max}
A1	0.00000°	0.01	1.00000	672	1×10^{-5}	0.1165
A2	0.00000°	0.10	1.00000	672	8×10^{-5}	0.0932
A3	26.56505°	0.01	1.13224	704	5×10^{-6}	0.0624
A4	26.56505°	0.10	1.13224	704	5×10^{-6}	0.0624
A5	43.50912°	0.01	1.34498	704	5×10^{-6}	0.0689
A6	56.30993°	0.01	1.65234	704	5×10^{-6}	0.0782

Table 4.6: Two–dimensional entropy spot–fast shock interaction DNS test cases. Upstream mean magnetic field angle (φ_1), amplitude of perturbation (ϵ), minimum M_1 used to seed shock (M_{min}), grid points in transverse direction (N_y and N_z), time–step (Δt) and maximum inviscid CFL number (CFL_{max}) shown.

Refraction coefficients are then computed for each point in Fourier space, $\chi_\mu(k_m, k_n)$ (for a given base flow). The real part of the inverse Fourier transform of $\chi_\mu(k_m, k_n)\boldsymbol{e}_\mu^{xy}\hat{F}(k_m, k_n)$ is evaluated and summed across all modes to reconstruct the downstream refracted field in physical space:

$$\begin{aligned}\boldsymbol{\mu}_2' &= \mathrm{Re}\left[\sum_{\mu=2}^{\mu=5}\frac{L^2}{(2\pi)^2}\int_{-k}^{+k}\int_{-k}^{+k}\left\{\boldsymbol{\xi}_\mu^{xy}(k_m,k_n)\hat{F}(k_m,k_n)\right\}\exp[\mathrm{i}\boldsymbol{k}_\mu\cdot\boldsymbol{x}]\mathrm{d}k_n\mathrm{d}k_n\right], \qquad (4.4.5)\\ &= \sum_{\mu=2}^{\mu=5}\frac{L^2}{(2\pi)^2}\int_{-k}^{+k}\int_{-k}^{+k}\Big\{(\boldsymbol{\xi}_\mu^{xy,r}\hat{F}^r - \boldsymbol{\xi}_\mu^{xy,i}\hat{F}^i)\cos(k_{x,\mu}^r x + k_n y) + \\ &- (\boldsymbol{\xi}_\mu^{xy,r}\hat{F}^i + \boldsymbol{\xi}_\mu^{xy,i}\hat{F}^r)\sin(k_{x,\mu}^r x + k_n y)\Big\}e^{-k_{x,\mu}^i x}\mathrm{d}k_m\mathrm{d}k_n,\end{aligned}$$

where $\mu = 2$, $\mu = 3$, $\mu = 4$ and $\mu = 5$, refer to the refracted entropy (E), forward fast ($f+$), forward slow ($s+$) and backward slow ($s-$) modes respectively, $\boldsymbol{\xi}_\mu^{xy} \equiv \chi_\mu \boldsymbol{e}_\mu^{xy}$, and superscripts "$r$" and "$i$" refer to the real and imaginary components of a quantity.

The vorticity field is similarly computed:

$$\begin{aligned}\omega_\mu' = -\sum_{\mu=3}^{\mu=5}\frac{L^2}{(2\pi)^2}\int_{-k}^{+k}\int_{-k}^{+k}\Big\{&(\Omega_\mu^r\hat{F}^r - \Omega_\mu^i\hat{F}^i)\cos(k_{x,\mu}^r x + k_n y) + \qquad (4.4.6)\\ &+ (\Omega_\mu^r\hat{F}^i + \Omega_\mu^i\hat{F}^r)\sin(k_{x,\mu}^r x + k_n y)\Big\}e^{-k_{x,\mu}^i x}\mathrm{d}k_m\mathrm{d}k_n.\end{aligned}$$

For all LIA reconstructions presented in this section, the incident entropy spot is generated on a $N \times N$ grid of resolution $N = 1401$ in the domain, $x, y \in [-12.5,\, 12.5]^2$. In Fourier space, we define a wavevector grid of 1401 modes in k_m and 1501 modes in k_n on the domain $k_m, k_n \in [-20,\, +20]^2$.

4.4.3 Two–dimensional post–shock field topology

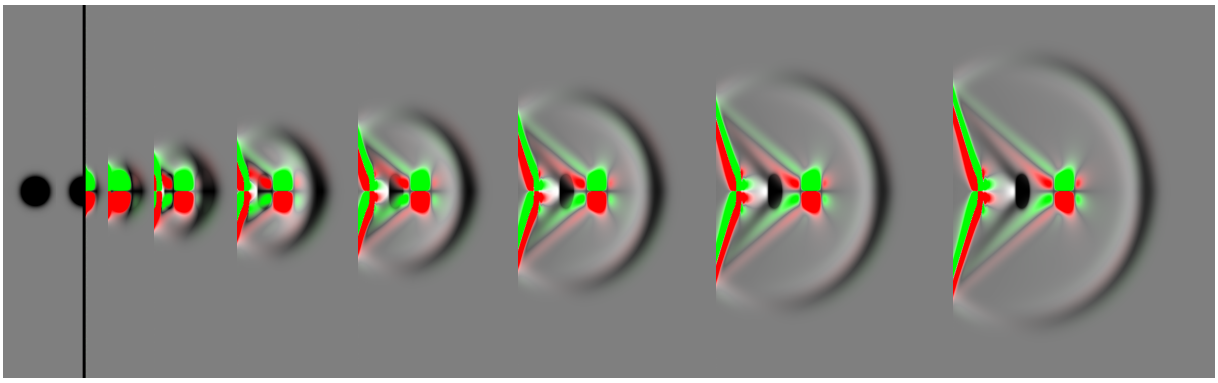
Figure 4.43 shows a time–lapse of density and vorticity contours for the DNS of an entropy spot refracted by a parallel (figure 4.43a, case A1) and oblique (figure 4.43b, case A3) fast shock respectively. In both plots the emergence of four distinct refracted modes is visible (labelled in figures 4.44 and 4.45 where the density/vorticity and pressure fields are shown at the later time of $t = 4.40$) with three of them transporting vorticity. These modes are generated as the incident entropy spot impinges on the shock. With respect to the refracted entropy mode, the post–shock topology is largely similar to that of a "hot spot" interacting with

Case	φ_1	ϵ	M_{min}	N_y	N_z	Δt	CFL_{max}
B1	0.00000°	0.01	1.00000	672	672	2.5×10^{-5}	0.0530
B2	26.56505°	0.01	1.13224	880	880	2.0×10^{-5}	0.0407

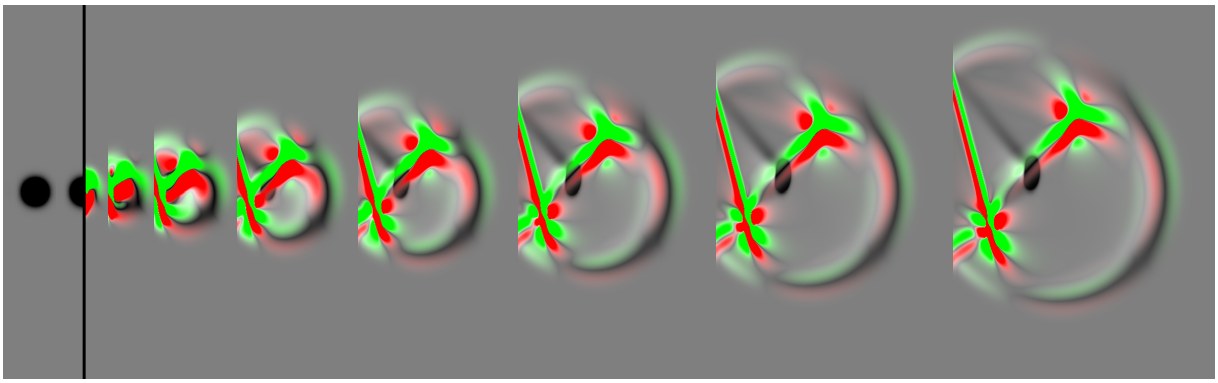
Table 4.7: Three–dimensional entropy spot–fast shock interaction DNS test cases. Upstream mean magnetic field angle (φ_1), amplitude of perturbation (ϵ), minimum M_1 used to seed shock (M_{min}), grid points in transverse directions (N_y and N_z), time–step (Δt) and maximum inviscid CFL number (CFL_{max}) shown.

an compressive shock in gas dynamics [Fabre et al., 2001], [Touber and Alferez, 2019]. Compression of the impinging spot occurs in the normal direction to the shock surface, resulting in the elliptic shape visible in figure 4.44. Deformation of the shock surface also occurs in the interaction. The low density region introduced just in front the shock by the incident entropy mode increases the local speed of sound (maximum local value given by $c_{o,1}^{max} = \sqrt{\gamma \bar{p}_1/(\bar{\rho}_1(1-\epsilon))}$), resulting in a lower local Mach number and thus lower pressure jump. This low pressure region behind the shock deforms the shock surface and in gas dynamics would propagate away from the shock as a cylindrical acoustic wave (also carrying density and velocity fluctuations). However, in MHD all three magneto–acoustic modes can transport pressure fluctuations, figure 4.44. The forward fast mode has a structure similar to the cylindrical acoustic wave [Fabre et al., 2001], whereas both slow modes display a markedly different structure. In figure 4.45 we see the loss of flow symmetry about the normal axis for an entropy spot–oblique shock interaction. The forward fast mode shape appears rotated, while the slow modes are propagating almost orthogonally to one another. The backward slow mode propagates at an angle nearly parallel to the shock surface whereas the forward slow mode diverges from the shock at a steeper angle. The forward fast mode, in which vorticity is now visible unlike the parallel fast shock case (for the shown colour ranges), is distorted away from the shock normal, which is no longer aligned with the downstream mean magnetic field, $\varphi_2 = 51.0°$. As mentioned in section 4.2.1, the direction perpendicular to the mean magnetic field corresponds to the highest fast mode phase speed and irrotational velocity fluctuations. The latter point can be seen in both 4.44 and 4.45, for which the forward fast mode displays a "quiet" vorticity region in the perpendicular direction. The "quiet" region is replicated in the direction parallel to the mean magnetic field ($\beta_2 \approx 15.83/\gamma$ for case A1 and $\beta_2 = 4.93/\gamma$ for case A3).

With respect to the forward fast mode, similarities in its structure with the cylindrical acoustic mode (from the entropy spot–gasdynamic shock interaction) can be understood if we first consider that the refracted field is essentially a summation of fast waves generated in the refraction of entropy modes incident across all angles. Upon entropy mode impingement, a "packet" of fast waves is propagated away from the shock surface at the group velocity, which, in result, influences their post–shock structure. From the phase and group velocities (normalised by the sound speed) in figure 4.46, we see the shape of the fast mode differs only slightly from that of the acoustic mode (for which phase and group velocities are equal). When the group velocity is parallel to the normal direction to the shock (and magnetic field), $\boldsymbol{V} \perp \boldsymbol{e}_n = \boldsymbol{0}$, the acoustic and fast mode coincide. From section 4.2.1, it was shown that for a flow in which $r < 1$ (as is the case for A1), the fast mode degenerates to an acoustic mode for wavevectors in the direction parallel to the magnetic field. However, in the direction perpendicular, the fast mode is longitudinal like the acoustic mode but has a phase speed $V = \sqrt{b^2 + c_o^2}$ (the fast phase and group speeds are almost equal in high β flows). If we consider that the outwards propagation of the fast mode is centered on the "drift" velocity (i.e. the local flow speed, $\bar{\boldsymbol{u}}_2$),



(a) $\varphi_1 = 0.00000^\circ$



(b) $\varphi_1 = 26.56505^\circ$

Fig. 4.43: Time–lapse of density/vorticity contours for entropy spot–fast shock interaction for two different upstream mean magnetic field angles, φ_1. Shock location indicated by solid black line. Cases A1 (a) and A3 (b) shown. Colour bars are given in figure 4.44.

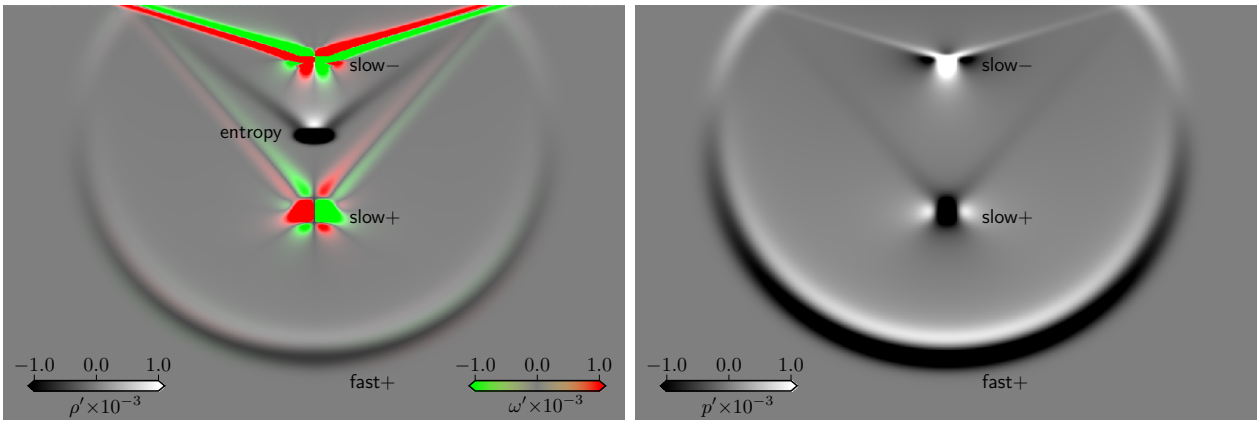


Fig. 4.44: Topology of entropy spot–parallel fast shock interaction (case A1). Entropy, forward fast (fast +), forward slow (slow +) and backward slow (slow −) modes indicated on plots. Density/vorticity (left) and pressure (right) shown at $t = 4.40$.

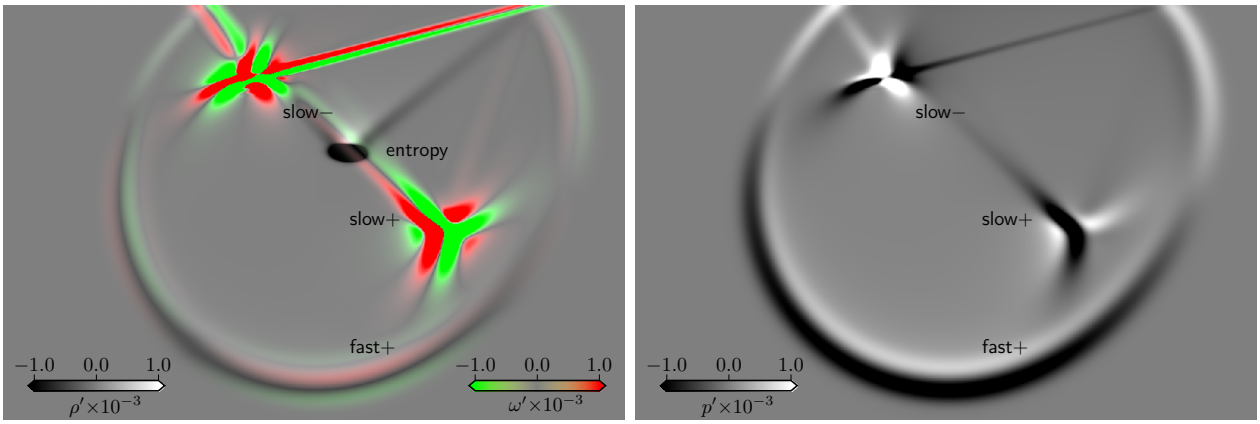


Fig. 4.45: Topology of entropy spot–oblique fast shock interaction (case A3). Entropy, forward fast (fast +), forward slow (slow +) and backward slow (slow −) modes indicated on image. Density/vorticity (left) and pressure (right) shown at $t = 4.40$.

alignment of a wavevector perpendicular to the magnetic field will occur at $\hat{V}\|\boldsymbol{e}_n = M_2 \approx 0.61$. In figure 4.46 we see that at this value of $\hat{V}\|\boldsymbol{e}_n$ the fast mode group and phase velocities diverge the most from that of the acoustic. This points to the anisotropic nature of magneto–acoustic modes in comparison to acoustic modes, which are isotropic thus have a perfectly circular shape centred on the "drift" velocity. From figure 4.46 we also see that fast mode anisotropy is enhanced when the magnetic field is no longer aligned with the normal direction (parallel to the shock normal). Significant divergence from the acoustic mode shape is given by the direction perpendicular to the magnetic field.

Vorticity generation in the gasdynamic interaction arises as a result of the baroclinic term [Fabre et al., 2001]. The entropy spot introduces gradients in density mis–aligned with the pressure gradient directed along the normal to the shock. Vorticity produced in this interaction takes the form of a vorticity dipole, which in turn is convected away, frozen in shape, by the vortical mode at the local flow speed. In MHD this baroclinic term also plays a role in vorticity generation, however, the presence of a magnetic field introduces

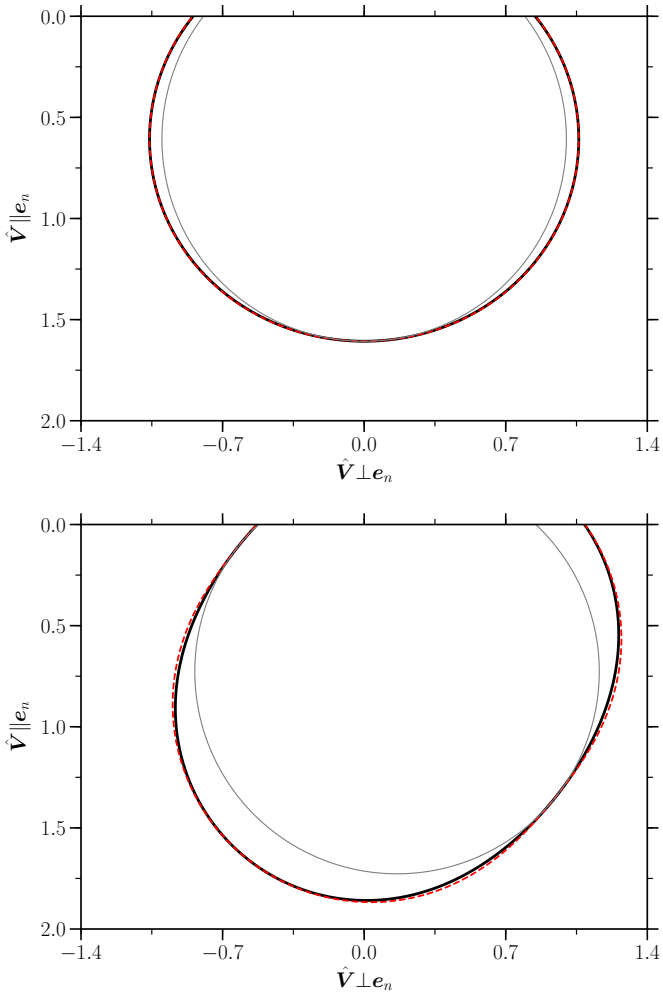


Fig. 4.46: Normalised group/phase velocity (with respect to speed of sound), $\hat{\boldsymbol{V}} = \boldsymbol{V}/c_{o,2}$, diagrams for acoustic and fast magneto–acoustic modes in a moving flow (i.e. non–zero drift velocity). Acoustic mode phase/group velocity (thin grey solid line), fast magneto–acoustic phase velocity (red dashed line), fast magneto–acoustic group velocity (black solid line). Plots shown for magnetic field and drift velocity parallel to the normal direction (top) and oblique to the normal direction (bottom).

an alternate vorticity production mechanism via the Maxwell stress term [Porter et al., 2015]. In figure 4.44, we see that vorticity transport in the slow modes is significantly higher than that of the forward fast mode. Following section 4.2.5, this is expected, as the vorticity coefficient is significantly lower in the fast mode across all incidence angles in the propagative regime. In the non–propagative regime, the intensity increases significantly, however, rapid damping in space as it penetrates the downstream flow minimises its contribution - as can be seen from figure 4.44.

With respect to vorticity distribution between modes, the fast mode retains a cylindrical wave type structure, however, from figure 4.47 we see how the forward slow mode structure evolves into a complex shape. Initially, the forward slow mode topology appears similar to vorticity dipole in gas dynamics. As it penetrates the downstream flow we observe a distortion in shape. From the normalised slow mode phase and group

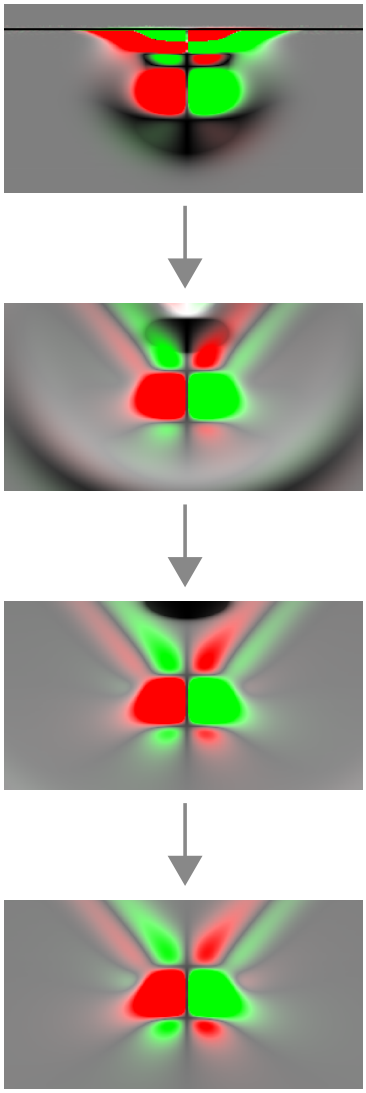


Fig. 4.47: Forward slow mode evolution in entropy spot–parallel fast shock interaction (case A1). Arrows in direction of increasing time. Colour bars are given in figure 4.44.

velocity diagrams in figure 4.48, we observe that, unlike the fast mode, the group velocity differs significantly from the phase velocity. The three–pronged slow mode group velocity shape bears similarities with the evolution of the vortical structure from a dipole into a multi–polar structure.

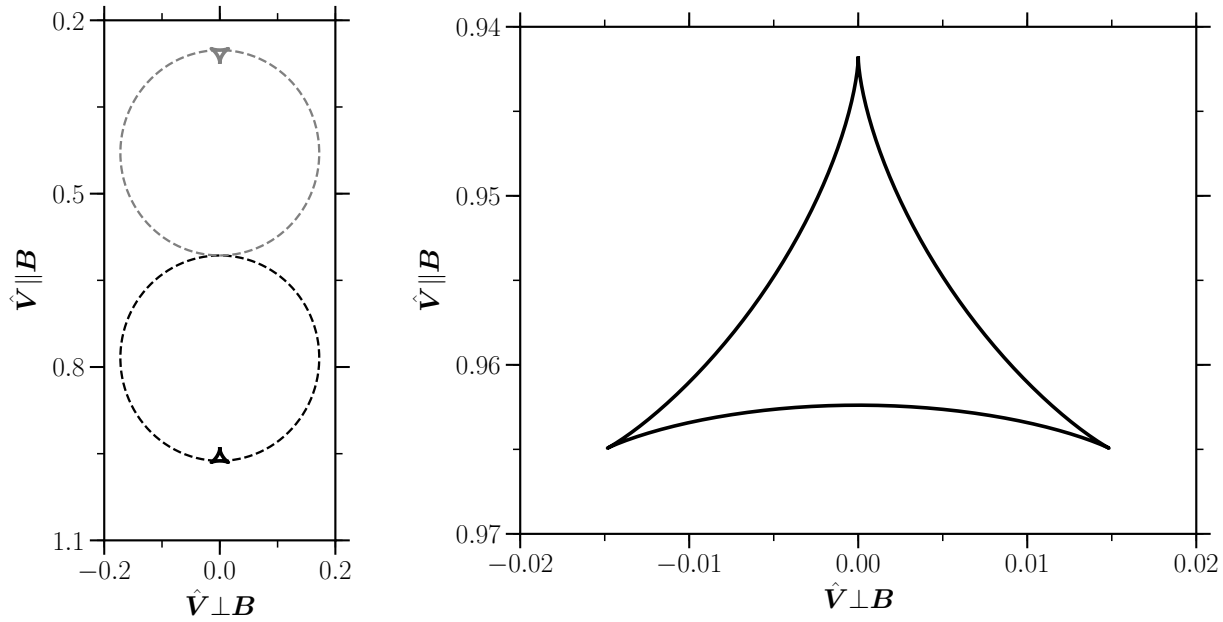


Fig. 4.48: Normalised group/phase velocity (with respect to speed of sound), $\hat{\boldsymbol{V}} = \boldsymbol{V}/c_{o,2}$, diagrams for backward (grey) and forward (black) slow magneto–acoustic modes in a moving flow (i.e. non–zero drift velocity). Phase velocity (dashed line) and group velocity (solid line) shown. Plot given for magnetic field and drift velocity parallel to the normal direction. Close–up of forward slow mode group velocity shown on the right.

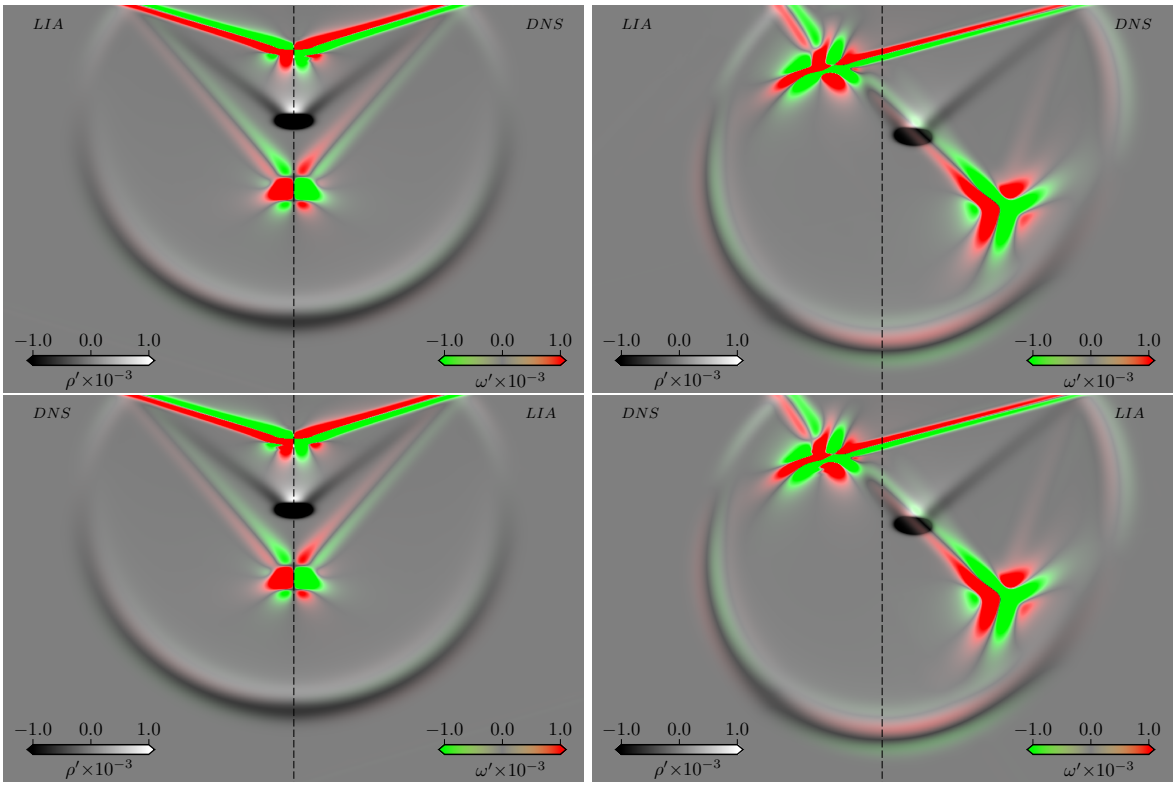


Fig. 4.49: DNS results vs. LIA reconstruction of entropy spot interacting with a parallel (left, case A1) and oblique (right, case A3) fast shock. Density and vorticity contours shown in left/right half–planes for LIA/DNS (top) and DNS/LIA (bottom). Asymmetry of oblique interaction well–captured by LIA reconstruction.

4.4.4 DNS vs. LIA reconstruction

Figure 4.49 shows the reconstructed density and vorticity fields for cases A1 and A3 at $t = 4.15$. Linear theory is shown to agree well with the DNS result for parallel and oblique shocks. Both cases involve amplitudes of 1% for the incident disturbance. In the gasdynamic case, 1% disturbance–shock interaction flows computed with nonlinear codes have been shown to agree well with LIA for ideal gases [Fabre et al., 2001] [Touber and Alferez, 2019].

From polar plots in figures 4.50 and 4.51, we see that quantitatively for the forward fast mode, DNS and LIA compares well with respect to maximum and minimum density fluctuations as a function of the anti–clockwise angle about the entropy mode centre–point. Analysis is restricted to a "shell" enclosing the fast mode. However, in figure 4.49 we observe a slight divergence between vorticity fields near the critical angle for the oblique shock case as the linear theory appears to overestimate vorticity by a small amount. Several factors may play a role such as grid refinement in both wavespace (for LIA) and physical space (for LIA and DNS). Additionally, results in section 4.3, did show divergence between DNS and LIA near the critical angle in interactions between plane entropy waves an fast shocks due to suspected numerical issues (e.g. initial transients and their reflections in domain boundaries).

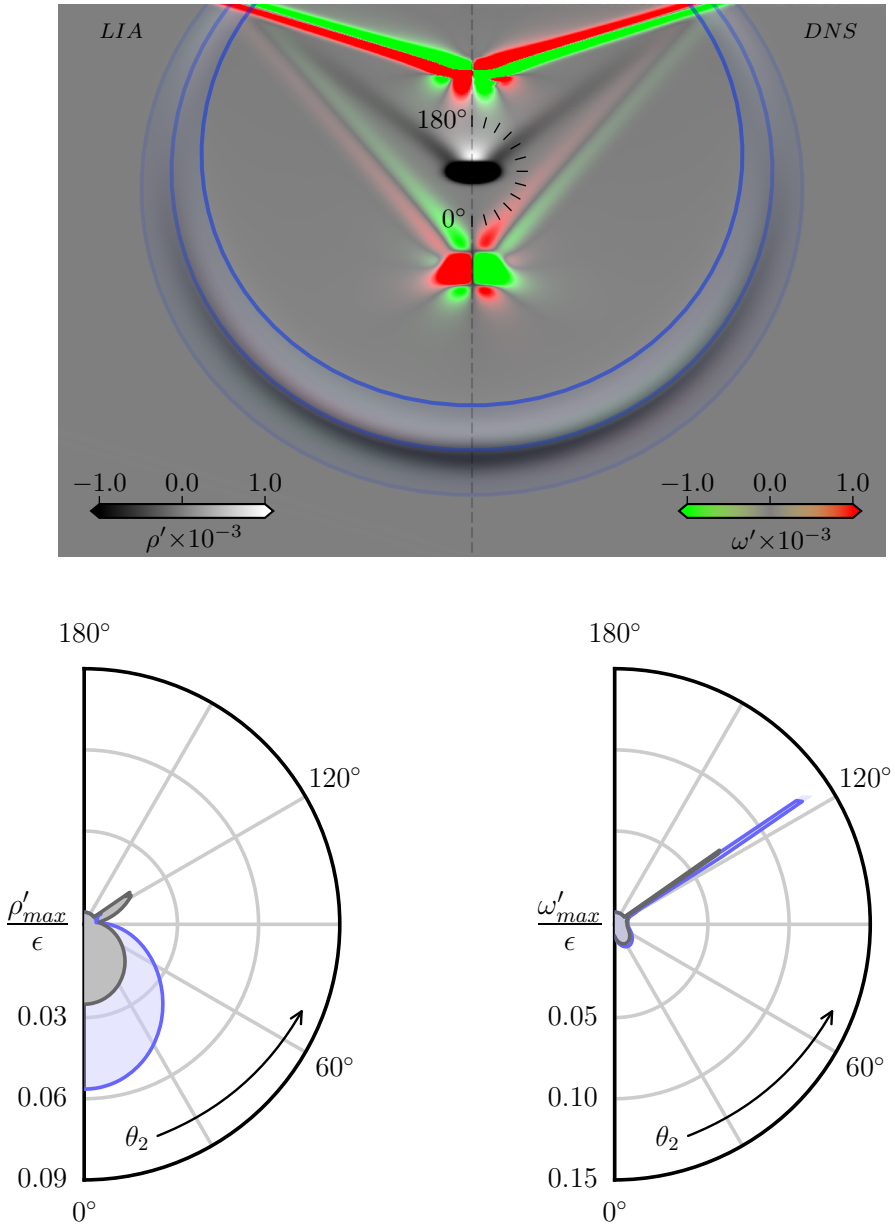


Fig. 4.50: Comparison of DNS and LIA for 1% amplitude entropy spot–parallel fast shock interaction (Case A1). Top: LIA (left) and DNS (right) half planes of density/vorticity contours, blue line indicates linear theory propagation of fast mode, $(x, y) = (V^g_{x,f+}(\theta_2)t, V^g_{y,f+}(\theta_2)t)$, where the fast mode group velocity, $\boldsymbol{V}^g_{f+}$, has been computed for the range of t values, $t = 0.9T_0, T_0, 1.1T_0$, in which T_0 is the time elapsed after the centre-line of incident entropy spot has passed through the shock, and $\theta_2 \in [\theta^{c-}_{f+}, \theta^{c+}_{f+}]$, in which θ^{c+}_{f+} (θ^{c-}_{f+}) correspond to the fast mode refraction angle at the critical incidence angle, θ^{c+} (θ^{c-}). Bottom: Dependency of maximum positive (negative) fluctuations shown in grey (blue) for the density (left), ρ', and vorticity (right), ω', fields within the region bounded by linear theory fast mode contours at $t \in [0.9T_0, 1.1T_0]$. Values given for DNS (solid line) and LIA (shaded region) data.

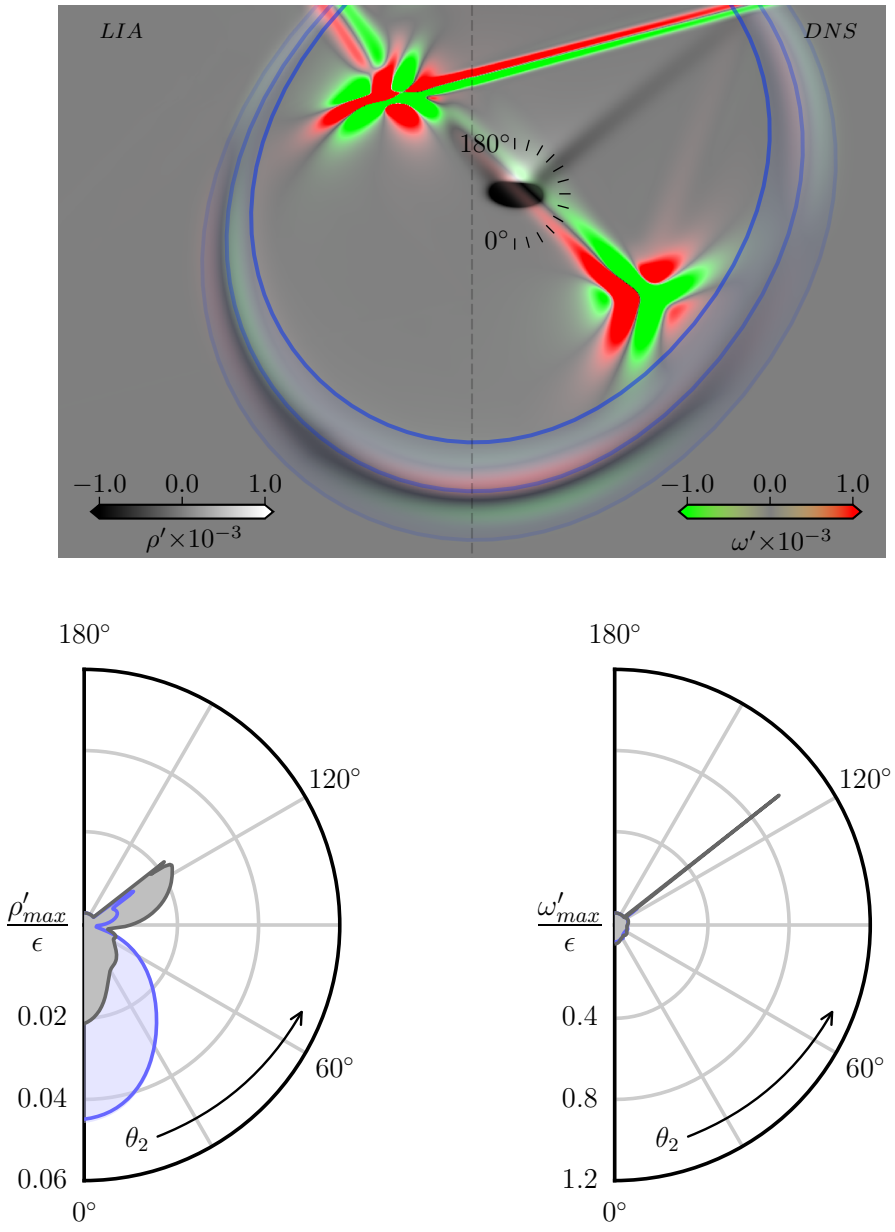


Fig. 4.51: Comparison of DNS and LIA for 1% amplitude entropy spot–oblique fast shock interaction (Case A3). See figure 4.50 for description.

In figures 4.52 and 4.53 the reconstructed density and vorticity fields for 10% fluctuations also show similar levels of agreement between the LIA and DNS (cases A2 and A4) results. A 10% fluctuation is similar to the turbulence intensities that might be expected upstream of a SWTI. However, we note the emergence of small nonlinearities for case A2 (figure 4.52) in which distortions are visible in vorticity transported by the backward slow mode (behind the attached wave structure and "ears" at the front). Additionally, the central vortical structure in the forward slow mode shows increased curvature along its side (closest to the shock) compared to the LIA result.

4.4.5 Mean magnetic field angle influence and the "magnetosonic" condition

In figure 4.54 we observe how increases in the upstream mean magnetic field angle affect the distribution and intensity of vorticity transport across the magneto–acoustic modes. From figure 4.54a we attain a visualisation of the convergent nature between modes in the "magnetosonic" condition, $\beta_2 = 2.00/\gamma$. Unlike in figure 4.54b (where $\beta_2 = 1.00/\gamma$) all modes remain attached in the final snapshot of figure 4.54a, a result of the coincidental wave speeds along the direction parallel to the downstream mean magnetic field, $\varphi_2 \approx 60.7°$. Vorticity intensity in the forward fast mode is noticeably increased (compared to $\varphi_1 = 0.0°$ and $\varphi_1 \approx 26.6°$ in figure 4.43) as predicted in section 4.2.5, however, there is difficulty in discerning at which point slow modes propagating in unison contribute to the forward fast mode structure. The quiet region in the direction perpendicular to the mean magnetic field remains, whereas the merging of magneto–acoustic modes means such a distinction cannot be made in the parallel direction. In the magnetic pressure–dominated flowfield (i.e. $\beta_2 < 2/\gamma$)), figure 4.54b, the forward fast mode vorticity distribution is similar to that of the oblique mean magnetic field case shown in figure 4.43b. However, the suppression effect of the mean magnetic field on the slow modes vorticity transport is clearly visible. Separation between magneto–acoustic modes is also observed. A quiet region in the direction parallel to the mean magnetic field, $\varphi_2 \approx 63.8°$ is no longer a feature of the forward fast mode structure, representing its transition to more "transverse" wave behaviour (see figure 4.4).

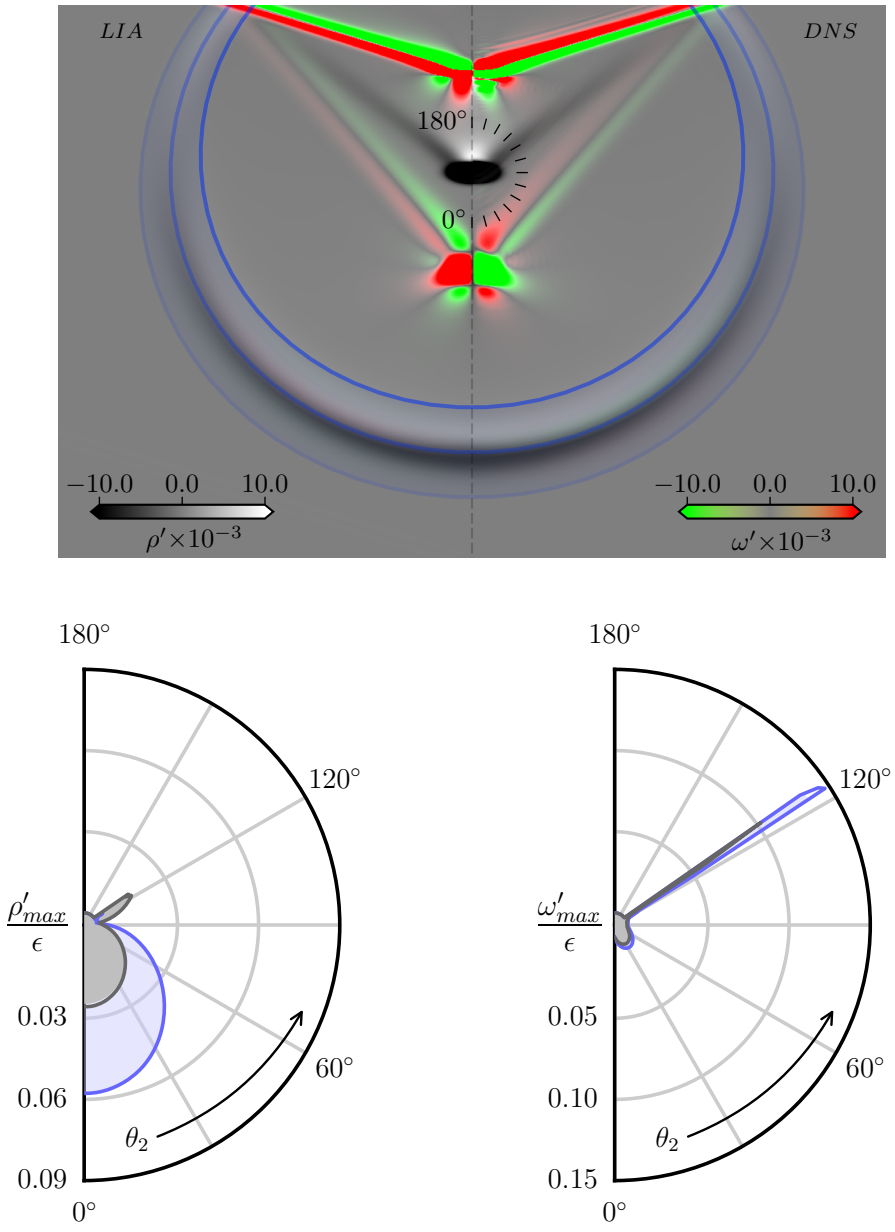


Fig. 4.52: Comparison of DNS and LIA for 10% amplitude entropy spot–parallel fast shock interaction (Case A2). See figure 4.50 for description.

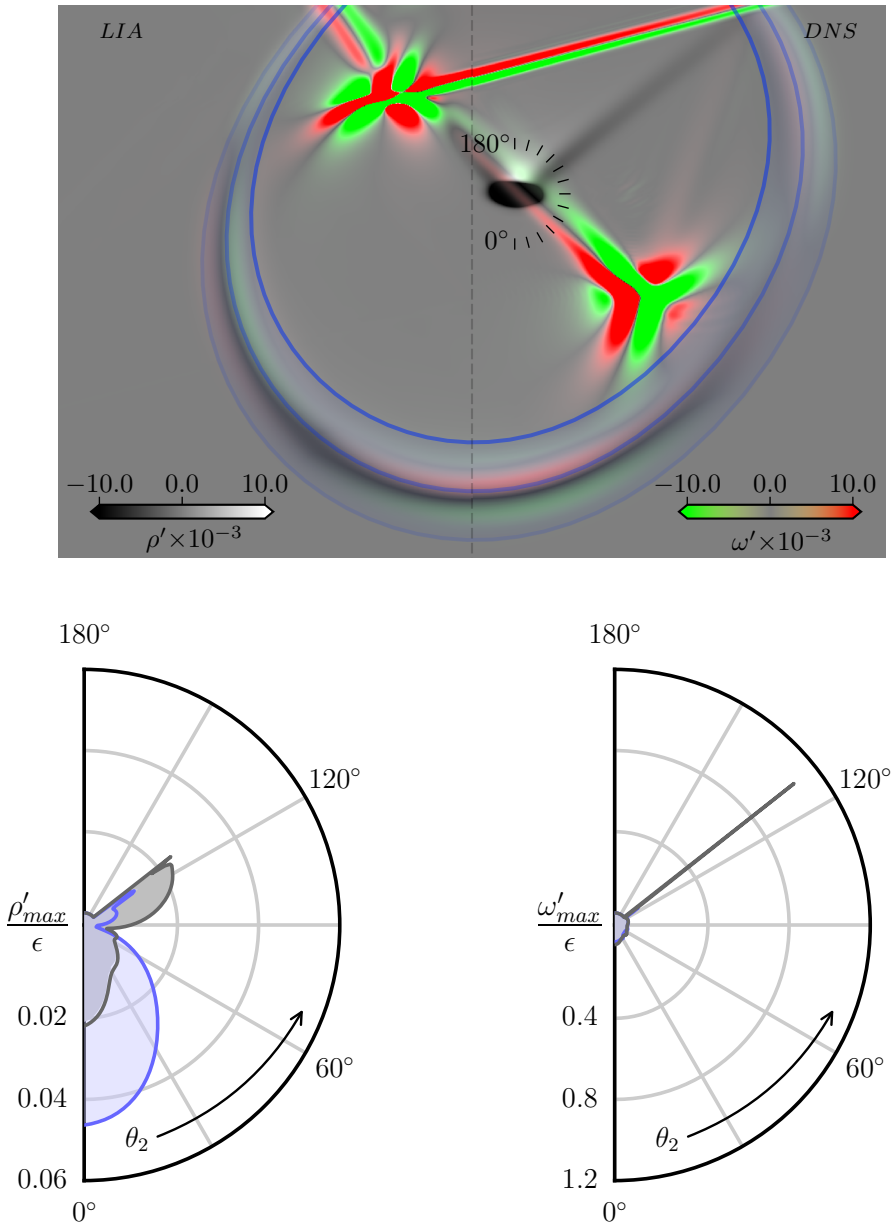
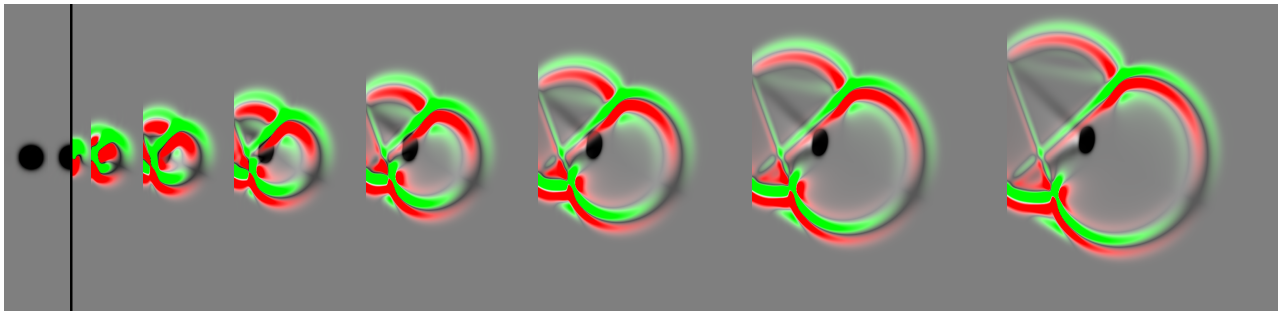
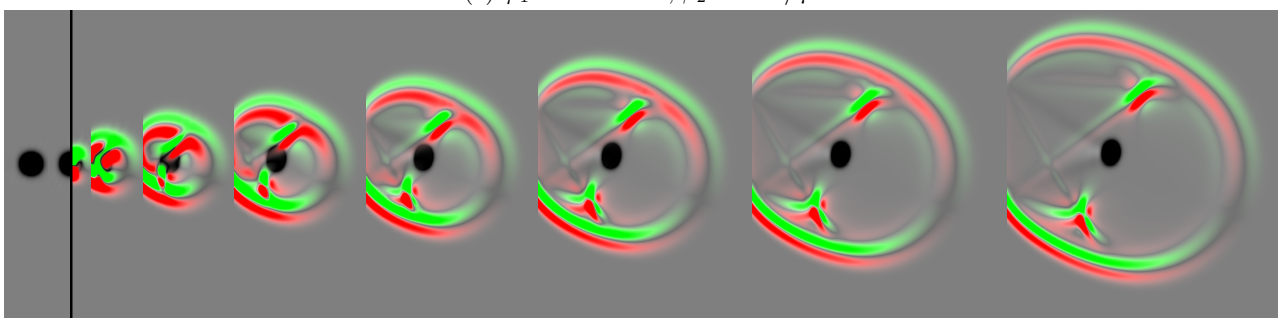


Fig. 4.53: Comparison of DNS and LIA for 10% amplitude entropy spot–oblique fast shock interaction (Case A4). See figure 4.50 for description.



(a) $\varphi_1 = 43.50912^\circ$, $\beta_2 = 2.00/\gamma$



(b) $\varphi_1 = 56.30993^\circ$, $\beta_2 = 1.00/\gamma$

Fig. 4.54: Time–lapse of density/vorticity contours for entropy spot–fast shock interaction with varying upstream mean magnetic field angle, φ_1. Downstream plasma beta, $\beta_2 = 2\bar{p}_2/||\bar{\boldsymbol{B}}||^2$, given. Shock location indicated by solid black line. Cases A5 (a) and A6 (b) shown.

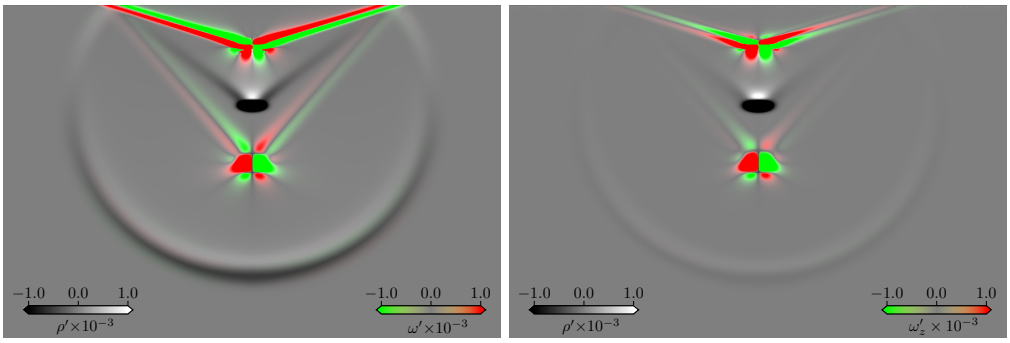


Fig. 4.55: Density and in–plane vorticity contours shown for entropy spot–parallel fast shock interaction in two–dimensions (left, case A1) and three–dimensions (right, case B1).

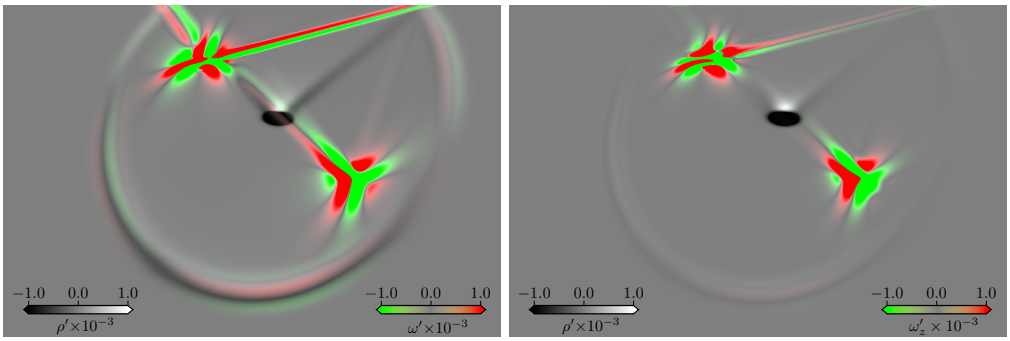
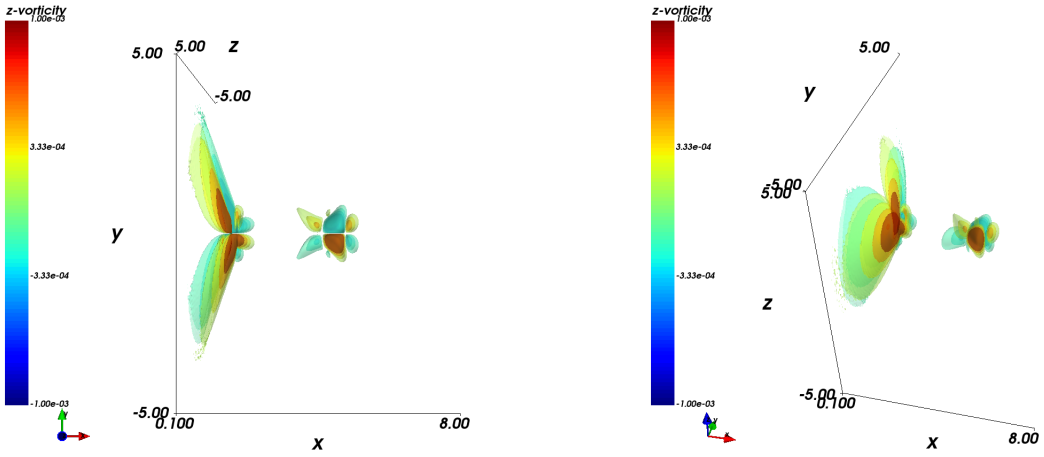


Fig. 4.56: Density and in–plane vorticity contours shown for entropy spot–oblique fast shock interaction in two–dimensions (left, case A2) and three–dimensions (right, case B2).

4.4.6 Three-dimensional interaction: in–plane vorticity generation

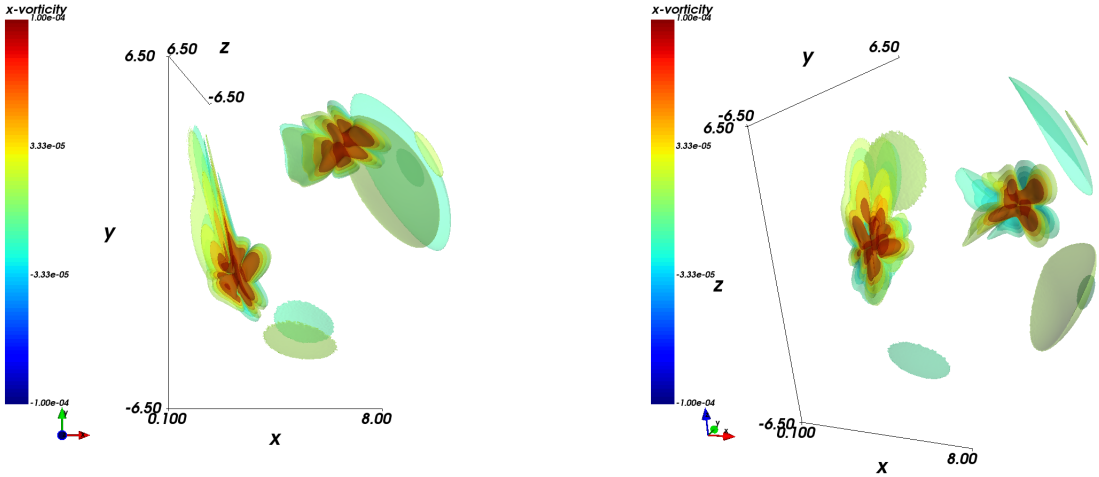
In both three–dimensional cases the magnetic field is kept in the $x - y$ plane with the velocity and shock normal. The conditions for the decoupling of the magneto–acoustic/entropy and Alfvén interaction is fulfilled for normal modes incident along this plane. The significance of this is visible in figures 4.55 and 4.56 which show contours of the in–plane vorticity, ω'_z, and density, ρ', fluctuations. Strong similarities are shared by structures in both two–dimensional and three–dimensional slices at $t = 4.40$. Symmetry and asymmetry in the shock normal axis are observed for the respective parallel and oblique shock cases. There does appear to be a reduction in intensity of both density and vorticity fluctuations in the three–dimensional interaction, however, as the three–dimensional reconstruction has not been completed, it cannot be ascertained whether this is in–line with theory or a result reduced grid resolution/increased shock thickness.

Figures 4.57 and 4.58 show give an iso–contour representation of ω'_z for both parallel and oblique shock cases (B1 and B2). Structures visible in the slice–cut appear almost extruded in the z-direction, indicating the two–dimensional interaction may be a useful predictor of vorticity distribution and strength in the three–dimensional problem. Vorticity transport in the forward fast mode is not visible for case B1 at the selected contour limits, however, a small cut of the spherical wave forward fast mode structure can be seen for case B2 (figure 4.58).



(a) top-view (b) iso-view

Fig. 4.57: Three–dimensional iso-contours of z-component vorticity in parallel MHD shock interaction. Top view (left) and iso–metric view (right) shown for case B1.



(a) top-view (b) iso-view

Fig. 4.58: Three–dimensional iso-contours of z-component vorticity in oblique MHD shock interaction. Top view (left) and iso–metric view (right) shown for case B2.

Chapter 5

Conclusions

In this thesis, vorticity produced in the interaction of an entropy disturbance with a fast MHD shock was investigated in two– and three–dimensions through linear analysis and DNS. The main interest stemmed from characterising the influence of a mean magnetic field on the amplification or suppression of post–shock vorticity production. With respect to linear theory, to solve the problem we considered the entropy mode as a small amplitude disturbance propagating through a fluid undergoing steady and uniform motion either side of a shock. The piece–wise uniform base flow is known a–priori while unknown amplitudes of perturbations in the refracted field are left to be solved from a set of boundary conditions given at the shock. Only for fast and slow shocks is this system determinate or "evolutionary". As an aim of this study was to draw comparisons with the gasdynamic entropy mode–shock interaction, in which no perturbations propagate upstream of the shock, only fast shocks were considered. The present study extended linear theory work by previous authors to include entropy modes impinging on a shock past a "critical angle" at which the refracted forward fast magneto–acoustic mode is damped as it penetrates the downstream flow. This enabled the use of linear theory to predict the interaction of disturbances that excite a large range of scales - e.g. a Gaussian-distributed spot or turbulence.

Properties of the downstream base flow were determined by solving the Rankine–Hugoniot jump conditions. In an MHD shock, the downstream state has three degrees of freedom with respect to dimensionless parameters in the upstream flow (M_1, $\beta_{n,1}$ and φ_1). Hugoniot curves were used to explore the locus of points in the $p-\vartheta$ phase plane and $U-V$ (where $U=\gamma p/B_n$ and $V=B_\perp/B_n$) of allowable downstream states a fluid may attain on passage through an MHD shock. Primary attention was paid to the ratio between thermodynamic and magnetic pressures, $\beta=2p/||\boldsymbol{B}||^2$, and the ratio between Alfvén and sound speeds, $r=b/c_o=||\boldsymbol{B}||/\sqrt{\gamma p}$. To explore the downstream magnetic field properties, $U-V$ phase space was considered for cases for different fixed values of U_1 for which V_1 varied. Analysis was restricted to fast and

compressive shocks. From this analysis a value of U_1 was selected for which downstream state $U_2/(1+V_2^2) = 1$ could be attained. This point denotes a downstream "magnetosonic" state, where the Alfvén speed and sound speeds are equal, $r_2 = 1$ ($\beta_2 = 2/\gamma$). Increasing V_1 from this value (at the fixed U_1) leads to magnetic pressure dominating the downstream state, $r_2 > 1$ ($\beta < 2/\gamma$), while reducing V_1 leads to thermodynamic pressure dominating, $r_2 < 1$ ($\beta > 2/\gamma$). Through varying V_1 at the selected U_1 value (corresponding to a fixed normal magnetic field strength at a given upstream pressure) exploration of both high and low β regimes in the post–shock flow could be attained.

Through an eigen–decomposition of the ideal MHD equations, we were able to ascertain the influence of different β regimes on perturbations within the flow. Seven wave modes were identified; backward/forward Alfvén, backward/forward fast magneto–acoustic, backward/forward slow magneto–acoustic and entropy, the first six of which can all transport vorticity at speeds faster and slower that the local flow. From the magneto–acoustic mode eigenvectors, it was shown that solenoidal velocity fluctuations (and thus vorticity transport) was heavily dependent on both r and the direction of the magnetic field. For flows in which $r < 1$, the fast magneto–acoustic modes have weak solenoidal velocity fluctuations and exhibit purely longitudinal behaviour in the wavevector direction parallel to the magnetic field (at which it degenerates to an acoustic wave). The opposite occurs for slow magneto–acoustic modes which display primarily transverse behaviour for $r < 1$ and become degenerate Alfvén modes when the wavevector is aligned with the magnetic field. This typology reverses for $r > 1$ in which fast magneto–acoustic modes become more transverse and slow magneto–acoustic modes more longitudinal (degenerating to an acoustic mode at wavevector–magnetic field alignment). At the magnetosonic condition, $r = 1$, fast and slow magneto–acoustic modes exhibit both longitudinal and transverse behaviour [Roe and Balsara, 1996] for wavevectors aligned with the magnetic field.

It was then shown for the fast shock refraction problem that downstream perturbations in the three–dimensional interaction will contain six eigenmodes; backward/forward Alfvén, backward/forward slow magneto–acoustic, forward fast magneto–acoustic and entropy. By assuming a Cartesian coordinate system in which the unperturbed shock front lies in the $x = 0$ plane, the Rakine–Hugoniot jump conditions were linearised at the shock and a system of equations derived which could be solved to obtain the unknown amplitudes of the downstream modes. A special case considered where the wavevector lies in the plane containing the shock normal and magnetic field decoupled the three–dimensional interaction into in–plane magneto–acoustic/entropy and out–of–plane Alfvén mode excitations. Results from this in–plane magneto–acoustic/entropy mode interaction were compared to results by previous authors [Westphal and McKenzie, 1969] for which it was indicated the previous author's formulation required a correction in the shock displacement contribution to the scattering matrix.

The modal response of vorticity transport in the magneto–acoustic modes was investigated in $M-\theta_1$ space for four different upstream magnetic magnetic field angles, $\varphi_1 = 0.00000°, 26.56505°, 43.50912°, 56.30993°$, at $\beta_{n,1} = 2.0$. Vorticity production in the forward fast magneto–acoustic mode for $\varphi_1 = 0.00000°$ and $\varphi_1 = 26.56505°$ (in which $r_2 < 1$ for both where $M_1 \leq 5$) was shown to be noticeably lower than the backward and forward slow magneto–acoustic modes in the propagative regime. In the non–propagative regime, the disparity in vorticity production reduced between the modes, however, the forward fast magneto–acoustic mode is rapidly damped in space as it penetrates the downstream flow, meaning contributions to the post–shock vorticity distribution away from the shock are minimal. Quiet regions in the vorticity coefficient maps were observed in the directions parallel and perpendicular to the magnetic field. For $\varphi_1 = 43.50912°$, the transition of longitudinal to transverse behaviour in the forward fast magneto–acoustic mode was observed at $M_1 = 2$ at which the magnetosonic condition is met. At $\varphi_1 = 56.30993°$, the forward fast magneto–acoustic mode displayed a modal response similar to the slow magneto–acoustic modes at $\varphi_1 = 0.00000°$ and $\varphi_1 = 26.56505°$.

Effects of singular–type behaviour near the critical angle was observed in the integrated quantity of the non–dimensional complex vorticity amplitude in θ_1 space, $\mathcal{I}_\mu$, for refracted modes "μ". At values of $M_1 \geq 2.2$ and $M_1 \geq 3.9$ for $\varphi_1 = 43.50912°$ and $\varphi_1 = 56.30993°$ respectively, spikes appear intermittently in the integrated value, up to nearly an order higher than the expected trend. As a result of these singularities, integration was restricted to the range $\theta_1 \in [\theta^{c-} + 1.0°, \theta^{c+} - 1.0°]$, within the propagative regime. Despite this restriction, the same trend in $\mathcal{I}_\mu$ with respect to M_1 was observed (rapid increase at low M_1 before plateauing at high M_1). Increasing in the φ_1 from 0.0° to 56.30993° resulted in the peak value of $\mathcal{I}_{s\pm}$ halving at $M_1 = 5.0$ whereas $\mathcal{I}_{f+}$ increased by an order of magnitude. From the sum of $\mathcal{I}_{f+}$, $\mathcal{I}_{s+}$ and $\mathcal{I}_{s-}$ we found that the total vorticity production is increasingly suppressed for increasing φ_1 and constant $\beta_{n,1}$. This effect was also observed (to a lesser extent) for increasing φ_1 at constant β_1.

LIA and DNS results of an entropy disturbance modelled as a plane wave refracted across parallel and oblique fast MHD shocks ($M_1 = 2.0$) were shown to compare reasonably well at incidence angles in both the propagative and non–propagative regime away from the critical angle. Discrepancy between the two results was most significant at near the critical angle for which the error in density and vorticity scaled to a significant proportion of the maximum amplitude of refracted modes in the post–shock region. Further study will be required to confirm that these issues are numerical in nature. Avenues of investigation centre around reducing the potential effect of reflections by the expected refracted modes or initial transients in domain boundaries (e.g. extending the domain length or refining the sponge region). A closer approximation of the linear theory by the DNS (i.e. thinner numerical shock and lower amplitude perturbations) was also suggested. However, these methods were deemed excessively computationally expensive for the present study

and were left to future work. In the entropy spot–fast shock interaction the topology of the post–shock field was shown to share similarities with the gasdynamic case. The forward fast magneto–acoustic mode evolved as a near–cylindrical wave while vorticity structures transported by backward/forward slow modes appear to emerge from the shock as a dipole before distorting to a form similar to the group velocities. For the interaction at the magnetosonic condition, fast and slow modes appear to propagate in unison away from the shock. LIA reconstruction compared well with DNS results for entropy spots with density fluctuations 1% and 10% the base flow value. Good agreement was seen in the maximum values of the forward fast mode density and vorticity fluctuations taken as a function of angle about a normal axis with the origin centred on the refracted entropy mode. In DNS results of the three–dimensional interaction, in–plane vorticity was observed as similar in distribution across modes as the two–dimensional interaction while weaker in intensity. The three–dimensional topology appeared to be an extrusion of these in–plane structures.

To summarise, vorticity production in the refraction of an entropy disturbance through a fast MHD shock has been shown to be closely linked to both the magnetic field strength and direction. Linear theory predicts a suppression of post–shock vorticity production as the upstream magnetic field angle is increased both at fixed total and normal magnetic field strength respectively (for a given upstream pressure). However, this suppression only occurs in the slow magneto–acoustic modes - vorticity transport in the fastest mode is amplified with increasing magnetic field angle. Singular behaviour near the critical angle for interactions involving high upstream Mach numbers and non–zero upstream mean magnetic field angles indicate there exist limitations of the LIA theory. Future work on the LIA theory presented in this study could potentially involve a linear stability analysis of strong oblique shocks. DNS results compare well with LIA for entropy plane waves incident on respective parallel and oblique fast MHD shocks in the propagative and non–propagative regimes away from the critical angle. Large discrepancies for the interaction near the critical angle require further investigation but are thought to be numerical in origin. LIA reconstruction of entropy spot–fast shock interaction appears robust to errors near the critical angle as very good agreement is observed with DNS results. Three–dimensional DNS studies indicate in–plane vorticity distribution can be predicted by two–dimensional interaction. Extension of LIA reconstruction to three–dimensions and turbulence would be the next step in application of present work to MHD flow control. LIA results have been shown to be a powerful tool in predicting turbulent kinetic energy amplification in the near–shock region in hydrodynamic SWTIs aiding both numerical and experimental work. Further development of techniques presented in this study will aim to provide a similar tool.

Bibliography

[Akhiezer et al., 1959] Akhiezer, A., Lubarski, G., and Polovin, R. (1959). The stability of shock waves in magnetohydrodynamics. *Soviet Phys. JETP*, 8:507–511.

[Anderson, 2003] Anderson, J. (2003). *Magnetohydrodynamic Shock Waves*. MIT Press Classics. MIT Press.

[Andreopoulos et al., 2000] Andreopoulos, Y., Agui, J. H., and Briassulis, G. (2000). Shock wave-turbulence interactions. *Annual Review of Fluid Mechanics*, 32(1):309–345.

[Atkinson et al., 2012] Atkinson, M. D., Poggie, J., and Camberos, J. A. (2012). Control of separated flow in a reflected shock interaction using a magnetically-accelerated surface discharge. *Physics of Fluids*, 24(12):126102.

[Balsara and Spicer, 1999] Balsara, D. S. and Spicer, D. S. (1999). A staggered mesh algorithm using high order godunov fluxes to ensure solenoidal magnetic fields in magnetohydrodynamic simulations. *Journal of Computational Physics*, 149(2):270–292.

[Barton, 1939] Barton, A. (1939). *A Text Book on Light*. Longmans, Green and Company.

[Bellei et al., 2013] Bellei, C., Amendt, P., Wilks, S., Haines, M., Casey, D., Li, C., Petrasso, R., and Welch, D. (2013). Species separation in inertial confinement fusion fuels. *Physics of Plasmas (1994-present)*, 20(1):012701.

[Bityurin et al., 2005] Bityurin, V., Bocharov, A., and Lineberry, J. (2005). MHD flow control in hypersonic flight. *AIAA Paper*, 3225:2005.

[Bityurin et al., 2003] Bityurin, V., Bocharov, A., Lineberry, J., and Suckomel, C. (2003). Studies on MHD interaction in hypervelocity ionized air flow over aero-surfaces. *AIAA paper*, 4303:23–26.

[Bityurin and Bocharov, 2010] Bityurin, V. A. and Bocharov, A. N. (2010). Ground mhd experiments in hypersonic flows. *High Temperature*, 48(6):874–880.

[Bletzinger et al., 2005] Bletzinger, P., Ganguly, B., Van Wie, D., and Garscadden, A. (2005). Plasmas in high speed aerodynamics. *Journal of Physics D: Applied Physics*, 38(4):R33.

[Bogey and Bailly, 2004] Bogey, C. and Bailly, C. (2004). A family of low dispersive and low dissipative explicit schemes for flow and noise computations. *Journal of Computational Physics*, 194(1):194–214.

[Borghi et al., 2006] Borghi, C., Cristofolini, A., Carraro, M., Gorse, C., Colonna, G., Passaro, A., and Paganucci, F. (2006). Non-intrusive characterization of the ionized flow produced by nozzle of an hypersonic wind tunnel. In *14th AIAA/AHI Space Planes and Hypersonic Systems and Technologies Conference*, page 8050.

[Boyd and Sanderson, 2003] Boyd, T. J. M. and Sanderson, J. J. (2003). *The physics of plasmas*. Cambridge University Press.

[Brackbill and Barnes, 1980] Brackbill, J. U. and Barnes, D. C. (1980). The effect of nonzero $\nabla \cdot \boldsymbol{B} = 0$ on the numerical solution of the magnetohydrodynamic equations. *Journal of Computational Physics*, 35(3):426–430.

[Braginskii, 1965] Braginskii, S. (1965). Transport processes in a plasma. *Reviews of plasma physics*, 1.

[Brio and Wu, 1988] Brio, M. and Wu, C. C. (1988). An upwind differencing scheme for the equations of ideal magnetohydrodynamics. *Journal of computational physics*, 75(2):400–422.

[Bulen et al., 1967] Bulen, A., Kranc, S., Nowak, R., Porter, R., and Yuen, M. (1967). Magnetogasdynamic re-entry phenomena. *Journal of Spacecraft and Rockets*, 4(11):1538–1542.

[Cho and Lazarian, 2005] Cho, J. and Lazarian, A. (2005). Generation of compressible modes in MHD turbulence. *Theoretical and Computational Fluid Dynamics*, 19(2):127–157.

[Cimino et al., 2016] Cimino, A., Krause, G., Elaskar, S., and Costa, A. (2016). Characteristic boundary conditions for magnetohydrodynamics: The brio–wu shock tube. *Computers & Fluids*, 127:194–210.

[Connor, 1973] Connor, J. (1973). The neo-classical transport theory of a plasma with multiple ion species. *Plasma Physics*, 15(8):765.

[Cook and Cabot, 2004] Cook, A. W. and Cabot, W. H. (2004). A high-wavenumber viscosity for high-resolution numerical methods. *Journal of Computational Physics*, 195(2):594–601.

[Crockett et al., 2005] Crockett, R. K., Colella, P., Fisher, R. T., Klein, R. I., and McKee, C. F. (2005). An unsplit, cell-centered godunov method for ideal mhd. *Journal of Computational Physics*, 203(2):422–448.

[Dafermos, 2006] Dafermos, C. (2006). *Hyperbolic Conservation Laws in Continuum Physics*. Grundlehren der mathematischen Wissenschaften. Springer Berlin Heidelberg.

[Dai and Woodward, 1994] Dai, W. and Woodward, P. R. (1994). An approximate riemann solver for ideal magnetohydrodynamics. *Journal of Computational Physics*, 111(2):354–372.

[de Moura and Kubrusly, 2012] de Moura, C. and Kubrusly, C. (2012). *The Courant–Friedrichs–Lewy (CFL) Condition: 80 Years After Its Discovery*. Birkhäuser Boston.

[Dedner et al., 2002] Dedner, A., Kemm, F., Kröner, D., Munz, C.-D., Schnitzer, T., and Wesenberg, M. (2002). Hyperbolic divergence cleaning for the MHD equations. *Journal of Computational Physics*, 175(2):645–673.

[Del Zanna et al., 2001] Del Zanna, L., Velli, M., and Londrillo, P. (2001). Parametric decay of circularly polarized alfvén waves: Multidimensional simulations in periodic and open domains. *Astronomy & Astrophysics*, 367(2):705–718.

[Fabre et al., 2001] Fabre, D., Jacquin, L., and Sesterhenn, J. (2001). Linear interaction of a cylindrical entropy spot with a shock. *Physics of Fluids*, 13(8):2403–2422.

[Farag et al., 2019] Farag, G., Boivin, P., and Sagaut, P. (2019). Interaction of two-dimensional spots with a heat releasing/absorbing shock wave: linear interaction approximation results. *Journal of Fluid Mechanics*, 871:865–895.

[Fujino et al., 2008] Fujino, T., Yoshino, T., and Ishikawa, M. (2008). Numerical analysis of reentry trajectory coupled with magnetohydrodynamics flow control. *Journal of Spacecraft and Rockets*, 45(5):911–920.

[Gaitonde and Poggie, 2000] Gaitonde, D. and Poggie, J. (2000). Simulation of magnetogasdynamic flow control techniques. In *Fluids 2000 Conference and Exhibit*, page 2326.

[Gaitonde, 2008] Gaitonde, D. V. (2008). High-speed magnetohydrodynamic flow control analyses with three-dimensional simulations. *Journal of Propulsion and Power*, 24(5):946–961.

[Gaitonde, 2013] Gaitonde, D. V. (2013). Progress in shock wave/boundary layer interactions. In *43rd AIAA Fluid Dynamics Conference*, page 2607.

[Ganapathisubramani et al., 2007] Ganapathisubramani, B., Clemens, N., and Dolling, D. (2007). Effects of upstream boundary layer on the unsteadiness of shock-induced separation. *Journal of Fluid Mechanics*, 585:369–394.

[Gardiner and Stone, 2005] Gardiner, T. A. and Stone, J. M. (2005). An unsplit godunov method for ideal mhd via constrained transport. *Journal of Computational Physics*, 205(2):509–539.

[Giacalone and Jokipii, 2007] Giacalone, J. and Jokipii, J. R. (2007). Magnetic field amplification by shocks in turbulent fluids. *The Astrophysical Journal Letters*, 663(1):L41.

[Gloeckler et al., 1992] Gloeckler, G., Geiss, J., Balsiger, H., Bedini, P., Cain, J., Fischer, J., Fisk, L., Galvin, A., Gliem, F., Hamilton, D., et al. (1992). The solar wind ion composition spectrometer. *Astronomy and Astrophysics Supplement Series*, 92:267–289.

[Goedbloed et al., 2004] Goedbloed, J. H., Goedbloed, J., and Poedts, S. (2004). *Principles of magnetohydrodynamics: with applications to laboratory and astrophysical plasmas*. Cambridge university press.

[Grasso and Capano, 1995] Grasso, F. and Capano, G. (1995). Modeling of ionizing hypersonic flows in nonequilibrium. *Journal of spacecraft and Rockets*, 32(2):217–224.

[Greene et al., 2015] Greene, B., Clemens, N., Magari, P., and Micka, D. (2015). Control of mean separation in shock boundary layer interaction using pulsed plasma jets. *Shock waves*, 25(5):495–505.

[Griffond, 2005] Griffond, J. (2005). Linear interaction analysis applied to a mixture of two perfect gases. *Physics of Fluids*, 17(8):086101.

[Griffond and Soulard, 2012] Griffond, J. and Soulard, O. (2012). Evolution of axisymmetric weakly turbulent mixtures interacting with shock or rarefaction waves. *Physics of Fluids*, 24(11):115108.

[Gurijanov and Harsha, 1996] Gurijanov, E. and Harsha, P. (1996). Ajax-new directions in hypersonic technology.

[Hedstrom, 1979] Hedstrom, G. (1979). Nonreflecting boundary conditions for nonlinear hyperbolic systems. *Journal of computational Physics*, 30(2):222–237.

[Helzel et al., 2011] Helzel, C., Rossmanith, J. A., and Taetz, B. (2011). An unstaggered constrained transport method for the 3d ideal magnetohydrodynamic equations. *Journal of Computational Physics*, 230(10):3803–3829.

[Huber et al., 1971] Huber, P., Evans, J., and Chexnayder, C. (1971). Comparison of theoretical and flight-measured ionization in a blunt body re-entry flowfield. *AIAA Journal*, 9(6):1154–1162.

[Inan and Gołkowski, 2011] Inan, U. and Gołkowski, M. (2011). *Principles of Plasma Physics for Engineers and Scientists*. Cambridge University Press.

[Jameson et al., 1981] Jameson, A., Schmidt, W., and Turkel, E. (1981). Numerical solution of the euler equations by finite volume methods using runge kutta time stepping schemes. Technical report, National Aeronautics and Space Administration, Moffett Field, CA (United âĂę.

[Ji et al., 2016] Ji, S., Oh, S. P., Ruszkowski, M., and Markevitch, M. (2016). The efficiency of magnetic field amplification at shocks by turbulence. *Monthly Notices of the Royal Astronomical Society*, 463(4):3989–4003.

[Kantrowitz, 1955] Kantrowitz, A. (1955). A survey of physical phenomena occurring in flight at extreme speeds. In *Proceedings of the conference on high-speed aeronautics*, pages 335–339. Polytechnic Institute of Brooklyn New York.

[Kawai, 2013] Kawai, S. (2013). Divergence-free-preserving high-order schemes for magnetohydrodynamics: An artificial magnetic resistivity method. *Journal of Computational Physics*, 251:292–318.

[Kawai and Lele, 2008] Kawai, S. and Lele, S. K. (2008). Localized artificial diffusivity scheme for discontinuity capturing on curvilinear meshes. *Journal of Computational Physics*, 227(22):9498–9526.

[Kawamura et al., 2009] Kawamura, M., Matsuda, A., Katsurayama, H., Otsu, H., Konigorski, D., Sato, S., and Abe, T. (2009). Experiment on drag enhancement for a blunt body with electrodynamic heat shield. *Journal of Spacecraft and Rockets*, 46(6):1171–1177.

[Kolesnichenko et al., 2004] Kolesnichenko, Y., Azarova, O., Brovkin, V., Khmara, D., Lashkov, V., Mashek, I., and Ryvkin, M. (2004). Basics in beamed mw energy deposition for flow/flight control. In *42nd AIAA Aerospace Sciences Meeting and Exhibit*, page 669.

[Kontorovich, 1959] Kontorovich, V. (1959). On the interaction between small disturbances and discontinuities in magnetohydrodynamics and on the stability of shock waves. *Soviet Physics JETP*, 35(8):851–858.

[Kovasznay, 1953] Kovasznay, L. S. G. (1953). Turbulence in supersonic flow. *Journal of the Aeronautical Sciences*, 20:657–682.

[Kunkel, 1966] Kunkel, W. B. (1966). *Plasma physics in theory and application*. McGraw-Hill.

[Landau and Lifschitz, 1984] Landau, L. and Lifschitz, E. (1984). *Electrodynamics of Continuous Media*. Pergamon Press.

[Larsson et al., 2013] Larsson, J., Bermejo-Moreno, I., and Lele, S. K. (2013). Reynolds-and mach-number effects in canonical shock–turbulence interaction. *Journal of Fluid Mechanics*, 717:293–321.

[Larsson and Lele, 2009] Larsson, J. and Lele, S. K. (2009). Direct numerical simulation of canonical shock/turbulence interaction. *Physics of Fluids*, 21(12):126101.

[Lee and Deane, 2009] Lee, D. and Deane, A. E. (2009). An unsplit staggered mesh scheme for multidimensional magnetohydrodynamics. *Journal of Computational Physics*, 228(4):952–975.

[Lee et al., 1997] Lee, S., Lele, S. K., and Moin, P. (1997). Interaction of isotropic turbulence with shock waves: effect of shock strength. *Journal of Fluid Mechanics*, 340:225–247.

[Lele and Larsson, 2009] Lele, S. K. and Larsson, J. (2009). Shock-turbulence interaction: what we know and what we can learn from peta-scale simulations. In *Journal of Physics: Conference Series*, volume 180, page 012032. IOP Publishing.

[Leonov et al., 2001] Leonov, S., Bityurin, V., and Kolesnichenko, Y. (2001). Dynamic of a single-electrode hf plasma filament in supersonic airflow. In *39th Aerospace Sciences Meeting and Exhibit*, page 493.

[LeVeque and Leveque, 1992] LeVeque, R. J. and Leveque, R. J. (1992). *Numerical methods for conservation laws*, volume 132. Springer.

[Lin, 2002] Lin, J. C. (2002). Review of research on low-profile vortex generators to control boundary-layer separation. *Progress in Aerospace Sciences*, 38(4-5):389–420.

[Londrillo and Del Zanna, 2000] Londrillo, P. and Del Zanna, L. (2000). High-order upwind schemes for multidimensional magnetohydrodynamics. *The Astrophysical Journal*, 530(1):508.

[Lowson, 1966] Lowson, M. (1966). The fluctuating pressures due to shock interactions with turbulence and sound (fluctuating surface pressures due to shock wave interactions with turbulence and sound waves). Technical Report WR 66âĂŞ35, Wyle Laboratories, Huntsville, Ala., Res. Staff.

[Lüst, 1955] Lüst, R. (1955). Stationäre magneto-hydrodynamische stosswellen beliebiger stärke. *Zeitschrift für Naturforschung A*, 10(2):125–135.

[Lynn, 1966] Lynn, Y. (1966). Magnetohydrodynamic shocks in nonaligned flow. *The Physics of Fluids*, 9(2):314–335.

[Macheret et al., 2000] Macheret, S., Ionikh, Y. Z., Chernysheva, N., Yalin, A., Martinelli, L., McAndrew, B., Barker, P., Schneider, M., and Miles, R. (2000). Shock propagation in weakly ionized gases and plasma control of high-speed flows. In *Proceedings of the 2nd Workshop on Magneto-Plasma-Aerodynamics in Aerospace Applications, Moscow, IVTAN*, pages 34–42.

[Macheret et al., 2001] Macheret, S. O., Shneider, M. N., and Miles, R. B. (2001). External supersonic flow and scramjet inlet control by MHD with electron beam ionization. *AIAA paper*, 492:2001.

[Macheret et al., 2002] Macheret, S. O., Shneider, M. N., and Miles, R. B. (2002). Magnetohydrodynamic control of hypersonic flows and scramjet inlets using electron beam ionization. *AIAA journal*, 40(1):74–81.

[Mahesh et al., 1997] Mahesh, K., Lele, S. K., and Moin, P. (1997). The influence of entropy fluctuations on the interaction of turbulence with a shock wave. *Journal of Fluid Mechanics*, 334(1):353–379.

[Martín and Puerta, 1999] Martín, P. and Puerta, J. (1999). *Plasma Physics: Proceedings of the 1997 Latin American Workshop (VII LAWPP 1997), held in Caracas, Venezuela, January 20–31, 1997*. Springer Science & Business Media.

[McKenzie, 1970] McKenzie, J. (1970). Hydromagnetic wave interaction with the magnetopause and the bow shock. *Planetary and Space Science*, 18(1):1–23.

[McKenzie and Westphal, 1968] McKenzie, J. and Westphal, K. (1968). Interaction of linear waves with oblique shock waves. *Physics of Fluids (1958-1988)*, 11(11):2350–2362.

[McKenzie and Westphal, 1969] McKenzie, J. F. and Westphal, K. O. (1969). Transmission of alfvén waves through the earth's bow shock. *Planetary and Space Science*, 17(5):1029–1037.

[McKenzie and Westphal, 1970] McKenzie, J. F. and Westphal, K. O. (1970). Interaction of hydromagnetic waves with hydromagnetic shocks. *The Physics of Fluids*, 13(3):630–640.

[Minton et al., 2005] Minton, D., Lewis, M., and Van Wie, D. (2005). Plasma and magnetohydrodynamic effects on incipient separation in a cold supersonic flow. In *AIAA/CIRA 13th International Space Planes and Hypersonics Systems and Technologies Conference*, page 3224.

[Mitchner and Kruger, 1973] Mitchner, M. and Kruger, C. H. (1973). *Partially ionized gases*, volume 8. Wiley New York.

[Myong and Roe, 1997] Myong, R. and Roe, P. (1997). Shock waves and rarefaction waves in magnetohydrodynamics. part 2. the mhd system. *Journal of plasma physics*, 58(3):521–552.

[Orszag and Tang, 1979] Orszag, S. A. and Tang, C.-M. (1979). Small-scale structure of two-dimensional magnetohydrodynamic turbulence. *Journal of Fluid Mechanics*, 90(01):129–143.

[Plotkin, 1975] Plotkin, K. J. (1975). Shock wave oscillation driven by turbulent boundary-layer fluctuations. *AIAA Journal*, 13(8):1036–1040.

[Poggie and Gaitonde, 2002] Poggie, J. and Gaitonde, D. V. (2002). Magnetic control of flow past a blunt body: Numerical validation and exploration. *Physics of Fluids*, 14(5):1720–1731.

[Poggie and Smits, 2005] Poggie, J. and Smits, A. J. (2005). Experimental evidence for plotkin model of shock unsteadiness in separated flow. *Physics of Fluids*, 17(1):018107.

[Porter et al., 2015] Porter, D. H., Jones, T., and Ryu, D. (2015). Vorticity, shocks, and magnetic fields in subsonic, icm-like turbulence. *The Astrophysical Journal*, 810(2):93.

[Potter, 2001] Potter, D. (2001). Introduction of the pirate program for parametric reentry vehicle plasma effects studies. In *37th AIAA Plasmadynamics and Lasers Conference*, page 3239.

[Powell, 1994] Powell, K. G. (1994). An approximate Riemann solver for magnetohydrodynamics (that works in more than one dimension).

[Quiroz et al., 2012] Quiroz, R., Embler, J., Jacobs, R., Tzong, G., and Liguore, S. (2012). Air vehicle integration and technology research (aviatr). task order 0023: Predictive capability for hypersonic structural response and life prediction: Phase 2-detailed design of hypersonic cruise vehicle hot-structure. Technical report, Boeing Co, Huntington Beach CA.

[Resler Jr., 1958] Resler Jr., E. L. (1958). The prospects for magneto-aerodynamics. *Journal of the Aerospace Sciences*, 25(4):235–245.

[Ribner, 1954] Ribner, H. S. (1954). Convection of a pattern of vorticity through a shock wave. Technical Report 1164, NACA.

[Ribner, 1955] Ribner, H. S. (1955). Shock-turbulence interaction and the generation of noise. Technical Report 1233, NACA.

[Ribner, 1969] Ribner, H. S. (1969). Acoustic energy flux from shock-turbulence interaction. *Journal of Fluid Mechanics*, 35(2):299–310.

[Roe and Balsara, 1996] Roe, P. and Balsara, D. (1996). Notes on the eigensystem of magnetohydrodynamics. *SIAM Journal on Applied Mathematics*, 56(1):57–67.

[Ryu and Jones, 1995] Ryu, D. and Jones, T. (1995). Numerical magetohydrodynamics in astrophysics: Algorithm and tests for one-dimensional flow. *The Astrophysical Journal*, 442:228–258.

[Salas, 2009] Salas, M. D. (2009). *A shock-fitting primer*. CRC Press.

[Shneider and Macheret, 2006] Shneider, M. and Macheret, S. (2006). Modeling of plasma virtual shape control of ram/scramjet inlet and isolator. *Journal of propulsion and power*, 22(2):447–454.

[Shneider et al., 2004] Shneider, M. N., Macheret, S. O., and Miles, R. B. (2004). Analysis of magnetohydrodynamic control of scramjet inlets. *AIAA journal*, 42(11):2303–2310.

[Shu and Osher, 1988] Shu, C.-W. and Osher, S. (1988). Efficient implementation of essentially non-oscillatory shock-capturing schemes. *Journal of computational physics*, 77(2):439–471.

[Sod, 1978] Sod, G. A. (1978). A survey of several finite difference methods for systems of nonlinear hyperbolic conservation laws. *Journal of computational physics*, 27(1):1–31.

[Soloviev et al., 2001] Soloviev, V., Krivtsov, V., Konchakov, A., and Malmuth, N. (2001). Simulation of supersonic body drag reduction produced by forebody filamentary plasmas. In *32nd AIAA Plasmadynamics and Lasers Conference*, page 2727.

[Somov, 2012] Somov, B. V. (2012). *Plasma Astrophysics, Part II: Reconnection and Flares*, volume 392. Springer Science & Business Media.

[Szemberg O'Connor, 2018] Szemberg O'Connor, T. (2018). *Bulk viscosity effects in compressible turbulent Couette flow*. PhD thesis.

[Tadmor, 1990] Tadmor, E. (1990). Shock capturing by the spectral viscosity method. *Computer Methods in Applied Mechanics and Engineering*, 80(1-3):197–208.

[Takizawa et al., 2006] Takizawa, Y., Matsuda, A., Sato, S., Abe, T., and Konigorski, D. (2006). Experimental investigation of the electromagnetic effect on a shock layer around a blunt body in a weakly ionized flow. *Physics of Fluids*, 18(11):117105.

[Tam and Webb, 1993] Tam, C. K. and Webb, J. C. (1993). Dispersion-relation-preserving finite difference schemes for computational acoustics. *Journal of Computational Physics*, 107(2):262–281.

[Thompson, 2013] Thompson, W. B. (2013). *An introduction to plasma physics*. Elsevier.

[Torrilhon, 2002] Torrilhon, M. (2002). Exact solver and uniqueness conditions for riemann problems of ideal magnetohydrodynamics. In *Research Report/Seminar für Angewandte Mathematik*, volume 2002. Eidgenössische Technische Hochschule, Seminar für Angewandte Mathematik.

[Tóth, 2000] Tóth, G. (2000). The $\nabla \cdot \boldsymbol{B} = 0$ constraint in shock-capturing magnetohydrodynamics codes. *Journal of Computational Physics*, 161(2):605–652.

[Touber and Alferez, 2019] Touber, E. and Alferez, N. (2019). Shock-induced energy conversion of entropy in non-ideal fluids. *Journal of Fluid Mechanics*, 864:807–847.

[Wang et al., 2015] Wang, J., Huang, Q., Liu, Z., and Li, K. (2015). Explicit high accuracy maximum resolution dispersion relation preserving schemes for computational aeroacoustics. *Mathematical Problems in Engineering*, 2015.

[Westphal and McKenzie, 1969] Westphal, K. and McKenzie, J. (1969). Interaction of magnetoacoustic and entropy waves with normal magnetohydrodynamic shock waves. *The Physics of Fluids*, 12(6):1228–1236.

[Whang et al., 1987] Whang, Y., Wei, F., and Du, H. (1987). Critical angles of incidence for transmission of magnetohydrodynamic waves across shock surfaces. *Journal of Geophysical Research: Space Physics*, 92(A11):12036–12044.

[Woods, 2008] Woods, L. (2008). *Physics of Plasmas*. Physics textbook. Wiley.

[Wu, 1987] Wu, C. (1987). On mhd intermediate shocks. *Geophysical Research Letters*, 14(6):668–671.

[Yang et al., 2016] Yang, Y., Wan, M., Shi, Y., Yang, K., and Chen, S. (2016). A hybrid scheme for compressible magnetohydrodynamic turbulence. *Journal of Computational Physics*, 306:73–91.

[Yao et al., 2012] Yao, Y., Rincon, D., and Zheng, Y. (2012). Shock induced separating flows in scramjet intakes. In *International Journal of Modern Physics: Conference Series*, volume 19, pages 73–82. World Scientific.

[Zhuang and Russell, 1982] Zhuang, H.-C. and Russell, C. (1982). Interaction of small-amplitude fluctuations with a strong magnetohydrodynamic shock. *The Physics of Fluids*, 25(5):748–758.

[Ziegler, 2004] Ziegler, U. (2004). A central-constrained transport scheme for ideal magnetohydrodynamics. *Journal of Computational Physics*, 196(2):393–416.

Appendix A

Magneto–acoustic eigenmodes

In this section, the magneto–acoustic unitary eigenvectors are derived and computed in the limit of parallel and perpendicular alignment respectively of the wavevector with the mean magnetic field.

A.1 Parallel alignment between wavevector and mean magnetic field

For alignment between the wavevector and mean magnetic field, $\boldsymbol{k} \cdot \boldsymbol{B} = kB$, the magneto–acoustic mode eigenfrequencies, $\omega_{0f,s}$:

$$\omega_{0f,s}^2 = \frac{k^2}{2}\left((b^2 + c_o^2) \pm \sqrt{(b^2 + c_o^2)^2 - 4\frac{(\boldsymbol{k} \cdot \boldsymbol{b})^2}{k^2}c_o^2}\right), \tag{A.1.1}$$

become degenerate with the Alfvén and gasdynamic acoustic modes. The respective magneto–acoustic mode degeneracies are dependent on the ratio between the Alfvén and the sound speeds, $r = b/c_o$:

$$\omega_{0f\pm} = \begin{cases} \pm kb, & \text{if } r > 1, \\ \pm kc_o, & \text{otherwise.} \end{cases} \tag{A.1.2}$$

$$\omega_{0s\pm} = \begin{cases} \pm kb, & \text{if } r < 1, \\ \pm kc_o, & \text{otherwise.} \end{cases} \tag{A.1.3}$$

From the magneto–acoustic eigenvector definition:

$$\boldsymbol{e}_{f,s\pm} = [\rho'_{f,s\pm},\, \boldsymbol{u}'^{\intercal}_{f,s\pm},\, c_o^2\rho'_{f,s\pm},\, \boldsymbol{B}'^{\intercal}_{f,s\pm}]^{\intercal}, \tag{A.1.4}$$

where,

$$\rho'_{f,s\pm} = \{1 - (\boldsymbol{k}\cdot\boldsymbol{b})^2/\omega^2_{0f,s\pm}\}, \tag{A.1.5}$$

$$\boldsymbol{u}'_{f\pm} = \{(\omega_{0f\pm}/k^2)\boldsymbol{k} - (\boldsymbol{k}\cdot\boldsymbol{b}/\omega_{0f\pm})\boldsymbol{b}\}/\bar{\rho}, \tag{A.1.6}$$

$$\boldsymbol{u}'_{s\pm} = sign(\boldsymbol{k}\cdot\boldsymbol{B})\{(\omega_{0s\pm}/k^2)\boldsymbol{k} - (\boldsymbol{k}\cdot\boldsymbol{b}/\omega_{0s\pm})\boldsymbol{b}\}/\bar{\rho}, \tag{A.1.7}$$

$$\boldsymbol{B}'_{f,s\pm} = \{\boldsymbol{b} - (\boldsymbol{k}\cdot\boldsymbol{b})\boldsymbol{k}/k^2\}/\sqrt{\bar{\rho}}, \tag{A.1.8}$$

it can be shown that magneto–acoustic modes for which $\omega_{0\mu\pm} = \pm kc_o$, are analogous to the gasdynamic acoustic mode - i.e. induce no magnetic field fluctuations and transport only irrotational fluid motions ($\nabla \times \boldsymbol{u}' = \boldsymbol{0}$) and thermodynamic perturbations. In the limit of Alfvén mode degeneracy, $\omega_{0\mu\pm} \rightarrow \pm kb$, it is trivial to show all eigenvector components given in (A.1.5) - (A.1.8) approach zero. This "trivial" eigenvector solution to the magneto–acoustic modes, $\boldsymbol{e}_{0\mu} = \boldsymbol{0}$, is a consequence of the initial assumption, $\omega^2_{0\mu} \neq k^2b^2$, applied when deriving the eigenvector formulation given in (A.1.5) - (A.1.8). If the eigenvectors were re–derived under the initial assumption, $\omega^2_{0\mu} = k^2b^2$, it is possible to show the respective magneto–acoustic modes transport solenoidal fluid motions (parallel to magnetic field perturbations) and no thermodynamic property fluctuations. For magneto–acoustic eigenvectors defined in a coordinate system orthogonal to the mean magnetic field vector basis, $\boldsymbol{e}_\mu = [\rho'_\mu,\, u'_{\perp,\mu},\, 0,\, u'_{\parallel,\mu},\, p'_\mu,\, B'_{\perp,\mu},\, 0,\, B'_{\parallel,\mu}]^\intercal$, in which the wavevector is also defined as $\boldsymbol{k} = [k_\perp,\, 0,\, k_\parallel]^\intercal$ and $\bar{\boldsymbol{B}} = [0,\, 0,\, \bar{B}]^\intercal$ (subscripts "$\parallel$" and "$\perp$" denote directions parallel and orthogonal to $\bar{\boldsymbol{B}}$ respectively), the degenerate Alfvén modes are given as:

$$\boldsymbol{e}_{f\pm} = [0,\, 1,\, 0,\, 0,\, 0,\, \mp\sqrt{\bar{\rho}},\, 0,\, 0]^\intercal, \quad \text{if } r > 1, \tag{A.1.9}$$

$$\boldsymbol{e}_{s\pm} = [0,\, 1,\, 0,\, 0,\, 0,\, \mp\sqrt{\bar{\rho}},\, 0,\, 0]^\intercal, \quad \text{if } r < 1. \tag{A.1.10}$$

However, it is possible to show a unitary formulation of the magneto–acoustic eigenvectors presented in (A.1.5) - (A.1.8), approach a form analogous to (A.1.9) and (A.1.10) in the limit of alignment between the wavevector and the mean magnetic field.

We first consider a normalised form of the magneto–acoustic eigenvectors:

$$\breve{\boldsymbol{e}}_{f,s\pm} = \boldsymbol{\Lambda}\boldsymbol{e}_{f,s\pm} = [\breve{\rho}_{f,s\pm},\, \breve{\boldsymbol{u}}^\intercal_{f,s\pm},\, \breve{\rho}_{f,s\pm},\, \breve{\boldsymbol{B}}^\intercal_{f,s\pm}]^\intercal, \tag{A.1.11}$$

where $\boldsymbol{\Lambda}$ is a diagonal matrix in which, $\Lambda_{11} = 1$, $\Lambda_{22} = \Lambda_{33} = \Lambda_{44} = \bar{\rho}/c_o$, $\Lambda_{55} = 1/(c_o^2)$, $\Lambda_{66} = \Lambda_{77} = \Lambda_{88} = \sqrt{\bar{\rho}}/c_o$ and,

$$\breve{\rho}_{f,s\pm} = 1 - (\boldsymbol{k}\cdot\boldsymbol{r})^2/\hat{\omega}^2_{0f,s\pm}, \tag{A.1.12}$$

$$\breve{\boldsymbol{u}}_{f\pm} = \{(\hat{\omega}_{0f\pm}/k^2)\boldsymbol{k} - (\boldsymbol{k}\cdot\boldsymbol{r}/\hat{\omega}_{0f\pm})\boldsymbol{r}\}, \tag{A.1.13}$$

$$\breve{\boldsymbol{u}}_{s\pm} = sign(\boldsymbol{k}\cdot\boldsymbol{B})\{(\hat{\omega}_{0s\pm}/k^2)\boldsymbol{k} - (\boldsymbol{k}\cdot\boldsymbol{r}/\hat{\omega}_{0s\pm})\boldsymbol{r}\}, \tag{A.1.14}$$

$$\breve{\boldsymbol{B}}_{f,s\pm} = \boldsymbol{r} - (\boldsymbol{k}\cdot\boldsymbol{r})\boldsymbol{k}/k^2, \tag{A.1.15}$$

in which $\hat{\omega}_{0f,s\pm} = \omega_{0f,s}/c_o$.

The unitary magneto–acoustic eigenvector is therefore computed as:

$$\hat{\boldsymbol{e}}_{f,s\pm} = \frac{\breve{\boldsymbol{e}}_{f,s\pm}}{||\breve{\boldsymbol{e}}_{f,s\pm}||} = [\hat{\rho}'_{f,s\pm},\, \hat{\boldsymbol{u}}'^{\intercal}_{f,s\pm},\, \hat{p}'_{f,s\pm},\, \hat{\boldsymbol{B}}'^{\intercal}_{f,s\pm}]^{\intercal}, \tag{A.1.16}$$

(note $\hat{p}'_{f,s\pm} \equiv \hat{\rho}'_{f,s\pm}$) where $||\breve{\boldsymbol{e}}_{f,s\pm}||$ is the principal root of $\breve{\boldsymbol{e}}_{f,s\pm}\cdot\breve{\boldsymbol{e}}_{f,s\pm}$,

$$\breve{\boldsymbol{e}}_{f,s\pm}\cdot\breve{\boldsymbol{e}}_{f,s\pm} = 2 + 2\frac{(\boldsymbol{k}\cdot\boldsymbol{r})^4}{\hat{\omega}^4_{0f,s}} - 4\frac{(\boldsymbol{k}\cdot\boldsymbol{r})^2}{\hat{\omega}^2_{0f,s}} + \frac{\hat{\omega}^2_{0f,s}}{k^2} + \left(\frac{\boldsymbol{k}\cdot\boldsymbol{r}}{\hat{\omega}_{0f,s}}\right)^2 r^2 - 3\frac{(\boldsymbol{k}\cdot\boldsymbol{r})^2}{k^2} + r^2. \tag{A.1.17}$$

In a coordinate system orthogonal to $\bar{\boldsymbol{B}}$ we define components of the normalised magneto–acoustic eigenvector, $\breve{\boldsymbol{e}}_{\mu} = [\breve{\rho},\, \breve{u}_{\perp},\, 0,\, \breve{u}_{\parallel},\, \breve{p},\, \breve{B}_{\perp},\, 0,\, \breve{B}_{\parallel}]^{\intercal}$, as:

$$\breve{\rho}_{f,s\pm} = 1 - k^2_{\parallel}r^2/\hat{\omega}^2_{0f,s\pm}, \tag{A.1.18}$$

$$\breve{u}_{\parallel,f\pm} = \{(\hat{\omega}_{0f\pm}/k^2) - r^2/\hat{\omega}_{0f\pm}\}k_{\parallel}, \tag{A.1.19}$$

$$\breve{u}_{\perp,f\pm} = \{\hat{\omega}_{0f\pm}/k^2\}k_{\perp}, \tag{A.1.20}$$

$$\breve{u}_{\parallel,s\pm} = sign(k_{\parallel}B)\{(\hat{\omega}_{0s\pm}/k^2) - r^2/\hat{\omega}_{0s\pm}\}k_{\parallel}, \tag{A.1.21}$$

$$\breve{u}_{\perp,s\pm} = sign(k_{\parallel}B)\{\hat{\omega}_{0s\pm}/k^2\}k_{\perp}, \tag{A.1.22}$$

$$\breve{B}_{\parallel f,s\pm} = rk^2_{\perp}/k^2, \tag{A.1.23}$$

$$\breve{B}_{\perp f,s\pm} = -rk_{\perp}k_{\parallel}/k^2, \tag{A.1.24}$$

and make the substitution, $\boldsymbol{k}\cdot\boldsymbol{r} = k_{\parallel}r$ in (A.1.17).

To evaluate $\hat{\boldsymbol{e}}_{f,s\pm}$ in the limit of parallel alignment between the wavevector and mean magnetic field we first define $\boldsymbol{k}\cdot\boldsymbol{B}$:

$$\boldsymbol{k}\cdot\boldsymbol{B} = kB\left(1 - \bar{\epsilon}^2\right)^{1/2}, \tag{A.1.25}$$

where $\bar{\epsilon}$ is a small parameter, $\bar{\epsilon} \ll 1$, and consequently set,

$$k^2_{\parallel} = \frac{(\boldsymbol{k}\cdot\boldsymbol{B})^2}{B^2} = k^2(1-\bar{\epsilon}^2), \quad \text{and} \quad k^2_{\perp} = k^2 - k^2_{\parallel} = k^2\bar{\epsilon}^2, \tag{A.1.26a,b}$$

The proceeding analysis is restricted to the fast magneto–acoustic mode eigenfrequencies and eigenvectors however, it is trivial to extend results to the slow magneto–acoustic mode.

Applying (A.1.25) and the Taylor series expansion of $(1+x)^{1/2}$ to (A.1.1), we compute $\hat{\omega}_{0f}^2$ in the limit of parallel wavevector alignment:

$$\hat{\omega}_{0f}^2 = k^2 r^2 \left(1 + \frac{\bar{\epsilon}^2}{r^2-1}\right) + \mathrm{O}(\bar{\epsilon}^4), \tag{A.1.27}$$

and $\hat{\omega}_{0f}$:

$$\hat{\omega}_{0f\pm} = \pm kr \left(1 + \frac{\bar{\epsilon}^2}{2(r^2-1)}\right) + \mathrm{O}(\bar{\epsilon}^4), \tag{A.1.28}$$

Applying (A.1.26), (A.1.27) and (A.1.28) in (A.1.18) - (A.1.24) and evaluating the result in the limit, $\bar{\epsilon} \to 0$, $\hat{\boldsymbol{e}}_{f\pm}$ can be computed in the case of parallel alignment between the wavevector and the mean magnetic field when $r > 1$:

$$\hat{\boldsymbol{e}}_{f\pm} = \frac{1}{\sqrt{2}}[0,\ 1,\ 0,\ 0,\ 0,\ \mp 1,\ 0,\ 0]^{\intercal}. \tag{A.1.29}$$

It can be easily shown that the expression for the slow magneto–acoustic mode unitary eigenvector is analogous to the form given above when $r < 1$:

$$\hat{\boldsymbol{e}}_{s\pm} = \frac{1}{\sqrt{2}}[0,\ 1,\ 0,\ 0,\ 0,\ \mp sign(\boldsymbol{k}\cdot\boldsymbol{B}),\ 0,\ 0]^{\intercal}. \tag{A.1.30}$$

A.2 Perpendicular alignment between wavevector and mean magnetic field

In the limit of orthogonal wave propagation with respect to the mean magnetic field, $\boldsymbol{k}\cdot\boldsymbol{b} \to 0$, it is trivial to show:

$$\omega_{0s}^2 = \frac{k^2}{2}\left((b^2+c_o^2) - \sqrt{(b^2+c_o^2)^2 - 4\frac{(\boldsymbol{k}\cdot\boldsymbol{b})^2}{k^2}c_o^2}\right) \to 0. \tag{A.2.1}$$

From (A.1.5) and (A.1.6) we note both density, $\rho'_{s\pm}$, and velocity, $\boldsymbol{u}'_{s\pm}$, components of the slow magneto–acoustic eigenvector contain a singularity when $\omega_{0s} = 0$. However, it is possible to derive expressions close to the singularity to show that in approach of the limit, $\omega_{0s} \to 0$, $\rho'_{s\pm}$ and $\boldsymbol{u}'_{s\pm}$ remain finite.

First, we make the following substitution:

$$\boldsymbol{k}\cdot\boldsymbol{b} = \bar{\epsilon}kb, \tag{A.2.2}$$

Applying (A.2.2) and the Taylor series expansion of $(1+x)^{1/2}$ to (A.2.1), we compute a second order approximation of $\hat{\omega}_{0s}^2$ with respect to $\bar{\epsilon}$:

$$\hat{\omega}_{0s}^2 = \frac{k^2 r^2 \bar{\epsilon}^2}{(1+r^2)} + \mathrm{O}(\bar{\epsilon}^4), \tag{A.2.3}$$

By injecting (A.2.2) and (A.2.3) into (A.1.12) and (A.1.14), we derive expressions for $\breve{\rho}_{s\pm}$ and $\breve{\boldsymbol{u}}_{s\pm}$ in the limit $\bar{\epsilon} \to 0$:

$$\breve{\rho}_{s\pm} = -r^2, \tag{A.2.4}$$

$$\breve{\boldsymbol{u}}_{s\pm} = \mp sign(\boldsymbol{k}\cdot\boldsymbol{B}) \left\{ (1+r^2)^{1/2} \boldsymbol{r} \right\}, \tag{A.2.5}$$

which therefore indicates that the slow magneto–acoustic mode will transport solenoidal fluid motions as $\boldsymbol{k}\cdot\boldsymbol{r} = 0$ and $\breve{\boldsymbol{u}}_{s\pm} \propto \boldsymbol{r}$. We also note:

$$\breve{\boldsymbol{B}}'_{s\pm} = \boldsymbol{r}. \tag{A.2.6}$$

Additionally, applying (A.2.2) and (A.2.3) to (A.1.17) in the limit $\bar{\epsilon} \to 0$:

$$\breve{\boldsymbol{e}}_{s\pm} \cdot \breve{\boldsymbol{e}}_{s\pm} = 4r^4 + 1 \tag{A.2.7}$$

Appendix B

Shock refraction problem

In this section, the scattering matrix is derived for the fast MHD shock refraction problem in a three–dimensional and decoupled perturbed shock system respectively.

B.1 Scattering matrix: Three–dimensional perturbed shock system

The three–dimensional linearised Rankine–Hugoniot jump conditions for a perturbation–shock interaction in which the wavevector, magnetic field and shock normal all lie in the $x-y$ plane:

$$\mathbf{T}_2\boldsymbol{\mu}_2' + \boldsymbol{R}\delta_s = \mathbf{T}_1\boldsymbol{\mu}_1', \tag{B.1.1}$$

where $\boldsymbol{\mu}' = [\rho',\, u',\, v',\, w',\, p',\, B_x',\, B_y',\, B_z']^{\intercal}$ and,

$$\mathbf{T} = \begin{bmatrix} \bar{u} & \bar{\rho} & 0 & 0 & 0 & 0 & 0 & 0 \\ \bar{u}^2 & 2\bar{\rho}\bar{u} & 0 & 0 & 1 & 0 & \bar{B}_y & 0 \\ \bar{v}/\bar{\rho} & \bar{v}/\bar{u} & 1 & 0 & 0 & -\bar{B}_y/(\bar{\rho}\bar{u}) & -\bar{B}_x/(\bar{\rho}\bar{u}) & 0 \\ 0 & 0 & 0 & 1 & 0 & 0 & 0 & -\bar{B}_x/(\bar{\rho}\bar{u}) \\ -c_o^2/\bar{\rho}(\gamma-1) & \bar{u}\bar{B}^2/\bar{B}_x^2 & 0 & 0 & \gamma/\bar{\rho}(\gamma-1) & -\bar{u}^2\bar{B}_y^2/\bar{B}_x^3 & \bar{u}^2\bar{B}_y/\bar{B}_x^2 & 0 \\ 0 & \bar{B}_y & -\bar{B}_x & 0 & 0 & -\bar{v} & \bar{u} & 0 \\ 0 & 0 & 0 & -\bar{B}_x & 0 & 0 & 0 & \bar{u} \end{bmatrix},$$

$$\boldsymbol{R} = \begin{bmatrix} -\mathrm{i}[\![\bar{\rho}(\omega - \bar{v}k_y)]\!] \\ \mathrm{i}\bar{\rho}\bar{u}[\![\bar{v}k_y]\!] \\ -\mathrm{i}[\![\omega\bar{v}/\bar{u}]\!] - \mathrm{i}[\![k_y(\bar{u} - \bar{v}^2/\bar{u} + \bar{B}_y^2/(\bar{\rho}\bar{u}))]\!] \\ -\mathrm{i}[\![k_z\bar{u}]\!] \\ -\mathrm{i}(1/\bar{B}_x^2)[\![\omega\bar{B}^2\bar{u}]\!] + \mathrm{i}[\![k_y(\bar{u}\bar{B}^2/\bar{B}_x^3)(\bar{v}\bar{B}_x - \bar{u}\bar{B}_y)]\!] \\ -\mathrm{i}[\![\omega\bar{B}_y]\!] \\ 0 \end{bmatrix}.$$

An arbitrary disturbance composed of a single wave mode, impinging the upstream side of the shock is given as:

$$\boldsymbol{\mu}_1' = \boldsymbol{\xi}_1 \mathrm{e}^{\mathrm{i}[\boldsymbol{k}_1 \cdot \boldsymbol{x} - \omega t]}, \tag{B.1.2}$$

in which $\boldsymbol{\xi}_1 \equiv \boldsymbol{e}_1$, where $\boldsymbol{e}_1$ is the eigenvector of the impinging mode and $\boldsymbol{k}_1 \equiv [k_{x,1}, k_y, k_z]^\intercal$.

Perturbations on the downstream side ($x > x_s$) decomposed into eigenmodes leaving the shock:

$$\begin{aligned} \boldsymbol{\mu}_2' = \boldsymbol{\xi}_E \mathrm{e}^{[\mathrm{i}(\boldsymbol{k}_E \cdot \boldsymbol{x} - \omega t)]} \quad + \quad \boldsymbol{\xi}_{f+} \mathrm{e}^{[\mathrm{i}(\boldsymbol{k}_{f+} \cdot \boldsymbol{x} - \omega t)]} \quad + \\ + \quad \boldsymbol{\xi}_{s+} \mathrm{e}^{[\mathrm{i}(\boldsymbol{k}_{s+} \cdot \boldsymbol{x} - \omega t)]} \quad + \quad \boldsymbol{\xi}_{s-} \mathrm{e}^{[\mathrm{i}(\boldsymbol{k}_{s-} \cdot \boldsymbol{x} - \omega t)]} + \\ + \quad \boldsymbol{\xi}_{A+} \mathrm{e}^{[\mathrm{i}(\boldsymbol{k}_{A+} \cdot \boldsymbol{x} - \omega t)]} \quad + \quad \boldsymbol{\xi}_{A-} \mathrm{e}^{[\mathrm{i}(\boldsymbol{k}_{A-} \cdot \boldsymbol{x} - \omega t)]}, \end{aligned} \tag{B.1.3}$$

where $\boldsymbol{k}_\mu \equiv [k_{x,\mu}, k_y, k_z]^\intercal$, such that $\boldsymbol{k}_\mu \cdot \bar{\boldsymbol{u}} = \omega - \omega_{0\mu}$ and $\boldsymbol{\xi}_\mu \equiv \chi_\mu \boldsymbol{e}_\mu$, in which χ_μ is the unknown refraction coefficient and $\boldsymbol{e}_\mu$ is the eigenvector of a given mode, computed as a function of the respective refracted wavevector and downstream base flow ($\bar{\boldsymbol{\mu}}_2$).

To transform the vector of perturbed variables to the eigenmode basis, we first define $\boldsymbol{\xi}_\mu$ in terms of a new refraction coefficient, $\hat{\chi}_\mu$, using (A.1.11) and (A.1.16):

$$\boldsymbol{\xi}_\mu = \chi_\mu \boldsymbol{e}_\mu = \hat{\chi}_\mu \boldsymbol{\Lambda}^{-1} \hat{\boldsymbol{e}}_\mu, \tag{B.1.4}$$

where $\hat{\chi}_\mu \equiv \chi_\mu ||\breve{\boldsymbol{e}}_\mu||$, and we note the entropy eigenvector is unitary, $\hat{\boldsymbol{e}}_E = \boldsymbol{e}_E$, and define the unitary eigenvectors of the Alfvén modes as,

$$\hat{\boldsymbol{e}}_{A\pm} = \frac{1}{\sqrt{2}}[0,\, \hat{\boldsymbol{u}}_{A\pm}'^\intercal,\, 0,\, \hat{\boldsymbol{B}}_{A\pm}'^\intercal]^\intercal, \tag{B.1.5}$$

where, $\hat{\boldsymbol{u}}_{A\pm}' = (\boldsymbol{k} \times \boldsymbol{b})/||\boldsymbol{k} \times \boldsymbol{b}||$ and $\hat{\boldsymbol{B}}_{A\pm}' \equiv \mp \hat{\boldsymbol{u}}_{A\pm}'$.

The transformation to the eigenmode basis is now given by:

$$\boldsymbol{\mu}_2' = \boldsymbol{\Lambda}^{-1} \hat{\mathbf{E}} \hat{\boldsymbol{Y}}, \tag{B.1.6}$$

where $\hat{\boldsymbol{Y}} = [\hat{\chi}_E,\, \hat{\chi}_{f+},\, \hat{\chi}_{s+},\, \hat{\chi}_{s-},\, \hat{\chi}_{A+},\, \hat{\chi}_{A-}]^{\intercal}$ and $\hat{\mathbf{E}}$ is a 8×6 linear mapping matrix whose columns are given by the unitary eigenvectors of the downstream eigenmodes:

$$\hat{\mathbf{E}} = \begin{bmatrix} 1 & \hat{\rho}'_{f+} & \hat{\rho}'_{s+} & \hat{\rho}'_{s-} & 0 & 0 \\ 0 & \hat{u}'_{f+} & \hat{u}'_{s+} & \hat{u}'_{s-} & \hat{u}'_{A+} & \hat{u}'_{A-} \\ 0 & \hat{v}'_{f+} & \hat{v}'_{s+} & \hat{v}'_{s-} & \hat{v}'_{A+} & \hat{v}'_{A-} \\ 0 & \hat{w}'_{f+} & \hat{w}'_{s+} & \hat{w}'_{s-} & \hat{w}'_{A+} & \hat{w}'_{A-} \\ 0 & \hat{p}'_{f+} & \hat{p}'_{s+} & \hat{p}'_{s-} & 0 & 0 \\ 0 & \hat{B}'_{x,f+} & \hat{B}'_{x,s+} & \hat{B}'_{x,s-} & \hat{B}'_{x,A+} & \hat{B}'_{x,A-} \\ 0 & \hat{B}'_{y,f+} & \hat{B}'_{y,s+} & \hat{B}'_{y,s-} & \hat{B}'_{y,A+} & \hat{B}'_{y,A-} \\ 0 & \hat{B}'_{z,f+} & \hat{B}'_{z,s+} & \hat{B}'_{z,s-} & \hat{B}'_{z,A+} & \hat{B}'_{z,A-} \end{bmatrix} \tag{B.1.7}$$

The following matrix augmentations are then performed:

$$\mathbf{A} = (\hat{\mathbf{T}}_2 | \boldsymbol{R}) \quad \text{and} \quad \mathbf{E} = \left(\frac{\mathbf{E}^*}{\boldsymbol{c}} \right), \tag{B.1.8a,b}$$

where $\hat{\mathbf{T}}_2 \equiv \mathbf{T}_2 \boldsymbol{\Lambda}^{-1}$, $\boldsymbol{c} = [0,\, 0,\, 0,\, 0,\, 0,\, 0,\, 1]$ and $\mathbf{E}^* = (\hat{\mathbf{E}} | \boldsymbol{d})$, in which $\boldsymbol{d}$ is an $8-$dimensional null column vector.

Applying (B.1.2) and (B.1.8) to (B.1.1), we now write the linearised Rankine–Hugoniot jump conditions in the form:

$$\mathbf{A}\mathbf{E}\boldsymbol{Y} = \mathbf{T}_1 \boldsymbol{\xi}_1, \tag{B.1.9}$$

where $\boldsymbol{Y} \equiv [\hat{\chi}_E,\, \hat{\chi}_{f+},\, \hat{\chi}_{s+},\, \hat{\chi}_{s-},\, \hat{\chi}_{A+},\, \hat{\chi}_{A-}, \delta_s]^{\intercal}$.

Finally, we multiply both sides of (B.1.9) by a 7×7 diagonal matrix, $\bar{\boldsymbol{\Lambda}}$, where $\bar{\Lambda}_{11} = 1/c_{o,2}$, $\bar{\Lambda}_{22} = 1/c_o^2$, $\bar{\Lambda}_{33} = \bar{\rho}_2/c_{o,2}$, $\bar{\Lambda}_{44} = \bar{\rho}_2/c_{o,2}$, $\bar{\Lambda}_{55} = \bar{\rho}_2/(c_{o,2}\bar{B}_x)$, and express the resulting system of equations as:

$$\mathbf{L} \cdot \boldsymbol{Y} = \boldsymbol{X}, \tag{B.1.10}$$

where the scattering matrix, $\mathbf{L}$, is defined as, $\mathbf{L} \equiv \bar{\boldsymbol{\Lambda}}\mathbf{A}$, in which the refracted entropy mode contribution is given by the 1^{st} column of $\mathbf{L}$:

$$L_{11} = M_2, \tag{B.1.11}$$

$$L_{21} = M_2^2, \tag{B.1.12}$$

$$L_{31} = M_2 \delta_2, \tag{B.1.13}$$

$$L_{41} = 0, \tag{B.1.14}$$

$$L_{51} = -\frac{1}{\gamma - 1}, \tag{B.1.15}$$

$$L_{61} = 0, \tag{B.1.16}$$

$$L_{71} = 0. \tag{B.1.17}$$

The 2^{nd}, 3^{rd} and 4^{th} columns represent the forward fast, forward slow and backward slow magneto–acoustic modes respectively. The 2^{nd} column is given by:

$$L_{12} = M_2\hat{\rho}'_{f+} + \hat{u}'_{f+}, \tag{B.1.18}$$

$$L_{22} = (1 + M_2^2)\hat{\rho}'_{f+} + 2M_2\hat{u}'_{f+} + r_{x,2}\varepsilon_2\hat{B}'_{y,f+}, \tag{B.1.19}$$

$$L_{32} = M_2\delta_2\hat{\rho}'_{f+} + \delta_2\hat{u}'_{f+} + \hat{v}'_{f+} - \frac{r_{x,2}}{M_2}(\varepsilon_2\hat{B}'_{x,f+} + \hat{B}'_{y,f+}), \tag{B.1.20}$$

$$L_{42} = \hat{w}'_{f+} - \frac{r_{x,2}}{M_2}\hat{B}'_{z,f+}, \tag{B.1.21}$$

$$L_{52} = \hat{\rho}'_{f+} + M_2(1 + \varepsilon_2^2)\hat{u}'_{f+} - \frac{M_2^2\varepsilon_2}{r_{x,2}}(\varepsilon_2\hat{B}'_{x,f+} - \hat{B}'_{y,f+}), \tag{B.1.22}$$

$$L_{62} = \varepsilon_2\hat{u}'_{f+} - \hat{v}'_{f+} - \frac{\delta_2 M_2}{r_{x,2}}\hat{B}'_{x,f+} + \frac{M_2}{r_{x,2}}\hat{B}'_{y,f+}, \tag{B.1.23}$$

$$L_{72} = -\hat{w}'_{f+} + \frac{M_2}{r_{x,2}}\hat{B}'_{z,f+}. \tag{B.1.24}$$

To generate 3^{rd} and 4^{th} columns,"$f+$" in (B.1.18)-(B.1.24) is replaced with "$s+$" and "$s-$" respectively.

The 5^{th} and 6^{th} columns correspond to the forward and backward Alfvén modes respectively. The 5^{th} column is given by:

$$L_{12} = \hat{u}'_{A+}, \tag{B.1.25}$$

$$L_{22} = 2M_2\hat{u}'_{A+} + r_{x,2}\varepsilon_2\hat{B}'_{y,A+}, \tag{B.1.26}$$

$$L_{32} = \delta_2\hat{u}'_{A+} + \hat{v}'_{A+} - \frac{r_{x,2}}{M_2}(\varepsilon_2\hat{B}'_{x,A+} + \hat{B}'_{y,A+}), \tag{B.1.27}$$

$$L_{42} = \hat{w}'_{A+} - \frac{r_{x,2}}{M_2}\hat{B}'_{z,A+}, \tag{B.1.28}$$

$$L_{52} = M_2(1 + \varepsilon_2^2)\hat{u}'_{A+} - \frac{M_2^2\varepsilon_2}{r_{x,2}}(\varepsilon_2\hat{B}'_{x,A+} - \hat{B}'_{y,A+}), \tag{B.1.29}$$

$$L_{62} = \varepsilon_2\hat{u}'_{A+} - \hat{v}'_{A+} - \frac{\delta_2 M_2}{r_{x,2}}\hat{B}'_{x,A+} + \frac{M_2}{r_{x,2}}\hat{B}'_{y,A+}, \tag{B.1.30}$$

$$L_{72} = -\hat{w}'_{A+} + \frac{M_2}{r_{x,2}}\hat{B}'_{z,A+}. \tag{B.1.31}$$

To generate 6^{th} column,"$A+$" in (B.1.25)-(B.1.31) is replaced with "$A-$".

The 7^{th} column of $\mathbf{L}$ denotes the shock displacement contribution:

$$L_{15} = -\mathrm{i}\omega\left\{(\frac{1}{\eta_c} - 1) - M_2(\delta_1 - \delta_2)\tilde{k}_y R\right\}, \tag{B.1.32}$$

$$L_{25} = -\mathrm{i}\omega\left\{ M_2^2(\delta_2 - \eta_c\delta_1)\tilde{k}_y R \right\}, \tag{B.1.33}$$

$$L_{35} = -\mathrm{i}\omega\left\{ (\delta_1 - \delta_2) + R\tilde{k}_y M_2\left[(\eta_c - 1) - (\eta_c\delta_1^2 - \delta_2^2) + \frac{\varepsilon_1^2 r_{x,1}^2 \eta_c}{M_1^2} - \frac{\varepsilon_2^2 r_{x,2}^2}{M_2^2} \right] \right\}, \tag{B.1.34}$$

$$L_{45} = -\mathrm{i}\omega\{R\tilde{k}_z M_2(1 - \eta_c)\}, \tag{B.1.35}$$

$$L_{55} = -\mathrm{i}\omega\left\{ M_2[(1+\varepsilon_1^2)\eta_c - (1+\varepsilon_2^2)] - M_2^2[\eta_c^2(1+\varepsilon_1^2)(\delta_1 - \varepsilon_1) - (1+\varepsilon_2^2)(\delta_2 - \varepsilon_2)]\tilde{k}_y R \right\}, \tag{B.1.36}$$

$$L_{65} = -\mathrm{i}\omega\{\varepsilon_1 - \varepsilon_2\}, \tag{B.1.37}$$

$$L_{75} = 0, \tag{B.1.38}$$

where $\tilde{k}_y = k_y/(\omega/c_{o,1})$ and $\tilde{k}_z = k_z/(\omega/c_{o,1})$.

The input vector, $\boldsymbol{X} \equiv \bar{\boldsymbol{\Lambda}}\mathbf{T}_1\boldsymbol{\xi}_1$, in (B.1.10), for an entropy mode, $\boldsymbol{e}_1 = [1,\, 0,\, 0,\, 0,\, 0,\, 0,\, 0,\, 0]^{\intercal}$, is given by:

$$X_1 = M_1/R, \tag{B.1.39}$$

$$X_2 = \frac{M_1^2}{R^2}, \tag{B.1.40}$$

$$X_3 = \frac{M_1\delta_1\eta_c}{R}, \tag{B.1.41}$$

$$X_4 = 0, \tag{B.1.42}$$

$$X_5 = -\frac{\eta_c}{R^2(\gamma - 1)}, \tag{B.1.43}$$

$$X_6 = 0, \tag{B.1.44}$$

$$X_7 = 0. \tag{B.1.45}$$

$\boldsymbol{X}$ for an impinging magneto–acoustic mode, $\boldsymbol{e}_1 = [\hat{\rho}'_{f,s\pm},\, \hat{\boldsymbol{u}}'^{\intercal}_{f,s\pm},\, \hat{\rho}'_{f,s\pm},\, \hat{\boldsymbol{B}}'^{\intercal}_{f,s\pm}]^{\intercal}$, computed as a function of the incident wavevector and upstream base flow ($\bar{\boldsymbol{\mu}}_1$), is given by:

$$X_1 = \frac{1}{R}\left\{ M_1\hat{\rho}'_m + \hat{u}'_m \right\}, \tag{B.1.46}$$

$$X_2 = \frac{1}{R^2}\left\{ (1 + M_1^2)\hat{\rho}'_m + 2M_1\hat{u}'_m + r_{x,1}\varepsilon_1\hat{B}'_{y,m} \right\}, \tag{B.1.47}$$

$$X_3 = \frac{\eta_c}{R}\left\{ M_1\delta_1\hat{\rho}'_m + \delta_1\hat{u}'_m + \hat{v}'_m - \frac{r_{x,1}}{M_1}(\varepsilon_1\hat{B}'_{x,m} + \hat{B}'_{y,m}) \right\}, \tag{B.1.48}$$

$$X_4 = \frac{\eta_c}{R}\left\{ \hat{w}'_m - \frac{r_{x,1}}{M_1}\hat{B}'_{z,m} \right\}, \tag{B.1.49}$$

$$X_5 = \frac{\eta_c}{R^2}\left\{ \hat{\rho}'_m + M_1(1+\varepsilon_1^2)\hat{u}'_m - \frac{M_1^2\varepsilon_1}{r_{x,1}}(\varepsilon_1\hat{B}'_{x,m} - \hat{B}'_{y,m}) \right\}, \tag{B.1.50}$$

$$X_6 = \frac{\eta_c}{R}\left\{ \varepsilon_1\hat{u}'_m - \hat{v}'_m - \frac{\delta_1 M_1}{r_{x,1}}\hat{B}'_{x,m} + \frac{M_1}{r_{x,1}}\hat{B}'_{y,m} \right\}, \tag{B.1.51}$$

$$X_7 = \frac{\eta_c}{R}\left\{ -\hat{w}'_m + \frac{M_1}{r_{x,1}}\hat{B}'_{z,m} \right\}, \tag{B.1.52}$$

where subscript "m" can represent "$f+$", "$f-$","$s+$" or "$s-$".

$\boldsymbol{X}$ for an impinging Alfvén mode, $\boldsymbol{e}_1 = [0,\, \boldsymbol{u}_A'^{\intercal},\, 0,\, \mp\sqrt{\bar{\rho}}\boldsymbol{u}_A'^{\intercal}]^{\intercal}$ computed as a function of the incident wavevector and upstream base flow ($\bar{\boldsymbol{\mu}}_1$), is given by:

$$X_1 = \frac{1}{R}\left\{\hat{u}_A'\right\}, \tag{B.1.53}$$

$$X_2 = \frac{1}{R^2}\left\{2M_1\hat{u}_A' + r_{x,1}\varepsilon_1\hat{B}_{y,A}'\right\}, \tag{B.1.54}$$

$$X_3 = \frac{\eta_c}{R}\left\{\delta_1\hat{u}_A' + \hat{v}_A' - \frac{r_{x,1}}{M_1}(\varepsilon_1\hat{B}_{x,A}' + \hat{B}_{y,A}')\right\}, \tag{B.1.55}$$

$$X_4 = \frac{\eta_c}{R}\left\{\hat{w}_A' - \frac{r_{x,1}}{M_1}\hat{B}_{z,A}'\right\}, \tag{B.1.56}$$

$$X_5 = \frac{\eta_c}{R^2}\left\{M_1(1+\varepsilon_1^2)\hat{u}_A' - \frac{M_1^2\varepsilon_1}{r_{x,1}}(\varepsilon_1\hat{B}_{x,A}' - \hat{B}_{y,A}')\right\}, \tag{B.1.57}$$

$$X_6 = \frac{\eta_c}{R}\left\{\varepsilon_1\hat{u}_A' - \hat{v}_A' - \frac{\delta_1 M_1}{r_{x,1}}\hat{B}_{x,A}' + \frac{M_1}{r_{x,1}}\hat{B}_{y,A}'\right\}, \tag{B.1.58}$$

$$X_7 = \frac{\eta_c}{R}\left\{-\hat{w}_A' + \frac{M_1}{r_{x,1}}\hat{B}_{z,A}'\right\}, \tag{B.1.59}$$

where subscript "A" can represent "$A+$"or "$A-$".

B.2 Scattering matrix: Decoupled perturbed shock system

The two–dimensional linearised Rankine–Hugoniot jump conditions for a perturbation–shock interaction in which the wavevector, magnetic field and shock normal all lie in the $x-y$ plane:

$$\mathbf{T}_2\boldsymbol{\mu}_{xy,2}' + \boldsymbol{R}\delta_s = \mathbf{T}_1\boldsymbol{\mu}_{xy,1}', \tag{B.2.1}$$

where $\boldsymbol{\mu}_{xy}' = [\rho', u', v', p', B_x', B_y']^{\intercal}$,

$$\mathbf{T} = \begin{bmatrix} \bar{u} & \bar{\rho} & 0 & 0 & 0 & 0 \\ \bar{u}^2 & 2\bar{\rho}\bar{u} & 0 & 1 & 0 & \bar{B}_y \\ \bar{v}/\bar{\rho} & \bar{v}/\bar{u} & 1 & 0 & -\bar{B}_y/(\bar{\rho}\bar{u}) & -\bar{B}_x/(\bar{\rho}\bar{u}) \\ -c_o^2/\bar{\rho}(\gamma-1) & \bar{u}\bar{B}^2/\bar{B}_x^2 & 0 & \gamma/\bar{\rho}(\gamma-1) & -\bar{u}^2\bar{B}_y^2/\bar{B}_x^3 & \bar{u}^2\bar{B}_y/\bar{B}_x^2 \\ 0 & \bar{B}_y & -\bar{B}_x & 0 & -\bar{v} & \bar{u} \end{bmatrix},$$

$$\boldsymbol{R} = \begin{bmatrix} \mathrm{i}[\![\bar{\rho}(\omega - \bar{v}k_y)]\!] \\ \mathrm{i}\bar{\rho}\bar{u}[\![\bar{v}k_y]\!] \\ -\mathrm{i}[\![\omega\bar{v}/\bar{u}]\!] - \mathrm{i}[\![k_y(\bar{u} - \bar{u}_y^2/\bar{u} + \bar{B}_y^2/(\bar{\rho}\bar{u}))]\!] \\ -\mathrm{i}(1/\bar{B}_x^2)[\![\omega\bar{B}^2\bar{u}]\!] + [\![k_y(\bar{u}\bar{B}^2/\bar{B}_x^3)(\bar{v}\bar{B}_x - \bar{u}\bar{B}_y)]\!] \\ -\mathrm{i}[\![\omega\bar{B}_y]\!] \end{bmatrix}.$$

An arbitrary disturbance composed of a single wave mode, impinging the upstream side of the shock is given as:

$$\boldsymbol{\mu}'_{xy,1} = \boldsymbol{\xi}_1^{xy} \mathrm{e}^{\mathrm{i}[\boldsymbol{k}_1 \cdot \boldsymbol{x} - \omega t]}, \tag{B.2.2}$$

where $\boldsymbol{\xi}_1^{xy} \equiv \boldsymbol{e}_1^{xy}$, in which $\boldsymbol{e}_1^{xy}$ is the eigenvector of the impinging mode redefined in the $x-y$ plane and $\boldsymbol{k}_1 \equiv [k_{x,1},\, k_y,\, 0]^\intercal$.

Perturbations on the downstream side decomposed into entropy/magneto–acoustic eigenmodes leaving the shock:

$$\begin{aligned} \boldsymbol{\mu}'_{xy,2} = \boldsymbol{\xi}_E^{xy} \mathrm{e}^{[\mathrm{i}(\boldsymbol{k}_E \cdot \boldsymbol{x} - \omega t)]} \quad + \quad \boldsymbol{\xi}_{f+}^{xy} \mathrm{e}^{[\mathrm{i}(\boldsymbol{k}_{f+} \cdot \boldsymbol{x} - \omega t)]} \quad + \\ + \quad \boldsymbol{\xi}_{s+}^{xy} \mathrm{e}^{[\mathrm{i}(\boldsymbol{k}_{s+} \cdot \boldsymbol{x} - \omega t)]} \quad + \quad \boldsymbol{\xi}_{s-}^{xy} \mathrm{e}^{[\mathrm{i}(\boldsymbol{k}_{s-} \cdot \boldsymbol{x} - \omega t)]}, \end{aligned} \tag{B.2.3}$$

where $\boldsymbol{k}_\mu \equiv [k_{x,\mu}, k_y, 0]^\intercal$, such that $\boldsymbol{k}_\mu \cdot \bar{\boldsymbol{u}} = \omega - \omega_{0\mu}$ and $\boldsymbol{\xi}_\mu^{xy} \equiv \chi_\mu \boldsymbol{e}_\mu^{xy}$, in which χ_μ is the unknown refraction coefficient and $\boldsymbol{e}_\mu^{xy}$ is the eigenvector of a given mode, redefined in the $x-y$ plane, for the entropy mode, $\boldsymbol{e}_E^{xy} = [1,0,0,0,0,0]^\intercal$, and the magneto–acoustic modes, $\boldsymbol{e}_{f,s\pm}^{xy} = [\rho'_{f,s\pm},\, u'_{f,s\pm},\, v'_{f,s\pm},\, c_o^2 \rho'_{f,s\pm},\, B'_{x,f,s\pm},\, B'_{y,f,s\pm}]^\intercal$, computed as a function of the respective refracted wavevectors and downstream base flow ($\bar{\boldsymbol{\mu}}_2$).

Analogously to (B.1.4):

$$\boldsymbol{\xi}_\mu^{xy} = \chi_\mu \boldsymbol{e}_\mu^{xy} = \hat{\chi}_\mu \boldsymbol{\Lambda}_{xy}^{-1} \hat{\boldsymbol{e}}_\mu^{xy}, \tag{B.2.4}$$

where $\hat{\chi}_\mu \equiv \chi_\mu ||\check{\boldsymbol{e}}_\mu^{xy}||$ and $\boldsymbol{\Lambda}_{xy}$ is a 6×6 diagonal matrix in which, $\Lambda_{xy,11} = 1$, $\Lambda_{xy,22} = \Lambda_{xy,33} = \bar{\rho}/c_o$, $\Lambda_{xy,44} = 1/(c_o^2)$, $\Lambda_{xy,55} = \Lambda_{xy,66} = \sqrt{\bar{\rho}}/c_o$.

As such, the transformation of perturbed flow properties to the eigenmode basis is given by:

$$\boldsymbol{\mu}'_{xy,2} = \boldsymbol{\Lambda}_{xy}^{-1} \hat{\mathbf{E}} \hat{\boldsymbol{Y}}, \tag{B.2.5}$$

where $\boldsymbol{Y}$ is a complex-valued vector of the unknown eigenmode refraction coefficients, $\hat{\boldsymbol{Y}} \equiv [\hat{\chi}_E, \hat{\chi}_{f+}, \hat{\chi}_{s+}, \hat{\chi}_{s-}]^\intercal$, where $\hat{\chi}_\mu = \chi_\mu ||\check{\boldsymbol{e}}_\mu||$, and $\hat{\mathbf{E}}$ is a 6×4 linear mapping matrix whose columns are given by the unitary eigenvectors of the downstream eigenmodes:

$$\hat{\mathbf{E}} = \begin{bmatrix} 1 & \hat{\rho}'_{f+} & \hat{\rho}'_{s+} & \hat{\rho}'_{s-} \\ 0 & \hat{u}'_{f+} & \hat{u}'_{s+} & \hat{u}'_{s-} \\ 0 & \hat{v}'_{f+} & \hat{v}'_{s+} & \hat{v}'_{s-} \\ 0 & \hat{p}'_{f+} & \hat{p}'_{s+} & \hat{p}'_{s-} \\ 0 & \hat{B}'_{x,f+} & \hat{B}'_{x,s+} & \hat{B}'_{x,s-} \\ 0 & \hat{B}'_{y,f+} & \hat{B}'_{y,s+} & \hat{B}'_{y,s-} \end{bmatrix} \tag{B.2.6}$$

The following matrix augmentations are then performed:

$$\mathbf{A} = (\hat{\mathbf{T}}_2|\boldsymbol{R}) \quad \text{and} \quad \mathbf{E} = \left(\frac{\mathbf{E}^*}{\boldsymbol{c}}\right), \tag{B.2.7a,b}$$

where $\hat{\mathbf{T}}_2 \equiv \mathbf{T}_2\boldsymbol{\Lambda}_{xy}^{-1}$, $\boldsymbol{c} = [0,\ 0,\ 0,\ 0,\ 1]$ and $\mathbf{E}^* = (\hat{\mathbf{E}}|\boldsymbol{d})$, in which $\boldsymbol{d}$ is a 6−dimensional null column vector. Applying and to (B.2.1), we now write the linearised Rankine–Hugoniot jump conditions in the form:

$$\mathbf{AE}\boldsymbol{Y} = \mathbf{T}_1\boldsymbol{\xi}_1, \tag{B.2.8}$$

where $\boldsymbol{Y} \equiv [\hat{\chi}_E,\ \hat{\chi}_{f+},\ \hat{\chi}_{s+},\ \hat{\chi}_{s-},\ \delta_s]^\intercal$.

Finally, we multiply both sides of (B.2.8) by a 5×5 diagonal matrix, $\bar{\boldsymbol{\Lambda}}$, where $\bar{\Lambda}_{11} = 1/c_{o,2}$, $\bar{\Lambda}_{22} = 1/c_o^2$, $\bar{\Lambda}_{33} = \bar{\rho}_2/c_{o,2}$, $\bar{\Lambda}_{44} = \bar{\rho}_2/c_{o,2}$, $\bar{\Lambda}_{55} = \bar{\rho}_2/(c_{o,2}\bar{B}_x)$, and express the resulting system of equations as:

$$\mathbf{L} \cdot \boldsymbol{Y} = \boldsymbol{X}, \tag{B.2.9}$$

where the scattering matrix, $\mathbf{L}$, is defined as, $\mathbf{L} \equiv \bar{\boldsymbol{\Lambda}}\mathbf{A}$, in which the refracted entropy mode contribution is given by the 1^{st} column of $\mathbf{L}$:

$$L_{11} = M_2, \tag{B.2.10}$$

$$L_{21} = M_2^2, \tag{B.2.11}$$

$$L_{31} = M_2\delta_2, \tag{B.2.12}$$

$$L_{41} = -\frac{1}{\gamma - 1}, \tag{B.2.13}$$

$$L_{51} = 0, \tag{B.2.14}$$

The 2^{nd}, 3^{rd} and 4^{th} columns represent the forward fast, forward slow and backward slow magneto–acoustic modes respectively. The 2^{nd} column is given by:

$$L_{12} = M_2\hat{\rho}'_{f+} + \hat{u}'_{f+}, \tag{B.2.15}$$

$$L_{22} = (1 + M_2^2)\hat{\rho}'_{f+} + 2M_2\hat{u}'_{f+} + r_{x,2}\varepsilon_2\hat{B}'_{y,f+}, \tag{B.2.16}$$

$$L_{32} = M_2\delta_2\hat{\rho}'_{f+} + \delta_2\hat{u}'_{f+} + \hat{v}'_{f+} - \frac{r_{x,2}}{M_2}(\varepsilon_2\hat{B}'_{x,f+} + \hat{B}'_{y,f+}), \tag{B.2.17}$$

$$L_{42} = \hat{\rho}'_{f+} + M_2(1 + \varepsilon_2^2)\hat{u}'_{f+} - \frac{M_2^2\varepsilon_2}{r_{x,2}}(\varepsilon_2\hat{B}'_{x,f+} - \hat{B}'_{y,f+}), \tag{B.2.18}$$

$$L_{52} = \varepsilon_2\hat{u}'_{f+} - \hat{v}'_{f+} - \frac{\delta_2 M_2}{r_{x,2}}\hat{B}'_{x,f+} + \frac{M_2}{r_{x,2}}\hat{B}'_{y,f+}. \tag{B.2.19}$$

To generate the 3^{rd} and 4^{th} columns,"$f+$" in (B.2.15)-(B.2.19) is replaced with "$s+$" and "$s-$" respectively. The 5^{th} column of $\mathbf{L}$ denotes the shock displacement contribution:

$$L_{15} = -\mathrm{i}\omega\left\{(\frac{1}{\eta_c} - 1) - M_2(\delta_1 - \delta_2)\tilde{k}_y R\right\}, \tag{B.2.20}$$

$$L_{25} = -\mathrm{i}\omega\left\{M_2^2(\delta_2 - \eta_c\delta_1)\tilde{k}_y R\right\}, \tag{B.2.21}$$

$$L_{35} = -\mathrm{i}\omega\left\{(\delta_1 - \delta_2) + R\tilde{k}_y M_2\left[(\eta_c - 1) - (\eta_c\delta_1^2 - \delta_2^2) + \frac{\varepsilon_1^2 r_{x,1}^2\eta_c}{M_1^2} - \frac{\varepsilon_2^2 r_{x,2}^2}{M_2^2}\right]\right\}, \tag{B.2.22}$$

$$L_{45} = -\mathrm{i}\omega\left\{M_2[(1+\varepsilon_1^2)\eta_c - (1+\varepsilon_2^2)] - M_2^2[\eta_c^2(1+\varepsilon_1^2)(\delta_1 - \varepsilon_1) - (1+\varepsilon_2^2)(\delta_2 - \varepsilon_2)]\tilde{k}_y R\right\}, \tag{B.2.23}$$

$$L_{55} = -\mathrm{i}\omega\{\varepsilon_1 - \varepsilon_2\}. \tag{B.2.24}$$

where $\tilde{k}_y = k_y/(\omega/c_{o,1})$.

The input vector, $\boldsymbol{X} \equiv \bar{\boldsymbol{\Lambda}}\mathbf{T}_1\boldsymbol{\xi}_1$, in (B.2.9), for an impinging entropy mode, $\boldsymbol{e}_1^{xy} = [1,\, 0,\, 0,\, 0,\, 0,\, 0]^\intercal$, is given by:

$$X_1 = \frac{M_1}{R}, \tag{B.2.25}$$

$$X_2 = \frac{M_1^2}{R^2}, \tag{B.2.26}$$

$$X_3 = \frac{M_1\delta_1\eta_c}{R}, \tag{B.2.27}$$

$$X_4 = -\frac{\eta_c}{R^2(\gamma - 1)}, \tag{B.2.28}$$

$$X_5 = 0, \tag{B.2.29}$$

and for an impinging magneto–acoustic mode, $\boldsymbol{e}_1^{xy} = [\hat{\rho}'_{f,s\pm},\, \hat{u}'_{f,s\pm},\, \hat{v}'_{f,s\pm},\, \hat{\rho}'_{f,s\pm},\, \hat{B}'_{x,f,s\pm},\, \hat{B}'_{y,f,s\pm}]^\intercal$, computed as a function of the incident wavevector and upstream base flow ($\bar{\boldsymbol{\mu}}_1$), is given by:

$$X_1 = \frac{1}{R}\left\{M_1\hat{\rho}'_m + \hat{u}'_m\right\}, \tag{B.2.30}$$

$$X_2 = \frac{1}{R^2}\left\{(1 + M_1^2)\hat{\rho}'_m + 2M_1\hat{u}'_m + r_{x,1}\varepsilon_1\hat{B}'_{y,m}\right\}, \tag{B.2.31}$$

$$X_3 = \frac{\eta_c}{R}\left\{M_1\delta_1\hat{\rho}'_m + \delta_1\hat{u}'_m + \hat{v}'_m - \frac{r_{x,1}}{M_1}(\varepsilon_1\hat{B}'_{x,m} + \hat{B}'_{y,m})\right\}, \tag{B.2.32}$$

$$X_4 = \frac{\eta_c}{R^2}\left\{\hat{\rho}'_m + M_1(1+\varepsilon_1^2)\hat{u}'_m - \frac{M_1^2\varepsilon_1}{r_{x,1}}(\varepsilon_1\hat{B}'_{x,m} - \hat{B}'_{y,m})\right\}, \tag{B.2.33}$$

$$X_5 = \frac{\eta_c}{R}\left\{\varepsilon_1\hat{u}'_m - \hat{v}'_m - \frac{\delta_1 M_1}{r_{x,1}}\hat{B}'_{x,m} + \frac{M_1}{r_{x,1}}\hat{B}'_{y,m}\right\}, \tag{B.2.34}$$

where subscript "m" can represent "$f+$", "$f-$","$s+$" or "$s-$".